



HAL
open science

Synthesis and characterization of nanoresonators for metamaterials application in the Visible range

Aurélie Le Beulze Le Beulze

► **To cite this version:**

Aurélie Le Beulze Le Beulze. Synthesis and characterization of nanoresonators for metamaterials application in the Visible range. Material chemistry. Université Sciences et Technologies - Bordeaux I, 2013. English. NNT : 2013BOR14898 . tel-01118724

HAL Id: tel-01118724

<https://theses.hal.science/tel-01118724>

Submitted on 19 Feb 2015

HAL is a multi-disciplinary open access archive for the deposit and dissemination of scientific research documents, whether they are published or not. The documents may come from teaching and research institutions in France or abroad, or from public or private research centers.

L'archive ouverte pluridisciplinaire **HAL**, est destinée au dépôt et à la diffusion de documents scientifiques de niveau recherche, publiés ou non, émanant des établissements d'enseignement et de recherche français ou étrangers, des laboratoires publics ou privés.

THÈSE

PRÉSENTÉE A

L'UNIVERSITÉ BORDEAUX 1

ÉCOLE DOCTORALE DES SCIENCES CHIMIQUES

Par **Aurélie LE BEULZE**

POUR OBTENIR LE GRADE DE

DOCTEUR

SPÉCIALITÉ : Physico-Chimie de la Matière Condensée

**Synthèse et caractérisation de nano-résonateurs pour une
application métamatériaux dans le domaine du Visible**

**Synthesis and characterization of nanoresonators for
metamaterials application in the Visible range**

Soutenue le : 20 Novembre 2013

Devant la commission d'examen formée de :

Mme TESTARD Fabienne,
M. PETIT Christophe,

Chercheur, CEA,
Professeur, UPMC,

Rapporteurs

M. MAGLIONE Mario,
M. CORREA-DUARTE Miguel,
M. SIMOVSKI Constantin,
M. BAROIS Philippe,

Directeur de Recherche, CNRS,
Professeur, Université de Vigo,
Professeur, Université d'Helsinki,
Directeur de Recherche, CNRS,

Président
Examineurs

M. DUGUET Etienne,
Mme TREGUER-DELAPIERRE Mona,

Professeur, Université de Bordeaux I,
Maitre de Conférence, Université de Bordeaux I

Directeurs de thèse

Remerciements

Cette thèse a eu lieu à l'Institut de Chimie de la Matière Condensée de Bordeaux au sein du groupe V « Chimie des nanomatériaux ». Je tiens donc en premier lieu à remercier Monsieur Claude Delmas pour m'avoir accueillie au sein de son laboratoire.

J'exprime toute ma gratitude à Fabienne Testard et Christophe Petit d'avoir accepté de rapporter cette thèse, ainsi qu'à Constantin Simovski, Miguel Correa-Duarte et Philippe Barois pour leur participation à mon jury de thèse et à Mario Maglione de l'avoir présidé. Je les remercie sincèrement pour l'intérêt qu'ils ont manifesté envers ces travaux.

Je souhaite maintenant remercier chaleureusement mes directeurs de thèse – Mona Tréguer-Delapierre et Etienne Duguet – de m'avoir fait confiance, il y a près de trois ans, en m'invitant à rejoindre l'aventure des métamatériaux. Leur encadrement m'a permis de progresser tous les jours un peu plus et de découvrir plein de nouvelles choses. Je les remercie également pour leur patience, leur gentillesse ainsi que pour toute la confiance et la liberté qu'ils m'ont accordées pendant ces trois années pour mener à bien ce travail. Je remercie plus particulièrement Mona Tréguer-Delapierre pour tout le temps et l'énergie qu'elle m'a accordés et ses encouragements notamment lorsque les manips ne marchaient pas toujours comme je l'espérais.

Cette thèse s'inscrit dans le cadre du projet européen Metachem regroupant neuf laboratoires partenaires de sept pays différents aux disciplines dominantes différentes mais complémentaires. J'ai ainsi pu côtoyer des chercheurs passionnés d'horizons divers et participer à des réunions toujours très intéressantes un peu partout dans l'Europe. Merci notamment à Serge Ravaine, Stéphane Mornet, Philippe Barois, Jacques Leng, Mattéo Albani, Miguel Correa-Duarte et Constantin Simovski pour les nombreuses discussions qui ont permis l'avancement de mes travaux.

Je tiens également à remercier les autres collaborateurs avec qui j'ai eu la chance de travailler : Jérôme Majimel, Yannick Petit, Benoit Da Costa Fernandes, Julien Burgin, Pierre Langot, Etienne Pertreux, Anna Lombardi, Paolo Maioli, Aurélien Crut, Natalia del Fatti, Fabrice Vallée, Ovidiu Ersen, Ileana Florea, ...

Je remercie sincèrement Pascal Massé, Anthony Désert et Hélène Géhan avec qui j'ai pu partager, à différent moments de cette thèse, la 'galère' de l'argent et des framboises et qui ont fortement contribué à l'avancement de ce travail. Je remercie également Camille Adam – la stagiaire de master I que j'ai eu le plaisir d'encadrer – pour tout le travail sérieux qu'elle a pu fournir, contribuant ainsi grandement aux résultats de cette thèse.

J'ai eu la chance d'évoluer au sein de l'ICMCB, un institut qui présente de nombreux services nous facilitant le travail au quotidien comme l'accueil, la bibliothèque, les services de mission, de gestions, d'infrastructure, ... Merci à tous !

J'adresse bien entendu mes remerciements à l'ensemble des personnes du groupe V que j'ai eu le plaisir de côtoyer pendant ces trois années. Un immense merci à Lydia toujours présente pour rendre service et surtout en cas de bobos ou de coup de blues (surtout n'oublies pas, tu es la meilleure !). Je n'oublie pas non plus MHD, Graziella (et Jamal, Eva, Tasha, ...), Guy; mes collocs de bureau : Anthony, Hakim, Nora, Cyril, Laurent, David, Sergio ; et mes collègues de paillasses : Pépito, Célaïne, Steph, Quentin, Brice, Cybille, Christophe, Miguel, Romain. Merci pour tous les bons moments, votre bonne humeur, votre soutien et vos encouragements. Je souhaite aussi bonne chance aux petits jeunots pour la suite de leur thèse, vous verrez on finit tous par y arriver ...

Plus personnellement, je remercie toutes les personnes que j'ai rencontrées au cours de ces trois merveilleuses années et avec qui j'ai pu passer des moments inoubliables. Petit clin d'œil notamment à la team ADoC (Filou, Lio, Fred, Martin, Benoit, et tous ceux qui ont pris la relève) et tous ceux que j'ai pu rencontrer par le biais de l'association. Bien sûr j'ai une pensée toute particulière pour Manu, Romain et Jerem mais aussi Addline, Alex, Lionel, Matthieu, Seb, Gilles ... Merci à vous pour tous ces merveilleux moments et ces innombrables fous rires ! Je n'oublie pas non plus Oihan et Pompom – les rescapés de la team MI Kimie 4ever – à qui je souhaite que de bonnes choses pour la fin de leur thèse.

Enfin je ne pourrai terminer sans remercier mes parents qui ont toujours été là pour moi ainsi que mon frère et Delphine pour leur soutien constant et leurs encouragements.

Mille merci à tous !

Résumé de la thèse en français

Les métamatériaux forment une nouvelle classe de matériaux composites artificiels aux propriétés électromagnétiques extraordinaires. Ces propriétés inédites reposent sur l'inclusion, dans le métamatériau, de résonateurs plasmoniques dont la fabrication et l'assemblage posent un défi auquel se heurtent les techniques de gravure habituellement utilisées. Cette thèse est consacrée à la synthèse de ces nano-résonateurs de morphologie framboise. L'architecture de ces nano-résonateurs a été proposée par C. Simovski et al. afin de générer une « meta-réponse » (à la fois électrique et magnétique) dans le domaine du visible [Simovski09, Morits11, Vallecchi11]. Ils sont constitués d'une particule centrale diélectrique de 100 nm recouverte de nanoparticules plasmoniques, sphériques de 25 nm ou triangulaires (50 nm de long et 15 nm d'épaisseur). La figure suivante présente les différentes géométries de nano-résonateurs étudiées :

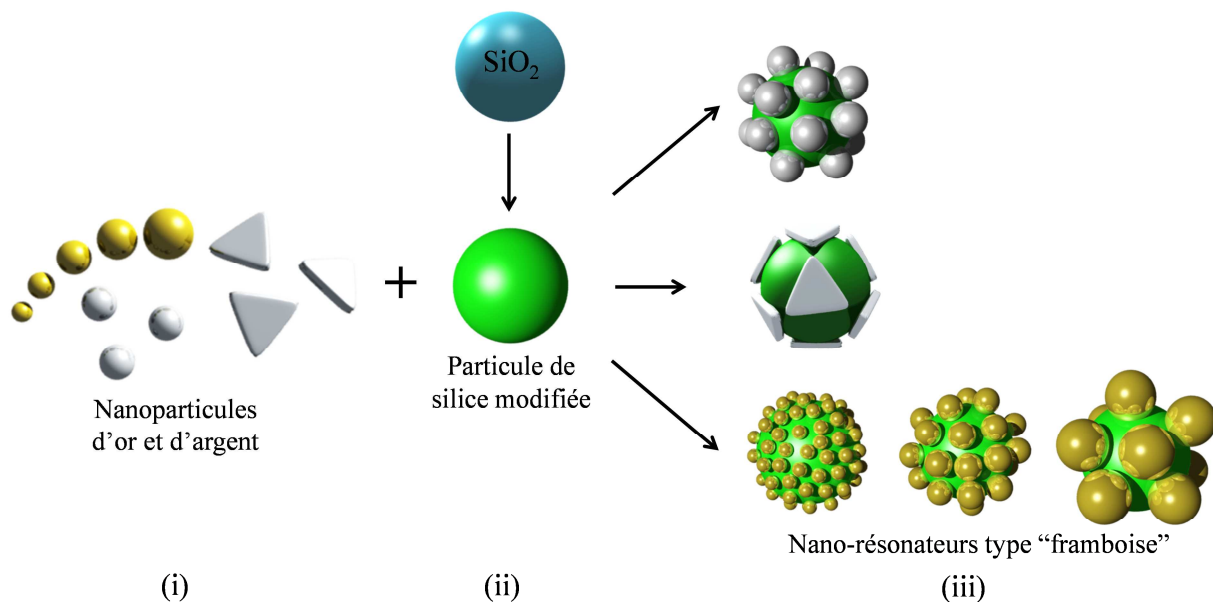


Figure 1 – Stratégie en 3 étapes adoptée dans cette thèse pour l'élaboration de nano-résonateurs type framboise : (i) synthèse des nanoparticules métalliques de différentes tailles, formes et compositions ; (ii) synthèse et modification de surface des particules de silice et (iii) assemblage des nanoparticules métalliques à la surface des particules de silice.

Si la synthèse des objets sphériques est relativement simple à mettre en œuvre, celle des nanoparticules triangulaires d'argent est délicate. L'objectif est de fabriquer ces différents nano-objets en grande quantité tout en respectant la contrainte du milieu effectif qui impose des tailles très inférieures à la longueur d'onde.

Le premier chapitre de cette thèse présente la synthèse des différentes nanoparticules métalliques élaborées au cours de cette étude (Figure 1-i et 2). Des nanoparticules sphériques d'argent de diamètre supérieur à 20 nm sont synthétisées en grande quantité par voie polyol. Des nanoparticules d'or de différents diamètres (de 10 à 50 nm) sont ensuite élaborées à l'aide d'une approche colloïdale de croissanceensemencée. Enfin deux stratégies de synthèse ont été étudiées

pour la croissance des nanoparticules triangulaires d'argent : la voie photochimique et la voie chimique par croissance de germes. La deuxième approche, permettant une production à plus grande échelle, a été optimisée afin d'obtenir une distribution en taille et en forme plus étroite des triangles d'argent synthétisés. L'étude systématique de différents paramètres (influence des germes, structure, influence des ligands, pH...) a permis de proposer un mécanisme de formation de ces triangles d'argent. La structure cristalline des objets a également été déterminée par microscopie électronique à transmission en haute résolution (HR-MET) et tomographie électronique. On a ainsi pu mettre en évidence la présence d'un défaut d'empilement dans le plan médian du triangle. A partir de ces triangles d'argent, des nano-disques d'argent, des nanocages d'or et des nano-triangles constitués d'un alliage or/argent ont pu être élaborés.

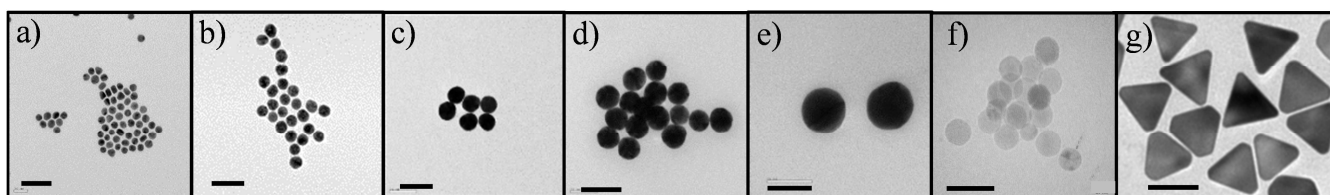


Figure 2 – Images MET des nanoparticules sphériques d'or de 10 à 50 nm (a – e), des nanoparticules sphériques d'argent de 26 nm (f), et des triangles d'argent mesurant 40 nm de côté et 5 nm d'épaisseur (g). Barres d'échelle : 50 nm.

Ces nanoparticules plasmoniques ont été ensuite assemblées à la surface d'une particule diélectrique (Figure 1-ii and -iii) pour former des nano-résonateurs type « framboises ». Ces objets ont été formés via des interactions électrostatiques entre les différentes entités.

- Une première stratégie a consisté à fonctionnaliser les particules de silice en greffant un aminosilane directement à la surface des particules. Cette méthode ne permet pas d'obtenir un bon taux de recouvrement des cœurs de silice et conduit à des problèmes d'instabilité colloïdale.

- Une deuxième stratégie de fonctionnalisation a donc été proposée. Celle-ci consiste au dépôt couche par couche de polymères chargés à la surface des particules de silice (Figure 3-a). Cette deuxième approche permet l'élaboration, de nano-résonateurs avec une forte densité de particules métalliques et une couverture plus homogène des cœurs de silice (Figure 3-d). Les nano-résonateurs formés par cette approche sont stables. L'objectif a donc été atteint, des nano-résonateurs type « framboises » ont été synthétisés en grande quantité. En encapsulant les nano-résonateurs dans une fine écorce de silice, leurs propriétés optiques ont été évaluées.

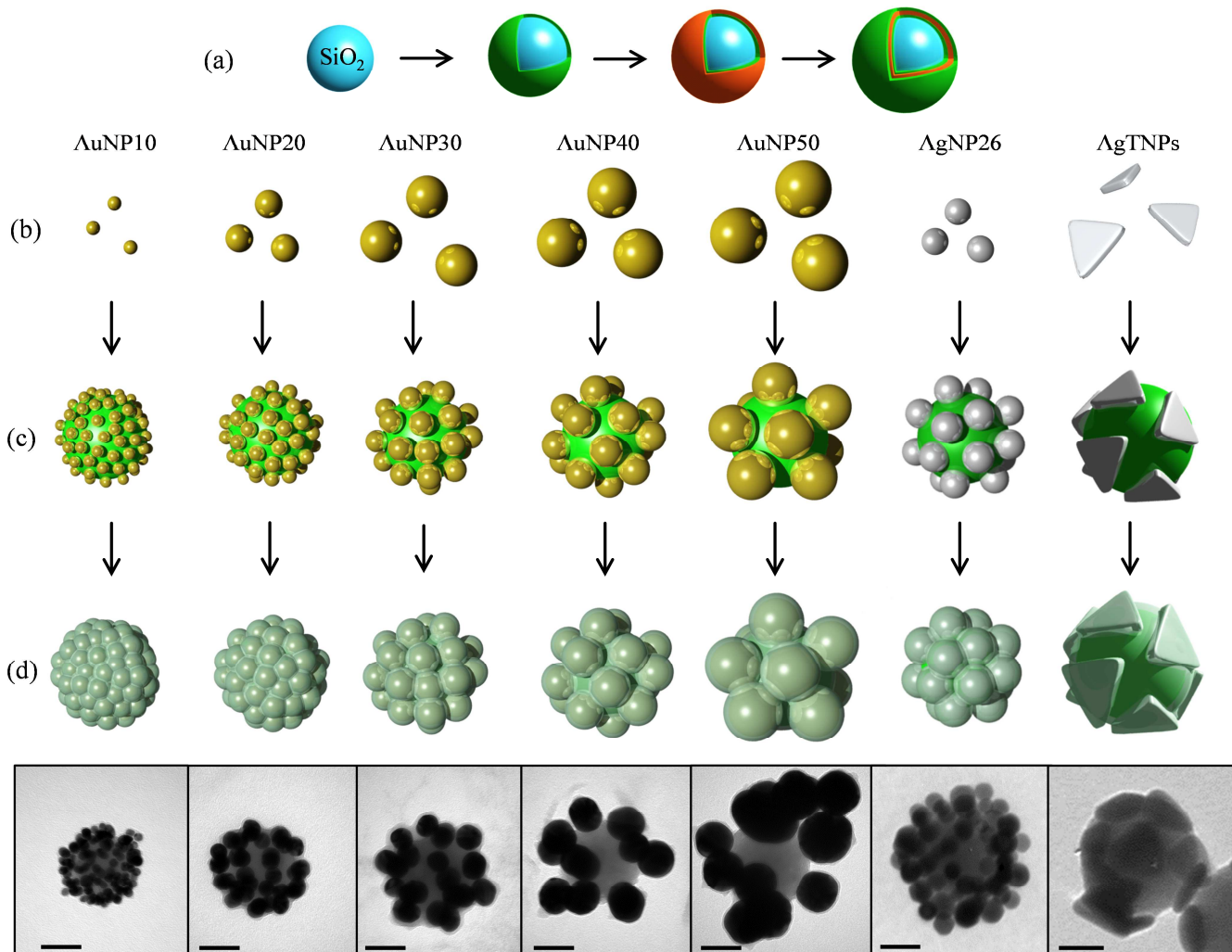


Figure 3 – Illustration des principaux objets colloïdaux obtenus. (a) Synthèse et modification de surface des particules de silice par dépôt couche à couche de polyélectrolytes ; (b) synthèse des nanoparticules métalliques ; (c) assemblage des nanoparticules métalliques à la surface des particules de silice pour former les nano-résonateurs type « framboises » ; (d) encapsulation des nano-résonateurs dans une fine écorce de silice et (bas) Images MET des nano-résonateurs type « framboises » obtenus par assemblage (de gauche à droite) de nanoparticules sphériques d’or (10 – 50 nm), de nanoparticules sphériques d’argent (26 nm), et de triangles d’argent (40 nm) sur des particules de silice de 100 nm. Barres d’échelle : 50 nm.

Les propriétés optiques de ces nano-résonateurs sont mesurées à la fois par spectroscopie d’absorption et/ou spectroscopie à modulation spatiale puis comparées aux simulations théoriques. La comparaison entre les spectres théoriques et expérimentaux suggère que les nano-résonateurs obtenus à partir des particules sphériques d’or ou d’argent ont les propriétés recherchées dans le visible (Figure 4). Des résonances électriques et magnétiques intenses ont été mises en évidence.

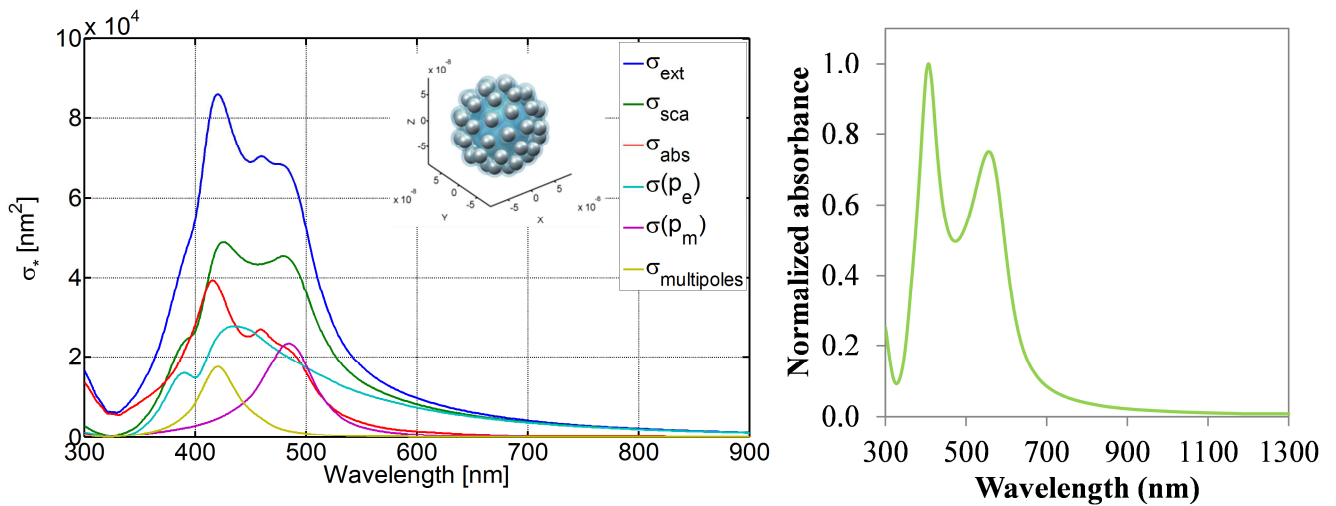


Figure 4 – Comparaison des spectres (gauche) théoriques et (droite) expérimentaux des nano-résonateurs type « framboises » obtenus à partir des nanoparticules d'argent de 26 nm.

Dans un futur proche, il serait intéressant de déterminer et quantifier expérimentalement ces deux contributions par diffusion de la lumière polarisée. [Sheikholeslami13] Il serait également intéressant de substituer la particule centrale de silice par des particules à « patches » - i.e. présentant des zones de fonctionnalités différentes – afin de contrôler le nombre et/ou l'orientation des particules satellites adsorbées en surface. Ceci devrait permettre de moduler et amplifier la réponse optique de ces nano-résonateurs.

L'ensemble de ces résultats est très prometteur pour la première réalisation de matériau massif à perméabilité magnétique artificielle.

References

- [Morits11] Morits D., Simovski C. *Metamaterials*, 2011. 5(4), p. 162
- [Sheikholeslami13] Sheikholeslami S.N., Alaeian H., Koh A.L., Dionne J.A. *Nano Lett.*, 2013. 13(9), p. 4137
- [Simovski09] Simovski C.R., Tretyakov S.A. *Phys. Rev. B*, 2009. 79(4), p. 045111
- [Vallecchi11] Vallecchi A., Albani M., Capolino F. *Opt. Express*, 2011. 19(3), p. 2754

Outline

List of abbreviations	1
Introduction	3
<i>What's a metamaterial?</i>	5
<i>Brief history</i>	6
<i>Some expected applications</i>	6
<i>The current challenges</i>	8
<i>Context of the European METACHEM project</i>	9
<i>Objectives of this thesis</i>	10
<i>References</i>	12
Chapter I – Synthesis of the metal satellite nanoparticles	13
<i>A. Main optical features of metallic nanoparticles</i>	15
<i>B. Synthesis of silver and gold spherical nanoparticles</i>	17
B.1 Synthesis of silver spherical nanoparticles of 20-30 nm diameter	18
B.2 Synthesis of gold spherical nanoparticles of 10-50 nm diameter	20
B.2.1 Synthesis of 10-nm gold nanoparticles	20
B.2.2 Growth of gold seeds into larger particles	22
<i>C. Synthesis of silver nanoprisms</i>	24
C.1 State of the art on the main features and the synthesis of silver nanoprisms.....	24
C.1.1 The main structural and optical features of silver nanoprisms	24
C.1.2 The different synthetic routes of silver nanoprisms	26
C.1.2.1 An example of template approach	27
C.1.2.2 The seed mediated growth	28
C.1.3 Synthesis strategy adopted in the present work	33
C.2 The photochemical route	35
C.2.1 Protocols	35
C.2.1.1 Synthesis of silver seeds	35
C.2.1.2 Photo-conversion process	35
C.2.2 Results	36
C.2.3 Conclusion	39
C.3 The chemical reduction approach	39
C.3.1 Optimized Experimental procedure	40
C.3.2 Study of the crystalline structure of the silver seeds and nanoprisms	42
C.3.3 Study of the influence of many parameters on the growth reaction of Ag nanoprisms	46
C.3.3.1 Influence of light and atmosphere	46
C.3.3.2 Role of seeds	47

C.3.3.3	Influence of seeds characteristics (size, nature) on the final morphology	49
C.3.3.4	Role of the capping agents	54
C.3.3.5	Role of the protonation state of the citrate and ascorbic acid on the final characteristic of nanoparticles	57
C.3.3.6	Can the citrate be substituted by another carboxyl compounds?	60
C.3.3.7	Considerations on the growth mechanism in carboxyl compounds additive systems	64
C.4	Chemical stability of the silver nanoprisms	68
C.5	Conclusion on the silver nanoprisms synthesis.....	71
D.	Summary	72
	References	73

Chapter II - Raspberry-like nanoclusters through the assembly of metal

	nanoparticles on silica beads	77
A.	<i>State of the art</i>	79
A.1	Driving forces for clustering of preformed nanoparticles	79
A.2	Raspberry-like nanoclusters by clustering of silica and metal nanoparticles	81
A.3	Summary	85
B.	<i>Synthesis of the silica beads as dielectric core particles</i>	86
B.1	Generalities	86
B.2	Synthesis of calibrated silica beads through the seeded-growth process	87
C.	<i>Assembly of metal nanoparticles on silica beads via the electrostatic approach</i>	90
C.1	“First generation” of raspberry-like nanoclusters	90
C.1.1	Functionalization of silica beads with an aminosilane	90
C.1.2	Assembly of silver spherical nanoparticles on EDPS-modified silica cores	94
C.1.2.1	Optical properties of the raspberry-like nanoclusters suspension	99
C.1.2.2	“Full” characterization of a single nanocluster	100
C.1.3	Assembly of silver nanoprisms on EDPS-modified silica beads	104
C.1.4	Conclusion	108
C.2	“Second generation” of raspberry-like nanoclusters	109
C.2.1	Surface modification of silica beads via Layer-by-Layer process	109
C.2.2	Assembly of silver spherical nanoparticles on PEM-modified silica beads	112
C.2.3	Assembly of gold spherical nanoparticles on PEM-modified silica beads	117
C.2.4	Assembly of silver nanoprisms on PEM-modified silica beads	123
C.2.6	Conclusion of the LbL assembly	124
C.3	Comparison of the UV-Visible absorption spectra with theoretical simulations	124
D.	Conclusion	131
	References	132

Overall conclusion	135
<i>Reference</i>	142
Annexes	143
<i>Annex 1: Characterization techniques</i>	145
<i>Annex 2: Anisotropic reactivity of silver nanoprisms</i>	155
<i>Annex 3: Principle of the microfluidic evaporation approach and preliminary test of extended assembly</i>	161
<i>Annex 4: Raman gain properties of the raspberry-like nanoclusters</i>	166
<i>Annex 5: List of reagents</i>	170
<i>Annex 6: Protocols</i>	171
<i>References</i>	178

List of Abbreviations

AA	Ascorbic acid
ADF	Angular dark field
APTES	(3-Aminopropyl)triethoxysilane
APTMS	(3-Aminopropyl)trimethoxysilane
BEM	Boundary element method
BF	Bright field
BIC	Bordeaux imaging center
BPE	Trans-1,2-bis(4-pyridyl)ethylene
BSPP	bis(p-sulfonatophenyl) phenylphosphine dehydrate dipotassium
CREMEM	Centre de Ressource en Microscopie Electronique et Microanalyse
CRPP	Centre de Recherche Paul Pascal
CTAB	Cethyltrimethylammonium bromide
DAS	4,4'-Diazido-2,2'-stilbenedisulfonic acid disodium salt
DDA	Discrete dipole approximation
DIISM	Department of information engineering and Mathematics
DLS	Dynamic light scattering
DMF	Dimethylformamide
DNA	Deoxyribonucleic acid
DRIFT	Diffuse reflectance infrared fourier transform
EDC	1-ethyl-3-(3-dimethylaminopropyl)carbodiimide
EDPS	<i>N</i> -[3-(Trimethoxysilyl)propyl]ethylenediamine
Fcc	Face-centered cubic
FDTD	Finite-difference time-domain
FEM	Finite element method
FWHM	Full width at half maximum
HRTEM	High resolution transmission electron microscopy
ICMCB	Institut de Chimie de la Matière Condensée de Bordeaux
ICP-OES	Inductively coupled plasma optical emission spectrometry
IEP	Isoelectric point
IPCMS	Institut de Physique et Chimie des Matériaux de Strasbourg
IR	Infrared
ITO	Indium Tin Oxide
LASIM	Laboratoire de Spectrométrie Ionique et Moléculaire
LB	Langmuir-Blodgett
LbL	Layer-by-Layer
LOF	Laboratory of Future
LS	Langmuir-Shaefer

MES	2-(<i>N</i> -morpholino)ethanesulfonic acid
MPS	sodium 3-mercapto-1-propanesulfate
MPTMS	(3-Mercaptopropyl)trimethoxysilane
MUA	11-mercaptoundecanoic acid
MUTAB	11-(Mercaptoundecyl)- <i>N,N,N</i> -trimethylammonium bromide
NC	Nanocluster
NIR	Near Infrared
NP	Nanoparticle
NSL	Nanospheres lithography
QCM	Quartz crystal microbalance
PA	Phenyl-acetylene
PAA	Polyacrylic acid
PAH	Poly(allylamine hydrochloride)
PBS	Phosphate buffered saline
PDDA	Polydiallyldimethylammonium chloride
PDI	Polydispersity index
PDMS	Polydimethylsiloxane
PEG	Poly(ethylene glycol)
PEI	Poly(ethyleneimine)
PEM	Polyelectrolytes multilayer
PS	Polystyrene
PSS	Poly(sodium styrene sulfonate)
PVP	Poly(vinylpyrrolidone)
SAM	Self-assembled monolayer
SDA	Single dipole approximation
SEM	Scanning electron microscopy
SERS	Surface enhanced raman scattering
SMS	Spatial modulation spectroscopy
SPLS	Single-particle light scattering
SPR	Surface plasmon resonance
SRR	Split-ring resonator
STEM	Scanning transmission electron microscopy
TEM	Transmission electron microscopy
TEOS	Tetraethylorthosilicate
TNP	Triangular nanoparticle
UPMC	Université Pierre et Marie Curie
UV-Vis	Ultraviolet-Visible

Introduction

A. What's a metamaterial?

Metamaterials are artificial composite materials exhibiting extraordinary physical properties, not observed in natural materials. This definition dates from the end of 1990s and qualifies different kind of artificial materials in electromagnetism, but also in optic, acoustic, mechanic, thermic, ...

In this study, we focused on electromagnetic metamaterials. In electromagnetism, a material could be described by both relative electric permittivity (ϵ_r) and magnetic permeability (μ_r). These two relative components allow to define the refractive index of the material:

$$n = \sqrt{\epsilon_r \mu_r} \quad (1)$$

It is possible to represent the different classes of materials in function of the values of the couple (ϵ , μ) (Figure 1). The white areas correspond to the conventional materials while the blue areas correspond to the metamaterials.

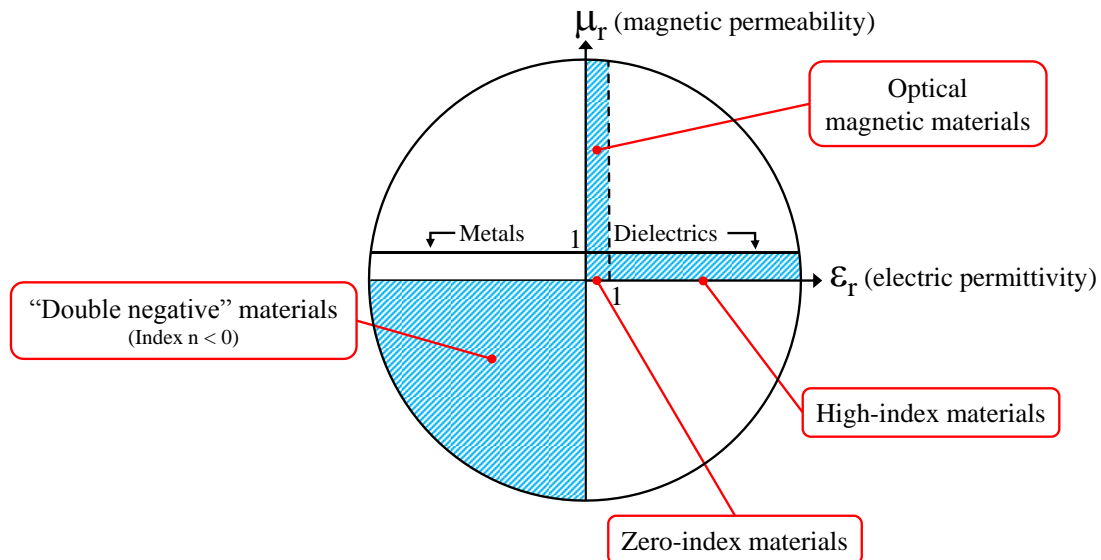


Figure 1 - Different values of permeability and permittivity that can adopt a material. White area: conventional materials, and blue area: metamaterials with values of μ and ϵ which don't yet exist.

The permittivity and permeability of a conventional material depend on the response of the different atoms (structural units) constituting the material. The original electromagnetic properties of the metamaterial are induced by an appropriate structuring of the material. The structural units of a metamaterial and the average distance between them have to be much smaller than the operational wavelength in order to the whole material appears macroscopically uniform. Thus for visible light, this “effective medium” requirement implies typical sizes of the structural units around a few tens of nanometers. Then the infinite possibilities to tailor shape and size of the building blocks but also to tune their composition, broaden the possibilities for the artificial material behavior.

B. Brief history

The notion of metamaterials was born in 1968 with V.G. Veselago which applied the Maxwell equations to materials with both negative relative permittivity and permeability in order to study the behavior of an electromagnetic wave in such material [Veselago68]. He showed that the electromagnetic wave propagation was permitted. He called these “double negative” materials “left-handed media” since the trihedral formed by the electric field, the magnetic field and the wave vector is indirect, contrary to conventional materials for which the trihedral is always direct. However the existence of this kind of materials remains hypothetical for thirty years because of the absence of materials with a negative magnetic permeability.

We are indebted to J.B. Pendry and coworkers for the first theoretical demonstration that it is possible to generate a magnetic response from objects without magnetic properties [Pendry98, Pendry99]. They proposed a medium constituted of “split-ring resonators” (SRR) with size much lower than the incident wavelength. Under the influence of the incident wavelength, the conductive material generates a circular current giving rise to a magnetic response.

It is in 2000 that D.R. Smith deserves credit [Smith00] for the experimental elaboration of the first double negative material in the gigahertz range by associating the network of split-ring resonators allowing the negative permeability with a material initially having a negative permittivity, the metals. Thus, their metamaterial was constituted to millimeter-sized square copper as split-ring resonators and copper wires, the whole giving both negative permeability and permittivity in the microwave regime (Figure 2). Later, they confirmed that double negative materials exhibited a negative refractive index [Shelby01].

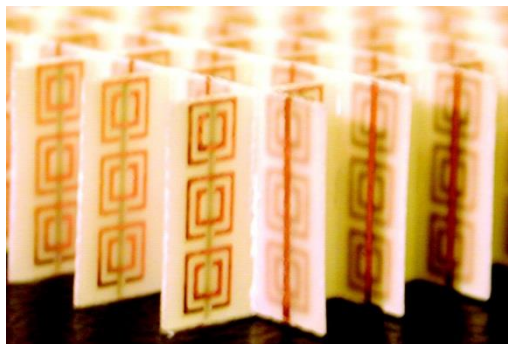


Figure 2 - Photograph of the first left-handed metamaterial consisting of square copper SRR and copper wire strips on fiber glass circuit board material. The rings and wires are on opposite sides of the boards, and the boards have been cut and assembled into an interlocking lattice [Shelby01].

C. Some expected applications

Since the first metamaterial manufactured in gigahertz range, the field of applications has been growing exponentially, opening up new horizons for optics, electromagnetism, telecommunications and information technology [Capolino09]. Many devices have been realized during the past years

and are based on the control of the wave propagation by using dynamic, re-configurable and tunable materials. An example of these devices is **superlenses** [Pendry00, Fang05]. These so-called perfect lenses use metamaterials to go beyond the diffraction limit, which is an inherent limitation in the conventional optical devices or lenses. Indeed, the light emitted or scattered from an object implies not only propagating waves but also evanescent waves, which carry the subwavelength detail of the object. The evanescent waves decay exponentially in any medium with a positive refractive index. Thus the evanescent waves cannot be collected at the image plane by using a conventional lens resulting in a diffraction-limited image. The use of a superlens, consisting of a planar metamaterial with a negative refractive index, allows to compensate for wave decay and to reconstruct the image of the object in the near field (Figure 3). Thus the resolution underneath the diffraction limit is possible.

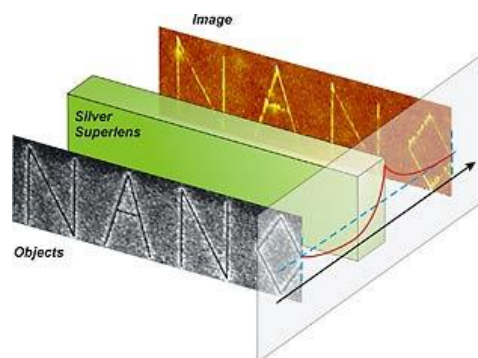


Figure 3 - Schematic drawing of nano-scale imaging using a silver superlens that achieves a resolution beyond the optical diffraction limit. The red line indicates the enhancement of "evanescent" waves as they pass through the superlens [Fang05].

Another application in optical field is **cloaking** where metamaterials are used to bend light around an object and so make it partially or wholly invisible to parts of the electromagnetic spectrum (Figure 4-left). The first experimental demonstration was another time proposed by the Pendry's team in the microwave range [Schurig06, Pendry06]. The metamaterial was a multilayer device constituted with an ensemble of circular films on which split-ring resonators are inscribed (Figure 4-right). The size of resonators evolves regularly from the inner circle to the outer circle conferring them different magnetic resonances. Thus the waveguide is allowed thanks to the modulation of the refractive index and more exactly of the magnetic permeability in the material.

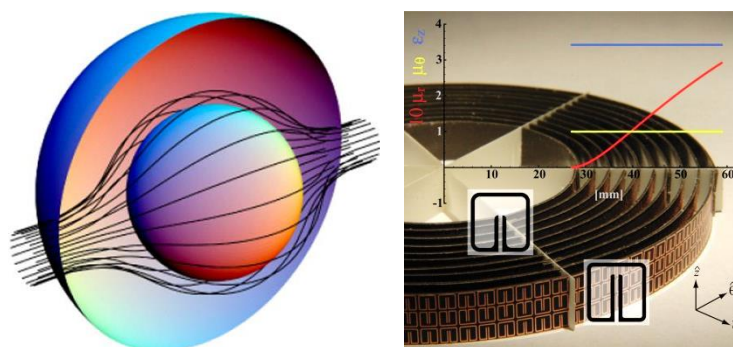


Figure 4 – (Left) 3D representation of an electromagnetic cloaking device [Pendry06]. (Right) Photograph of the first prototype cloaking device operating in microwaves range [Schurig06].

Metamaterials can also exhibit a strong localization and enhancement of fields so they can be used to actually improve the sensor selectivity of detecting nonlinear substances and to enable detection of extremely small amounts of analytes [Ishimaru05, Jaksic10].

D. The current challenges

With the powerful modern techniques of micro- and nano-lithography, the size of resonators has been stepwise decreased allowing the decrease of the operating wavelengths of metamaterials into the visible domain [Soukoulis11]. The Figure 5 presents the progresses in the operating frequencies of the metamaterials.

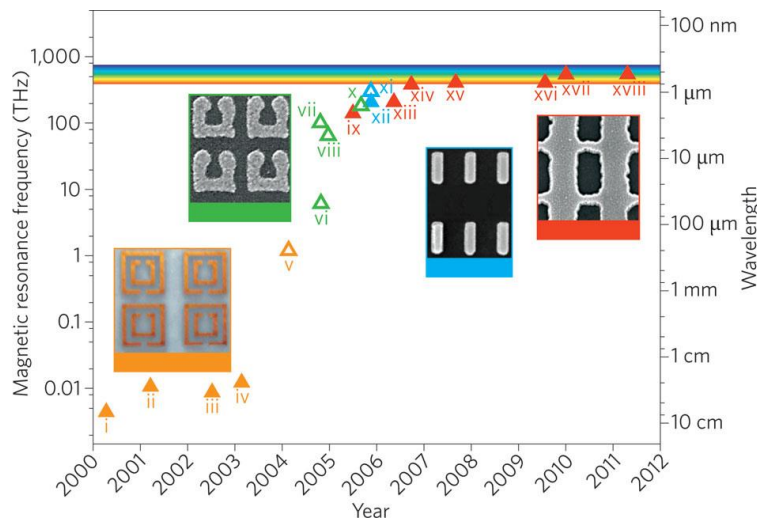


Figure 5 - Progress in metamaterial operating frequency over the past decade. The empty triangles corresponds to metamaterials with negative permeability and the solid triangles to metamaterials with a negative refractive index.

[Soukoulis11]

So far, theoretical and numerical studies on metamaterials for visible light have largely been conducted. However, the current limit to the advance of this kind of metamaterials remains the experimental section. Up to now, metamaterials have mostly been manufactured by “top-down” technologies like the electron beam lithography [Boltasseva08]. These techniques have the disadvantage of being quite expensive, slow and obtaining large areas and regular three-dimensional arrangements is difficult. Thus, huge fabrication challenges remain, especially for the most important case of three-dimensional devices: to manufacture a millimeter-size metamaterial sample from individual structural units, that requires the assembly of 10^{12} to 10^{15} nano-resonators together. The individual and direct manipulation of such a huge number of nano-objects seems unrealistic for large-scale applications. Thus, the combination of nano-chemistry, which is able to finely engineer the required building blocks, with self-assembly techniques (“bottom-up” approach), in which individual objects spontaneously organize under the effect of complex pair interactions into highly organized 2D or 3D structures of various symmetries, will open the way to new routes for the fabrication of metamaterials operating in the visible range.

E. Context of the European METACHEM project

This thesis is part of the European METACHEM research project which gathers 9 partners from 7 countries. The goal of METACHEM is to combine the extreme versatility of nano-chemistry with the science of self-assembly in order to design and manufacture a new generation of metamaterials operating in the infrared and visible range at a much lower cost than by electron lithography techniques. One of strategies proposed in the project consists in the fabrication of 3D isotropic metamaterials by self-assembling original nanoresonators which have precisely defined internal architecture and are able to generate meta-responses (both magnetic and electric). This concept is based on a very original idea from Alù *et al.* [Alu06] and its further extension by Simovski *et al.* [Simovski09]. The model consists in the use of raspberry-like nanoclusters made of plasmonic nanoparticles (gold or silver) covering a central dielectric particle as illustrated in the Figure 6 (left image).

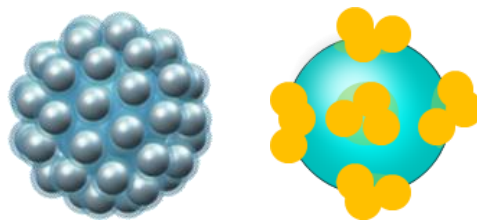


Figure 6 – Proposed design for nanocluster isotropic nanoresonators; (Left) General view of a cluster of metal colloids with dielectric core (Right) a nanocluster made of six plasmonic trimers on a dielectric core.

Simovski *et al.* [Simovski09, Morits11] demonstrated that this particular type of architecture allows the rise of both magnetic and electric resonances in the visible regime. The proposed design possesses an electric resonance due to the polarization of the metal nanoparticles being mainly parallel to the incident electric field (Figure 7-left) and a magnetic resonance by the effective polarization rings of metal nanoparticles around the dielectric core (Figure 7-right) [Vallecchi11]. This creates a negative magnetic permeability in a certain frequency range within the optical spectrum. Since this cluster structure also has a negative electric permittivity, it has been shown that, in a given frequency region, an optically dense array of these magnetic nanoclusters will make a double negative medium (negative index) operating in the visible range.

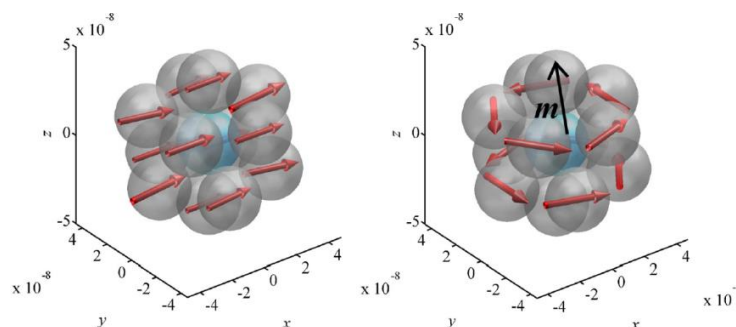


Figure 7 - (Left) Electric and (Right) magnetic resonant modes for a nanocluster. [Vallecchi11]

However, later they showed that the magnitude of the resonance was not enough for this cluster if the Drude model is replaced by experimental data obtained for permittivity of silver [Morits10].

Thus to overcome the strong Ohmic losses in order to obtain a real negative permeability, they proposed modifications of the nanocluster by replacing the plasmonic isotropic nanoparticles by plasmonic trimers (Figure 6-right) that should provide a stronger robustness of the magnetic response to Ohmic absorption in silver. Finally in 2011, they suggested a new modification of the magnetic nanocluster [Morits11], which is now formed by eight silver triangular nanoplates covering the dielectric core as illustrated in the Figure 8.

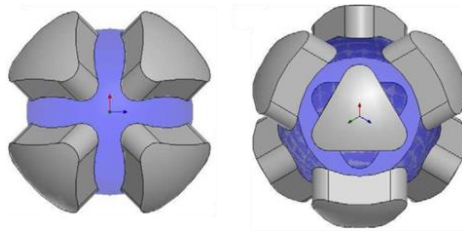


Figure 8 - A cluster made of eight plasmonic nanoprisms on a dielectric core (two points of view) [Morits11].

In both cases, the clusters diameter should be close to 100 nm to match the effective medium requirement in assembled composites (nanoclusters diameter $\ll \lambda$). Other phenomena such as diffuse scattering, diffraction, photonic band gap may occur as the clusters' diameter approaches the wavelength λ . From experiment point of view, Mühlig *et al.* have claimed optical magnetism at 660 nm for nanoclusters of size of 300 nm made of adhesion of gold particles of 20 nm onto a silica core of diameter 260 nm [Muhlig11]. The size to wavelength ratio is only $\frac{1}{2}$ and no effective medium can be formed with so big clusters. So far, no experimental data are available for smaller sizes.

F. Objectives of this thesis

The objective of this work is to fabricate the isotropic nanoresonators that will be self-assembled in order to fabricate artificial materials possessing 'meta' electromagnetic properties. Among the numerous synthetic methods that have been developed, the chemical solution approaches have been demonstrated to be a valuable route for obtaining nanocrystals and nanoparticles with high control on size, shape, monodispersity, which are crucial parameters for defining the final properties of such nano-sized matter. Such materials present many advantages over those obtained by other means owing to the flexibility, not only in synthesis conditions but also in post-synthesis processing.

Colloidal strategies in particular provide highly processable nano-objects, thanks to organic molecules layer present at the surface, which represents an adjustable interface with the external environment, thus allowing a careful control of the solubility and their specific chemical reactivity toward the surroundings.

Within this study, several nanostructures will be developed corresponding to electric and/or magnetic nanoresonators. They will be obtained by associating a small number of plasmonic particles in a well-controlled geometry. The goal is to focus on the synthesis of silver satellite

particles which is less lossy metal than gold. The following figure shows the geometry of the different nano-clusters under investigation:

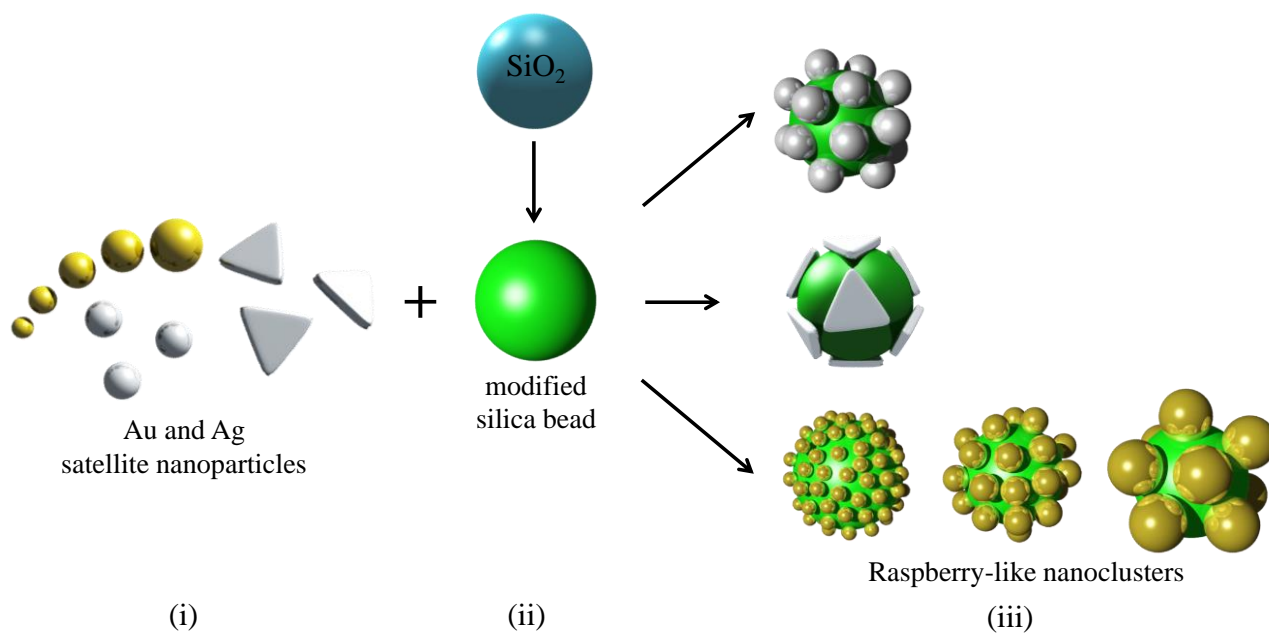


Figure 9 – Strategy in three steps adopted in this work to prepare the raspberry-like nanoclusters: (i) synthesis of various metal nanoparticles exhibiting different size, shape and composition; (ii) synthesis and surface modification of the silica beads and (iii) assembly of metal satellite nanoparticles on the silica core beads to form the raspberry-like nanoclusters.

Some of the design are very challenging for fabrication, in particular the one based on triangular silver particles. Other challenge will be to control the overall outer diameter of the different nanoclusters. The present project will be based on the development of nanoclusters based on the adhesion of spherical metallic particles of 25 nm and of triangular particles of 50 nm length and 15 nm thick onto a dielectric core of 80 nm. Of course, efforts will be also required to scale-up the synthesis so that a sufficient quantity of nanoclusters can be produced to form a 3D dense material made of a large number of nanoclusters. Once the nanoclusters will be prepared, they will be concentrated and assembled into a real material in a form of a solid sample suitable for optical characterization, without alteration of their magneto-electric response.

In the first chapter, the preparation of the different metal nanoparticles, subsequently used for the elaboration of the nanoclusters, is presented (Figure 9-i). These nanoparticles can be synthesized and scaled-up to produce sufficient quantities.

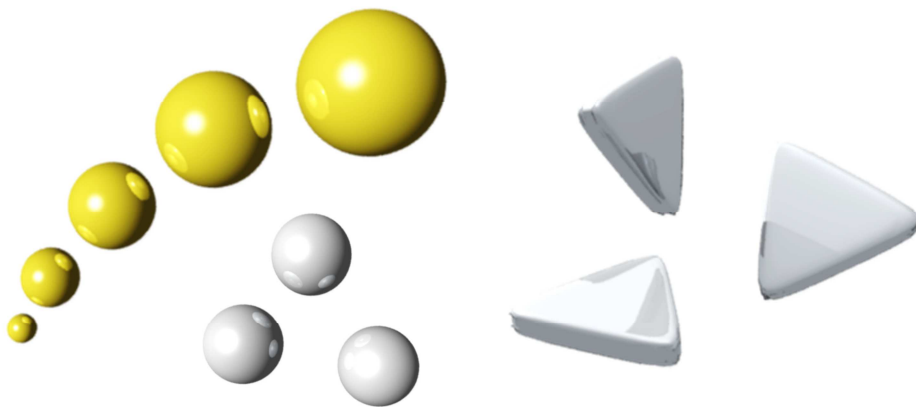
These optimized individual nanoparticles will be then self-assembled onto a preformed dielectric spherical colloid (Figure 9-ii and -iii) using direct chemistry functionalization approaches or exploiting electrostatic interactions. This is described in the Chapter 2. The optical properties of the as-produced nanoclusters will be also measured and compared to the computed-ones.

References

- [Alu06] Alu A., Salandrino A. *Opt. Express*, 2006. 14(4), p. 1557
- [Boltasseva08] Boltasseva A., Shalaev V.M. *Metamaterials*, 2008. 2(1), p. 1
- [Capolino09] Capolino F. *Applications of Metamaterials*. Taylor & Francis Group, 2009
- [Fang05] Fang N., Lee H., Sun C., Zhang X. *Science*, 2005. 308(5721), p. 534
- [Ishimaru05] Ishimaru A.S., Jaruwatanadilok, Kuga Y. *Progress In Electromagnetics Research*, 2005. 51, p. 139
- [Jaksic10] Jaksic Z., Vukovic S., Matovic J., Tanaskovic D. *Materials*, 2010. 4(1), p. 1
- [Morits10] Morits D.K., Simovski C.R. *Phys. Rev. B*, 2010. 81(20), p. 205112
- [Morits11] Morits D., Simovski C. *Metamaterials*, 2011. 5(4), p. 162
- [Muhlig11] Muhlig S., Cunningham A., Scheeler S., Pacholski C., BÅ¼rgi T., Rockstuhl C., Lederer F. *ACS Nano*, 2011. 5(8), p. 6586
- [Pendry98] Pendry J.B., Holden A.J., Robbins D.J., Stewart W.J. *J. Phys.: Condens. Matter*, 1998. 10, p. 4785
- [Pendry99] Pendry J., Holden A., Robbins D., Stewart W. *Microwave Theory and Techniques, IEEE Transactions on*, 1999. 47(11), p. 2075
- [Pendry00] Pendry J.B. *Phys. Rev. Lett.*, 2000. 85, p. 3966
- [Pendry06] Pendry J.B., Schurig D., Smith D.R. *Science*, 2006. 312, p. 1780
- [Schurig06] Schurig D., Mock J.J., Justice B.J., Cummer S.A., Pendry J.B., Starr A.F., Smith D.R. *Science*, 2006. 314(5801), p. 977
- [Shelby01] Shelby R.A., Smith D.R., Schultz S. *Science*, 2001. 292(5514), p. 77
- [Simovski09] Simovski C.R., Tretyakov S.A. *Phys. Rev. B*, 2009. 79(4), p. 045111
- [Smith00] Smith D.R., Padilla W.J., Vier D.C., Nemat-Nasser S.C., Schultz S. *Phys. Rev. Lett.*, 2000. 84, p. 4184
- [Soukoulis11] Soukoulis C.M., Wegener M. *Nat. Photonics*, 2011. 5, p. 523
- [Vallecchi11] Vallecchi A., Albani M., Capolino F. *Opt. Express*, 2011. 19(3), p. 2754
- [Veselago68] Veselago V.G. *Sov. Phys. Usp.*, 1968. 10, p. 509

Chapter I

Synthesis of the metal satellite nanoparticles



This chapter describes the solution-phase colloidal approaches that we used to prepare the gold and silver satellite particles for the further fabrication of the raspberry-like nanoclusters. We first summarize the main optical features of the metallic nanoparticles and the synthetic procedures for the production of relatively large silver and gold particles of spherical shape in high yield and high amount. We then review the synthesis of silver nanoprisms. This section primarily focuses on the advances made over the last ten years to the synthesis of monodisperse silver nanoprisms by colloidal chemistry approaches. We then describe the seed-mediated growth approach that we have developed. A mechanism of growth is finally proposed.

A. Main optical features of metallic nanoparticles

In the nanometer range size, metals are known to have physicochemical properties different from those of the bulk. The size decrease implies the increase of surface/volume ratio and the appearance of specific properties especially in electronic, catalysis and optics. In the nanometer size regime, metals and more particularly silver and gold, have unique optical properties highly attractive for optical applications where large extinction cross-sections and high electric field enhancements are desired. The optical properties of gold and silver nanoparticles are characterized by the presence of surface plasmon resonances (SPR) in the visible range. Surface plasmons are collective oscillations of the conduction electrons that are confined to surface of the nanoparticle and that interact strongly with an incident electromagnetic field (Figure I.1).

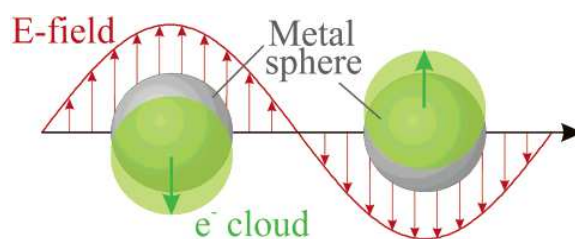


Figure I.1 - Schematic illustration of the cloud of free electrons in the metal responding to an oscillating electromagnetic field.

The plasmon resonance manifests as an absorption band whose width and position depend on the metal characteristics and envioning medium [Kreibig95]. For spherical particles, the plasmon resonance occurs at a single frequency situated in the visible range. This absorption is responsible of the yellow coloration of silver colloidal suspensions and the red coloration in the case of gold colloidal suspensions (Figure I.2).

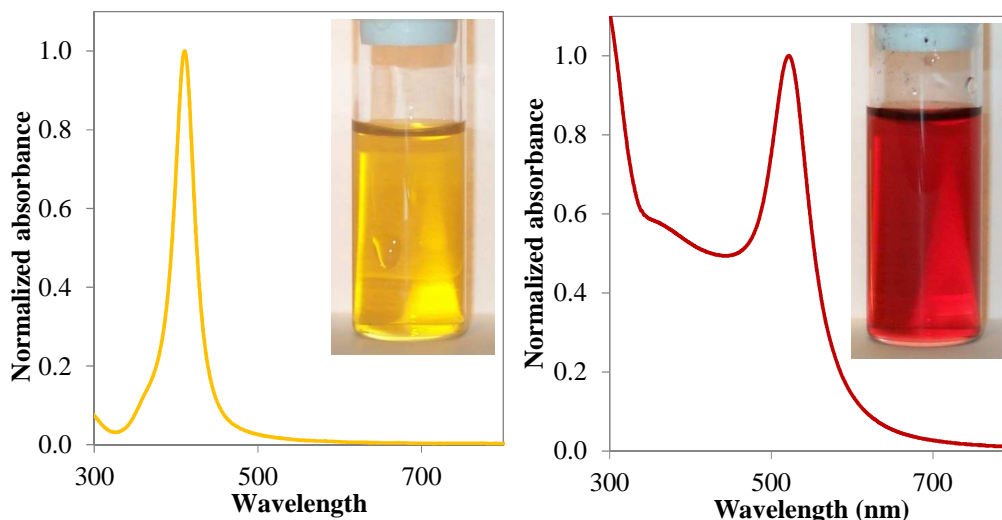


Figure I.2 - Pictures and absorption spectra of colloidal suspension of spherical (left) silver and (right) gold nanoparticles.

For the small size particles (< 30 nm), the plasmon frequency slightly depends on their size. For spherical silver particles, the main plasmon frequency can be tuned from 390 to 440 nm. Large particles can exhibit additional bands, corresponding to quadrupole and higher multipole plasmon excitation. For non-spherical particles, the absorption and scattering cross-sections can be calculated as soon as the polarizability is known [Wiley07, Jin01, Ozin05]. According to Mie theory, in the case of oblate particles, the system possesses two separate plasmon frequencies depending on which axis the electrons are oscillating along (Figure I.3-left). The resonance frequency along the short axis is similar to the one of spherical nanocrystals, but the additional resonance appearing to long axis is located at much lower frequencies (*i.e.* at longer wavelengths) and can be widely modulated by altering the length of the elongated nanoparticle (Figure I.3-right). For other shapes, the absorption and scattering cross-sections have been largely predicted through numerical solutions using approaches such as discrete dipole approximation (DDA), finite-difference time-domain method (FDTD) and boundary element method (BEM) [Wiley06]. The number of plasmon modes increases the more that the shape differs from a sphere. It is generally observed that the vertices of the nanoparticles play an important role in the optical response, because the sharper they become, the greater the number of resonance. It is also observed that the more symmetric the nanoparticle becomes, the more blue-shifted the main absorption.

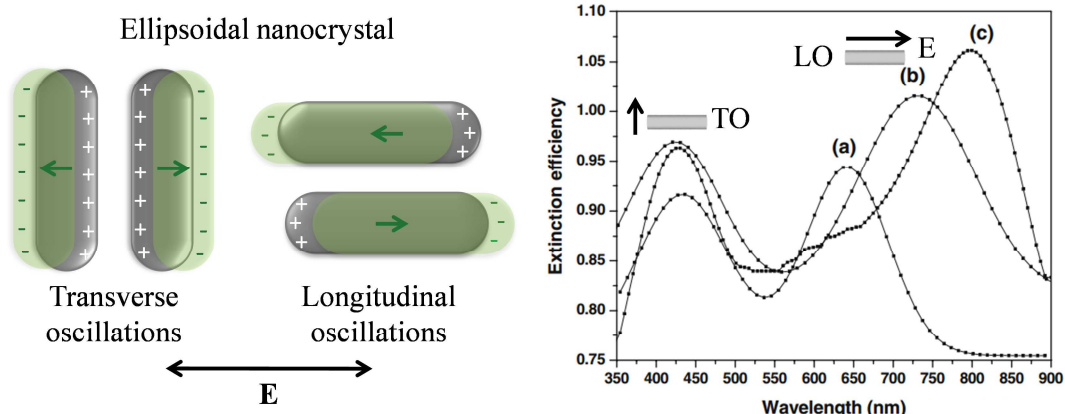


Figure I.3 – (Left) Schematic illustration of the two dipole oscillation modes observed in the case of elongated nanoparticles along the longitudinal (LO) and orthogonal (transverse (TO)) axis. (Right) DDA-simulated extinction spectra of silver nanorods having various aspect ratios (R) – a) R = 2, b) R = 3 and c) R = 4 [Sarkar11].

B. Synthesis of silver and gold spherical nanoparticles

Spherical silver and gold nanoparticles with controllable sizes have been synthesized by a wide range of chemical synthetic procedures as well as alternative synthetic processes, including photochemical, sonochemical and microwave assisted methods that do not require the use of chemical reducing agents. The synthesis of spherical particles follows either the “nucleation and growth” or “the seed-mediated growth” models [Faraday57, Frens73, Brust94, Turkevich51, Brown98, Jana01]:

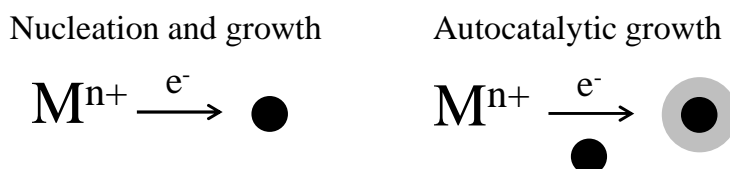


Figure I.4 - Schematic illustration of (left) “nucleation and growth” and (right) “seed-mediated growth” models.

In the case of homogeneous nucleation, the particle size can be precisely controlled by the ratio of metal precursor to the capping ligand. In the other case, as an advantage over homogeneous nucleation, seed-mediated growth allows to disentangle growth from nucleation, making easier the control of the size of a product by simply varying concentrations on the growth step. The particle size is generally controlled by the ratio of the preformed nuclei to the metallic precursor. Both approaches are versatile for accessing bulk particles. Regarding gold, it is possible nowadays to prepare almost any imaginable particle size with good yield and monodispersity by using one of these two approaches [Millstone09, Sau04]. For silver, although different approaches have been developed over the past decade, the progress in the control of the possible sizes is not comparable to that for gold. The synthesis is more difficult due to the strong reactivity of silver toward oxygen. We describe in the following section the approaches that we have used to elaborate silver nanoparticles in the range size of 20-30 nm and gold particles in the range size of 10-50 nm.

B.1 Synthesis of silver spherical nanoparticles of 20-30 nm diameter

Despite the myriad of synthetic protocols reported over the past 30 years for the preparation of Ag particles with any desired geometry [Xia09, Zhang10b, Zhang09, Pyatenko07, Silvert96, Cogley09, Dong09, Mafune00, Pastoriza-Santos09], notably lacking is a simple and robust procedure for the preparation of a large amount of spheroidal particles with diameter larger over 15 nm with a relatively narrow size distribution. Xia *et al.* have reported a polyol preparation of large silver nanoparticles with low size-dispersity in one step [Zhang09]. This method is based on the reduction of AgNO₃ in ethylene glycol as reductive liquid at high temperature in the presence of hydrosulfide sodium and poly(vinylpyrrolidone) (PVP) as capping agent. Once the concentration of silver atoms reaches the supersaturation level, they begin to nucleate and grow into large cubic-shaped nanoparticles. It was found that by introducing an aged solution of sulphide ions in the reaction medium the formation of cubic or other anisotropic shapes can be avoided and the process can yield to the formation of large spherical silver particles in high yield. This is based on previous findings from silver photographic technology where the presence of traces of sulfides and polysulfides, in the range of ppm, affects the particle growth by accelerating the rate of silver ion reduction. Due to the low solubility of silver sulfide species, (Ag₂S)_n nanocrystallites form immediately and serve as a catalyst for the reduction of silver ions. Thereby, the introduction of sulfide ions results in the fabrication of spherical particles bounded by lower-energy surface facets. The protocol was developed by Dr. Pascal Massé during his postdoctoral fellowship at the ICMCB [Masse13]. It is described in the following section:

Protocol 1 - Synthesis of silver spherical nanoparticles

In two different vials, 16.9 mg of sodium hydrosulfide were dissolved into 10 mL of ethylene glycol (EG) and 450 mg of PVP (Mw ~ 55,000 g.mol⁻¹) in 15 mL of EG. Both solutions were left to age for 4 h under stirring. One hour and half after the preparation of both solutions, 60 mL of EG were introduced in a three-necked rounded flask equipped with a reflux condenser and heated at 150°C for 2 h 30, under stirring. The two others necks were sealed with septa. Two hours later, Argon flow was introduced in the rounded-beaker via needle with a large diameter. The extremity of the needle should be placed at the surface of the EG (not in the solution). Thirty min later, 35 µL of NaHS solution and 15 mL of PVP solution were introduced via a syringe in the EG. Then, 5 mL of EG solution containing 120 mg of silver nitrate were quickly introduced. During the first 5 min, the solution colored dark yellow, then orange after about 6 min. At this time, the reaction should be stopped. For that, the rounded-beaker was placed in an ice-bath and 50 mL of absolute ethanol was added to decrease more quickly the temperature of the reaction. Finally, the silver nanoparticles dispersion was firstly concentrated (from 130 to ~ 10 mL) by using a Millipore Stirred Ultrafiltration Cell with a regenerated cellulose membrane (100 kDa). Then they were transferred from EG to water by

repeating 5 times the ultrafiltration cycle with an ethanol solution containing PVP (3 g/L) to ensure the colloidal stability of the particles and finally 5 times with ultrapure water.

Absorption spectra regarding the reaction time and transmission electron microscopy (TEM) images of the as-produced silver spherical nanoparticles transferred in water are shown in Figure I.5. After 6 min, the absorption spectrum of the colloidal suspension exhibited a sharp band around 405 nm characteristic of the dipole resonance of the silver nanospheres. The full width at half maximum (FWHM) was 27 nm confirming the size monodispersity of the as-produced particles. As the particle size increased with time, the band red-shifted. By simply quenching the reaction with ice-cooled water, it was possible to obtain silver nanoparticles in the 20-30 nm size range. For all samples, smaller than 30 nm, polydispersity never exceeded 10%.

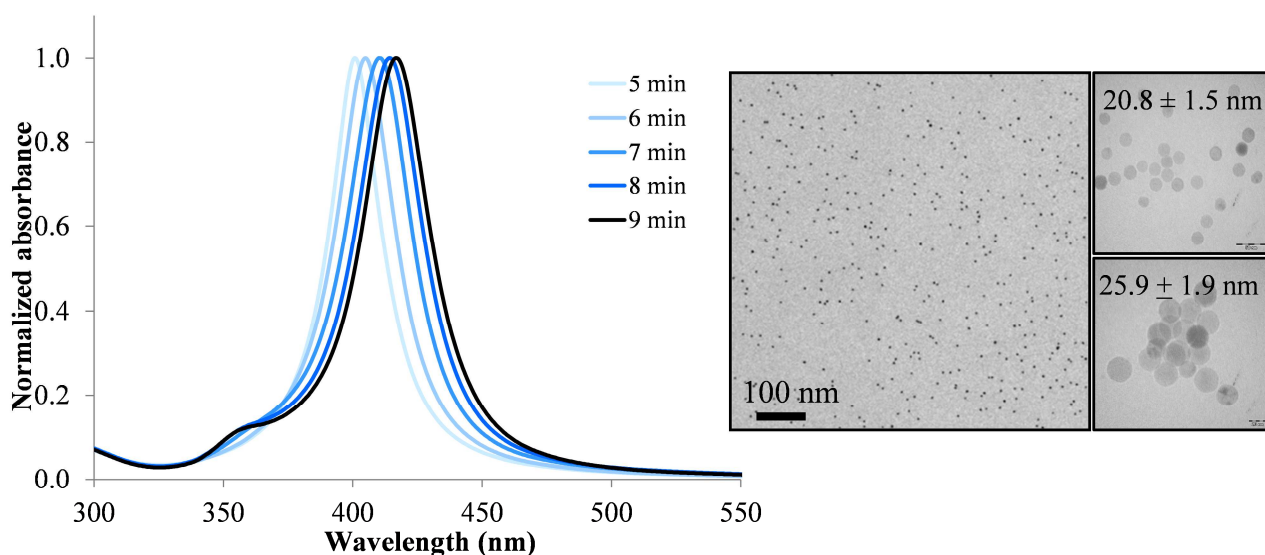


Figure I.5 – (Right) Time evolution of normalized absorption spectra of silver spherical nanoparticles obtained via the polyol approach after transfer from EG to water and (Right) corresponding TEM images after 5 min (top right) and (left and bottom right) 8 min of reaction.

The diameter of the particles was systematically determined from the TEM images, by using the software ImageJ, in order to analyse a large number of particles (> 100). The corresponding polydispersity index (PDI), which is the ratio between the mean diameter in mass (D_w) and the mean diameter in number (D_n) was calculated with the Equation I.1. For example, the silver particles obtained after 6 min of reaction exhibited a PDI of 1.12 that confirming the size monodispersity of the particles.

$$PDI = \frac{D_w}{D_n} = \frac{\sum n_i \sum n_i \cdot d_i^4}{\sum n_i \cdot d_i \sum n_i \cdot d_i^3} \quad (I.1)$$

Since the reaction was stopped before completion, we could not estimate the final concentration of silver nanoparticles by assuming that all the salt reacted. The final concentration was actually determined by inductively coupled plasma optical emission spectrometry (ICP-OES, Annex 1).

Note that this method allowed the production of a very large amount of silver spherical nanoparticles. Typically, the concentration of silver nanoparticles, before washing, was about 3.9×10^{15} particles.L⁻¹. After washing, the particles were concentrated and the final concentration was typically [AgNPs] = 8×10^{16} particles.L⁻¹. The as-prepared silver nanoparticles were stabilized with the PVP adsorbed on their surfaces. This capping agent induced a negative overall charge of silver nanoparticles, as confirmed by the measurement of the zeta potential. As shown on the Figure I.6, when the pH of the suspension was above 2, the particles exhibited a negative value of the zeta potential evidencing a negative overall charge of the particles. However when the pH exceeded 8, the overall charge (in absolute value) strongly decreased due to a destabilization of the particles.

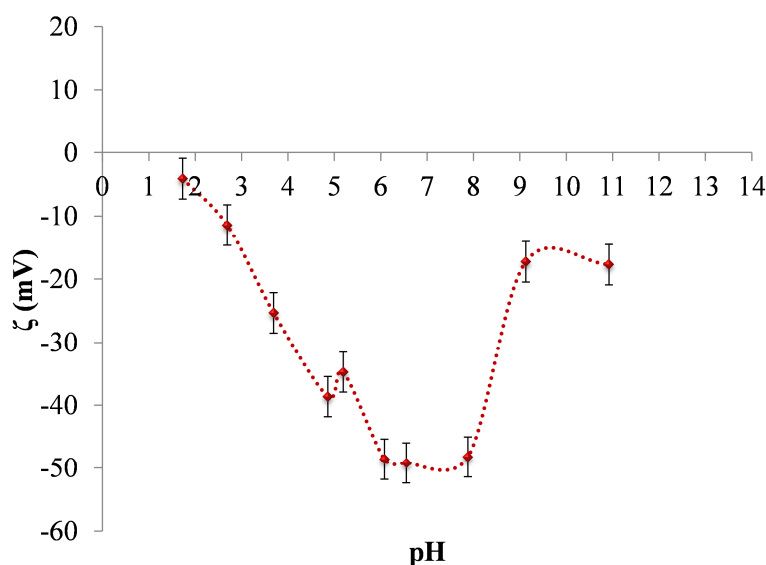


Figure I.6- Curve of zeta potential of silver spherical nanoparticles stabilized by PVP.

This one-step synthesis allowed us to produce a large amount of silver spherical particles. They clearly exhibited a net negative overall charge in the range of pH 3-8.

B.2 Synthesis of gold spherical nanoparticles of 10-50 nm diameter

B.2.1 Synthesis of 10-nm gold nanoparticles

Contrarily to silver, the synthesis of large gold nanoparticles was performed via a seeded growth approach which was adapted from the protocol proposed by Ziegler *et al.* [Ziegler11]. The 10-nm gold nanoparticles were firstly elaborated through the conventional Turkevitch's method. Then these particles were used as seeds for further growth in order to obtain larger particles. The synthesis was developed by Dr. H  l  ne G  han during her postdoctoral fellowship at the ICMCB.

The 10-nm gold nanoparticles are usually synthesized through the simple and well-known "Turkevitch's method" which was pioneered by J. Turkevich *et al.* in 1951 [Turkevich51], then refined by G. Frens in 1973 [Frens73]. This approach consists in the reduction of the chloroauric acid as gold precursor with sodium citrate at high temperature. Due to the citrate ions serving as

both reducing and stabilizing agent, well-dispersed gold nanoparticles were formed. The mechanism of this well-known reaction is still discussed nowadays. The gold nanoparticles obtained by this approach exhibited usually diameters between 10 and 30 nm. It was shown that the size of gold nanoparticles could be modulated by varying the molar ratio between citrate and gold salt [Ji07]. Here, a modified protocol inspired from the Turkevitch's method was chosen to produce the 10-nm gold nanoparticles in high yield and high amount (Protocol 2).

Protocol 2 - Synthesis of 10-nm gold nanoparticles

700 mL of ultrapure water were placed in a two-necked rounded flask mounted with a reflux condenser and heated at 100-110°C under moderate stirring. Then 50 mL of aqueous potassium gold(III) chloride solution (0.83 mM) were introduced in the reaction medium. When the gold salt solution reached 100°C, 75 mL of aqueous trisodium citrate solution (5.2 mM) were quickly added. The solution progressively colored from yellow to deep red. The stirring was maintained for 15-20 min at 110°C.

The concentration of gold nanoparticles [AuNPs] (in particles.L⁻¹) was estimated by considering the full reduction of the gold salt and calculated as follows:

$$[\text{AuNPs}] = \frac{[\text{Au}] * \text{M}(\text{Au})}{\frac{4}{3}\pi r^3 * \rho(\text{Au})} \quad (\text{I.2})$$

where [Au] is the concentration of gold salt in the medium (mol.L⁻¹), M(Au) = 196.97 g.mol⁻¹, and ρ(Au) 19.3 g.cm⁻³ are the molar mass and the density, respectively, and r corresponds to the radius (cm) of the produced gold nanoparticles.

The as-prepared gold nanoparticles exhibited a spherical shape with a mean diameter of (10 ± 1) nm and a PDI of 1.02 (Figure I.7). The absorption spectrum of the colloidal suspension exhibited a band around 520 nm characteristic of dipole resonance of the gold nanospheres.

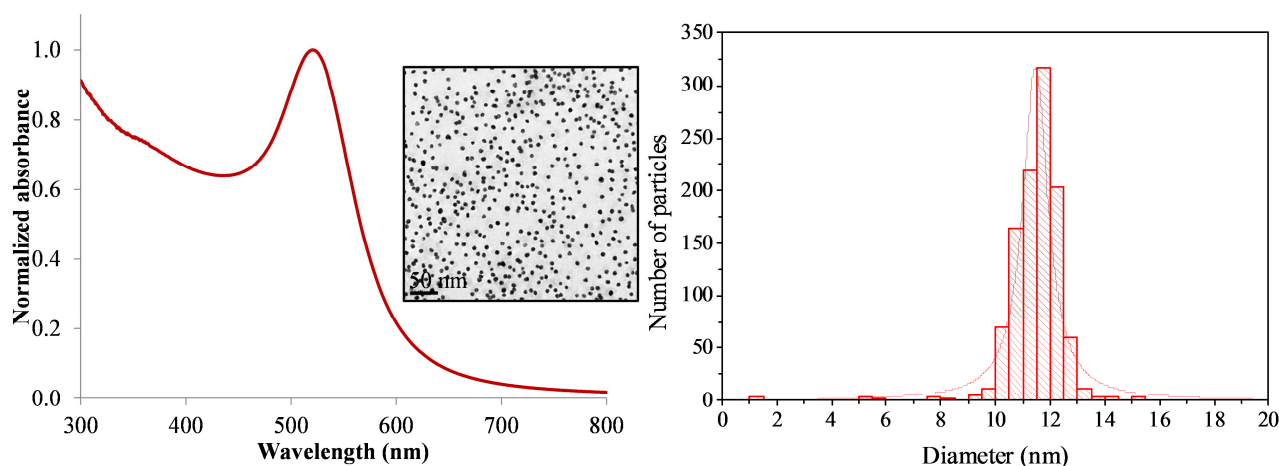


Figure I.7 - (Left) Absorption spectrum and TEM image of 10-nm gold nanoparticles obtained via the Turkevitch's method and (right) the size-distribution calculated from 1090 particles.

Note that the 10-nm gold nanoparticles were stabilized with citrate ensuring them an overall negative charge.

B.2.2 Growth of gold seeds into larger particles

Once the diameter and the concentration of 10-nm gold nanoparticles were determined, they were used as seeds for further growth in order to obtain larger particles. This seed-growth approach was an adaptation of the protocol proposed by Ziegler *et al.* [Ziegler11]. The gold precursor was reduced by a mild agent, the ascorbic acid (AA), in presence of citrate which acts as stabilizing agent. They proposed a growth mechanism of the larger gold particles wherein small gold clusters were formed on the surface of the gold seeds, which subsequently grow and result in a “blackberry-like” intermediate shape of the gold nanoparticles. Applying heat caused an intra-particle ripening process, which finally lead to a smooth spherical particle shape.

The general procedure to grow the gold seeds is described below. Moreover, for clarity an example of growth from 10-nm gold nanoparticles to obtain 20-nm gold nanoparticles was described in details at the end of the Protocol 3.

Protocol 3 - Synthesis of gold spherical nanoparticles

A certain amount of 10-nm gold seeds dispersion was diluted to 20 mL of deionized water in a three-necked flask. Then 10 mL of a solution A containing KAuCl_4 and 10 mL of the reducing solution B containing trisodium citrate and AA, were added simultaneously but separately to the medium at room temperature via two syringe pumps under stirring and over a time of 45 min. As soon as the addition was complete, the mixture was brought to boiling ($T = 90^\circ\text{C}$) and was maintained at this temperature for about 1 h under stirring. Finally the solution was allowed to cool down. The solution A was prepared by diluting a KAuCl_4 stock solution (5.29 mM) to 10 mL and the solution B was prepared by diluting a mixture of an AA stock solution (56.8 mM) and a trisodium citrate stock-solution (34 mM) again to 10 mL. Note that the relative volume ratio (Au:AA:Citrate) of all three stock solutions were maintained constant for every growth (8:2:1). Once the diameter and the concentration of the gold nanoparticles determined, it was possible to use them as seed-particle for a next growth to calculate the required amount of gold precursor to achieve a certain particle diameter for a next growth.

For example, the synthesis of 20-nm gold nanoparticles using 10-nm gold seeds was performed as follows: 2 mL of 10-nm gold seeds ($[\text{AuNP10}] = 2 \times 10^{15} \text{ particles.L}^{-1}$) was added to 18 mL of deionized water in a three-necked flask. The solution A was prepared by adding 2.71 mL of KAuCl_4 stock solution to 10 mL, corresponding to the quantity of gold salt required ($n_{\text{Au}^{3+}} = 14.3 \times 10^{-6} \text{ mol}$). The solution B was separately prepared by adding 677 μL ($= 2.71/4$) of AA stock solution and 339 μL ($= 2.71/8$) of citrate stock solution to 10 mL of deionized water. The A and B solutions were added simultaneously but separately to the medium at room temperature via two syringe pumps under stirring and over a time of 45 min. Directly after the addition was complete, the mixture was brought to boiling ($T = 90^\circ\text{C}$) and is maintained at this temperature for about 1 h under stirring. Finally the solution was allowed to cool down.

From this protocol four batches of gold nanoparticles were produced with different diameters, noted AuNP20, AuNP30, AuNP40 and AuNP50, respectively. The Figure I.8 shows TEM images and UV-Vis spectrum of each batch. They were characterized by a plasmon band near 525 nm. The larger the diameter of the particles (from 20 to 50 nm), the more red-shifted the plasmon band (from 518 to 530 nm).

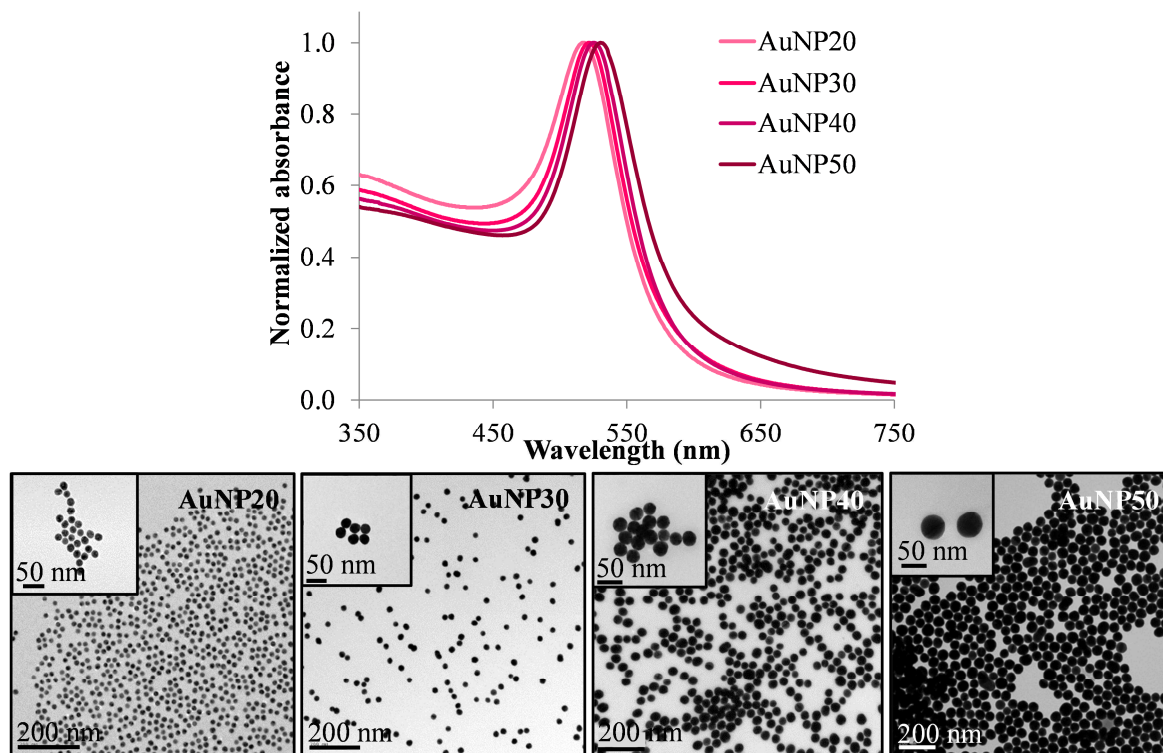


Figure I.8 - Absorption spectra and TEM images of gold nanoparticles with a mean diameter of 20, 30, 40 and 50 nm.

The TEM images of each batch revealed that all the synthesized gold nanoparticles were spherical and low faceted. The diameter and the PDI for each gold nanoparticles batch were calculated from the TEM images and are summarized in the Table I.1. It reveals the high monodispersity in size of the particles.

Table I.1 - Diameter and PDI of the AuNP20, AuNP30, AuNP40 and AuNP50 calculated from TEM images and from a minimum of 100 particles.

	AuNP20	AuNP30	AuNP40	AuNP50
Diameter (nm)	20 ± 3	33 ± 6	40 ± 9	50 ± 8
PDI	1.04	1.07	1.09	1.07

As previously, the concentration of gold particles was determined by assuming that one gold seed gives one larger gold particle. Note that the gold nanoparticles from growth steps were stabilized with citrate and ascorbate ensuring them an overall negative charge.

C. Synthesis of silver nanoprisms

Despite the advances in the colloidal synthesis of silver anisotropic particles, it is still challenging to generate uniform silver nanoprisms with controllable size in bulk quantities. Before describing the seed-mediated growth approach that we have developed, we first describe the main characteristics of silver nanoprisms as well as the main reliable routes to produce them.

C.1 State of the art on the main features and synthesis of silver nanoprisms

C.1.1 The main structural and optical features of silver nanoprisms

Silver nanoprisms are commonly described with a flat and triangular morphology (Figure I.9). They exhibit three congruent edge lengths (l), a defined thickness (t), and more or less sharp tips that contribute significantly to their optical and electronic properties [Kelly03, Blaber12].

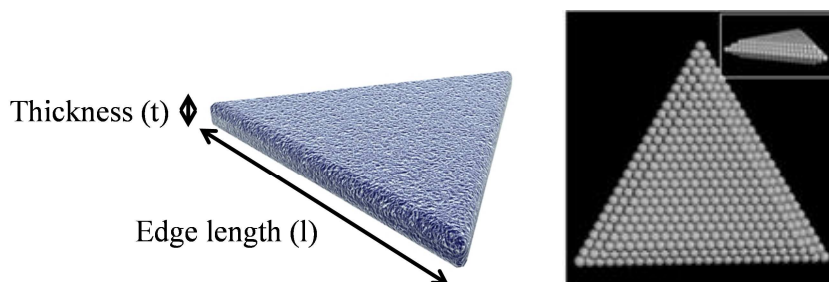


Figure I.9 – (Left) Sketch of a nanoprism and (Right) schematic model of a single twin plane platelet. [Elechiguerra06]

The nanoprisms are covered by $\{111\}$ facets at both top and bottom surfaces and contain twin planes and stacking fault(s) extending across the entire nanostructure [Bastys06, Murayama09, Germain03, Rocha07, Rodriguez-Gonzalez06]. Yet, the exact nature of the side-facets geometry has not been fully established. Their side faces would be built up with $\{100\}$, $\{110\}$ or $\{111\}$ faces and one or more stacking faults [Lofton05, Elechiguerra06].

The triangular nanoplates display four plasmon bands. A main resonance with a dipolar character is always present with other secondary resonances with lower intensities. By resolving Maxwell's equations for light interacting with a silver nanoprism, Schatz *et al.* have successfully attributed these different extinction bands [Jin01, Kelly03]. The 700-nm and 470-nm peaks are assigned to the in-plane dipole and quadrupole plasmon resonances, respectively, whereas the 410 and 340 nm peaks are the out-of-plane dipole and quadrupole resonances, respectively. The main resonance is very sensitive to the tips truncation. For example, if a 12-nm region at each tip of a prism of 100 nm is removed, the long-wavelength resonance at 770 nm for the perfect prism shifts to 670 nm without changing the other resonances (Figure I.10).

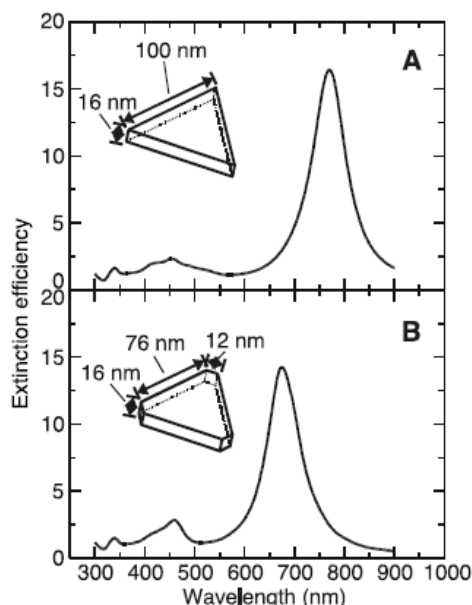


Figure I.10 - DDA simulations of the orientation averaged extinction efficiency spectra of two silver nanoprisms in water. (A) A perfect nanoprism (8512 dipoles are used in the calculation) and (B) a truncated nanoprism (7920 dipoles are used in the calculation) [Jin01]

A red-shift in the position of maximal wavelength of the main resonance but also the appearance of higher multipole resonances at shorter wavelength are expected as the edge length and hence aspect ratio increases [Charles11]. A decrease of prisms' thickness induces a red-shift accompanied with an intensity increase of the main resonance [Amendola10]. Recently, Blaber *et al.* have studied the optical response of a single, truncated and not-truncated, silver nanoprism [Blaber12]. They showed that silver nanoprisms with both different truncation and size can have similar maximum wavelength position (λ_{\max}) and FWHM of surface plasmon resonances. By contrast, the optical properties of silver nanoprisms with the same truncation and size but different thicknesses significantly vary.

Wiley *et al.* showed that the dipole resonance peak of the circular disks is blue-shifted compared to the one of triangular nanoplates since they lack the sharp corners (Figure I.11). Note also that disks absorb and scatter the light more strongly than the triangular nanoplates; their circular symmetry gives them a larger effective dipole moment [Wiley06].

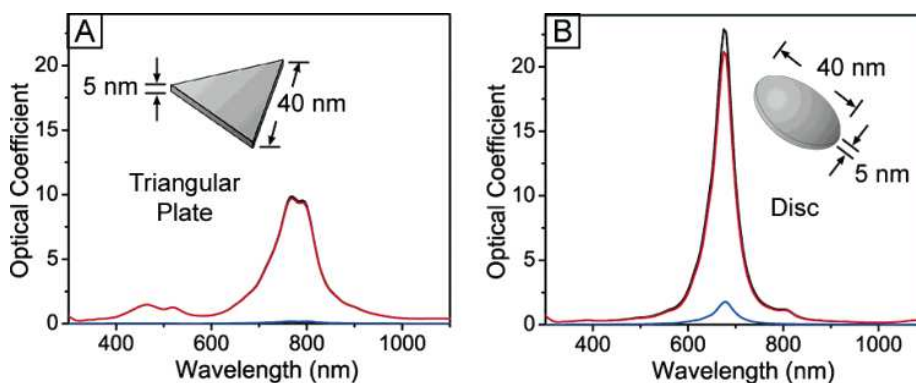


Figure I.11 - UV-Vis-NIR extinction (black curve), absorption (red) and scattering (blue) spectra of silver (A) flat triangular and (B) disk-like nanoparticles obtained using the DDA calculation. [Wiley06]

The following figure summarizes how the position of the main extinction band changes when thickness, edge length and truncation of nanoprisms vary. Note that the position of the weak resonance near 340 nm is also sensitive to the nanoprisms thickness.

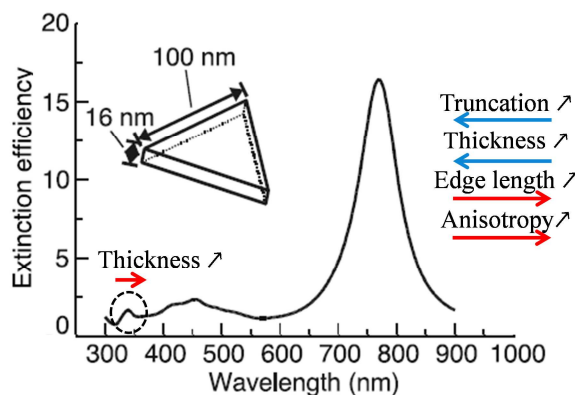


Figure I.12 - Theoretical spectrum of Ag nanoprisms (100-nm long and 16-nm thick) in water. The arrows describe the evolution of maximum wavelength position when thickness, edge length and truncation of nanoprisms vary.

Since the dipolar mode have extremely high extinction cross-sections at relatively long wavelengths and can be widely tuned by altering the length of the nanoprisms, that offers to silver nanoprisms a number of interesting applications in fields as diverse as photonics, ultrasensitive chemical and biological sensors, labeling, and optoelectronics [Pastoriza-Santos10, Kelly03, Jin01, Schatz06, Bastys06, Willets07, Charles11].

C.1.2 The different synthetic routes of silver nanoprisms

The anisotropic nanoparticles are usually prepared using a template-directed approach or a seeded growth approach (Figure I.13).

- Via the template-directed approach (Figure I.13-a), the reduction of the metallic precursor occurs *in situ*, within a soft or hard template. Spatially confined templates allows to produce nanocrystals with shape different from the one induced from crystallography.

- Via the seed-mediated approach, the anisotropic surface chemistry may be controlled by a capping ligand which specifically adsorbs on specific crystalline facets of the seeds and strongly influence the growth direction (Figure I.13-b).

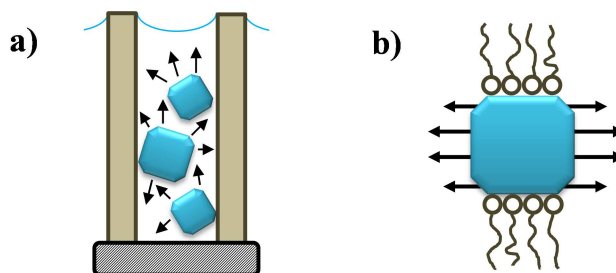


Figure I.13 – Schematic illustrations of a) the template-directed approach and b) the seed-mediated growth by using a protecting agent.

Three recent reviews [Pastoriza-Santos10, Rycenga11, Wiley05] and a book chapter [Tapan K. Sau12] summarize the main approaches reported in literature to fabricate silver nanoprisms. We briefly describe below some of the most efficient and/or simple and versatile routes.

C.1.2.1 An example of template approach

Van Duyne and coworkers have mainly developed the nanospheres lithography (NSL) to prepare arrayed triangular islands of silver deposited on metal oxide substrates [Hulteen95, Hulteen99, Haynes01]. The NSL is a powerful technique to fabricate nanoparticle arrays with precisely controlled shape, size, and interparticle spacing [Hulteen95]. This strategy has been demonstrated to be suitable for tuning particles size between 20 to 1000 nm and can be applied to silver with a good control over the shape and interparticle spacing. This multistep method begins with self-assembly of monodisperse colloidal nanospheres (typically polystyrene or silica) onto a substrate, which are then used as a mask during the deposition of silver. After deposition, the nanosphere mask was removed by sonication in ethanol resulting in surface-confined particles with triangular footprints (Figure I.14). The final size and interparticle distance are determined by the nanospheres diameter. Later on, the same authors have demonstrated the possibility of releasing into solution silver nanoprisms prepared by NSL, through functionalization of the particles with thiolated molecules prior to their release, to prevent nanoparticle aggregation [Haes05]. However, some nanoparticles broke up during sonication in the release step, thus limiting further applications.

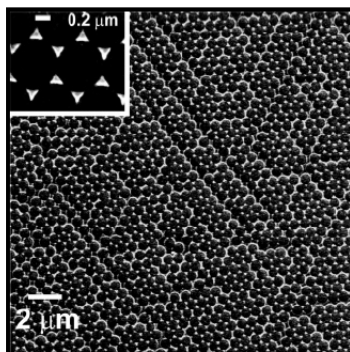


Figure I.14 - SEM images of silver nanoparticle arrays on indium tin oxide (ITO). The nanosphere diameter was 590 nm, and the mass thickness of the silver film was 67 nm. [Zhang05]

Although this approach allows a good control of the nanoparticles shape, the number of particles produced per batch is low. Moreover, the step of releasing the nanoparticles from the substrate is difficult, limiting its use. Furthermore, sol-gel approach does not allow producing small silica particles (< 20 nm); consequently only large nanoprisms (> 50 nm) can be generated.

C.1.2.2 The seed-mediated growth

The seed-mediated growth consists in the reduction of silver ions by a given reducing agent in the presence of a capping agent (surfactant, polymer, or small molecule) to guide the growth on the surface of preformed seeds. The capping agent plays a crucial role in acting as shape-structuring agent. Indeed, these molecules may block preferentially certain crystallographic faces and favor the development of anisotropic nanoparticles. Silver nanoprisms synthesis has to be induced via chemical or photochemical reduction by using PVP, citrate or cetyltrimethylammonium bromide (CTAB) as capping agents.

- The chemical reduction

Reduction of silver salt in the presence of seeds, reducing agent and specific organic stabilizer has been shown as a simple and easy process to generate silver nanoprisms in aqueous or organic environments. It “only” requires mixing of the reagents under well-controlled external conditions. These conditions have to be finely controlled in order to avoid the formation of anisotropic particles different from triangular nanoparticles.

- *In aqueous media*

Stabilizers such as CTAB, PVP and citrate have been successfully used to prepare silver nanoprisms in aqueous dispersions. For example, Carroll and Chen reported an approach consisting in the reduction of silver ions (Ag^+) by ascorbic acid in the presence of silver seeds (≈ 15 nm) and highly concentrated CTAB capping agent [Chen02]. CTAB may adsorb onto silver in a bilayer fashion with the trimethylammonium headgroups of the first monolayer facing {111} surface. However, the TEM images as well as the absorption spectrum of the resulting particles show that the size and shape dispersity are large and the Ag nanoprisms are highly truncated (Figure I.15-a and b)).

PVP and citrate are also representative surface regulating agents that are well-known to kinetically control the growth rates of various facets for the formation of anisotropic silver nanoparticles on the basis of their excellent adsorption ability. In 2003, Xia *et al.* showed that tiny silver seeds (smaller than 5 nm in diameter) could be transformed into triangular nanoplates with sharp corners by refluxing an aqueous silver seeds dispersion in presence of PVP and citrate (Figure I.15-c and -d) [Sun03]. However, in the final colloidal suspension the size dispersity is rather large; small triangular nanoparticles coexist with larger ones. Both PVP and citrate ions would bind to the specific seeds facets and slow down their growth rate promoting anisotropic growth [Washio06].

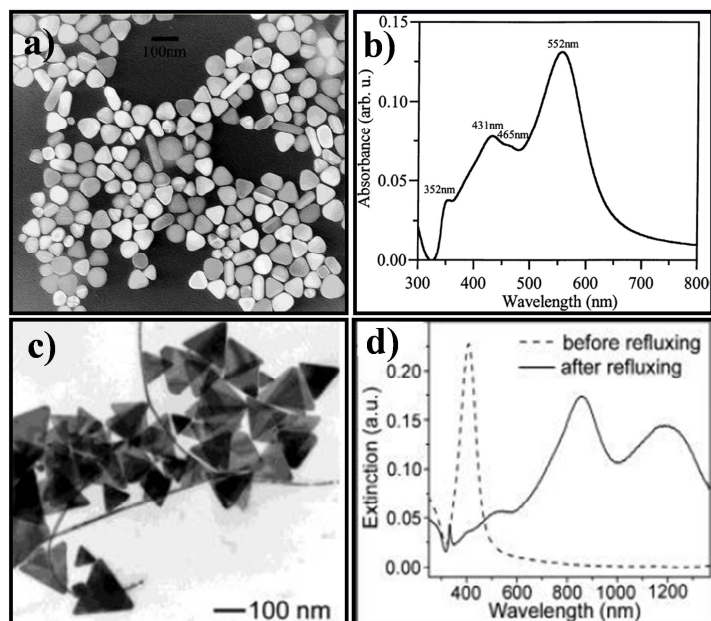


Figure I.15 - a) and b) TEM image and absorption spectrum of a dispersion containing truncated silver triangular nanoplates obtained with CTAB as capping agent [Chen02]; c) TEM image of the silver nanoparticles obtained in presence of PVP and citrate after a reflux treatment for 10 h and d) UV-Vis-NIR extinction spectra of the corresponding aqueous dispersion before and after refluxing. [Sun03]

Later on, the same authors proposed that the triangular-shaped nanoparticles would be rather based on the existence of trimeric silver precursors [Xiong07]. These authors found that trimeric clusters of silver are abundant species in commercial AgNO_3 powder and subsequent aqueous solutions. These clusters may behave as nucleation sites promoting the formation of nanoprisms. By varying the reaction conditions, Xia *et al.* proposed a more pertinent method to prepare the silver nanoprisms over a tunable range of 30 - 200 nm. They show that silver nanoprisms dimensions can be adjusted by simply varying the ratio of PVP and citrate concentrations used at room temperature [Zeng10b, Zeng10c].

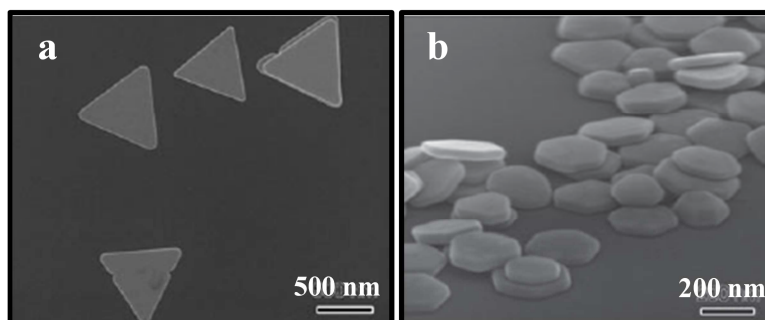


Figure I.16 - SEM images of silver nanoplates obtained by repeating the seeded growth 4 times in the presence of a) citrate or b) PVP, as capping agent [Zeng10b].

The presence of citrate in the growth medium may result in controlled particle growth laterally (Figure I.16-a) whereas the presence of PVP results in controlled particles growth vertically (Figure I.16-b). The Figure I.17 summarizes the growth mechanism. According to these authors, the method could produce particles with 45 nm - 5 μm thick and 5 nm - 200 nm large, respectively, by confining the growth to a lateral or vertical mode.

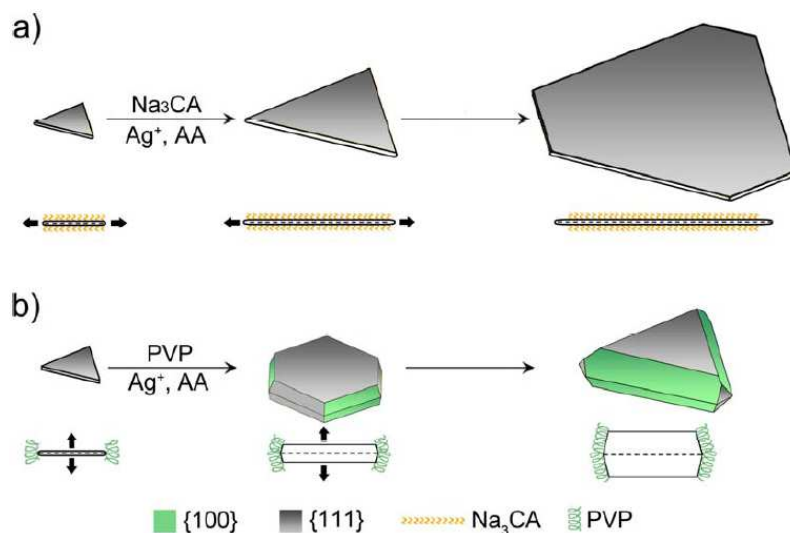


Figure I.17 - Schematic illustration detailing the major differences in terms of morphological and structural changes during the successive, seeded growth of Ag nanoplates in the presence of (a) Citrate (Na_3CA) and (b) PVP. For the cross-sectional views from the sides, the major directions of Ag growth are indicated by thick black arrows. The stacking faults are indicated by dash lines [Zeng10b].

However, the authors did not show any absorption spectra; therefore it is not possible to determine the actual size- and shape-dispersity of the resulting products.

- *In organic media*

In organic media, a few methods of production of Ag nanoprisms have been reported. Pastoriza-Santos and Liz-Marzan introduced the synthesis of silver nanoprisms by boiling DMF and reducing silver ions in the presence of PVP [Pastoriza-Santos02]. After the reduction, the resulting particles are particularly size polydisperse (Figure I.18).

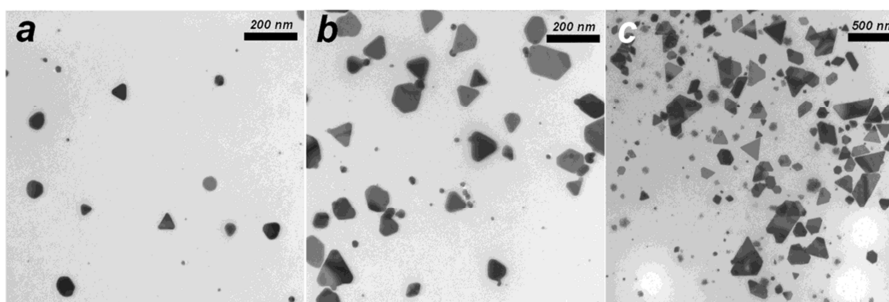


Figure I.18 - TEM images showing the growth of Ag nanoprisms obtained by reduction in DMF in the presence of PVP, at high Ag^+ concentration (0.02 M): (a) 5 min; (b) 15 min; (c) 60 min. [Pastoriza-Santos02]

They recently showed that the crystallinity of the initial seeds (performed or generated *in situ*) is the main factor controlling the final particle morphology [Pastoriza-Santos09]. Yang *et al.* also reported a one-step seedless solvothermal reduction route also in DMF and PVP to synthesize high-yield silver nanocrystallites with different shapes including triangular, hexagonal, and enneahedral plates, nanocubes, nanorods, and polyhedrons [Yang07]. Sonolysis approach has also been reported to produce Ag nanoplates but with a large size distribution [Jiang04].

- The photoinduced method

Although chemical reduction methods with various reagents are simple and convenient, the reaction has to be carefully adjusted for particular applications. An excess of reducing agents, their oxidation products and the surfactants used for chemical reduction may contaminate the final particles. Alternative approaches such as photochemical methods that do not require the use of chemical reducers and thermal heating have been thus developed to produce anisotropic particles.

We described below the most pertinent approach to prepare silver nanoprisms in high yield and low size dispersity [Jin01]. In this method, the silver nanoprisms were synthesized through the irradiation of preformed citrate-capped silver seeds (diameter = 6 - 8 nm) with visible light by using a conventional fluorescent tube and in the presence of bis(p-sulfonatophenyl) phenylphosphine dehydrate dipotassium (BSPP). They showed that the resulting colloids were single crystal silver nanoprisms with thickness of (16 ± 1) nm and edge length of (100 ± 15) nm. Initially, the authors proposed a simple mechanism based on the formation of extremely small spherical silver clusters (2 to 4 nm) and small nanoprisms (5 to 10 nm edge lengths) due to a photoinduced fragmentation of larger silver seeds. These nanoprisms then serve as seeds and grow as the small spheres are digested (Figure I.19).



Figure I.19 - Conversion of silver nanospheres into nanoprisms. [Jin01]

Later on, they reported the possibility to synthesize relatively monodisperse nanoprisms with larger edge lengths (30 - 120 nm range) and a thickness of (9.8 ± 1.0) nm, by using a dual-beam illumination of the nanoparticles (Figure I.20) [Jin03].

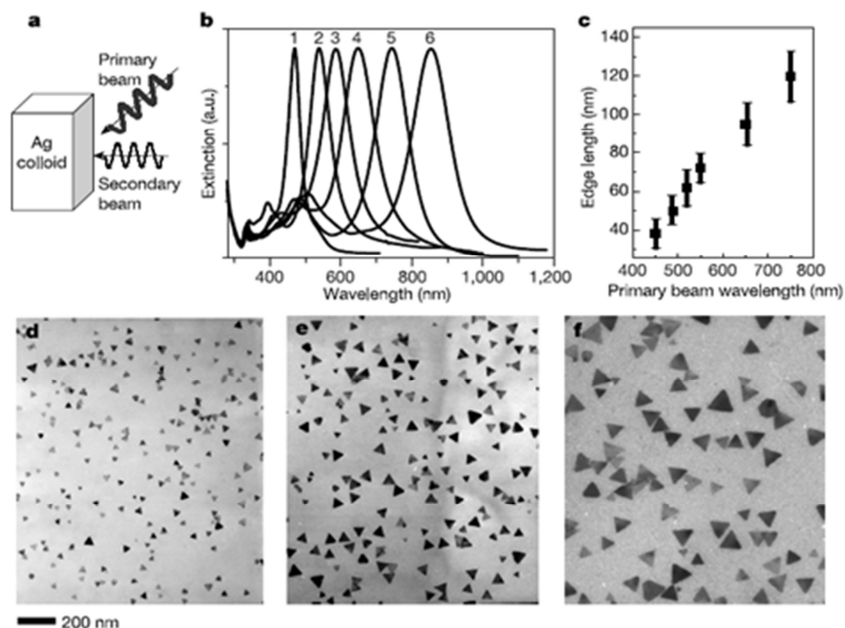


Figure I.20 - Unimodal growth of nanoprisms using dual beam excitation. (a) Schematic diagram of dual-beam excitation. (b) Optical spectrum (normalized) for 6 different-sized nanoprisms (1-6 edge length: 38 ± 7 , 50 ± 7 , 62 ± 9 , 72 ± 8 , 95 ± 11 , and 120 ± 14 nm) prepared by varying the primary excitation wavelength with secondary beam at 340 ± 10 nm. (c) Edge length as a function of the primary excitation wavelength. (d-f) TEM images of Ag nanoprisms with average edge lengths of 38 ± 7 nm (d), 72 ± 8 nm (e), and 120 ± 14 nm (f). Scale bar applies to panel d-f. [Jin03]

The irradiation has to be performed at two appropriate wavelengths that overlap the dipole and quadrupole plasmon resonances of the final silver nanoprisms. The primary one may facilitate slow growth of the prism and the secondary one may suppress prism fusion (Figure I.21).

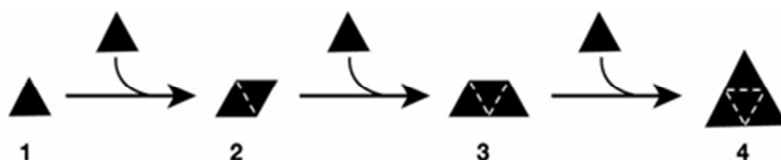


Figure I.21 - Schematic diagram of the proposed light-induced fusion growth of Ag nanoprisms. [Jin03]

The conversion time was long (about 20 ~ 50 h) but it could change significantly with different excitation wavelengths and intensities [Wu08]. Xue *et al.* proposed that the citrate ions involved in the reduction of silver cations onto the silver seeds surface and that the BSSP which strongly coordinated to Ag^+ promote the oxidative dissolution of the small silver clusters (Figure I.22) [Xue08].

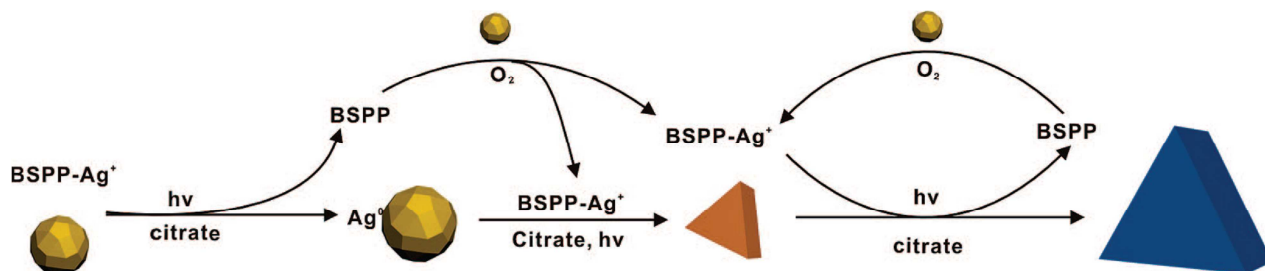


Figure I.22 - Proposed photo-mediated growth pathway of Ag nanoprisms from spherical nanoparticles [Xue08].

It has been observed that the BSPP can be replaced by the PVP, but the conversion rate of seeds into anisotropic particles becomes lower [Machulek Junior03]. If the reduction mechanism has been determined, it is still challenging to understand the main parameters at the origin of the anisotropic growth.

C.1.3 Synthesis strategy adopted in the present work

The last decade is marked by great advances in the synthesis of silver nanoplates, especially in controlling the yield and monodispersity. The Table I.2 summarizes the possible length and thickness ranges accessible by these different approaches as well as their main advantages and limitations. This study reveals that the most successful approach for producing triangular nanoparticles with desired dimensions for this work (50-nm length and 15-nm thick) is the photochemical one. It allows the production of silver nanoparticles with a narrow size distribution in aqueous environment. It has thus been tested even it does not allow to produce the triangles in large-scale. In the meantime, the seed-mediated route in aqueous medium developed by Xia *et al.* has also been considered since it would allow to generate silver nanoprisms in bulk quantity. This latter may also allow a control of length and thickness [Zeng10b]. The results obtained via these two approaches are described in following section.

Table 1.2– Main approaches reported in the literature for the synthesis of silver triangular nanoparticles.

Method	Authors	Steps' number	Details	Size: edge length (l); thickness(t)	Advantages	Limitations
Nanosphere lithography	Van Duyn <i>et al.</i>	3+	<ul style="list-style-type: none"> •Self-assembly of nanospheres onto a substrate •Deposition of silver •Removal of nanosphere mask by sonication •Releasing of Ag nanoprisms into solution 	(l) = 50-1000 nm	<ul style="list-style-type: none"> •Precise control of size •Inexpensive method 	<ul style="list-style-type: none"> •Difficulties to redisperse into solution without break up Ag nanoprisms •Low quantity
Photo-induced method	Mirkin <i>et al.</i>	2	•Irradiation with visible light of citrate-capped Ag seeds (6-8 nm), in the presence of BSPP	(l) = 100 ± 15 nm; (t) = 15.6 ± 1.4 nm	•Reliable and high yielding method	•Bimodal growth
		2	•Double-beam excitation (450-750 nm and 340 nm) of preformed Ag seeds	(l) = 30-120 nm; (t) = 9.8 ± 1.0 nm	<ul style="list-style-type: none"> •Control of the size •monodispersity 	
		2	<ul style="list-style-type: none"> •Single-beam irradiation with 550-nm light •Adjusting pH solution 	(l) = 30-120 nm; (t) = 9.8 ± 1.0 nm	<ul style="list-style-type: none"> •Control of the size •monodispersity 	
Wet chemical reduction in aqueous medium	Chen and Carroll	3	•Reduction of Ag ⁺ by ascorbic acid on preformed Ag seeds in alkaline solution of CTAB	(l) = 68 ± 11 nm; (t) = 24 ± 3.5 nm	•Large scale preparation	Truncation of Ag nanoprisms
Thermal process in aqueous medium	Xia <i>et al.</i>	2	•Reflux for 10h of aqueous Ag colloidal dispersion in presence of PVP and citrate	Not mentioned	<ul style="list-style-type: none"> •Perfectly sharp corners •95% of Ag triangular nanoplates and 5% of nanobelts 	•Large size distribution
Seed-mediated-protocol in aqueous medium		2	•Reduction of Ag ⁺ by ascorbic acid in presence of preformed Ag seeds, PVP and citrate	(l) = 30-60 nm; (t) ≈ 5 nm	<ul style="list-style-type: none"> •Sharp corners •Structural instability (time-temperature indicators) 	•Structural instability during ageing process
Successive deposition of Ag		3+	<ul style="list-style-type: none"> •Reduction of Ag⁺ by ascorbic acid in presence of preformed Ag seeds (5 nm), PVP and citrate •Growth in lateral or vertical mode depending on the capping agent present. 	(l) = 45 nm-5µm; (t) = 5-200 nm	•Well-defined and controllable dimensions	• truncation of nanoprisms in vertical growth with PVP
Thermal process in organic medium	Liz-Marzan and Pastoriza-Santos	1	•Boiling AgNO ₃ in DMF in presence of PVP	(l) ≈ 200 nm; (t) ≈ 30 nm	•Size control through reaction time	•Large size distribution
Chemical reduction in organic medium under microwave irradiation		1	•Reduction of AgNO ₃ by DMF in presence of PVP under microwave irradiation	(l) ≈ 200 nm; (t) ≈ 30 nm	•Easier control than reactions at reflux in DMF	
Sonochemical approach	Zhu <i>et al.</i>	1	•Reduction of AgNO ₃ by DMF in presence of PVP	(l) = 120 ± 10 nm; (t) ≈ 20 nm	•Control of the particle size by changing the ultrasonic intensity	

C.2 The photochemical route

As outlined earlier, the synthesis of silver nanoprisms via the photochemical route appears to be the most reliable approach to prepare monodisperse Ag triangular particles over a tunable range of 40-60 nm length. Trials were thus performed and are described in the following section.

C.2.1 Protocols

C.2.1.1 Synthesis of silver seeds

Tiny silver clusters were used as seeds for the conversion into larger silver triangular nanoparticles. These suspensions of seeds were prepared as follows:

Protocol 4 - Synthesis of silver seeds for the photochemical route

A 47.5 mL aqueous solution containing silver nitrate (0.10 mM) and trisodium citrate (0.31 mM) was prepared in a 100 mL two-neck round beaker and immersed in an ice-bath. Argon was bubbled through the solution for 20 min to remove oxygen then the Argon flow was kept constant at the surface of the solution throughout the reaction. Under vigorous stirring, 1 mL of cold and freshly prepared aqueous sodium borohydride (50 mM) was quickly added into the solution. Finally, 0.5 mL of aqueous BSPP (5 mM) was added. After 1 h of reaction, the flask was removed from the ice bath. Stirring and argon flow were maintained for 5 h at room temperature. The solution colored light yellow after NaBH₄ addition and the color intensified as the reaction continued at room temperature reflecting the formation of tiny particles ($d < 5$ nm) in the solution. The seeds were then used for the photo-conversion process 4 h after their preparation.

C.2.1.2 Photo-conversion process

The dispersion of preformed silver seeds was then irradiated in order to convert them into triangular nanoparticles. The photo-conversion of nanospheres was performed in quartz cell (1 cm) by keeping the dispersion under stirring over the process. All the photosynthetic reactions were monitored by UV-Vis spectroscopy after few hours of irradiation. The reaction was stopped when the spectrum stopped to change. Two facilities were used: one using laser sources with different emission wavelengths (OXXIUS) and one using Xenon lamp equipped of optical bandpass filters to select the irradiation wavelength. Only the results obtained with the Xenon lamp are shown below, *i.e.* with a set-up similar to the one described in the literature. With the laser as excitation sources, we found that the frequency of irradiation used has a drastic effect on the transformation of the silver clusters. When the irradiation was performed at a wavelength higher than 500 nm, the preliminary seeds evolve into anisotropic nanoparticles with polyhedral shape. However, the size and the shape dispersity were rather large due to the high photo-conversion rate induced by the use of laser.

With the use of the Xenon lamp set-up shown in Figure I.23, silver nanoprisms could be generated. The set-up was based on the use of a Novalight lamp as a light source (150 W) with different optical bandpass filters (diameter = 25 mm, band width = 40 nm, Thorlabs). The optical filters allowed investigating the effect of excitation wavelength on the size and the shape of the final nanoparticles. The Xenon lamp source showed nearly flat emission in the visible range and was thus ideal for our experiments.

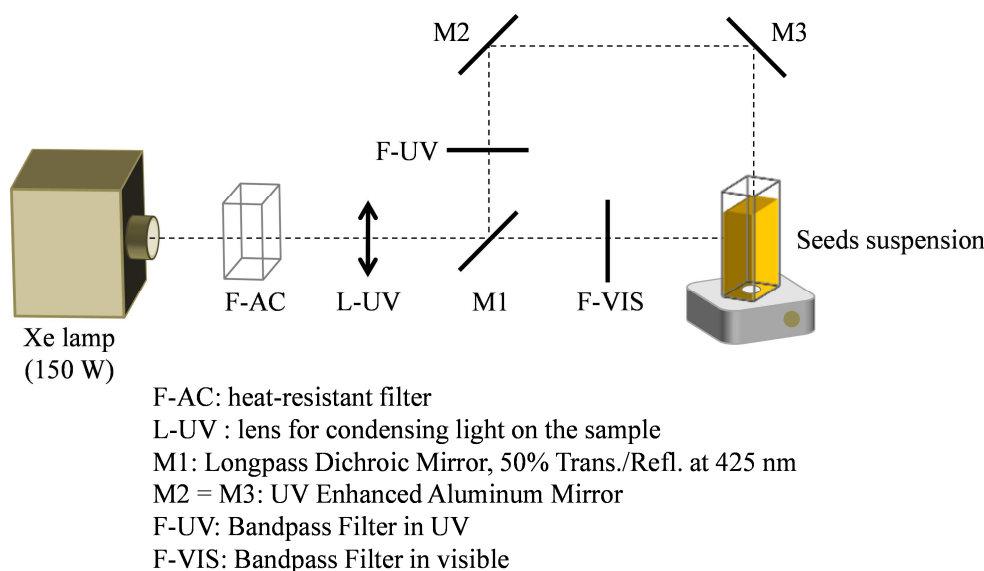


Figure I.23- Schematic illustration of the set-up equipped with a Xenon lamp

The distance between the reactor and the light output window was ~ 30 cm. The double irradiation was performed by placing a dielectric mirror between the Xe lamp and the sample. This mirror allowed transmitting the visible and reflecting UV light (50%) at 425 nm. By taking into account the results of the literature [Jin03], the irradiation of seeds dispersion at a wavelength comprised between 400 and 550 nm may yield to the production of triangular nanoplates with length of 30-70 nm. A second beam at 340 nm or 450 nm should prevent the fusion of particles in formation. A lens was placed between the Xe lamp and the sample in order to allow the irradiation of the whole suspension and thus to obtain more monodisperse objects with narrow size and shape distribution.

C.2.2 Results

Seeds were produced by reaction between AgNO_3 and NaBH_4 . The reduction (Equation I.3) is known to be fast due to the large difference existing between the redox potentials of NaBH_4 ($E_{\text{NHE}}^0(\text{NaBH}_4/\text{NaB}(\text{OH})_4) = -1.24$ V) and Ag^+ ions ($E_{\text{NHE}}^0(\text{Ag}^+/\text{Ag}_{\text{metal}}^0) = 0.80$ V).



In the experimental conditions described above, the reaction was expected to be quantitative since the borohydride was used in excess. Note that the reaction was performed at low temperature to reduce the decomposition of NaBH_4 in water (Equation I.4).



The citrate ions and BSPP, whose chemical structures are shown below, were used as stabilizers during the seeds production.

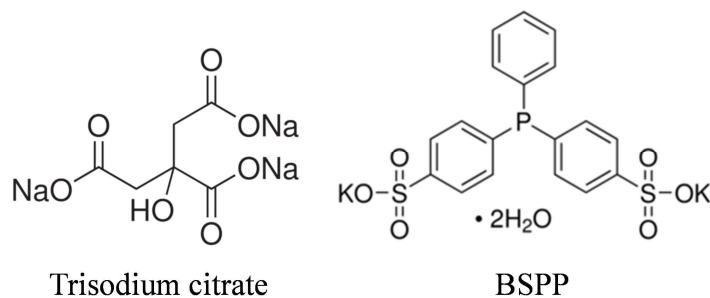
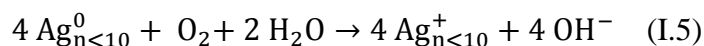


Figure I.24 - Chemical structure of trisodium citrate and BSPP.

Seeds had an average diameter of (4.1 ± 0.8) nm and are characterized by a narrow plasmon resonance at 385 nm (Figure I.25-yellow). A dual-beam irradiation at 340 and 500 nm of the suspension containing the silver seeds was performed. Magnifying the spectrum of seeds revealed that their absorbance spanned the entire visible range which means that these nanoparticles could be excited by a visible light. Thus, an excitation at 500 nm of the seeds induces a photo-fragmentation of a small proportion of the seeds absorbing at this wavelength and their further dissolution into Ag^+ ions by the oxygen present in the dispersion through the following equation:



The smaller silver seeds were progressively consumed and the Ag^+ ions were concomitantly reduced by citrate on the nanoparticles surface to form new objects with a SPR greater than the excitation wavelength. As shown on the TEM image (Figure I.25), by submitting the silver seeds dispersion to a dual-beam irradiation at 340 nm and 500 nm, small triangular nanoplates, with an edge length of (19 ± 3) nm and a thickness of (8 ± 1) nm were generated. These particles were characterized by a narrow and intense band at 530 nm and a lower intense one at 335 nm on their corresponding absorption spectrum (Figure I.25-purple curve). The band near 400 nm revealed the presence of a low amount of residual spherical seeds.

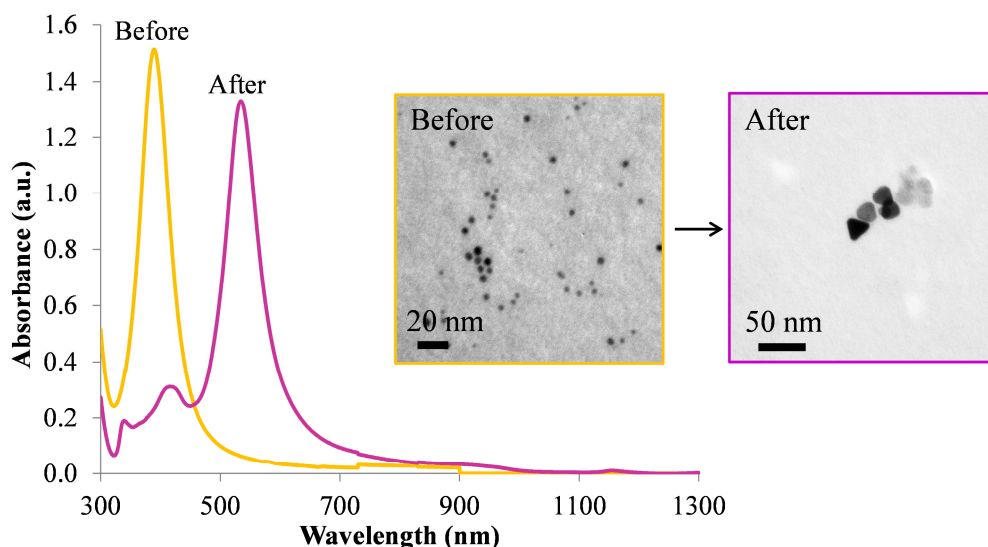


Figure I.25 - Absorption spectra and TEM images of the silver nanoparticles dispersion before and after the dual-beam irradiation at 340 nm + 500 nm for 44 h of the seed dispersion stabilized by BSPP.

This first test appeared very promising for producing triangular nanoparticles in the desired range size. In order to get nanoprisms of a larger length (50 nm), irradiation at longer wavelength of the primary beam (550 nm) was performed while the secondary beam was kept at 340 nm wavelength. In such conditions, the dispersion turned progressively green then blue upon irradiation after few hours. Then, it became slightly turbid after 50 h. The corresponding absorption spectra were drawn on the Figure I.26. A decrease in intensity of the plasmon band at 400 nm with the concomitant growth of a small band at 335 nm and an intense plasmon band near 700 nm was observed. After 42 h, the 400-nm band had totally disappeared while the 700-nm plasmon band had increased in intensity and large shoulders at higher wavelengths were appeared, evidencing the formation of triangular nanoplates and the fusion of some of them. The TEM image corresponding to the 42-h-spectrum confirmed the formation of flat triangular nanoparticles with an edge length of 20-200 nm and a thickness of 8 nm.

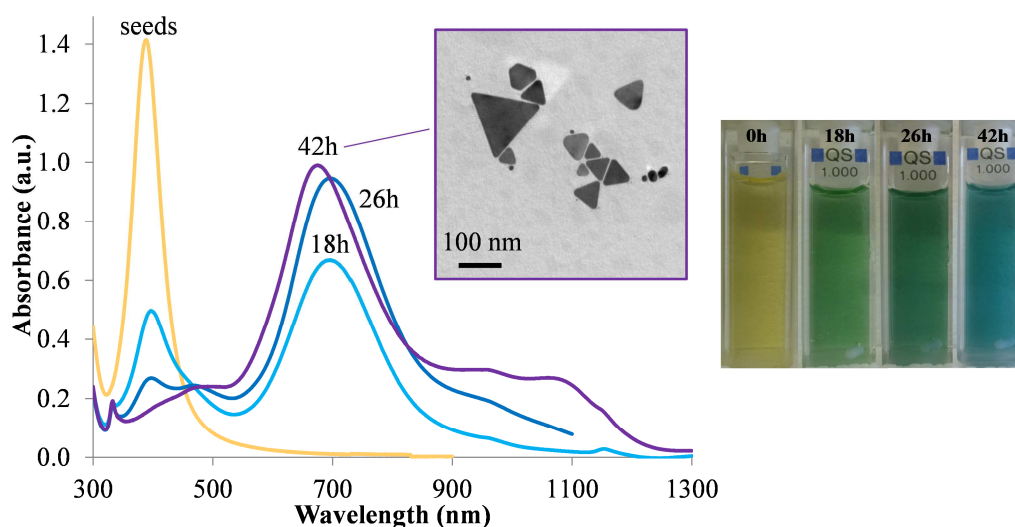


Figure I.26 – (Left) Absorption spectra and TEM image of the 5-h-aged silver nanoparticles dispersion obtained before and after the dual-beam irradiation at 340 nm + 550 nm; (Right) Photograph of the silver nanoparticles dispersion at different times upon irradiation.

C.2.3 Conclusion

Although this approach seemed very promising, the performed experiments did not reach our expectations. The irradiation of a seed dispersion stabilized with BSSP yielded indeed to the formation of Ag nanoprisms. However, narrow size dispersion was not achieved. The use of a second beam at lower wavelength did not inhibit the fusion of nanoprisms. The particle size distribution was systematically broad when the elaboration of nanoprisms with length lower than 70 nm was attempted. The study of some experimental parameters allowed us to better understand the conversion mechanism, but not to resolve the problem of inhomogeneity. Since the project's specifications requires large amount of particles for further 3D assembly, a more appropriate synthetic method was developed.

C.3 The chemical reduction approach

In this section, we introduce the results that we obtained with an alternative synthetic process, based on the seed-mediated growth approach. Based on the literature study introduced earlier, we have chosen to adopt the seed-mediated procedure developed by Xia *et al.* [Zeng10b] which allows a control of both length and thickness of the nanoprisms by using citrate and PVP as capping agents. The principle is the following: initially, a suspension of crystalline silver seeds is synthesized by reduction of AgNO_3 with NaBH_4 in presence of citrate as stabilizing agent. After 5 h of aging at room temperature, these seeds are then placed in a growth solution containing the silver precursor, PVP and citrate. This solution is slowly dropped into an aqueous solution of ascorbic acid which plays the role of reducing agent. At the end of the reaction, they obtained a cyan solution containing nanoprisms with an edge length and thickness estimated to 45 ± 15 nm and 5.0 ± 0.5 nm, respectively. Then, these nanoplates can be used as seeds for successive depositions of silver to produce plates with larger edge lengths and thicknesses. They showed that adding citrate promotes the lateral growth and the formation of silver thin plates with large lateral dimensions from 45 nm to 5 μm by repeating this seeded growth while adding PVP promotes a thickness increase from 5 nm to 200 nm after several seeded growths.

The first tests performed using the existing protocol led to the formation of Ag nanoprisms but with a large size distribution. The Figure I.27 shows a photograph of the resulting blue dispersion, the corresponding TEM image and the absorption spectrum. As it may be seen, the synthesized objects were predominantly triangular in shape but had a very broad size distribution resulting in a wide absorption band to longer wavelengths and a cloudy and diffusing dispersion.

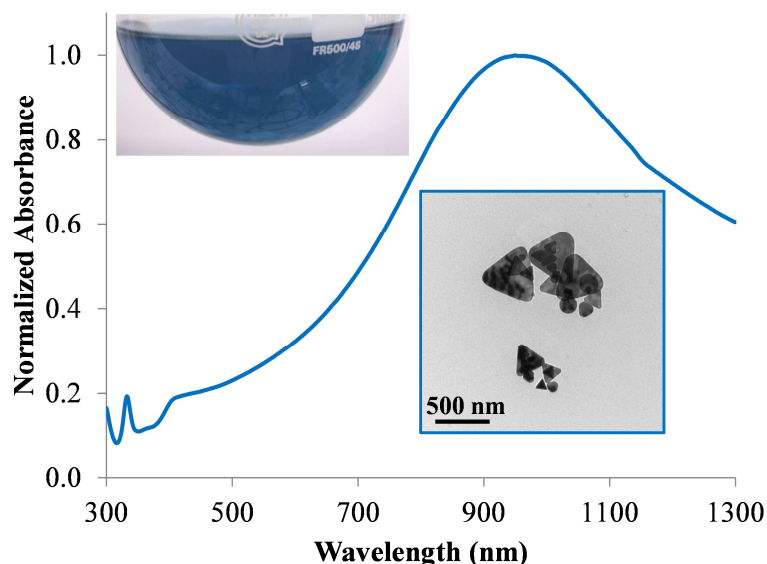


Figure I.27 – Photograph, TEM image and absorption spectrum of silver triangular particles obtained with $[\text{AgNO}_3] = 0.07 \text{ mM}$, $[\text{AA}] = 0.35 \text{ mM}$, $[\text{citrate}] = 1.25 \text{ mM}$, $[\text{PVP}] = 0.03 \text{ mM}$ and 0.2 mL of seed dispersion.

In order to optimize the size and shape distribution, identify the most critical components and understand their contributions to the nanostructure evolution, a set of experiments was conducted. The following part describes this study and reveals in which conditions homogeneous thin plates can be formed. A growth mechanism is proposed.

C.3.1 Optimized experimental procedure

The suspension of seeds was prepared as follows:

Protocol 5 - Synthesis of silver seeds by the chemical approach

Typically, 49 mL of an aqueous solution containing AgNO_3 (0.1 mM) and trisodium citrate (0.3 mM) were prepared in a 100 mL two-necked round bottom flask and immersed in an ice-bath. The solution was bubbled with argon under constant stirring for 30 min to remove oxygen. Then the argon flow was kept constant at the surface of the solution throughout the reaction. Under vigorous stirring, 0.5 mL of aqueous NaBH_4 (cold and freshly prepared, 50 mM) was quickly added into the ice-cold solution. The reaction was allowed to proceed for 15 min, and during this time, 3-5 drops of NaBH_4 solution were added every 2 min to the solution to ensure complete reduction of the Ag^+ ions. Finally, 0.5 mL of aqueous PVP or PSS (5 mg/mL) and 0.25 mL of NaBH_4 were added to the solution in a drop wise fashion over a 5-min time period. After 1 h of reaction, the flask was removed from the ice bath. Stirring and argon flow were maintained for 4 h at 20°C to allow the excess of borohydride to be decomposed by water.

The clear solution immediately turned light yellow after NaBH_4 addition and the color intensified as the reaction continued at room temperature evidencing the formation of small silver spherical particles in the solution.

The seed suspension was then used directly for the preparation of the silver nanoprisms. During the growth step of the Ag seeds, we observed that the order of addition of the reagents had a strong influence on the kinetics of formation of the anisotropic particles and therefore their size dispersity. The order of addition of reagents was changed with regard to the Xia's protocol (Figure I.28).

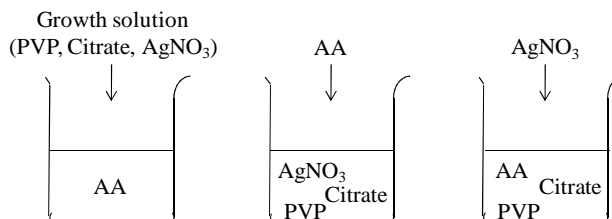


Figure I.28 - Illustration of different order of addition of the reagents.

In the procedure described in the literature [Zeng10b], the growth dispersion containing silver seeds, PVP, citrate and AgNO₃ was dropwise introduced into the aqueous solution containing ascorbic acid (AA). As shown earlier, this procedure yielded to the synthesis of triangular nanoplates with a large size distribution (Figure I.29-green curve). The progressive addition of the growth solution into AA favored the direct nucleation onto seeds as well as the additional nucleation due to the low seed concentration into the reaction medium. The concentration of AA being larger than the one of silver ionic precursor ($[AA] \gg [Ag^+]$), the rate of reduction was relatively fast leading to the progressive growth of the both types of seeds. Consequently, nanoparticles of different sizes were produced. In order to narrow the size distribution, the order of addition of the reagents was modified.

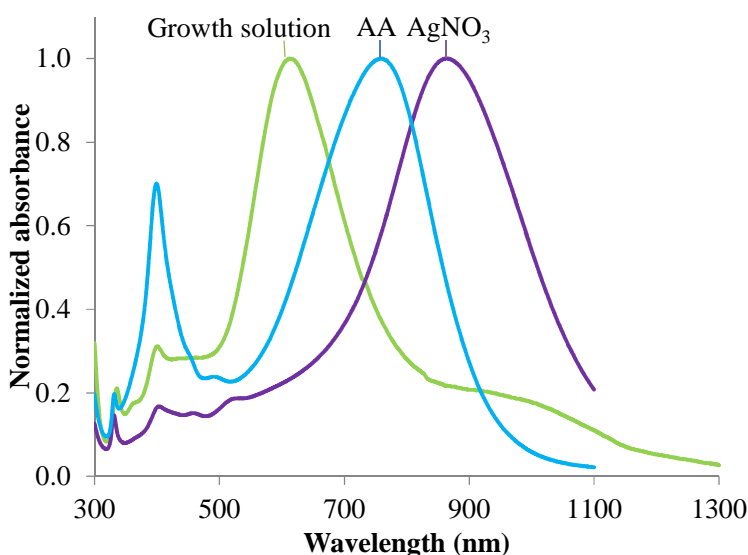


Figure I.29 - Absorption spectra of silver nanoprisms dispersion obtained for different order of reagents addition, with $[AgNO_3] = 0.09$ mM, $[AA] = 0.14$ mM, $[citrate] = 1.63$ mM, $[PVP] = 0.04$ mM and $[seeds] = 1.2\%$ vol.

When the aqueous solution containing AA was introduced into the growth solution, the solution colored gradually and became green. This mode of addition narrowed the size distribution of new formed silver nanoprisms. However, it strongly favored the secondary nucleation and the formation of spherical particles.

When AgNO_3 was introduced progressively into the growth solution, the nanoprisms became the dominant population without bimodal distribution. In this third mode of introduction, Ag^+ ions were in default in the solution ($[\text{AA}] \gg [\text{Ag}^+]$) promoting their fast reduction. The silver atoms and clusters formed in the early stages of the reaction combined with the silver preformed seeds favoring the preparation of relatively uniform dispersion. This mode of addition was thus adopted in the following study. The protocol developed was the following one:

Protocol 6 - Preparation of silver nanoprisms

Typically, 100 mL of ultrapure water were mixed with 100 mL of aqueous AA (0.5 mM), 3.5 mL of as-prepared 4 h-aged seeds, 38 mL of aqueous PVP (0.7 mM in terms of monomer units), 38 mL of aqueous trisodium citrate (30 mM) in a 500 mL round flask. Then, under magnetic stirring, 12.5 mL of aqueous AgNO_3 (2.5 mM) was added to the solution in a dropwise fashion with a rate of addition fixed at 10 mL/h. The solution progressively changed color via yellow, orange, pink, purple and finally blue then it was intensifying as the addition of silver precursor was continuing. Throughout the reaction, the mixture was maintained under ambient atmosphere and at $\sim 20^\circ\text{C}$. Moreover, the silver precursor solution and the round flask containing the growth solution were protected from light exposure.

C.3.2 Study of the crystalline structure of the silver seeds and nanoprisms

These silver seeds were similar to the ones used in the previous photochemical route. Only the nature of the polymer used as stabilizing agent was changed (PSS or PVP vs. BSPP). The absorption spectrum, TEM and HRTEM images and size distribution of these small clusters, formed under high supersaturation conditions, are shown in Figure I.30.

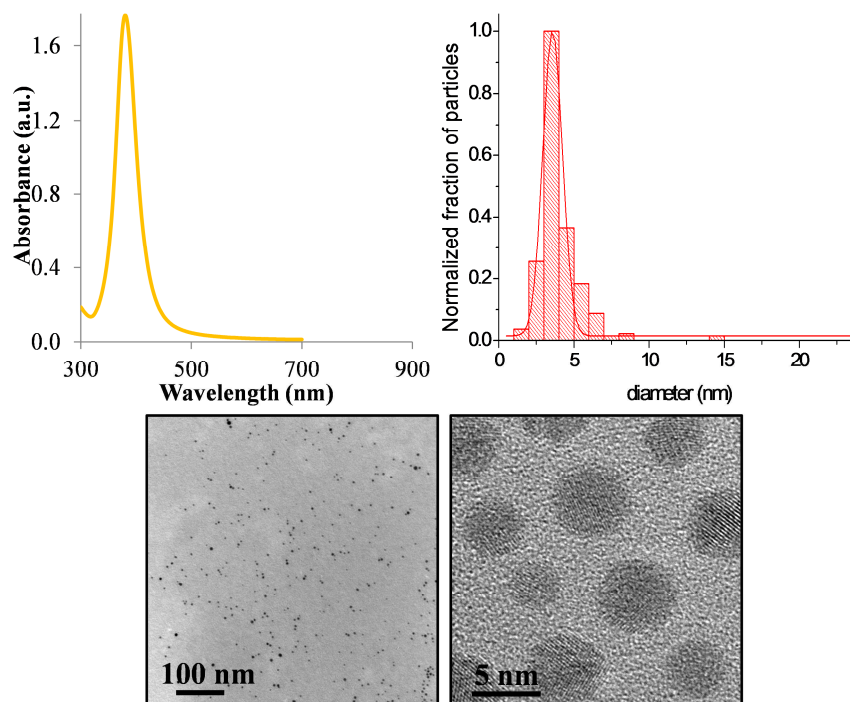


Figure I.30 – (Top) Absorption spectrum, size distribution (from 273 particles), (Bottom) TEM and HRTEM images of silver seeds prepared with $[\text{AgNO}_3] = 0.09$ mM, $[\text{NaBH}_4] = 1.22$ mM, $[\text{Citrate}] = 0.30$ mM and $[\text{PSS}] = 0.05$ g/L.

As determined by statistical analysis from TEM images, the average particle size was (3 ± 1) nm. The colloidal suspension absorbed at 383 nm, characteristic of dipole SPR of small Ag nanospheres, and possessed an exceptionally narrow band (FWHM = 43 nm) confirming the high monodispersity of the as-produced particles. A characterization of their crystalline structure was performed by scanning transmission electron microscopy (STEM). The bright-field (BF) and corresponding annular dark-field (ADF) STEM images reveal that silver seeds were crystallized in face-centered cubic (fcc) structure (Figure I.31).

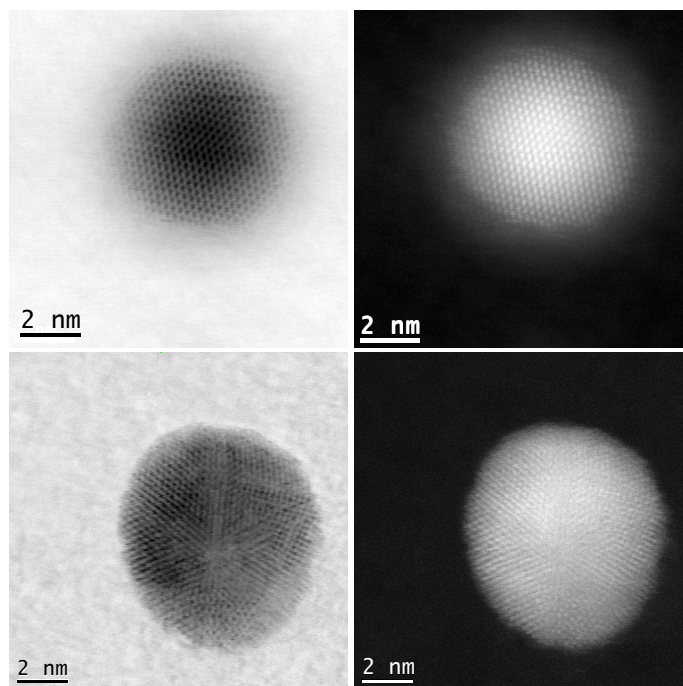


Figure I.31 – (Left) BF- and (Right) ADF-STEM images of Ag seeds viewed from (top) side or from (bottom) the top.

Most of the seeds seemed exhibit an icosahedral morphology with a five-fold symmetry when the particle was viewed from the top and a three-fold symmetry when it was viewed from the side. Icosahedron exhibits twenty $\{111\}$ facets and corresponds to one of the more stable structure shapes of very small silver clusters (< 5 nm).

When a small amount of the seeds dispersion was introduced in a growth medium containing silver nitrate, AA, PVP and citrate at room temperature, the Ag nanospheres could be quasi-entirely transformed into thin and flat nanoparticles, yielding a transparent blue dispersion with an absorbance maximum in the NIR (Figure I.32). Four localized surface plasmon resonance peaks were observed, indicating the presence of thin and flat nanoparticles once the seeded growth was initiated. The dominant extinction peak at 700 nm was the in-plane dipole resonance mode, whereas the three weak bands near 332 nm, 450 nm and 500 nm were the out-of-plane quadrupole, out-of-plane dipole and in-plane quadrupole modes, respectively.

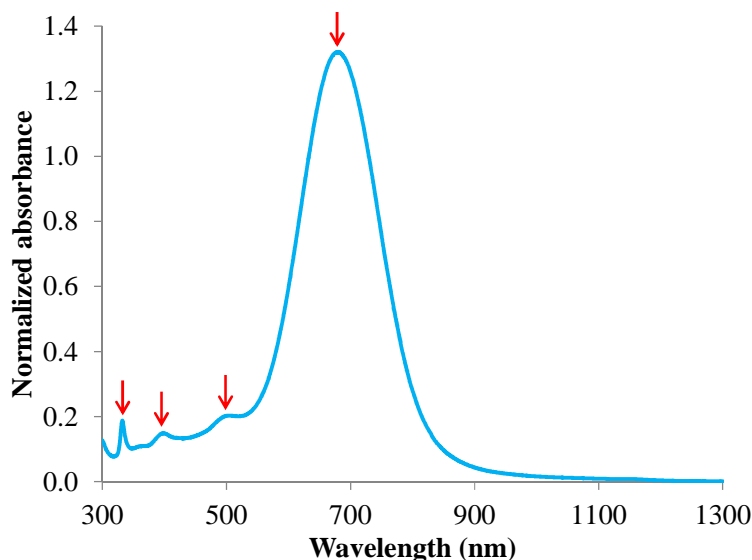


Figure I.32 - Absorption spectrum of the nanoprisms synthesized in a growth medium containing PVP and citrate.

These observations were consistent with the characteristic resonance bands for Ag triangular nanoplates of ~ 55 -nm length [Jin03]. TEM analysis confirmed that the prevailing shapes were triangular nanoplates (95%) coexisting with hexagonal and circular ones (5%) (Figure I.33). As observed when they were stacked perpendicularly to the substrate, they were thin and flat in agreement with the optical observations. Their thickness was ~ 5 nm, *i.e.* slightly higher than the dimension of the seeds (3 nm).

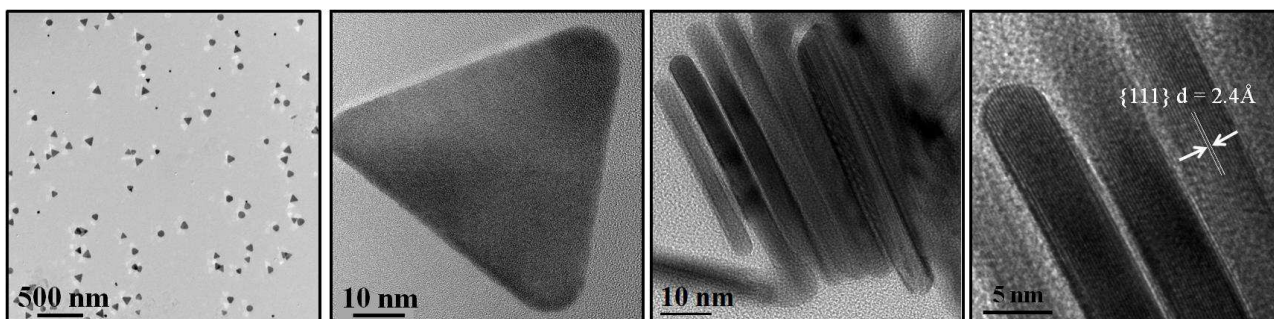


Figure I.33 - TEM and HRTEM of Ag nanoprisms synthesized in a growth containing PVP and citrate viewed from the top (left) and from the side (right).

Their crystalline structure, in particular, their side-face structure was finely characterized in order to disclose the mechanism involved in the nanoparticles growth using HRTEM and electron tomography. HRTEM characterization revealed that each particle was a single crystal. The corresponding Fast Fourier Transform (FFT) of the triangle aligned along a $\langle 111 \rangle$ zone axis is shown in Figure I.34 - right. Two sets of spots were identified based on d -spacing and the corresponding reticular spacings were measured on the HRTEM micrograph associated to the previous FFT (Figure I.34 - left).

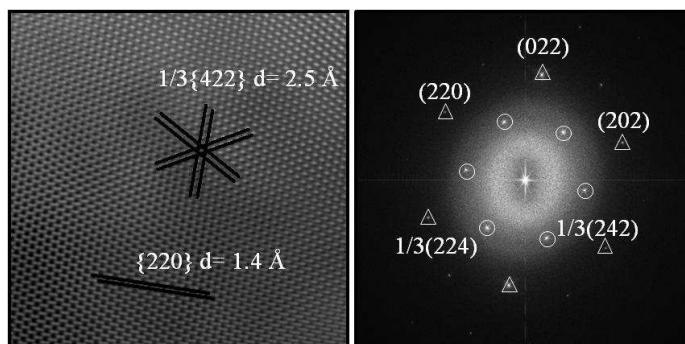


Figure I.34 – Zoom of a HRTEM filtered image of a silver nanoprism and the corresponding FFT along a $\langle 111 \rangle$ zone axis.

The outer set one with a spacing of 1.4 Å (triangles) was indexed as $\{220\}$ planes whereas the inner one with a spacing of 2.5 Å (circles) was assigned to the $1/3 \{422\}$ forbidden Bragg reflection and justified as $3 \times \{422\}$ lattice spacing of the fcc silver crystal [Germain03]. This forbidden reflection was already observed for both silver and gold nanoplates [Jin01]. The existence of this forbidden reflection presumably reveals the presence of a single $\{111\}$ stacking fault lying parallel to the flat top and bottom $\{111\}$ surfaces and extending across the entire nanoplate.

This stacking fault was clearly evidenced by electron tomography which allowed a detailed morphological and structural 3D-characterization of the nano-objects. The electron tomography analysis was performed in collaboration with O. Ersen and I. Florea at the Institut de Physique et Chimie des Matériaux de Strasbourg (IPCMS, Strasbourg) and its principle and experimental procedure are described in Annex 1. The electron tomography was performed in STEM mode in order to collect simultaneously two complementary images. Commercial 5-nm gold beads were previously deposited on the microscopy grid, which played the role of fiducial markers for the alignment step of projections images. The nanoprism chosen for the acquisition should be in the orientation of tilt axis and surrounded by few gold beads. STEM images were then collected every 2.5° from -72.5° to $+70^\circ$.

The 3D-reconstruction of the volume of the analyzed nanoprism made evident the single stacking fault parallel to the large $\{111\}$ faces (Figure I.35). The existence of that kind of single stacking fault led to a triangle side constituted by two inclined lateral planes as previously described by Bögels [Bogels97, Bogels98]. HRTEM as well as electron tomography experiments allowed to identify those lateral planes as $\{100\}$ ones because an angle of $\sim 55^\circ$ was systematically measured between the stacking fault and the two facets of thickness corresponding to the interplanar angle between $\{100\}$ and $\{111\}$ planes in a cubic system.

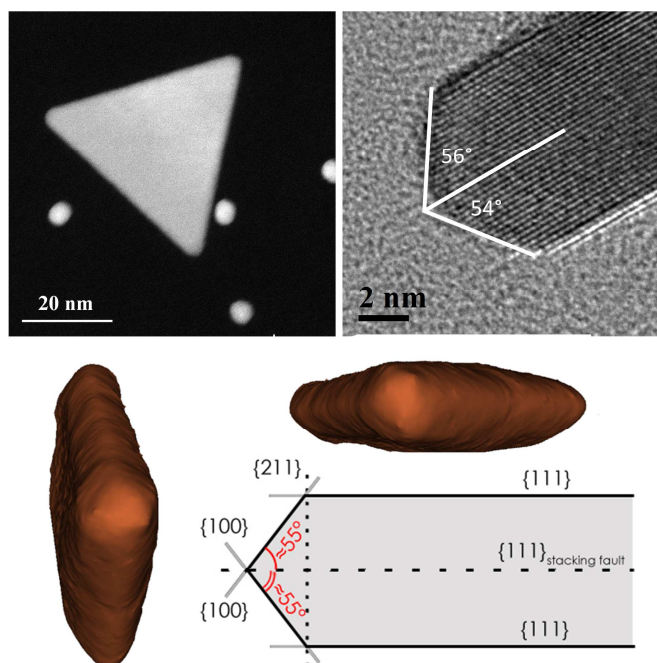


Figure I.35 - Up (left) ADF-STEM projection at 2.5° tilt angle of a nanoprism (scale bar = 20 nm). 5-nm gold beads were previously deposited on the grid as fiducial markers for alignment; (right) High resolution lateral view of the Ag nanoprism laying on its side. Down: Two outside views of the 3D modeling of the nanoprism showing the presence of the stacking fault parallel to the flat faces and extending across the entire nanoplate. Schematic illustration of a section of one side of the triangle with the identification of surface planes constituting the edges of side faces.

This kind of particle shape is deriving from a cuboctahedron composed by six $\{100\}$ square faces and eight $\{111\}$ triangular ones. It is generated by truncating the vertices of a cube or octahedron at $1/2$ edge-length. The remaining challenge is now to understanding the mechanisms leading to such a geometrical feature.

C.3.3 Study of the influence of many parameters on the growth reaction of Ag nanoprisms

A set of experiments was performed in order to determine the influence of many parameters (*e.g.* the order of reagents addition, the atmosphere, *etc.*) and identify the specific roles of each reagent (*e.g.* metallic precursor (AgNO_3), reducing agent (AA), seeds and capping agents (citrate, PVP)) in the growth process and finally to propose a growth mechanism of silver nanoprisms. All the studied parameters are not detailed in this section, but only the most influencing on the final shape, size and distribution of the final products.

C.3.3.1 Influence of light and atmosphere

Silver is known to be strongly sensitive to light as well as oxidation. We thus studied the influence of light and atmosphere on the nanoprisms synthesis. By following the evolution of the pAg ($\text{pAg} = -\log [\text{Ag}^+]$, where $[\text{Ag}^+]$ corresponds to the free Ag^+ ions concentration) of an aqueous silver nitrate solution with time, we observed a progressive decrease of the amount of free Ag^+

when the solution was exposed to light in comparison to the one maintained in the dark (Figure I.36). The experimental protocol to measure the evolution of the pAg is described in Annex 1. This decrease of pAg was due to the presence of residual Cl^- ions naturally present in water. UV-light initiated a redox reaction between Ag^+ and Cl^- ions as:

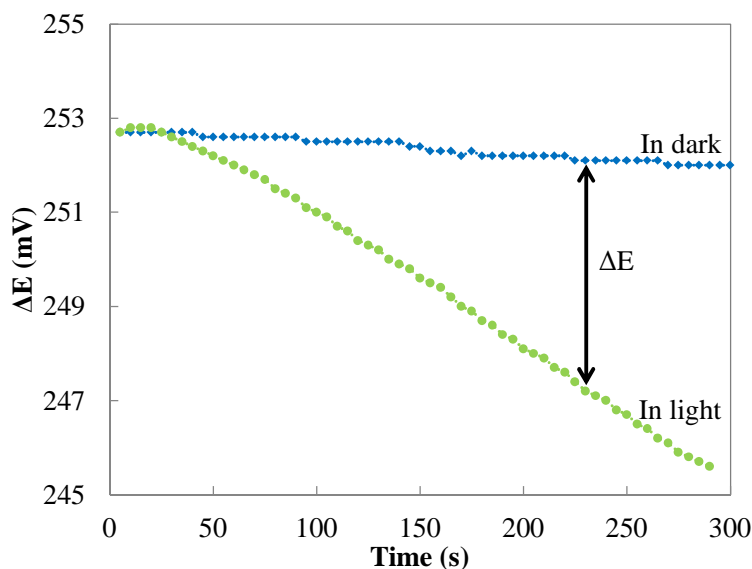
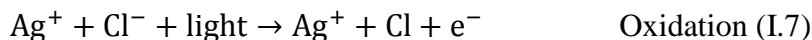


Figure I.36 – Evolution of electrode potential of a silver solution ($[\text{AgNO}_3] = 0.21 \text{ mM}$) protected or exposed to daylight.

Silver is also well known to be sensitive to oxidation (Equation I.5). No significant change of particles size was observed once oxygen was removed via argon bubbling. However, we found that oxygen slightly affected the morphology of the sharp nanoparticles via the oxidation of the atoms at highly energetic sites (the corners of the nanoprisms) [Zeng10a]. Synthesis in the presence of O_2 yielded to the formation of more rounded nanoparticles. In the meantime, we observed that the synthesis under argon favored the secondary nucleation during the growth step and the formation of spherical by-product particles. Inert atmosphere preserved the nascent silver clusters to oxidation. Thereafter, all experiments were performed under ambient atmosphere and protected from the light.

C.3.3.2 Role of seeds

In the absence of seeds, a typical Ag nanocrystals synthesis produced irregularly shaped particles with size from 50 nm to 100 nm (Figure I.38 - right). The standard redox potential of free Ag^+/Ag^0 ($-1.75 \text{ V}_{\text{NHE}}$) was so negative that the spontaneous formation of Ag_n clusters was unfavorable in an aqueous solution [Henglein93]. The reduction reaction of silver ions with AA (Equation I.9) required many hours for completion. Note that ascorbic acid lost 2 electrons by its oxidation to form the dehydroascorbic acid (Dha) and these electrons were used in the reduction of silver ions into metallic atoms as follows:

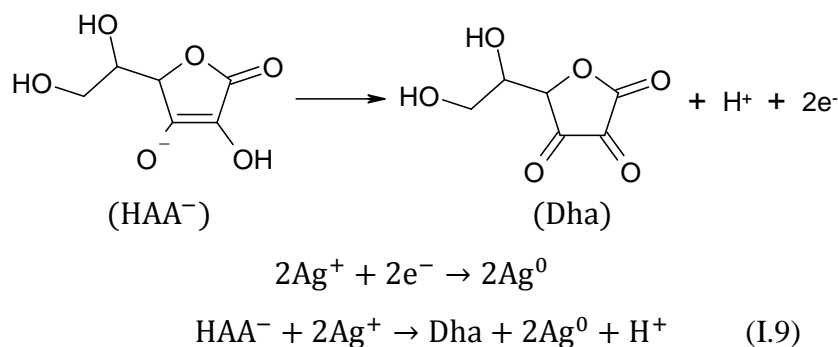


Figure I.37 – (Top) Half-reactions of ascorbic acid and (Middle) silver ions and (Bottom) the final reduction reaction.

Rather drastic changes occurred when the tiny silver seeds were added to the growth solution. In presence of seeds, the reaction produced, within few minutes, nanoplates with a narrow size distribution and the spectrum systematically exhibited a main absorption band in the 650-750 nm range. As explained in the following sections, their shape was strongly dependent on the chemical and redox environment. Seeds served as favored nucleation sites for the heterogeneous nucleation during silver ion reduction, since the energetic barrier for heterogeneous nucleation is much lower than for homogeneous nucleation. The change of reaction rate induced by the presence of seeds was monitored by recording the decrease of redox potential *vs.* silver electrode of an aqueous solution of silver nitrate as function of time after the addition of AA in absence or in presence of Ag seeds (Figure I.38 - left). Note that before the addition of the reducing agent, no strong change of potential occurred upon addition of seeds into the aqueous solution of silver ions, indicating that the majority of the silver ions were still free in solution.

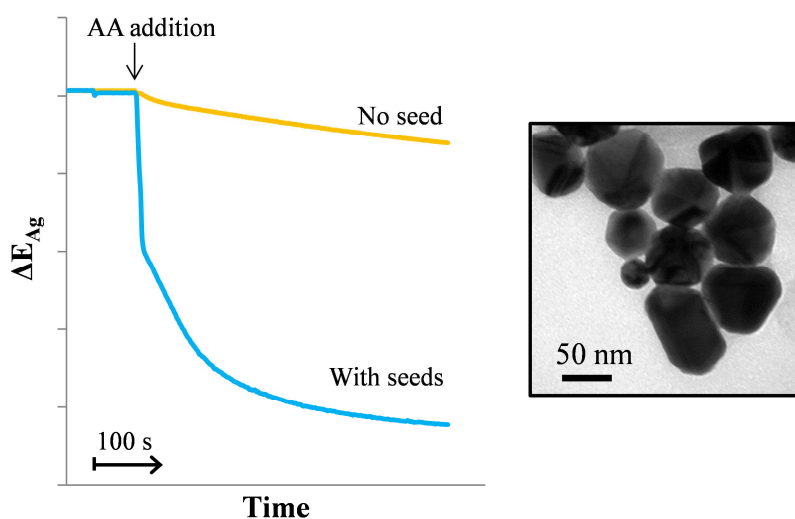
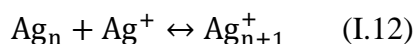
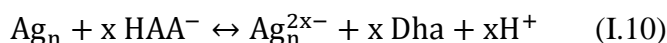


Figure I.38 – (Left) Time evolution of the potential of a silver electrode (*vs.* Ag/AgCl) upon addition of AA (0.17 mM) in an aqueous solution of Ag⁺ (0.2 mM; [seeds] = 1.2 vol.%; initial pH = 6.5; after 400 s pH = 3.8). No stabilizer was added.

(Right) TEM image of the irregularly-shaped silver nanoparticles formed without pre-made seeds in presence of PVP and citrate.

In presence of seeds, the introduction of ascorbic acid led to a sudden drop in the number of free silver ions (Figure I.38 – blue curve). It was attributed to the reduction of Ag⁺ onto the silver nuclei.

The metal particles possess a large surface area which serves as a substrate for electron-transfer reaction. It clearly helps to efficiently catalyze the decomposition of AA through the Equation I.10 [Henglein93, Novo08]. The shape analysis of the Ag^+ consumption curve showed that it could not be fitted to a first or second order rate law. It must therefore be concluded that several processes contributed to the decay of the Ag^+ concentration. Kinetically, the transfer of two electrons to the seeds forms Ag_n^{2x-} , followed by reaction Ag_n^{2x-} with Ag^+ to yield Ag_{n+2x} (Equation I.11). A second kinetic path could consist in the addition of Ag^+ to Ag_n (Equation I.12) and the electron transfer from the AA to formed Ag_{n+1} (Equation I.13).



The rate of the reduction is controlled by the rate of the electrons picked-up from AA by the particle and the migration of silver ions to the seeds. Both reactions can efficiently compete with the conventional reduction reaction of silver ions with AA (Equation I.9), even when few seeds are present. At longer times, a decrease in the reduction rate was observed due to the increase of the seed size as well as a continuous decrease of the pH of the solution. The larger particles grow slower than the smaller ones. Moreover, the reduction of Ag^+ with HAA^- releases H^+ ions in solution. Changes in pH as dramatic as 3 or 4 units were observed after introducing AA in the absence of stabilizer. This induces a deceleration of the reduction rate of silver ion which is consistent with the pH dependent reduction activity of the ascorbate.

C.3.3.3 Influence of seeds characteristics (size, nature) on the final morphology

Control experiments confirmed the importance of the seeds size on the catalytic anisotropic growth process.

- Influence of size and crystalline structure of seeds

Seeds of different sizes were produced by changing the nature of the stabilizer used during their production. Seeds were prepared with both citrate and PVP or with citrate or PVP only or by replacing PVP by PSS. TEM images of each seeds dispersions are displayed on the Figure I.39 with the temporal evolution of their corresponding absorption spectrum in air.

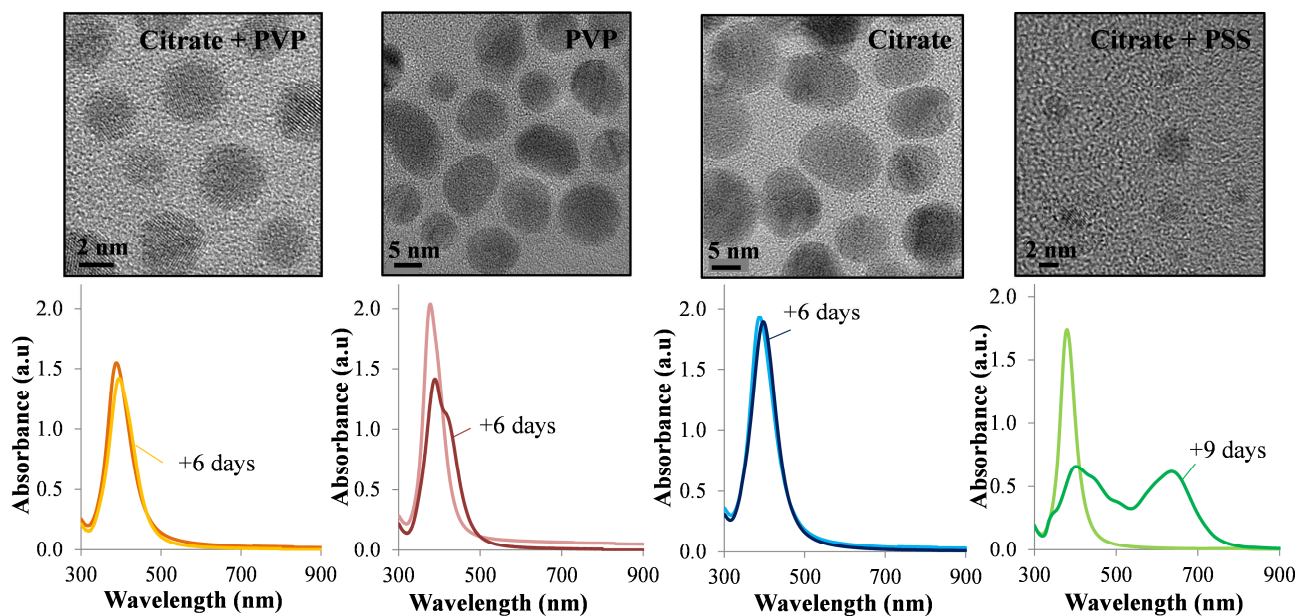


Figure I.39 – (Top) HRTEM images and (Bottom) the corresponding absorption spectra with time evolution of the different Ag seeds suspensions with $[\text{AgNO}_3] = 0.1 \text{ mM}$, $[\text{NaBH}_4] = 1 \text{ mM}$, $[\text{citrate}] = 0.3 \text{ mM}$ and $[\text{PVP or PSS}] = 5 \text{ }\mu\text{g/mL}$.

When both PVP and citrate were present in the nucleation step, the extremely fast nucleation yielded to the formation of pseudo-spherical structure seeds with an average size of $(4 \pm 1) \text{ nm}$ as observed by TEM. Seeds had little imperfections. About 87 % of the particles were single-crystalline structures; the rest had a twinned one. The twin contacts formed during the nucleation were probably due to error-stackings of atoms or mismatches of lattices. The absorption spectrum exhibited a plasmon resonance at 392 nm characteristic of small spherical Ag nanoparticles. No change was detected up to the 6th day when a slight red-shift of the plasmon band was observed.

By producing seeds in the presence of citrate only or PVP only, the size and the stability of the tiny particles changed. The HRTEM analysis revealed that large silver seeds ($> 10 \text{ nm}$) with a large number of imperfections (stacking faults or twins) were produced. We observed a strong tendency for two, three or more seeds to stick together by Ostwald ripening and adopt an elongated morphology. The electrostatic repulsion provided by the citrate molecules was too weak to avoid the seeds agglomeration. After one day, the final product was Ag nanoparticles absorbing both at 400 and 420 nm due to the coexistence of both isolated and agglomerated seeds. In contrast, well-separated particles with almost spherical morphology of diameter about $(10 \pm 2) \text{ nm}$ were found when the reduction of the silver precursor was carried out in presence of PVP only. The seeds size increased compared to the ones obtained with both citrate and PVP which was evidenced by a slight red-shift of the characteristic plasmon band compared to the one observed when both citrate and PVP were present. No strong evolution of the absorption spectrum was observed within few days revealing that the presence of the polymer prevents the seeds from coalescence. PVP clearly ensured a better stabilization of the Ag seeds than the citrate ions. Moreover, we observed that the

reduction rate was faster in presence of PVP only than with citrate only confirming also the poor complexation of the Ag^+ ions with the functional groups of the polymer.

By substituting the PVP by the poly(sodium 4-styrenesulfonate) (PSS), which is known to strongly interact with Ag species via its sulfonate group, tiny seeds of 2.5 ± 0.6 nm could be obtained. The tiny Ag seeds absorbed at 380 nm and possessed an exceptionally narrow band (FWHM = 50 nm). However due to their very small size, seeds stabilized with both citrate and PSS were not stable overtime. They were highly reactive and sensitive to Ostwald ripening. The color of the seeds dispersion gradually changed from yellow to dark green in few days when it was kept under stirring in ambient conditions (air atmosphere, daylight). The colloidal destabilization was followed by spectroscopy (Figure I.39). An intensification of the plasmon band was first observed up to the 5th hour when a decrease in intensity accompanied with an enlargement and a red-shift occurred. After several days, the plasmon band characteristic of small silver nanospheres continued to decrease but it was accompanied with the concomitant apparition of a shoulder near 340 nm and a plasmon band at higher wavelengths. These new plasmon bands were characteristic of the formation of large, polydisperse and aggregated nanoparticles.

The UV-Vis spectra of the silver nanoparticles derived from the previous different seeds under the same growth conditions are described in the Figure I.40. Note that during the catalytic process, we observed that the large seeds (~ 10 nm) affected the rate of reaction by at least one order of magnitude. For example, it took about few minutes for complete reduction of a 2.1 mM Ag^+ ions solution in the presence of tiny seeds (< 5 nm), while about 60 h were required in the presence of large seeds (~ 10 nm) due to their lower reactivity. The large seeds which possess a large number of imperfections had a lower chance in changing their shape and became stuck in their initial morphology. When used during the growth step, they systematically produced slowly pseudo-spherical particles which absorb around 425 nm in high yield (75%), the rest (25%) being irregular-shaped nanoparticles. In contrast, the small seeds (< 5 nm), once introduced in the growth medium, yielded mainly to plate-like nanostructures in the presence of a metal-coordinating stabilizer.

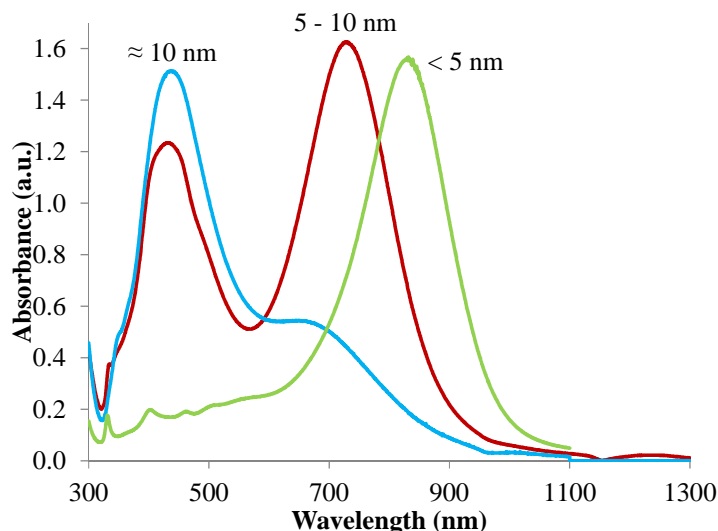


Figure I.40 – UV-Vis spectra of Ag nanoparticles grown from citrate-stabilized seeds (10 nm), PVP-stabilized seeds (10 nm and 5 nm), PSS/citrate-stabilized seeds (2.5 nm) ($[\text{AgNO}_3] = 0.21 \text{ mM}$, $[\text{AA}] = 0.34 \text{ mM}$, $[\text{citrate}] = 3.90 \text{ mM}$, $[\text{PVP or PSS}] = 0.09 \text{ mM}$ and $[\text{seeds}] = 1.2 \text{ vol. \%}$).

These observations demonstrated the importance of the seed size on the anisotropic growth. The smaller the seeds, the higher the active surface area and the better the yield in nanoplates.

- Highlighting of the growth process from Ag seeds

To elucidate how the growth proceeds, *i.e.* from oriented agglomeration of seeds or a single seed, the silver precursor was substituted by a gold precursor, the potassium gold(III) chloride, in the step-growth. Similarly with silver precursor, the reduction of gold ions by ascorbic acid (Figure I.41) was promoted on the surface of the Ag seeds.

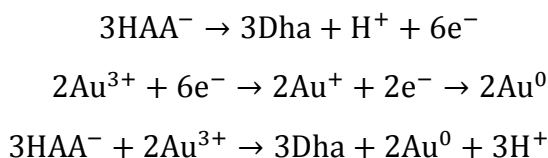
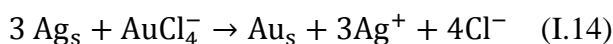


Figure I.41 - (Top) Half reactions of ascorbic acid, (middle) gold ions and (bottom) the final reduction reaction.

The Figure I.42 shows TEM micrographs of the gold nanoparticles produced by using the silver seeds stabilized with both citrate and PSS in a growth solution containing gold ionic precursor. Two populations of particles were present: large flat nanoparticles and spherical particles of smaller size produced by new nucleation. Close inspection of the flat nanoparticles showed that they possessed a hole of $(2.5 \pm 0.6) \text{ nm}$ diameter in their core, *i.e.* close to the dimension of the PSS-citrate Ag seeds. The phenomenon was due to the slow growth conditions applied here which did not allowed the deposition of a sufficient layer of Au atoms onto Ag seeds to protect them against etching by Cl^- and AuCl_4^- . Consequently, Ag seeds were galvanically oxidized by the gold salt (Equation I.15) thanks to the difference in the redox potentials between Ag^+/Ag ($+0.799 \text{ V}_{\text{NHE}}$) and $\text{AuCl}_4^-/\text{Au}$ ($+0.93 \text{ V}_{\text{NHE}}$) [Skrabalak07].



In contrast, the spherical particles produced from homogeneous nucleation, did not exhibit such a hole. These observations clearly indicate that Au nanoplates emerged from the growth of a single seed and not from agglomerated seeds.

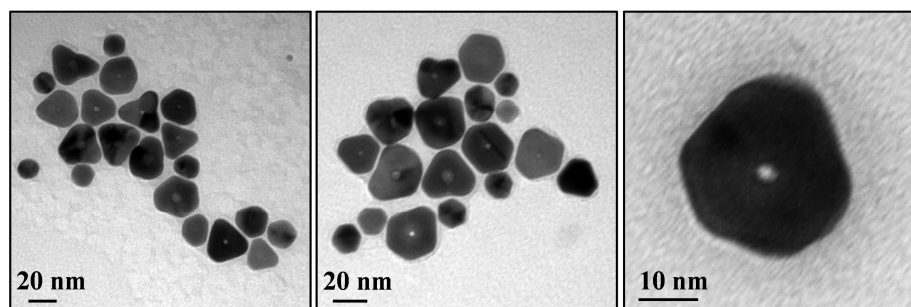


Figure I.42 –TEM images of gold nanoparticles synthesized from silver seeds.

[K₂AuCl₄] = 0.21 mM, [AA] = 0.34 mM, [citrate] = 3.90 mM, [PVP] = 0.09 mM and [silver seeds] = 1.2% vol.

A similar scenario might be operative in the case of the formation of Ag nanoplates wherein the introduction of seeds smaller than 5 nm led to the selective reduction of Ag⁺ on the seed surface. Hence, these overall results confirm that the reduction of Ag⁺ to Ag⁰ only occurs at the surface of the seeds and each seed gives rise to a single nanoplate.

- Influence of seed nature

Besides the size of the seeds, their nature was also important. Interestingly, we observed that when gold crystals seeds (3 - 4 nm) stabilized only by citrate (Protocol 7) were introduced in the growth medium, octahedral nanoparticles were produced with a relatively narrow size distribution (Figure I.43).

Protocol 7 - Synthesis of gold seeds stabilized with citrate only

250 μ L of an aqueous solution of KAuCl₄ (10 mM) and 500 μ L of an aqueous citrate solution (10 mM) were introduced into 20 mL of water under moderate stirring. Then 30 μ L of a cold aqueous NaBH₄ (0.1 M) solution was quickly added under vigorous stirring. Stirring was maintained for 1 h at 20°C.

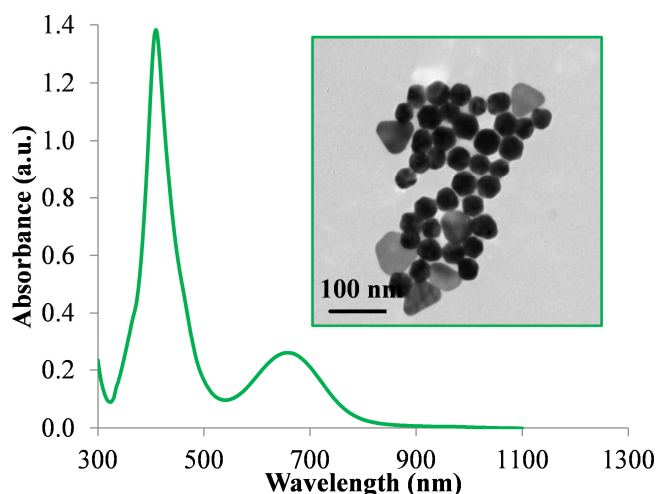


Figure I.43 – TEM and absorption spectrum of silver nanoparticles obtained by growth of gold seeds stabilized with citrate.

[AgNO₃] = 0.21 mM, [AA] = 0.34 mM, [citrate] = 3.90 mM, [PVP] = 0.09 mM and [gold seeds] = 1.9% vol.

Some flat nanoparticles were also formed but in low amount. The size- and shape-monodispersity was evidenced by a very narrow absorption band at 412 nm. In the presence of gold instead of silver seeds, the growth rate of the Ag^+ onto {111} and {100} faces of the Au seeds was probably similar leading to the cuboctahedral shape observed.

C.3.3.4 Role of the capping agents

As illustrated in the Figure I.44, the chemical environment of the growth medium had a strong effect on the shape of the final nanostructures.

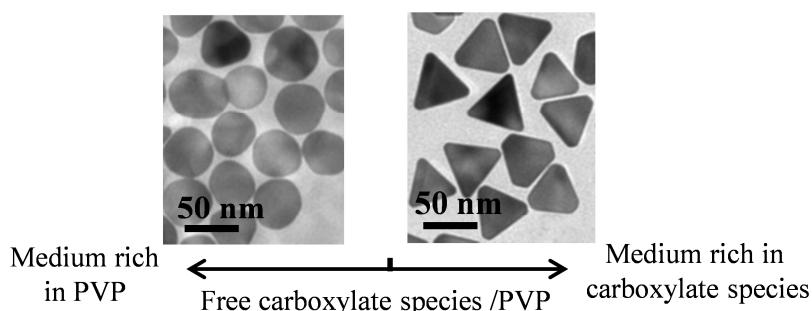


Figure I.44 - Morphology dependence of silver nanoparticles grown with pre-made seeds (stabilized with PSS and citrate).

In a medium rich in citrate ions, thin nanostructures with sharp corners and high aspect ratio were obtained. The citrate species strongly affect the chemical potential and the relative growth rates of the different seed faces. The use of citrate ions alone results in triangular nanoparticles; but in order to control the size distribution and avoid the coalescence, it is important to induce the growth in the presence of a weak amount of the usual protective polymer. In the absence of a protective agent, monodisperse triangular particles were prepared only in an extremely diluted solution.

In a medium rich in PVP, we also obtained plate-like nanostructures, but with rounded aspects. This indicates that PVP also alters the kinetics of the relative growth rates of the {100} and {111} faces, but the difference from each other is lower than that induced by the citrate species. This is assigned to the weak interactions of the macromolecules with the metal precursor and the seeds in comparison to the citrate species as evidenced from electrochemical measurements.

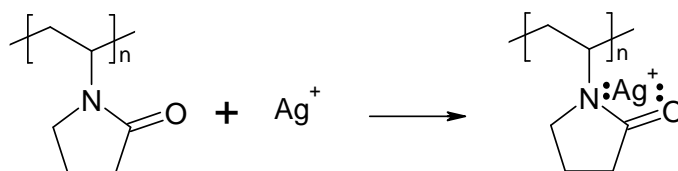


Figure I.45 - Complexation of Ag^+ ions by PVP.

Upon addition of PVP to an aqueous solution of silver nitrate, a slight decrease of the relative concentration of free Ag^+ was observed ($\Delta V_{\text{Ag}} = V_{\text{Ag}_{\text{wo}}} - V_{\text{Ag}_{\text{w}}} = 0.6 \pm 0.1$ mV) where $V_{\text{Ag}_{\text{wo}}}$ and $V_{\text{Ag}_{\text{w}}}$ are the electrochemical potential before and after the introduction of the stabilizer,

respectively; whereas the introduction of citrate systematically yielded to a net decrease of the relative concentration of free silver ($\Delta V_{Ag} = 5.0 \pm 0.2$ mV) (Figure I.46).

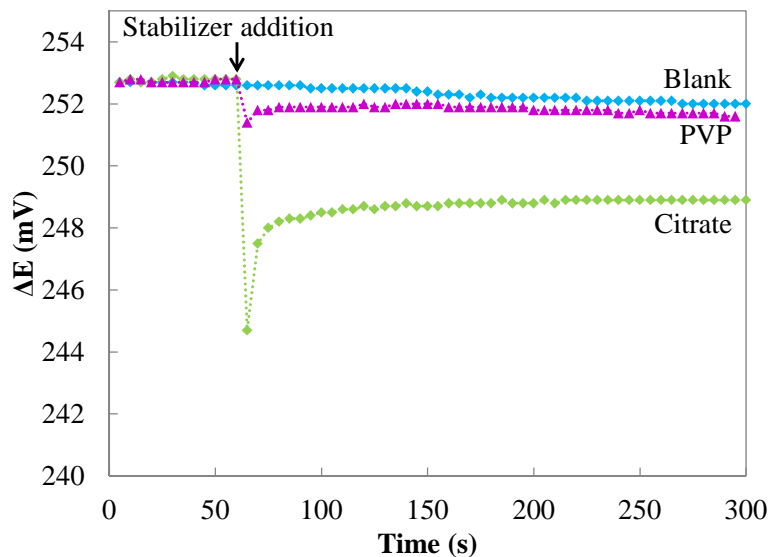


Figure I.46 – Time evolution of the silver electrode potential of an aqueous solution of silver ions (0.21 mM) upon addition of organic stabilizers. ([Citrate] = 3.90 mM, [PVP] = 0.091mM).

The citrate formed a complex with silver ions via the carboxylate groups which absorb around 300 nm (Figure I.47-top) [Dong10, Jiang10, Henglein99]. Clear sols were obtained for solutions with molar ratio [Cit] / [Ag⁺] higher than or equal to 3.0 (Figure I.47-bottom). In the case of smaller ratio, the sols were more or less turbid. At the ratios of 18-20, mostly used, only a small fraction of Ag⁺ ions is bound to the citrate. The latter conclusion is based on the observation that the UV-absorption of the Cit-Ag⁺ complex had not reached a saturation value when the Ag⁺ concentration was further increased [Djokic08].

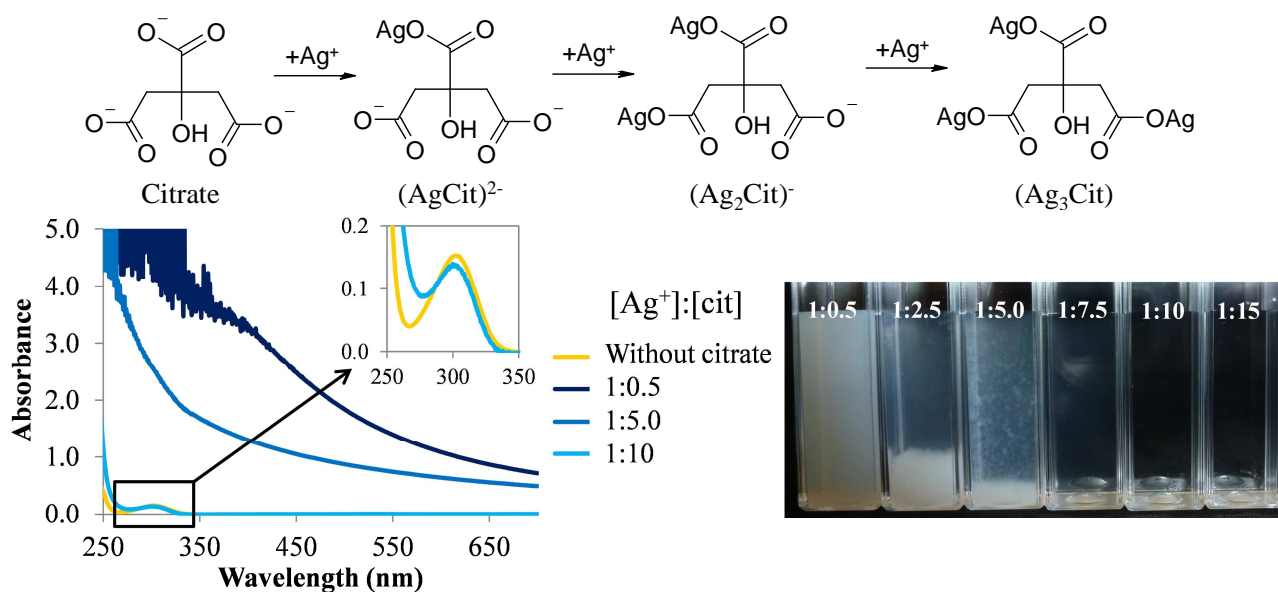


Figure I.47 – (Top) Complexation of silver ions by citrate. (Bottom) Absorption spectra and corresponding photograph of mixture solution of AgNO₃ and citrate with different molar ratios.

Figure I.48 compares the kinetics traces obtained with an aqueous solution of silver ions which contained citrate or PVP as additive after the addition of ascorbic acid. The citrate considerably delayed the consumption of Ag^+ in the earlier stages of the growth. After 30 s, only 5 % of Ag^+ had reacted with ascorbic acid. After this long incubation time, a sudden consumption of Ag^+ took place, the result being a smooth curve of sigmoidal shape with a half-height time of 5 min.

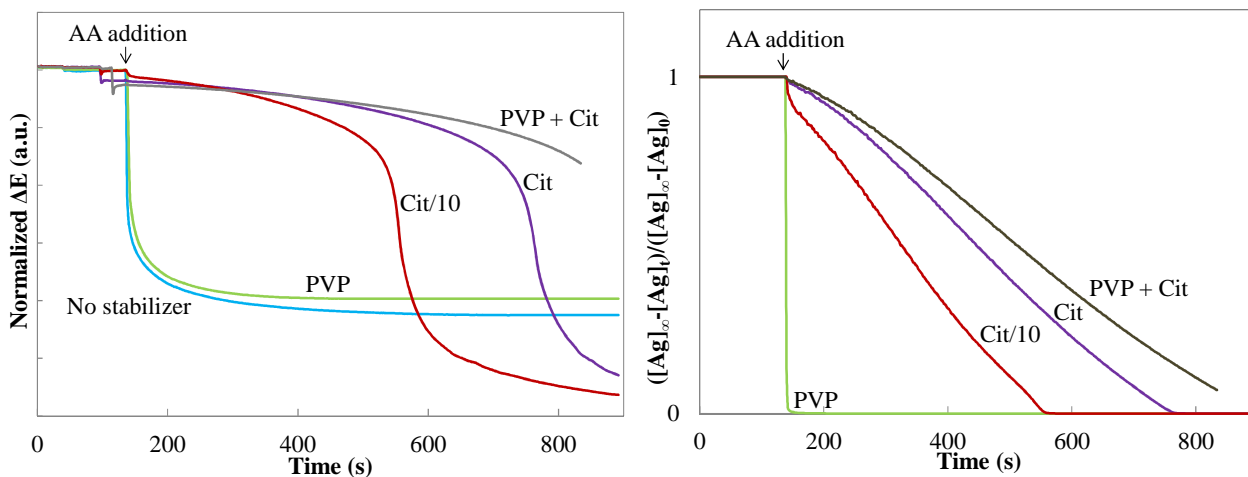


Figure I.48 - (Left) Change in intensity of the electrochemical potential of silver upon addition of ascorbic acid in aqueous solution of silver ions in the presence of seeds and various stabilizers (no stabilizer, citrate and/or PVP). (Right) Kinetics traces as function of the nature of the organic stabilizer.

By comparison of the rate constant for the reduction of silver ions with no stabilizer, one can roughly estimate that the reaction was slowed down by a factor 10^2 to 10^3 . The rate constant decreased as the concentration of citrate increased. This delayed reduction was caused by the complexation of the free silver ions as well as the binding of the seeds surface with citrate. Surface atoms with incomplete coordination are always found on silver particles [Henglein99]. The weak nucleophile carboxylate groups donate some electron density to the particle surface [Henglein99, Munro95]. By this time, the citrate ions became the dominant capping agent on the nanoparticles. It formed like a monolayer at the metal surface involving hydrogen-bonding interactions. This created a strong electrostatic repelling layer on surface which retarded the particle-mediated electron transfer from ascorbic acid to silver ion as well as the migration of the silver ion and the anionic complexes $(\text{Ag}_x\text{Cit})^{(3-x)-}$. It is this kind of silver reduction which made the particles grow smoothly. The slow and continuous supply rate of the reactive precursors results in deposition to sites of lowest free energy. This clearly aids anisotropic development. Citrate also serves as buffer, as it binds the H^+ forms. Homogeneous reduction conditions can be maintained throughout the solution ($\text{pH} = 6.8$). Stable pH avoids a decapping of the organic stabilizer from seeds that could be observed in acidic medium when the citrate species are entirely protonated. The effect was not as pronounced when PVP was used as stabilizer. The polymer chains did weakly complex the silver ions (Figure I.46) and conferred a lower surface charge to the particle. In the presence of PVP only, the pH continually decreased during the growth as in the experiment without stabilizer.

Consequently, the reduction process was only approximately 80% complete after 5 min. In the presence of both stabilizers, the retarding effect was not surprisingly more pronounced than that observed in the presence of citrate. Owing to its buffering action, the citrate stabilized the concentration of H^+ yielding to the formation of nanoplates which were more uniform in size.

C.3.3.5 Role of the protonation state of the citrate and ascorbic acid on the final characteristics of nanoparticles

From the first sets of experiments, we observed that citrate has a strong influence on the complexation of silver species and therefore the kinetic rate of the growth and that the nanoparticles growth process in the citrate/PVP medium was highly sensitive to the experimental pH values. The pKa values of citrate are 3.1, 4.8 and 6.4 (Figure I.49) while the pKa values of ascorbic acid are 4.1 and 11.6.

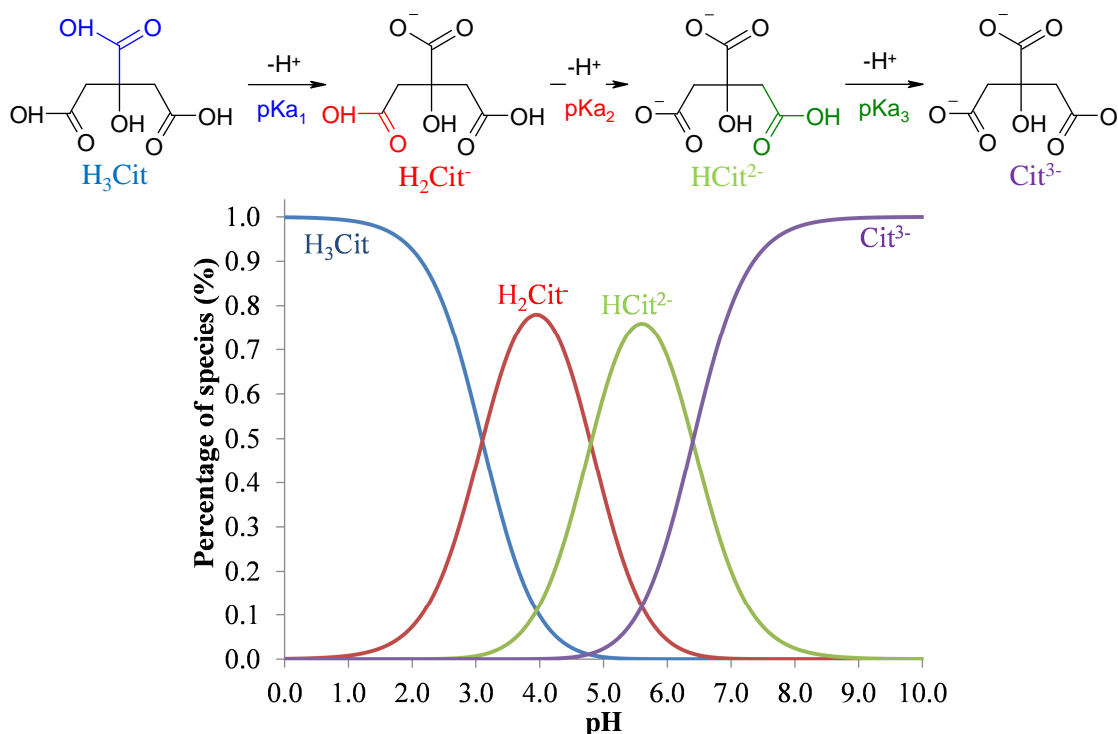


Figure I.49 – The different molecular structures and percentage of citrate species present in solution as function of pH.

The pH of the growth solution was adjusted to various pH values and then kept constant throughout the reaction by adding a solution of nitric acid (10 mM) or a solution of sodium hydroxide (10 mM). It was observed that the regulating capacity of the citrate was small in the 7.5-10 pH range and thus the pH dropped during the preparation due to the formation of silver hydroxide ($AgOH$) and the release of H^+ produced by oxidation of AA. The amount of OH^- added in the solution had thus to be increased for keeping the pH of the reacting medium constant in this pH range. The pH regulation was monitored on a titrator T70 from Mettler Toledo (*cf.* Annex 1). Distinct coloration was apparent at the end of the reaction for the different preparations in the 3-10

pH range. The Figure I.50 shows the photographs, absorption spectra and corresponding TEM images of the dispersions at the most significant pH values.

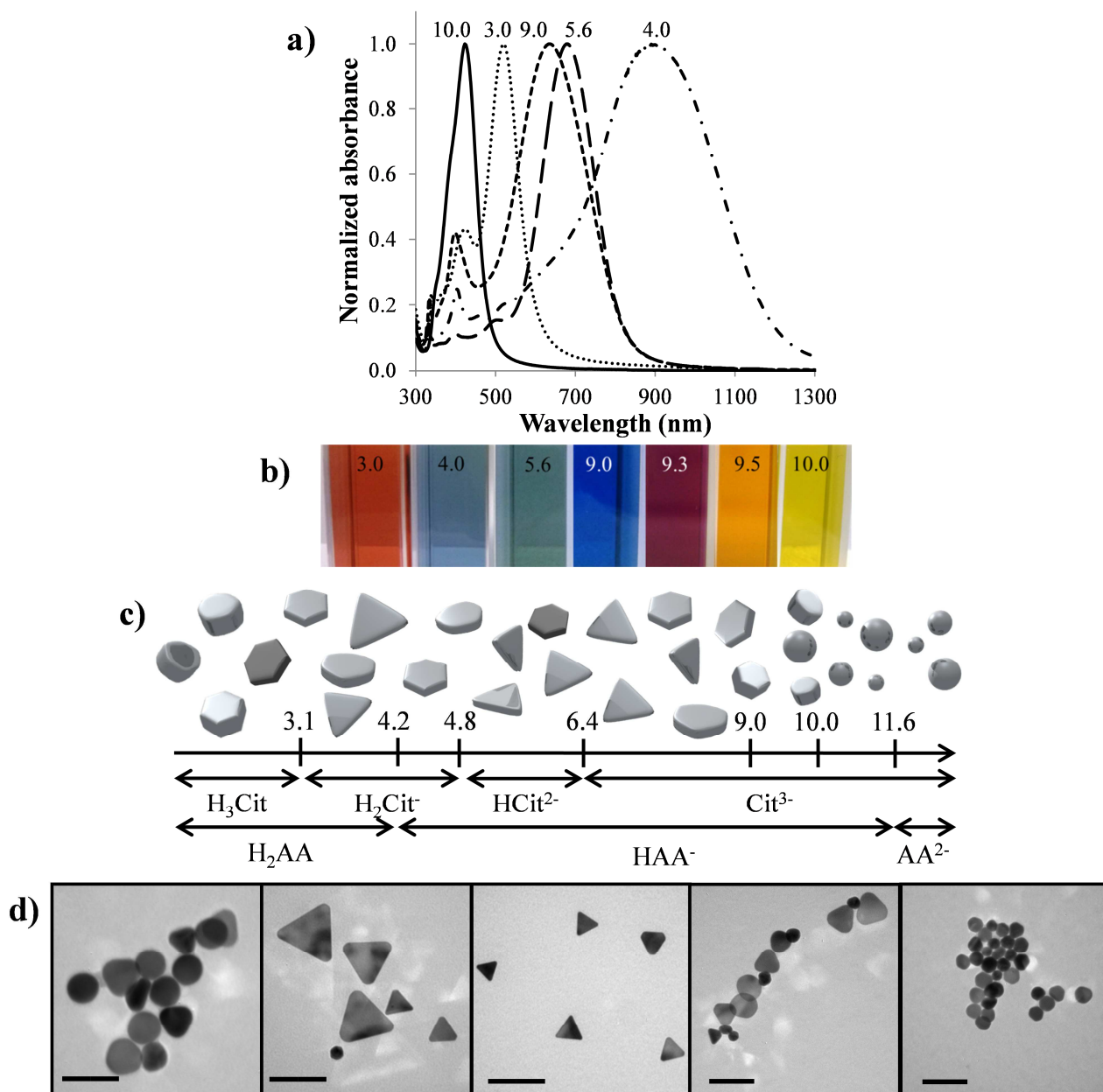


Figure I.50 - (a) UV-Vis absorption spectra of Ag nanoparticles synthesized at different pH values. (b) Photographs of the corresponding colloidal suspensions. (c) Schematic illustration of the morphology of the silver nanostructures observed as function of pH. (d) TEM images of the as-synthesized silver nanostructures. Scale bars = 50 nm. ($[AgNO_3] = 0.14$ mM; $[AA] = 0.19$ mM; $[citrate] = 3.99$ mM; $[PVP] = 0.09$ mM; $[seeds] = 1.2$ vol.%).

- At pH 3.0, the dispersion turned to orange gradually. The absorption spectrum, characteristic of non-triangular thin particles (disk-like), was recorded at the end of the reaction. It exhibited an intense band at 550 nm and two weak bands at 450 and 335 nm. TEM confirmed that circular nanocrystals were the dominant products with a mean diameter of 50 nm.

- At $3.0 < pH < 5.0$, a net color change was obtained. The blue color characteristic of high-aspect ratio nanoparticles was observed. A large fraction of large triangular nanoparticles that were irregularly shaped and of different sizes was formed as evidenced by the broad plasmon band

centered in the near IR in the absorption spectrum. Ionization of the surface by citrate carboxylate groups induced a net elongation of the nanoplates and favored the formation of flat crystals (~ 74%) with a triangular shape compared to the case of $\text{pH} < 3$ with identical silver concentration.

- As the pH was further increased up to 6.4, the size and shape became more uniform and a higher proportion of flat nanoparticles were produced (~ 90%). The monodispersity of the Ag nanoparticles was reflected by the narrower and more symmetrical band centered at about 700 nm and the weak intensities of the shoulder in the 400-500 nm area in the extinction spectrum. As the preparation was performed at higher pH value (up to 6.4), the triangular particles became more truncated.

- In basic media, a net blue-shift of the main absorption band was observed. It was accompanied by an increase of the band characteristic of the spherical particles. There was significant nucleation of new particles favored by an increase of the reduction reaction rate due to the unprotonated form of the ascorbic acid (noted AA^{2-}). Additionally, the presence of a high concentration of OH^- interfered directly on the process of coordination of Ag^+ and Ag seeds by the citrate species. The strong binding of AgOH rationalized in terms of the value of K_s of AgOH (1.52×10^{-8}) resulted in isotropic passivation of the overall seeds surface via an AgOH layer and promoted isotropic growth.

- Finally above pH 10, fast coloration to deep yellow was obtained and there was no longer evidence of nanoplate formation.

The scheme of Figure I.50 summarizes the predominant shapes obtained as well as the variation of charge of citrate ions and ascorbic acid with pH. Altering the protonation state of the carboxylate groups of the citrate as well as the ascorbate during the growth process has dramatic impacts on the uniformity in size and shape of the nanoplates.

The generation of uniform triangular nanoplates was clearly favored in slightly acidic solutions when the pH was maintained constant at about 5.6, *i.e.* in the presence of a high proportion of citrate (HCit^{2-}) and ascorbate monoanion (HAA^-). The rate of nanoparticle growth was dependent on the concentration of the monoanion and was consequently highly pH-dependent around the pKa of the ascorbic acid. Moreover, a change in the conformation of the adsorbed species at the particle surface might also occur as a function of the pH. In a slightly acidic solution, the citrate would be predominantly present as HCit^{2-} form. This chemical specie probably adsorbed in a rather flat conformation. As the acidity of the solution was increased, protonation of the citrate species occurs and the possibility existed that the H_2Cit^- and H_3Cit species extend further in solution than does the HCit^{2-} specie. Previous investigations had shown that only two of the carboxylate groups would bind to the surface, leaving the third one normal for the surface [Kilin08, Henglein99]. This would explain why HCit^{2-} was key specie for achieving the uniformity of particles shape. The selective

adhesion of HCit^{2-} on a given facet had not been observed directly during the nanocrystal growth, but the theoretical studies and the experimental observations might suggest that the adsorption of the HCit^{2-} would be favored on the {111} surface relative to the {100} one because of geometrical considerations. This would explain why the yield of triangular shape increased at $\text{pH} = 5.6$.

C.3.3.6 Can the citrate be substituted by another carboxylated compounds?

Since the monoprotonated citrate allowed to get a fine size and shape control, we explored the possibility of substituting the citrate with other carboxylated compounds containing two deprotonated carboxylate groups similarly to other research groups [Zhang11b].

Disodium succinate and disodium malate were tested. The succinate exhibits only two carboxylate functions while the disodium malate exhibits two carboxylate and one alcohol functions (Figure I.51).

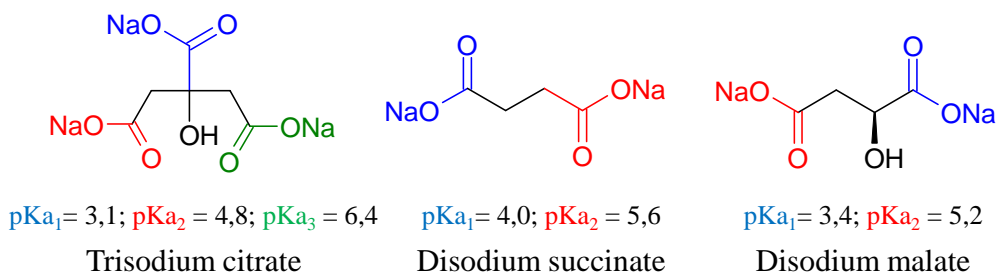


Figure I.51 - Molecular structures of trisodium citrate, disodium succinate and sodium malate.

Absorption spectra and corresponding TEM micrographs of the colloidal suspensions obtained with the various carboxylated compounds are shown in the Figure I.52. The use of malate instead of citrate induced the formation of flat objects with a more or less triangular shape. The obtained particles were more rounded and thicker than with citrate. This resulted in a blue-shift of the main resonance from 700 nm (with citrate) to 510 nm and a red-shift of the weak resonance characteristic of the thickness from 333 nm to 340 nm. The use of succinate induced the formation of thin nanoplates with a thickness intermediate (7.9 ± 1.0 nm) than that of citrate (4.7 ± 0.5 nm) and malate (14.5 ± 1.8 nm). An additional band at 450 nm emerged probably due to the presence of hexagonal nanoparticles in the dispersion.

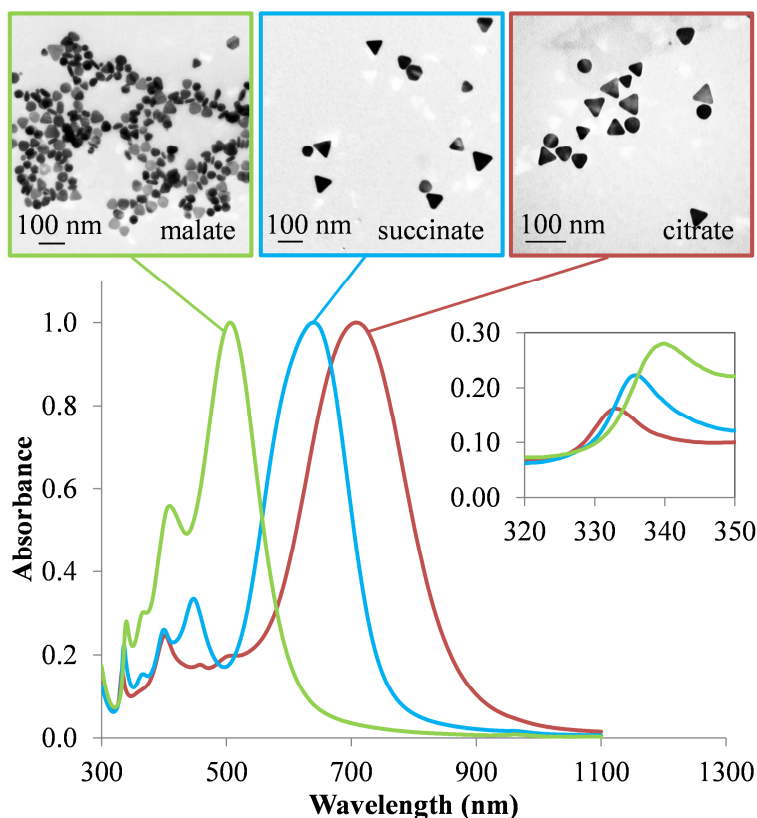


Figure I.52 – TEM images and corresponding absorption spectra of dispersions obtained by using citrate (red), succinate (blue) or malate (green) as capping agent and with $[AA] = 0.17$ mM, $[AgNO_3] = 0.21$ mM, $[citrate]$ or $[succinate]$ or $[malate] = 3.90$ mM, $[PVP] = 0.09$ mM, and $[seeds] = 1.2$ vol.%.

We observed that the reaction rate of reduction of Ag^+ species was faster with succinate than the one with citrate. This could be explained by the lower amount of Ag^+ complexed with succinate in comparison to citrate species. This was confirmed by the electrochemical measurements (Figure I.53). The addition of succinate in an aqueous solution of silver ionic precursor induced a lower decrease of the potential ($\Delta V_{Ag} = 1.8 \pm 0.2$ mV) than the one observed with citrate (vs. 5 mV in the presence of citrate) for identical concentrations of silver ions.

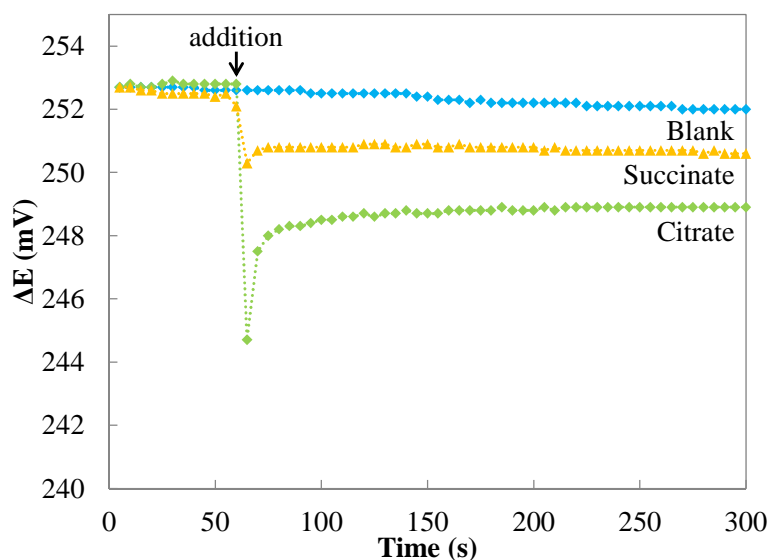


Figure I.53 – Time evolution of electrode potential of a silver solution when citrate is added. $[AgNO_3] = 0.21$ mM and $[Succinate]$ or $[Citrate] = 3.90$ mM.

Moreover, in the presence of succinate, the kinetic traces essentially keep their sigmoid-shape but were temporally reduced by a factor 2 (Figure I.54). This confirmed that the colloids were produced more rapidly in presence of succinate than in presence of citrate. Consequently, thicker (8 nm vs. 5 nm for citrate) and smaller nanoprisms were produced in comparison to those obtained in the presence of HCit^{2-} .

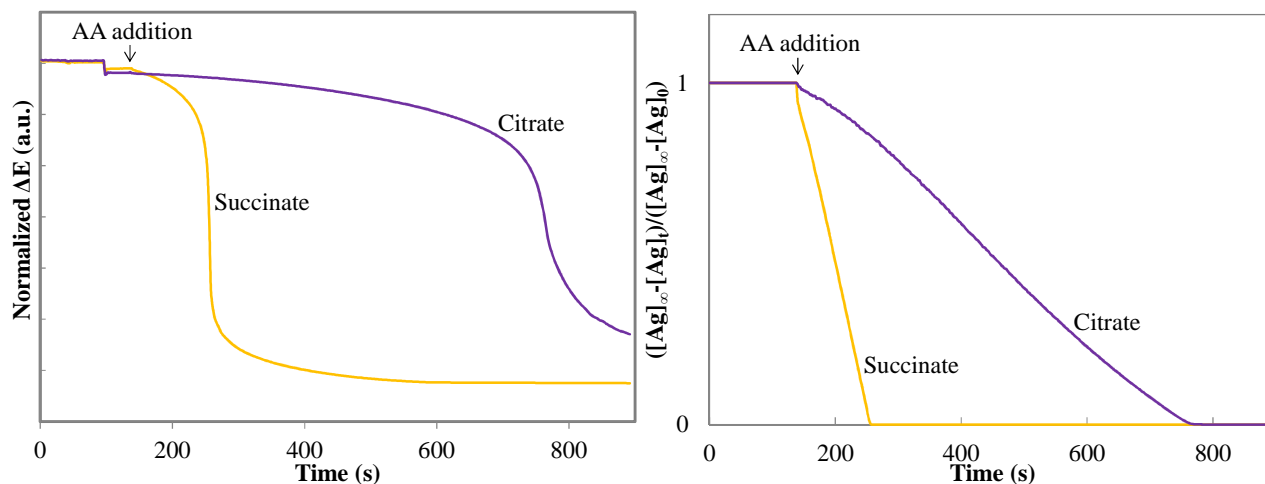


Figure I.54 - (Left) Comparison of the variation of the electrochemical potential of silver upon addition of ascorbic acid in aqueous solution of silver ions in the presence of seeds and succinate or citrate and **(Right)** the corresponding kinetics traces.

As for citrate, the uniformity in size and shape was strongly dependent on the protonation state of the carboxylate groups. Figure I.55 presents the absorption spectrum and typical TEM image of colloidal suspensions obtained with succinate as additive instead of citrate at two different pH values.

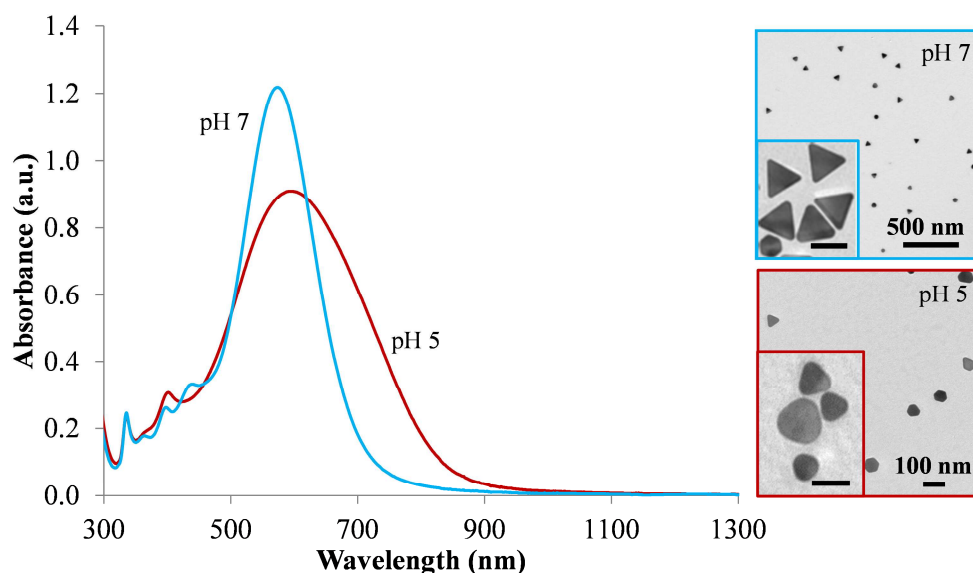


Figure I.55 - Absorption spectra and corresponding TEM images of silver nanoplates obtained with succinate at pH 5.0 (red curve) and 7.0 (blue curve), with $[\text{AgNO}_3] = 0.21$ mM, $[\text{AA}] = 0.34$ mM, $[\text{succinate}] = 3.90$ mM, $[\text{PVP}] = 0.09$ mM and $[\text{seeds}] = 1.2$ vol.%. Scale bar of the insets = 50 nm.

While fully protonated (H_2Succi) or partially protonated (HSucci^-) succinate caused a greater percentage of shape impurities (disk, spheres), the unprotonated succinate led to nanoparticles with

a well-defined triangular morphology and well-defined SPR features in the absorption spectrum. At $\text{pH} = 7$ (*i.e.* above the pK_a values of succinate (Figure I.56)) the bands were sharper and more symmetrical, which reflected more uniform size distributions than at $\text{pH} = 5$. The pH of the solution should be around 7 and lower than 9 to avoid high concentration of OH^- ions and the formation of AgOH .

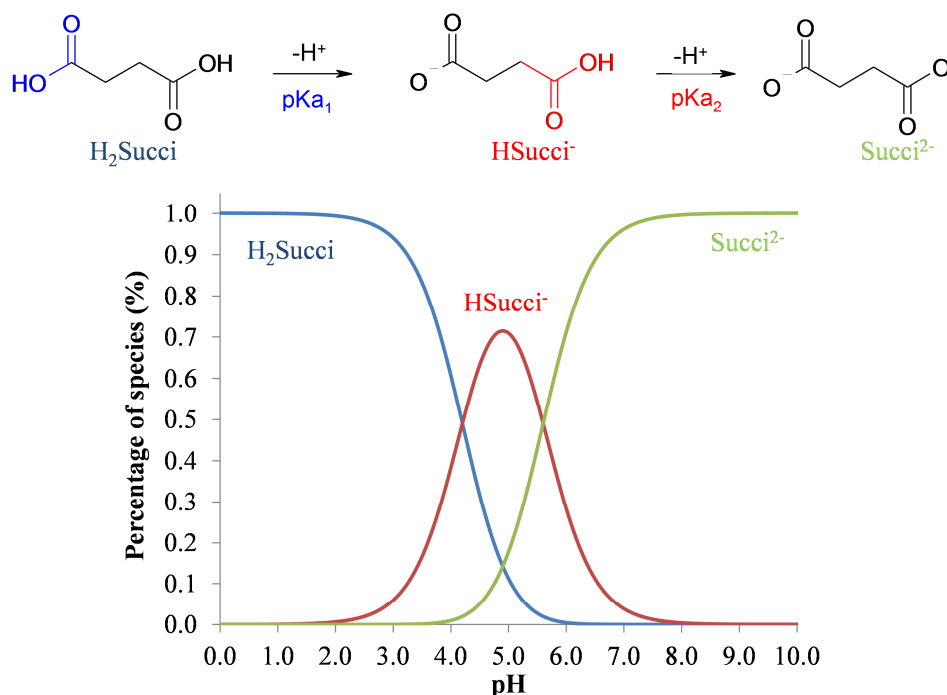


Figure I.56 - The different molecular structures and the percentage of succinate species as function of pH .

We also wondered if polyacrylic acid (PAA) exhibiting a carboxylate group in its repeat unit (pK_a 4 - 4.5) could allow to control the shape and size distributions (Figure I.57).

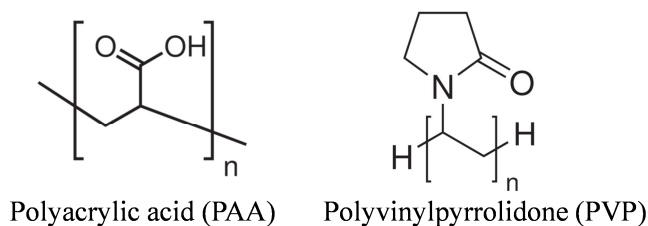


Figure I.57 - Molecular structure of PAA and PVP.

As shown in the Figure I.58, the use of PAA instead of PVP in the growth step induced an increase of the thickness from $(8 \pm 1 \text{ nm})$ to $(20 \pm 2) \text{ nm}$ with a reduction of the average length and a strong truncation of the nanoparticles. That was evidenced by a red-shift of the weak resonance in the UV from 337 to 346 nm due to the thickness increase and a blue-shift of the main resonance near 680 nm (with PVP) to 470 nm (with PAA) due to the size reduction and truncation. The presence of only one carboxylate function did not allow a selective adsorption of the polymer on some crystalline faces like citrate or succinate which exhibit two or three carboxylate functions. In the PAA case, the molecules adsorbed on all the crystal facets of silver promoting the growth of more isotropic nanoparticles and thus increasing the thickness of the final particles.

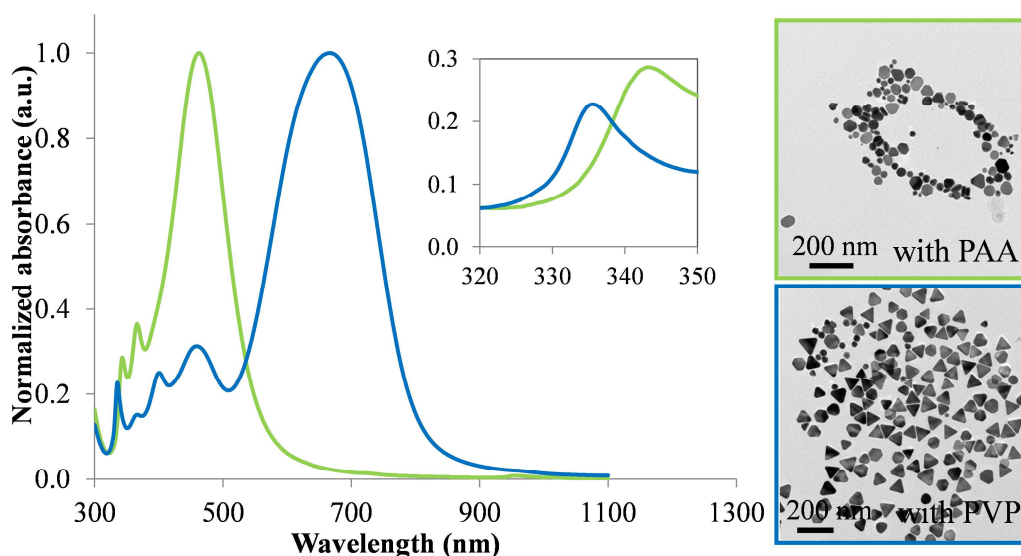


Figure I.58 - TEM images and corresponding absorption spectra of dispersions obtained by using PAA (green) or PVP (blue) as capping agent at pH 7.0 and with [AA] = 0.17mM, [AgNO₃] = 0.21 mM, [succinate] = 3.90 mM, [PVP] or [PAA] = 0.09 mM, and [seeds] = 1.2 vol.%.

C.3.3.7 Considerations on the growth mechanism in carboxylated compounds additive systems

Silver nanoplates grow in non-equilibrium conditions and their growth is clearly influenced by the factors contributing to the reaction kinetics, *i.e.* the rate at which silver atoms are generated from silver precursor and added to the surface of the growing seeds. By carefully controlling the reaction kinetics, newly formed atoms can be selectively added to specific sites rather than the entire surface of the growing seeds. In this section, we address several key points relevant for the mechanistic understanding of their formation and outline a few questions that need to be addressed by future research:

- First, we demonstrated in this study that when the synthesis is conducted with a silver precursor, a carboxylated compound and a long-chain polymer with tiny crystalline seeds (< 5 nm), the yield of silver nanoplate is dramatically improved. Because of their ultra-large specific surface area, the fine seeds serve as efficient catalysts for the decomposition of ascorbic acid. Even if a small fraction of AA reduces Ag⁺ directly in solution, the newly formed Ag⁰ atoms reach the surface of the Ag nuclei and contribute to the mantle of deposited metal. The smaller the seeds, the higher the active surface area and the better the yield of nanoplates.

- Second, the crystallinity of the initial tiny seeds is important for plate-like formation. It seems plausible, although not proven by direct experiment, that the key deciding factor for initial symmetry-breaking needed to avoid spherical growth is the formation of a single [111] planar twinning defect on the growing seeds. Since lamella twinning planes are formed by chance and are randomly distributed among seeds, it is difficult to target their formation at the nucleation stage. However, it is possible to control the formation of the lamella twinning plane via kinetically

controlled collision of newly formed Ag atoms with the surface of the growing single crystal-seed. The landing of atom on an inappropriate site on the seed surface is considered to be the beginning and is easily followed by the formation of a twin plane which enhances grain growth. It has been known for a long time that a nanoplate seed with a single [111] twin plane or two parallel twin planes can grow faster than other seeds, since its side surfaces have a rough structure with re-entrant corners, which are believed to be suitable places for incorporation of solute ions [Berry68]. As soon as the [111] twin plane formation begins, it self-catalyzes the reduction in the direction parallel to this plane. The growth may be much slower in the direction perpendicular to the [111] planes yielding the generation of elongated spheres which evolve to form nanoplates. This hypothesis implies the initial presence of single crystalline ultra-fine seeds. Tiny seeds are prepared in a high degree of supersaturation conditions which favors the formation of twin planes. Twinning takes places at random among seeds. Nevertheless, one observed that by controlling the degree of supersaturation in the nucleation step, it became possible to limit the formation of seeds that have a large number of imperfections. A high degree of supersaturation including a high concentration of reducing agent, a high concentration of stabilizers (PSS and citrate) is effective in forming single crystal seeds at the expense of the twinned ones.

- Third, we believe that the symmetry breaking by twinning which introduces anisotropy is dependent not on the reaction rate at the grain surface but on the supply rate of ad-atoms by diffusion from the bulk of the solution to the seed surface. In the range where the reduction rate runs very fast, the amount of atoms supplied from the bulk is too large for the seed surface to readily incorporate them regardless of the structure of the seed surface. Consequently, a rapid growth of the different seeds facets results in quasi-spherical particles displaying a large number of structural defects. It could also lead to the formation of new nuclei with different shapes. In practice, it happens when the reduction is performed with a strong reducing agent, *e.g.* sodium borohydride and unprotonated ascorbic acid, or when the injection rate of the metallic precursor is fast. In the range where the reduction rate is sufficiently slow, the amount of Ag^0 atoms supplied by diffusion is thought to be limited and to be incorporated into growing grains depending upon the grain surface. As a result, the formation of twin planes is limited. The seeds gradually become anisotropic and take the form of flat nanoparticles. A moderate reduction rate is clearly achieving by using a weak reducing agent such as monoprotonated ascorbic acid AA^- , by simply decreasing the injection rate of silver nitrate in the reaction medium or by reducing the concentration of free silver ions in the presence of a silver-complexing agent. The carboxylated compounds as well as some long chain polymers are known for a long time to strongly coordinate silver ions and silver seeds [Zeng10c, Dong10, Jiang10, Henglein99]. In the case of the citrate or succinate, they cap the seed nanoparticles and complex the silver ions. Their adsorption creates a strong negative charge at

the surface of the seeds. The ascorbate monoanion and the metallic complexes negatively charged need to penetrate the negative potential field surrounding the seeds particle. Consequently the rate of silver reduction is one order of magnitude slower than the rate observed for the same system when the seeds grow as spheres in the absence of carboxylated compounds. The process is highly pH-dependent. The optimal pH for citrate and succinate species is in a narrow window. It is around 5.6 for citrate and 7 for succinate medium. This avoids an increase of the concentration of H_3O^+ , the protonation of the organics and thus protects the capped seeds from decapping. In the case of long chain polymers such as PVP, the rates of the reactions are mainly governed by steric aspects. The polymer has a few effects on the silver ionic precursor. It thus slows down the reaction owing its adsorption onto the initial silver nuclei. The origin of the plate-like morphology is thus assigned to a slow deposition of newly formed silver atoms to the seeds during the early stage of the growth. Low reduction rates also avoid self-nucleation. Reaction kinetics are thus the dominant factors affecting the particle growth and shape. The essential elements of the mechanism are illustrated in the Figure I.59.

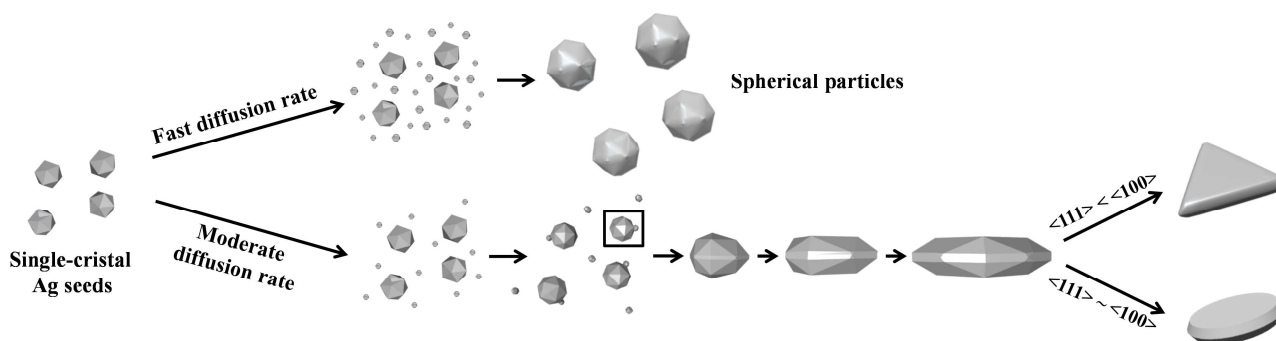


Figure I.59 - Illustration of the mechanism responsible for Ag nanoprism formation. Reduction of Ag^+ takes places on Ag seeds. By careful control of the reaction kinetics, newly formed atoms and clusters can be selectively added to specific sites rather than the entire surface of the growing seeds. This favors the creation of twin plane, leading to nanoplates formation.

- Last, the elongated seeds grow into either circular, hexagonal or triangular plates. This depends on the ratio of the difference of growth rate $\{111\}$ and $\{100\}$ surfaces. Our experiments indicate that the ratio of growth rates between the $\{111\}$ and $\{100\}$ faces could be adjusted by varying the protonation state of the carboxylated compounds. The HCit^{2-} or Suc^{2-} species may selectively bind to the Ag $\{111\}$ faces rather Ag $\{100\}$. With more HCit^{2-} or Suc^{2-} adsorbed to the $\{111\}$ faces, they more repel the $[\text{AgCit}]^-$ complexes and grow at a slower rate. The $\{100\}$ faces grow themselves almost out of their existence and mostly the $\{111\}$ faces remain. When the growth rate in the $[111]$ direction is greater than that in the $[100]$ direction, triangular particles result. The formation of triangular plate-like nanocrystals is thus clearly associated to the stability and the diffusion rate in between the reactive monomer species and the growing nanocrystal seed surface. Choosing an appropriate complexing agent is one of the key steps in obtaining control over reaction kinetics and anisotropic nanocrystal growth. A good choice allows to finely adjust the relative

growth rates of {100} and {111} faces and modify the shape of the plate-like nanocrystals. Such conclusions are in agreement with work reporting that the reaction kinetics is the key in directing the growth of nanoparticles [Zhang11a, Zhang10a].

The proposed mechanism fits with the spectral evolution observed during the growth, since a gradual rise of the visible-NIR band is observed (Figure I.60). Moreover, the particle size could be finely tuned from side lengths of 20 nm to (at least) 70 nm by simply varying the molar ratio between seeds and AgNO_3 in the growth solution (Figure I.61). This effect goes along with a color change of the samples from light yellow to blue and a progressive intensification of the dispersion color. The possibility of changing the size provides a straightforward way to tailor the spectroscopic features of the silver nanoprisms

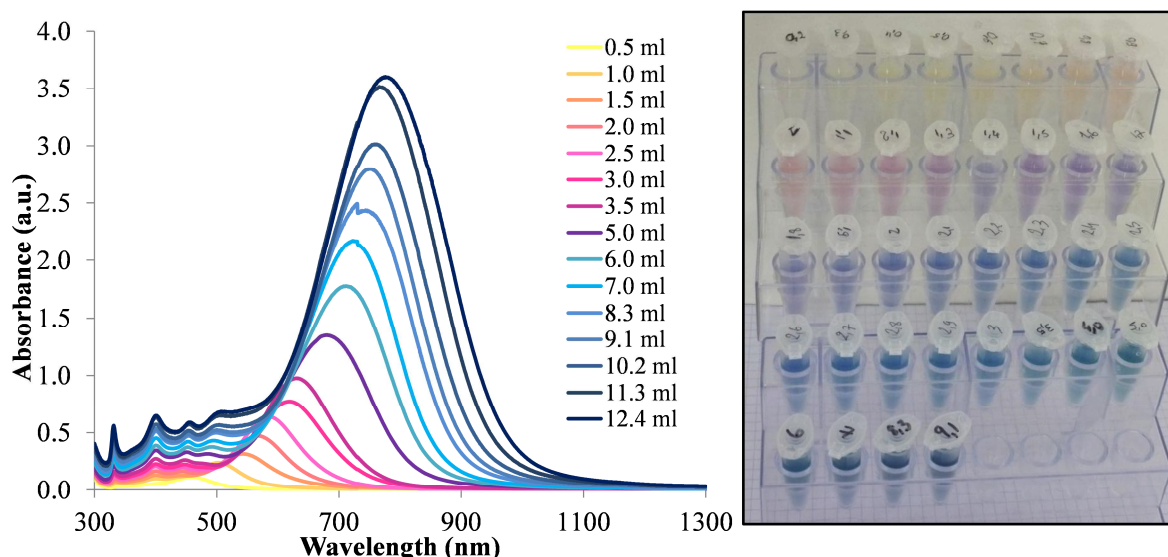


Figure I.60 – (Left) Evolution of the absorption spectrum and (right) corresponding picture of growth solution depending on the AgNO_3 volume added from 1 to 12.5 mL ([AA] = 0.34 mM, [citrate] = 3.90 mM, [PVP] = 0.09 mM, and [seeds] = 1.2% vol).

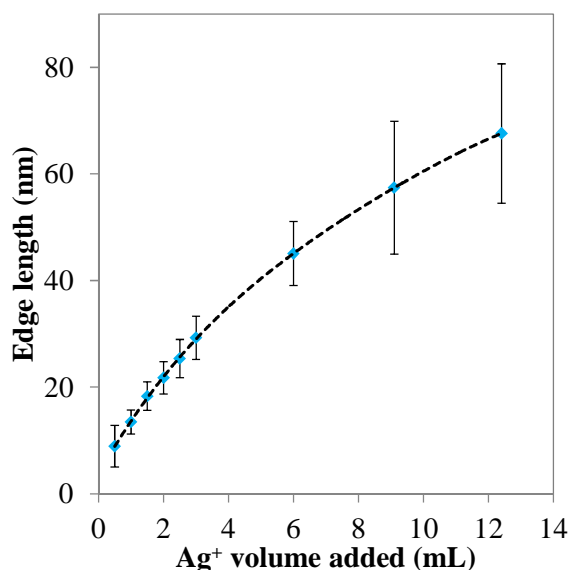


Figure I.61 – Evolution of the edge length of Ag nanoprisms depending to the AgNO_3 volume added with [AA] = 0.34 mM, [citrate] = 3.90 mM, [PVP] = 0.09 mM, and [seeds] = 1.2% vol.

C.4 Chemical stability of the silver nanoprisms

With respect to colloidal stability, we observed that the as-prepared Ag nanoparticles gradually evolve to rounded plates over a couple of days when stored in air at room temperature. This sensitivity of the particles toward oxygen can be strongly decreased by protecting them with chemisorbed molecules such as thiol-alkanes. The displacement of the weakly adsorbed surfactants (citrate or succinate and PVP) by a thiol-alkane is strongly helpful for stabilizing the triangular shape of the nanoparticles. Different molecules were used: 11-mercaptoundecanoic acid (MUA), sodium 3-mercapto-1-propanesulfate (MPS) and 11-mercaptoundecyl)-*N,N,N*-trimethylammonium bromide (MUTAB) (Figure I.62). Each molecule exhibits a thiol function as head group which has a strong affinity with Ag surface and a more or less long carbon chain with a carboxylate, sulfonate or trimethyl-ammonium function, respectively, as tail group to ensure a negative (with MUA and MPS) or positive (with MUTAB) overall charge to the silver particles.

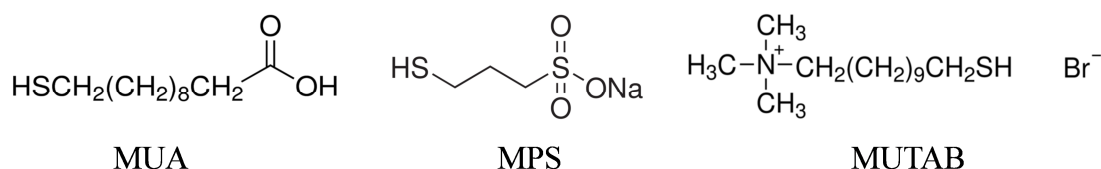


Figure I.62 - Molecular structures of MUA, MPS and MUTAB.

These molecules exhibit a “head thiol group” which has a strong affinity with the silver and a “tail group” (Figure I.63). Their self-assembly are created by chemisorption of the headgroup onto the silver followed by a slow organization of the “tail groups”. As the molecular coverage of the substrate increases, the headgroups assemble together on the substrate, while the tail groups assemble far from the substrate. Areas of oriented, densely-packed molecules nucleate and grow until the surface of the substrate is covered in a single monolayer.

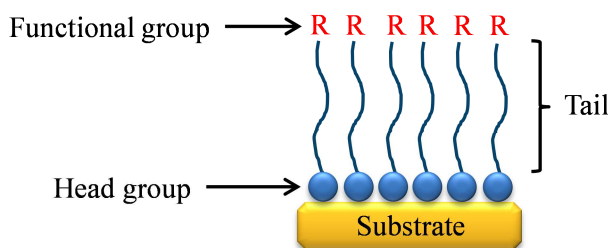


Figure I.63 - SAM schematic.

Although the self-assembly took place rapidly, we observed that a clean environment of the silver nanoprisms was a key step to prepare stable colloidal dispersions (Protocol 8).

Protocol 8 - Coupling of MUA (or MPS or MUTAB) in aqueous medium

The grafting of MUA on the silver particles surface was performed directly in the growth medium. A volume V_{MUA} – calculated by the equation I.16 – of a 25 mM MUA aqueous solution adjusted at pH 10 corresponding to an excess of 50 compared to the grafting density of MUA ($d_{MUA} = 4$ molecules/nm²), was quickly added into the silver suspension, under magnetic stirring. The growth solution and the MUA solution were pre-adjusted to pH 10 in order to solubilize the molecules in water. The reaction mixture was stirred overnight. In order to eliminate the excess of thiols, the mixture was placed in two 45-mL tubes and centrifuged at 8000 g during 20 min at 20°C. The supernatant containing free thiols was removed and the bottom, containing the modified particles, was redispersed in water by sonication. This washing step was repeated 4 times. Same protocol was performed for the grafting of MPS (by considering $d_{MPS} = 4$ molecules/nm²) and MUTAB (by considering $d_{MUTAB} = 2$ molecules/nm²). However, for these two coatings it was not necessary to initially adjust the pH value of the solution.

The volume V_{MUA} was calculated as follows:

$$V_{MUA} = \frac{d_{MUA} * S_T * \text{purity of EDPS} * \text{excess}}{[MUA] * N_A} \quad (\text{I.15})$$

with N_A the Avogadro number and S_T the total surface of silver (m²) calculated as follows:

$$S_T = N_p * S_{Ag} \quad (\text{I.16})$$

with N_p is the number of Ag particles and S_{Ag} the surface of one Ag triangle calculated as follows:

$$S_{Ag} = 2(B * h) + 3(t * B) \quad (\text{I.17})$$

where B, h and t are the edge length, height and thickness of the Ag triangle, respectively.

The Figure I.64 shows the absorption spectra of silver nanoprisms before (blue curve) and after the functionalization with MUA, MUTAB and MPS. The main plasmon band of Ag nanoprisms slightly red-shifted when MUA was added to the suspension evidencing the coating of particles. However when MPS was added to the dispersion, a blue-shift was observed due to an etching of nanoprisms as previously observed in presence of halides. Finally, when MUTAB was added a red-shift was firstly observed then 24-h later a strong enlargement and decrease in intensity of the plasmon band. That was associated to a destabilization and aggregation of nanoprisms due to the presence of bromide in large amount.

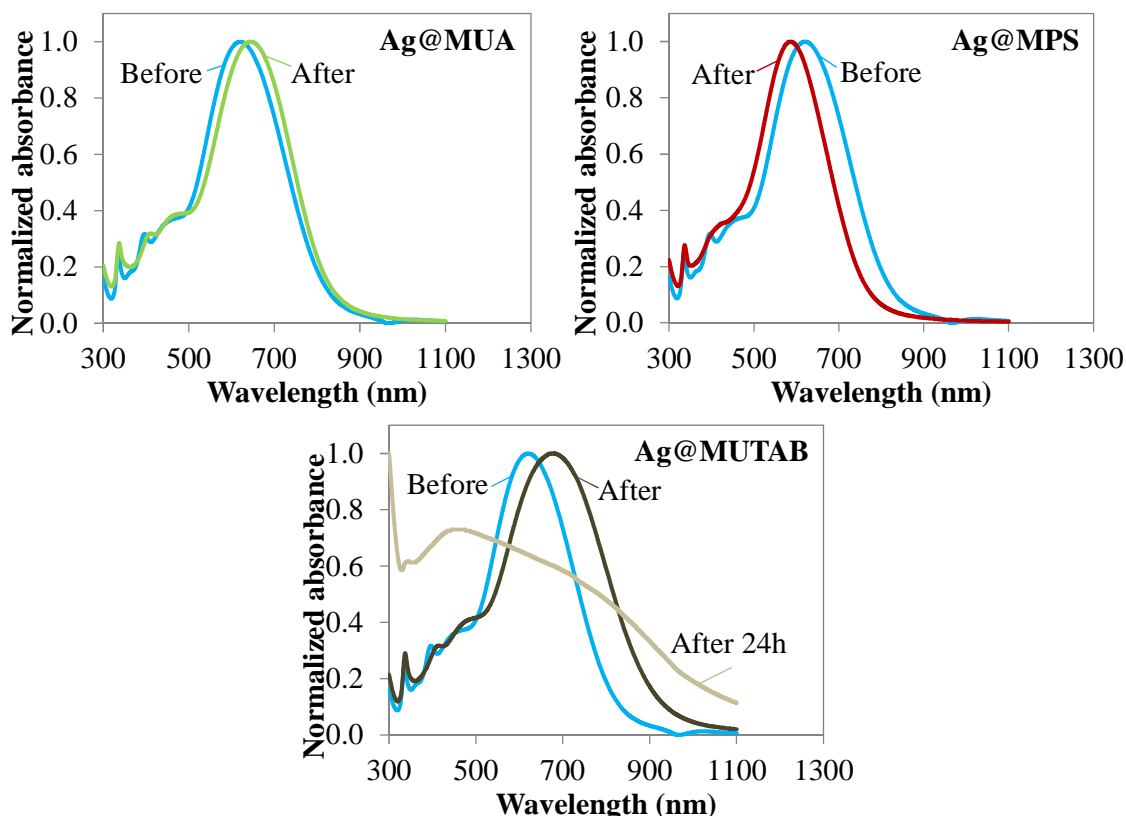


Figure I.64 – Absorption spectra before and after functionalization of Ag nanoprisms with MUA, MPS and MUTAB.

The MUA-protected Ag nanoplates remained unchanged, even after several months at ambient temperature and in the presence of air. They also remained stable in strong oxidative medium such as H_2O_2 that easily destroys unprotected Ag nanoparticles. Finally, by comparing the TEM images of silver nanoprisms before and after functionalization with MUA, we observe that nanoprisms were better dispersed after coating due to a higher distribution of charges on the surface of nanoprisms.

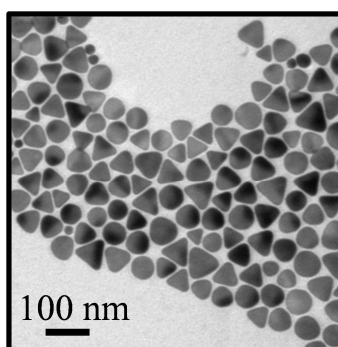


Figure I.65 - TEM images of silver nanoprisms functionalized with MUA.

The adsorption of MUA on the silver nanoparticles modified the physicochemical properties on the surface of silver particles. The measurements of zeta potential (ζ) of the colloidal suspensions, before and after the surface modification with MUA, allowed to determine the overall charge of the particles (Figure I.66).

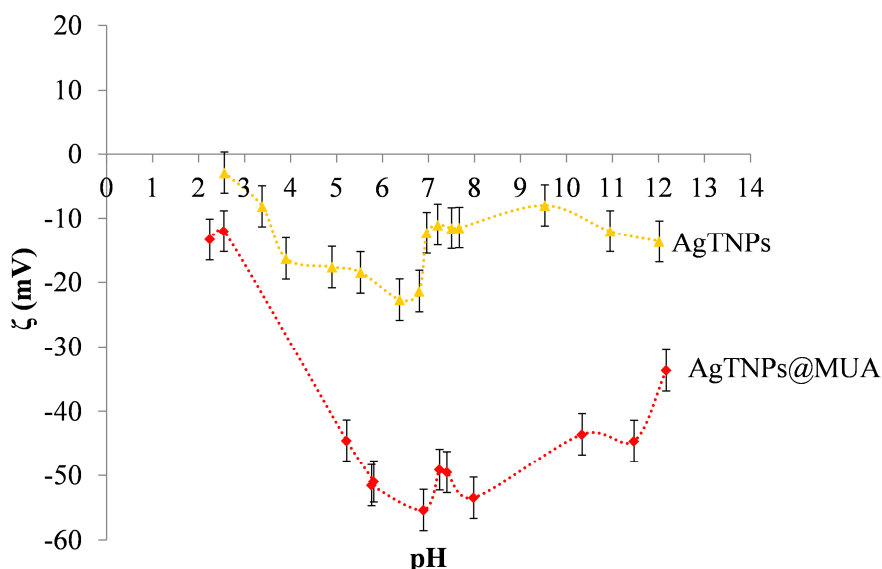


Figure I.66 – Isothermal variation of zeta potential of silver nanoparticles before (AgTNPs) and after (AgTNPs@MUA) the surface modification with MUA in function of pH.

Before and after the surface modification with MUA, the silver nanoprisms exhibited a negative charge with an isoelectric point (IEP) around pH ~ 1.5 - 2.5 due to the carboxylate groups of citrate or MUA adsorbed on their surface. However, after functionalization, the absolute zeta potential was almost twice higher than at the output of synthesis and only stabilized with citrate and PVP evidencing a higher density of negative charges with MUA and thus confirming the silver surface modification.

C.5 Conclusion on the silver nanoprisms synthesis

This study provides a number of important information and conclusions for the seed-mediated synthesis of silver nanoprisms produced in aqueous medium in the presence of citrate, succinate and PVP. Optimum conditions producing triangular shape particles were achieved. Tiny single crystalline Ag seeds (1.2 vol.%) can be best transformed into triangular shape particles by addition of HCit^{2-} or Suc^{2-} (with a molar ratio $[\text{HCit}^{2-} \text{ ou } \text{Suc}^{2-}]/[\text{AgNO}_3] = 18$) at pH = 5.6 for citrate and 7.0 for succinate. This knowledge may enhance the reproducibility and scalability of seed-mediated growth synthesis of Ag triangular colloidal particles. The 3D-structural analysis provided clear evidence that the single crystalline nanoprisms are enclosed by three identical $\{100\}$ facets and a single twin-plane. Apart from the relevance of these results for understanding the mechanisms involved in their formation, these findings are important to understand the anisotropic reactivity of Ag nanoprisms towards different types of molecules [Roh10, An08]. Therefore an additional study, described in annex 2, was performed on the development of new morphologies from the silver nanoprisms such as silver disks, gold nanocages and silver/gold nanobowes.

D. Summary

The works presented in this first chapter allowed us a large scale production of various metal nanoparticles:

- Monodisperse 26-nm silver spherical nanoparticles were produced in one step via a polyol approach. They are monodisperse in size and shape and they exhibit an overall negative charge due to the presence of PVP as stabilizing agent during the process.
- Gold spherical nanoparticles with different diameters from 10 to 50 nm were obtained through a seeded-growth approach. They were produced in high amount and high yield. They exhibit a negative overall charge thanks to the citrate ions used as stabilizing agent.
- Silver triangular nanoplates were produced through a seed-mediated growth. The mechanistic study of the formation of these anisotropic particles allowed us to significantly improve the reproducibility and the yield of the silver nanoprisms synthesis especially by controlling the reaction kinetics.

All of these nanoparticles will be used as satellite particles during the elaboration of the raspberry-like nanoclusters.

References

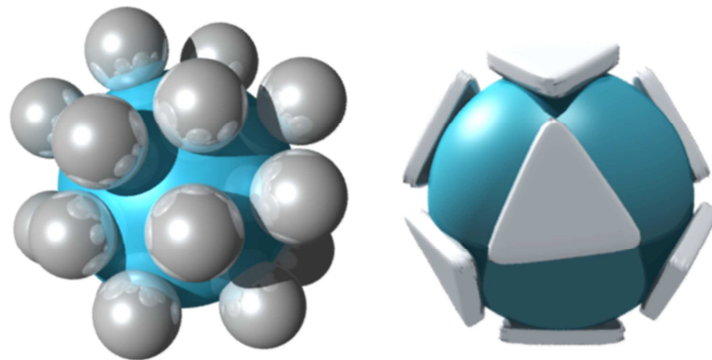
- [Amendola10] Amendola V., Bakr O., Stellacci F. *Plasmonics*, 2010. 5(1), p. 85
- [An08] An J., Tang B., Zheng X., Zhou J., Dong F., Xu S., Wang Y., Zhao B., Xu W. *J. Phys. Chem. C*, 2008. 112(39), p. 15176
- [Bastys06] Bastys V., Pastoriza-Santos I., Rodriguez-Gonzalez B., Vaisnoras R., Liz-Marzan L.M. *Adv. Funct. Mater.*, 2006. 16, p. 766
- [Berry68] Berry C.R., Skillman D.C. *J. Photogr. Sci.*, 1968. 16, p. 137
- [Blaber12] Blaber M.G., Henry A.I., Bingham J.M., Schatz G.C., Van Duyne R.P. *J. Phys. Chem. C*, 2012. 116, p. 393
- [Bogels97] Bogels G., Pot T.M., Meekes H., Bennema P., Bollen D. *Acta Crystallographica Section A*, 1997. 53(1), p. 84
- [Bogels98] Bogels G., Meekes H., Bennema P., Bollen D. *J. Cryst. Growth*, 1998. 191(3), p. 446
- [Brown98] Brown K.R., Natan M.J. *Langmuir*, 1998. 14, p. 726
- [Brust94] Brust M., Walker M., Bethell D., Schiffrin D.J., Whyman R. *J. Chem. Soc., Chem. Commun.*, 1994. p. 801–802
- [Charles11] Charles D.E., Gara M., Aherne D., Ledwith D.M., Kelly J.M., Blau W.J., Brennan-Fournet M.E. *Plasmonics*, 2011. 6, p. 351
- [Chen02] Chen S., Carroll D.L. *Nano Lett.*, 2002. 2(9), p. 1003
- [Cobley09] Cobley C.M., Rycenga M., Zhou F., Li Z.Y., Xia Y. *J. Phys. Chem. C*, 2009. 113, p. 16975
- [Djokic08] Djokic S. *Bioinorg. Chem. Appl.*, 2008
- [Dong09] Dong X., Ji X., Wu H., Zhao L., Li J., Yang W. *J. Phys. Chem. C*, 2009. 113, p. 6573
- [Dong10] Dong X., Ji X., Jing J., Li M., Li J., Yang W. *J. Phys. Chem. C*, 2010. 114(5), p. 2070
- [Elechiguerra06] Elechiguerra J.L., Reyes-Gasga J., Yacamán M.J. *J. Mater. Chem.*, 2006. 16, p. 3906
- [Faraday57] Faraday M. *Philosophical Transactions of the Royal Society of London*, 1857. 147, p. 145
- [Frens73] Frens G. *Nature (London), Phys. Sci.*, 1973. 241, p. 20
- [Germain03] Germain V., Li J., Ingert D., Wang Z.L., Pileni M.P. *J. Phys. Chem. B*, 2003. 107, p. 8717
- [Haes05] Haes A.J., Zhao J., Zou S., Own C.S., Marks L.D., Schatz G.C., Van Duyne R.P. *J. Phys. Chem. B*, 2005. 109(22), p. 11158
- [Haynes01] Haynes C.L., Van Duyne R.P. *J. Phys. Chem. B*, 2001. 105, p. 5599
- [Henglein93] Henglein A. *J. Phys. Chem.*, 1993. 97(21), p. 5457
- [Henglein99] Henglein A., Giersig M. *J. Phys. Chem. B*, 1999. 103, p. 9533
- [Hulteen95] Hulteen J.C., Van Duyne R.P. *J. Vac. Sci. Technol., A*, 1995. 13, p. 1553
- [Hulteen99] Hulteen J.C., Treichel D.A., Smith M.T., Duval M.L., Jensen T.R., Van Duyne R.P. *J. Phys. Chem. B*, 1999. 103, p. 3854
- [Jana01] Jana N.R., Gearheart L., Murphy C.J. *Chem. Mater.*, 2001. 13, p. 2313
- [Ji07] Ji X., Song X., Li J., Bai Y., Yang W., Peng X. *J. Am. Chem. Soc.*, 2007. 129(45), p. 13939
- [Jiang04] Jiang L.P., Xu S., Zhu J.M., Zhang J.R., Zhu J.J., Chen H.Y. *Inorg. Chem.*, 2004. 43, p. 5877
- [Jiang10] Jiang X.C., Chen C.Y., Chen W.M., Yu A.B. *Langmuir*, 2010. 26(6), p. 4400
- [Jin01] Jin R., Cao Y., Mirkin C.A., Kelly K.L., Schatz G.C., Zheng J.G. *Science*, 2001. 294, p. 1901

- [Jin03] Jin R., Cao Y.C., Hao E., Metraux G.S., Schatz G.C., Mirkin C.A. *Nature (London)*, 2003. 425, p. 487
- [Kelly03] Kelly K.L., Coronado E., Zhao L.L., Schatz G.C. *J. Phys. Chem. B*, 2003. 107, p. 668
- [Kilin08] Kilin D.S., Prezhdo O.V., Xia Y. *Chem. Phys. Lett.*, 2008. 458(1-3), p. 113
- [Kreibig95] Kreibig U., Vollmer M. *Optical properties of metal clusters*. Springer, 1995, 532 p.
- [Lofton05] Lofton C., Sigmund W. *Adv. Funct. Mater.*, 2005. 15, p. 1197
- [Machulek Junior03] Machulek Junior A., Moises de Oliveira H.P., Gehlen M.H. *Photochemical & Photobiological Sciences*, 2003. 2, p. 921
- [Mafune00] Mafune F., Kohno J.y., Takeda Y., Kondow T., Sawabe H. *J. Phys. Chem. B*, 2000. 104, p. 9111
- [Masse13] Masse P., Mornet S., Duguet E., Treguer-Delapierre M., Ravaine S., Iazzolino A., Salmon J., Leng J. *Langmuir*, 2013. 29(6), p. 1790
- [Mie08] Mie G. *Ann. Phys.*, 1908. 25, p. 377
- [Millstone09] Millstone J.E., Hurst S.J., Metraux G.S., Cutler J.I., Mirkin C.A. *Small*, 2009. 5(6), p. 646
- [Munro95] Munro C.H., Smith W.E., Garner M., Clarkson J., White P.C. *Langmuir*, 1995. 11(10), p. 3712
- [Murayama09] Murayama H., Hashimoto N., Tanaka H. *Chem. Phys. Lett.*, 2009. 482, p. 291
- [Novo08] Novo C., Funston A.M., Mulvaney P. *Nat. Nanotechnol.*, 2008. 3, p. 598
- [Ozin05] Ozin G.A., Arsenault A.C., Cademartiri L. *Nanochemistry: A Chemical Approach to Nanomaterials*, volume 2nd ed. Royal Society of Chemistry Publishing Cambridge, UK, 2005, 820p p. ISBN: 978-1-84755-895-4
- [Pastoriza-Santos02] Pastoriza-Santos I., Liz-Marzan L.M. *Nano Lett.*, 2002. 2, p. 903
- [Pastoriza-Santos09] Pastoriza-Santos I., Liz-Marzan L.M. *Adv. Funct. Mater.*, 2009. 19, p. 679
- [Pastoriza-Santos10] Pastoriza-Santos I., Alvarez-Puebla R.A., Liz-Marzan L.M. *Eur. J. Inorg. Chem.*, 2010. (27), p. 4288
- [Pyatenko07] Pyatenko A., Yamaguchi M., Suzuki M. *J. Phys. Chem. C*, 2007. 111, p. 7910
- [Rocha07] Rocha T.C.R., Zanchet D. *J. Phys. Chem. C*, 2007. 111(19), p. 6989
- [Rodriguez-Gonzalez06] Rodriguez-Gonzalez B., Pastoriza-Santos I., Liz-Marzan L.M. *J. Phys. Chem. B*, 2006. 110(24), p. 11796
- [Roh10] Roh J., Yi J., Kim Y. *Langmuir*, 2010. 26, p. 11621
- [Rycenga11] Rycenga M., Cobley C.M., Zeng J., Li W., Moran C.H., Zhang Q., Qin D., Xia Y. *Chem. Rev.*, 2011. 111(6), p. 3669
- [Sarkar11] Sarkar P., Bhui D., Bar H., Sahoo G., Samanta S., Pyne S., Misra A. *Plasmonics*, 2011. 6(1), p. 43
- [Sau04] Sau T.K., Murphy C.J. *J. Am. Chem. Soc.*, 2004. 126(28), p. 8648
- [Schatz06] Schatz G.C., Van Duyne R.P. *Electromagnetic Mechanism of Surface-Enhanced Spectroscopy*, John Wiley & Sons, Ltd. 2006
- [Silvert96] Silvert P.Y., Herrera-Urbina R., Duvauchelle N., Vijayakrishnan V., Elhsissen K.T. *J. Mater. Chem.*, 1996. 6, p. 573
- [Skrabalak07] Skrabalak S.E., Au L., Li X., Xia Y. *Nature Protocols*, 2007. 2, p. 2182
- [Sun03] Sun Y., Mayers B., Xia Y. *Nano Lett.*, 2003. 3, p. 675
- [Tapan K. Sau12] Tapan K. Sau A.L.R. *Complex-Shaped Metal Nanoparticles: Bottom-Up Syntheses and Applications*. 2012, 582 p.
- [Turkevich51] Turkevich J., Stevenson P.C., Hillier J. *Discuss. Faraday Soc.*, 1951. 11, p. 55

- [Washio06] Washio I., Xiong Y., Yin Y., Xia Y. *Adv. Mater.*, 2006. 18, p. 1745
- [Wiley05] Wiley B., Sun Y., Mayers B., Xia Y. *Chem. Eur. J.*, 2005. 11, p. 454
- [Wiley06] Wiley B.J., Im S.H., Li Z.Y., McLellan J., Siekkinen A., Xia Y. *J. Phys. Chem. B*, 2006. 110, p. 15666
- [Wiley07] Wiley B., Sun Y., Xia Y. *Acc. Chem. Res.*, 2007. 40, p. 1067
- [Willets07] Willets K.A., Van Duyne R.P. *Annu. Rev. Phys. Chem.*, 2007. 58, p. 267
- [Wu08] Wu X., Redmond P.L., Liu H., Chen Y., Steigerwald M., Brus L. *J. Am. Chem. Soc.*, 2008. 130, p. 9500
- [Xia09] Xia Y., Xiong Y., Lim B., Skrabalak S.E. *Angew. Chem., Int. Ed.*, 2009. 48, p. 60
- [Xiong07] Xiong Y., Washio I., Chen J., Sadilek M., Xia Y. *Angew. Chem., Int. Ed.*, 2007. 46, p. 4917
- [Xue08] Xue C., Metraux G.S., Millstone J.E., Mirkin C.A. *J. Am. Chem. Soc.*, 2008. 130(26), p. 8337
- [Yang07] Yang Y., Matsubara S., Xiong L., Hayakawa T., Nogami M. *J. Phys. Chem. C*, 2007. 111, p. 9095
- [Zeng10a] Zeng J., Roberts S., Xia Y. *Chem. Eur. J.*, 2010. 16, p. 12559
- [Zeng10b] Zeng J., Xia X., Rycenga M., Henneghan P., Li Q., Xia Y. *Angew. Chem. Int. Ed.*, 2010. 49, p. 1
- [Zeng10c] Zeng J., Zheng Y., Rycenga M., Tao J., Li Z.Y., Zhang Q., Zhu Y., Xia Y. *J. Am. Chem. Soc.*, 2010. 132(25), p. 8552
- [Zhang05] Zhang X., Hicks E.M., Zhao J., Schatz G.C., Van Duyne R.P. *Nano Lett.*, 2005. 5, p. 1503
- [Zhang09] Zhang Q., Cobley C., Au L., McKiernan M., Schwartz A., Wen L.P., Chen J., Xia Y. *ACS Appl. Mater. Interfaces*, 2009. 1, p. 2044
- [Zhang10a] Zhang Q., Hu Y., Guo S., Goebel J., Yin Y. *Nano Lett.*, 2010. 10, p. 5037
- [Zhang10b] Zhang Q., Xie J., Yu Y., Lee J.Y. *Nanoscale*, 2010. 2, p. 1962
- [Zhang11a] Zhang Q., Li N., Goebel J., Lu Z., Yin Y. *J. Am. Chem. Soc.*, 2011. 133, p. 18931
- [Zhang11b] Zhang W., Yao Y., Li K., Huang Y., Chen Y. *Environ. Pollut.*, 2011. 159(12), p. 3757
- [Ziegler11] Ziegler C., Eychmuller A. *J. Phys. Chem. C*, 2011. 115(11), p. 4502

Chapter II

Raspberry-like nanoclusters through the assembly of metal nanoparticles on silica beads



In this chapter, we fabricate and characterize 3D-isotropic plasmonic nanoclusters that exhibit a raspberry-like morphology. They consist of dielectric core spheres, which are smaller than the wavelength of the incident radiation, and are decorated by a large number of metallic satellite nanoparticles. A state of the art of the different existing approaches to achieve such nanoresonators is first exposed. Then, we describe the procedure that we have developed to assemble the metal nanoparticles onto the silica beads. After assembly, their optical properties were analyzed and compared to theoretical investigations.

A. State of the art

Using classical bottom-up fabrication, two main approaches have been developed to produce nanoclusters with raspberry-like morphology: (i) the direct nucleation/growth of the metal nanoparticles on the surface of a preformed dielectric spherical core and (ii) the controlled assembly of preformed satellite particles around a dielectric core. The first approach, largely described in literature, is not pertinent in our case because it may induce the formation of satellite nanoparticles with random interspacing and number of particles. There is also the problem of irregularity and non-uniformity of the metallic particles in terms of size, shape, crystallinity and overall morphology [Westcott98, Jankiewicz12]. The second route allows a better control not only of the dimensions and morphology of the satellite particles but also of their number and position around the central dielectric bead.

A.1 *Driving forces for clustering of preformed nanoparticles*

Several different driving forces have been proposed to induce the clustering of preformed colloids of different sizes, shapes and compositions to generate well-defined structures (*e.g.* covalent, electrostatic, hydrogen, Van der Waals, depletion, capillarity ...). For example, salt-induced random aggregation of Ag or Au colloidal particles in solution phase has allowed the generation of dimers or trimers in relatively high yield [Wang08]. The clusters could be then “frozen” by encapsulation within diblock copolymers (polystyrene₁₅₄-block-poly(acrylic acid)₆₀) in a DMF/water medium yielding very stable clusters (Figure II.1).

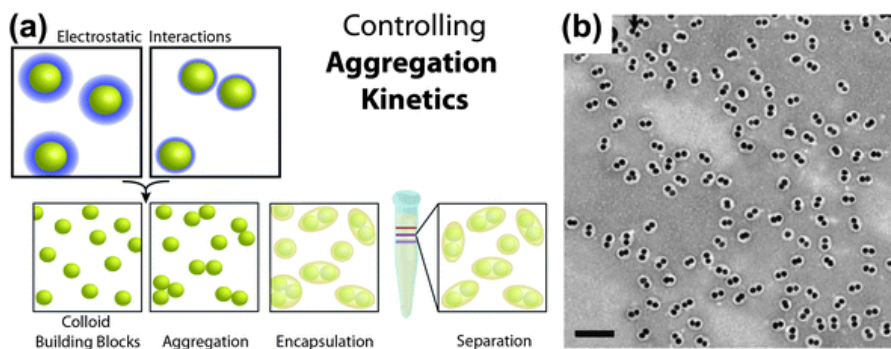


Figure II.1 - (a) Schematic illustration of clustering assisted by electrostatic interactions.

(b) Colloidal sample with high yield of gold dimers [Romo-Herrera11]

The clustering of particles can also be assisted by organic or biological linkers to direct their aggregation [Brousseau III99, Novak01]. For instance, Novak *et al.* used rigid phenyl-acetylene oligomers with two, three or four thioacetyl groups to bridge gold nanoparticles (Figure II.2).

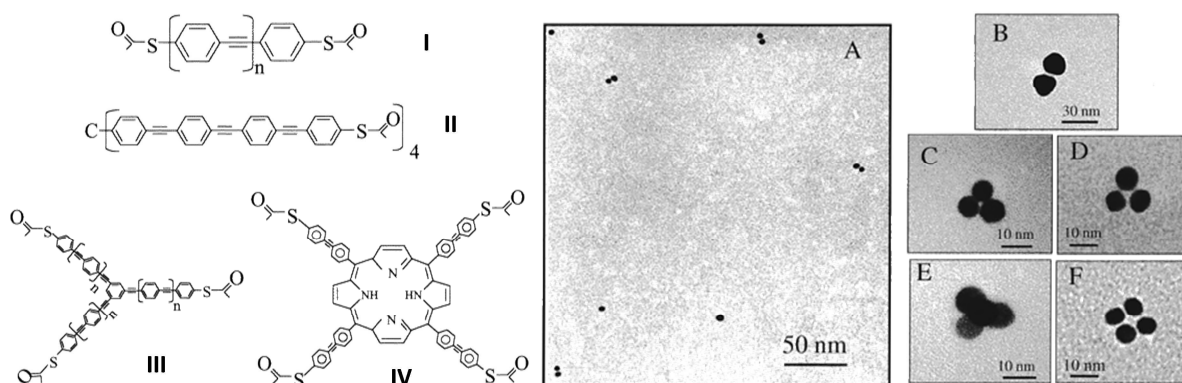


Figure II.2 - (Right) TEM images of gold nanoparticles clusters formed using linkers I (A, B) and III with $n=1$ (C),

III with $n=2$ (D), II (E) and IV (F) [Novak01].

Alivisatos *et al.* made use of DNA to synthesize dimers or trimers of gold nanoparticles [Alivisatos96] (Figure II.3). DNA has been shown to be an interesting functional molecule for posing as both the scaffold and the linker for construction of interesting assembly architectures because of their inherent molecular recognition properties. Later on, the process was extended to the assembly of nanoparticles of different sizes [Loweth99].

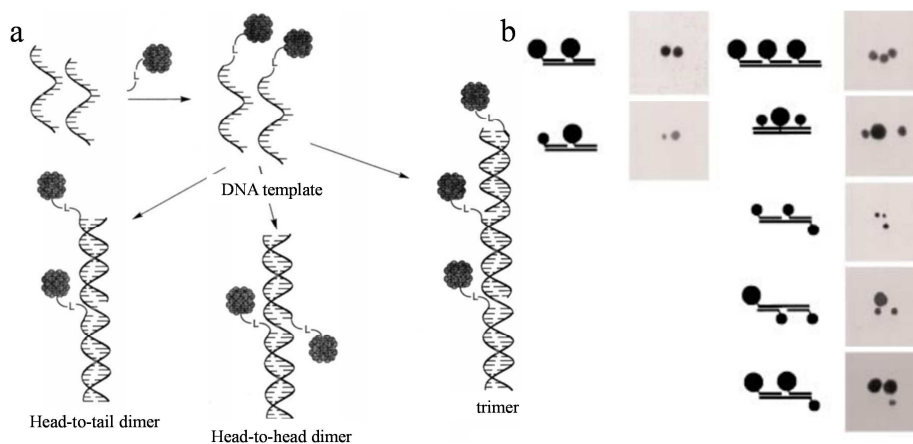


Figure II.3 - (a) Thiolated DNA strands to bind the nanoparticles together and form head-to-tail dimer or head-to-head dimers or trimers [Alivisatos96]. (b) Schematic representation and TEM images for specific nanocrystals molecules obtained with nanoparticles of different sizes [Loweth99].

Gang *et al.* showed that asymmetric functionalization of nanoparticles via sequential bio-recognition could promote the formation of (gold and silver) dimers in a high yield (80%) as well as the engineering of anisotropic Janus-like assemblies [Maye09].

Alternatively, 2D- or 3D-templates with defined dimensions have also been used to construct clusters of nanoparticles. Various clusters containing gold nanoparticles could be formed by confinement within cylindrical holes of a substrate patterned by lithographic techniques [Yan09] (Figure II.4). The results of the latter studies clearly show that well-defined nanoclusters can be produced. However, their amount per batch is limited and it is quasi-impossible to redisperse them without damage.

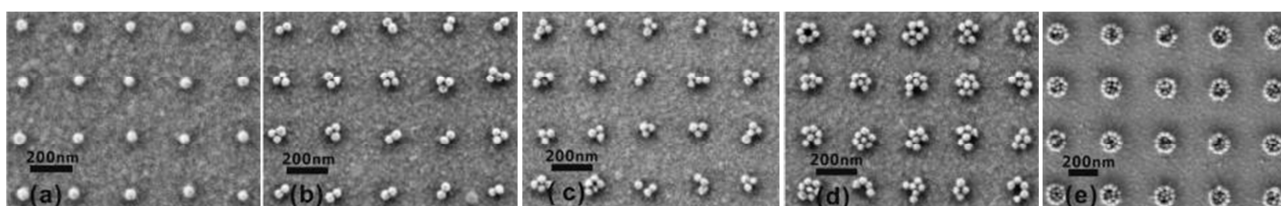


Figure II.4 - SEM images of 40-nm gold nanoparticles cluster arrays with varying diameters of holes $D = 50$ nm (a), 80 nm (b), 100 nm (c), 130 nm (d), 200 nm (e). [Yan09]

Micro-emulsion droplets have been also employed as 3D-template to confine the clustering of spherical particles [Yi04]. For that, Yan *et al.* prepared an emulsion toluene-in-water. Silica particles, previously dispersed in toluene, bounded to the interface of the toluene droplets. The subsequent controlled removal of the toluene from the droplets by evaporation generated compressive forces drawing the particles together and form small clusters (Figure II.5).

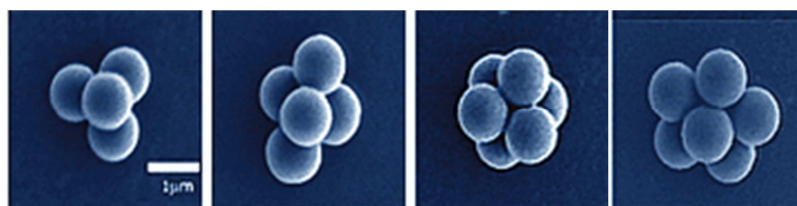


Figure II.5 – SEM images of silica microspheres clusters obtained by using emulsion droplets as 3D-template. [Yi04]

The technique allows to produce large amounts of clusters with a varying number of spherical particles from 2 to 15. [Yi04] Nevertheless, time-consuming centrifugation steps are necessary for recovering batches of identical clusters

A.2 Clustering strategies for dielectric and metallic component nanostructures

These different self-assembly approaches can provide convenient and versatile processes for the controlled preparation of multi-component nano-architectures. Through these approaches, different nanoscale materials can, in principle, be combined into one entity that exhibits novel physico-chemical properties or enhanced properties. In the case of raspberry-like nanoclusters, strategies makes use of electrostatic interactions, covalent bonding and bio-interactions have been so far

proposed to assemble the metallic particles on the surface of the dielectric core. In most of the cases, silica or polystyrene beads have been used as dielectric core because of their easy synthesis, modulation in size and surface functionalization.

For instance, a series of raspberry-like nanostructures have been developed by using organosilanes bearing amine (-NH₂), diphenylphosphine (-PPh₂) or thiol group (-SH) as linkers. The amine, phosphine and thiol groups are known to be suitable for the grafting to metal nanoparticles, in particular gold and silver, thanks to the available electron lone pair that coordinates to the metal surface. Halas *et al.* showed that the nature of the organosilane strongly influences the density of coverage [Westcott98]. High-density gold nanoparticles (2-3 nm) could be obtained by using NH₂- and SH-modified silica particles rather than PPh₂-modified ones (Figure II.6).

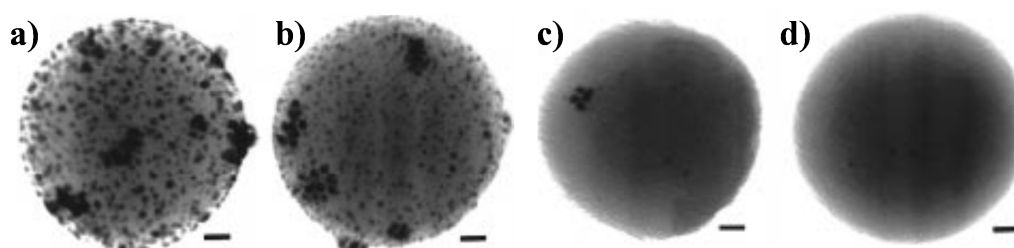


Figure II.6 - TEM images of silica nanoparticles ($d = 100$ nm) after deposition of Au nanoparticles ($d = 2-3$ nm). Silica particles were modified with (a) EDPS (-NH₂), (b) MPTMS (-SH), (c) DPPETES (-PPh₂) and (d) unfunctionalized. The assemblies were generated in a mixture of 40% water and 60% ethanol. All scale bars are 10 nm [Westcott98].

Amino- and thiol-modified silica particles are easily prepared via several approaches. Usually, the introduction of amine or thiol groups has to be carried out in one-step by simultaneous hydrolysis of the specific organosilane and the silica precursor. It is also possible to react the organosilane with preformed silica particles dispersed in an appropriate liquid [Ashayer08, Kim06, Nakamura08, Westcott98]. This approach via coordination bonding has also been widely used in order to form a uniform metallic layer onto dielectric core of various size [Pham02, Liang11].

Recently, Mühlig *et al.* extended this approach for 8-nm gold nanoparticles [Muhlig11]. 150-nm silica particles were modified with thiol groups by using (3-mercaptopropyl)trimethoxysilane (MPTMS) according to a protocol developed by Nakamura *et al.* [Nakamura08]. Then the gold nanoparticles were added to the modified silica particles in toluene medium. High density of gold nanoparticles could be supported on the surface of silica as shown in Figure II-7 (left). They also showed that the raspberry-like nanoclusters could be constructed by using *N*-[3-(trimethoxysilyl)propyl]-ethylenediamine (EDPS) as a linker (Figure II.7-right). At neutral pH, the amine groups are positively charged promoting electrostatic interactions with gold nanoparticles.

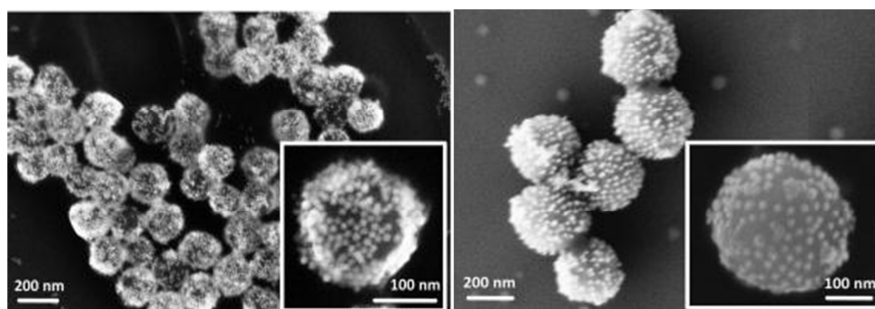


Figure II.7 - SEM images of core-shell clusters obtained via (left) thiol- and (right) amine-assembly. [Muhlig11]

Xue *et al.* also employed the same approach to coat silica particles with different sized gold nanoparticles (3.5 - 32 nm) [Xue07]. They showed that a surface modification of 60-nm silica spheres with the (3-aminopropyl)trimethoxysilane (APTMS, Figure II.8) allowed the assembly of small gold nanoparticles but not the assembly of larger ones (13 and 32 nm). In their study, they compared the density coverage obtained by such direct coating to the one obtained by using polyelectrolyte having an amine groups: the poly(ethyleneimine) (PEI, Figure II.8).

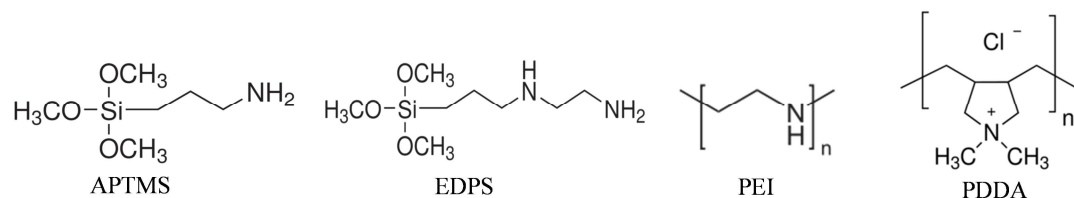


Figure II.8 - Molecular structures of APTMS, EDPS, PEI and PDDA.

PEI easily adsorb on the silica surface through electrostatic interactions between amine groups of PEI and -OH groups of silica surface. Unlike with APTMS-modified silica, they showed that polyelectrolytes facilitate the deposition of large metallic particles (32 nm) (Figure II.9). However, higher the diameter of the gold nanoparticles (tending to become close to the diameter of silica core particles), the lower the coverage density.

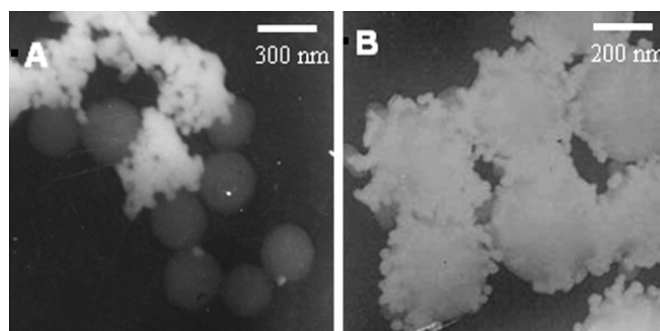


Figure II.9 - TEM images of the clusters obtained by assembly of 32-nm gold nanoparticles on (A) APTMS- and (B) PEI-modified 340-nm silica particles. [Xue07]

Similar comparative studied was performed by Ashayer *et al.* by using silica particles functionalized with APTMS or polydiallyldimethylammonium chloride (PDDA, Figure II.8) [Ashayer08]. The PDDA has the advantage to exhibit a quaternary ammonium group on each monomer unit, ensuring a permanent and strong positive charge and therefore a higher density of gold nanoparticles on the silica particles (Figure II.10).

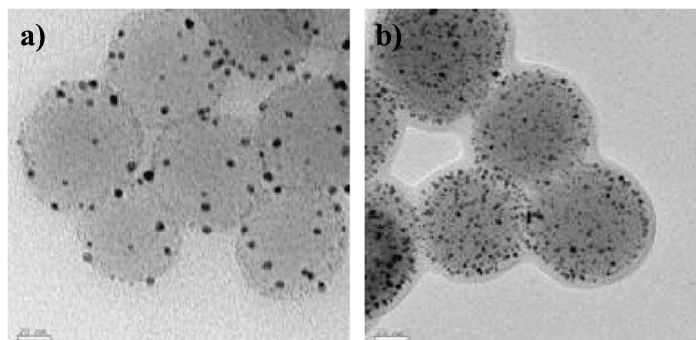


Figure II.10 - TEM images of gold nanoparticles adsorbed on (a) APTMS- and (b) PDDA-modified silica particles.

[Ashayer08]

By exploiting the electrostatic interaction between oppositely charged polyelectrolyte layers, various inorganic nanoparticles could be deposited onto colloidal beads [Liu07]. This process is called as “Layer-by-Layer (LbL) approach. It was first developed to assemble nanoparticles thin films on flat substrates (Figure II.11).

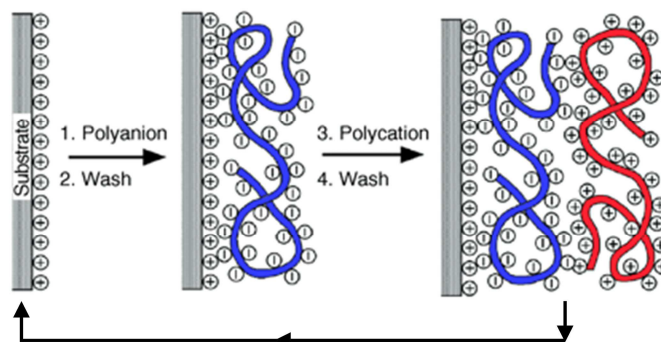


Figure II.11 - Schematic illustration of the first two adsorption steps, depicting film deposition starting with a positively charged substrate. The polyanion conformation and layer interpenetration are an idealization of the surface charge reversal with each adsorption step. [Decher97]

By modulating the number of polyelectrolyte layers, the shell thickness, the composition and the loaded amount of inorganic content of resulting composite particles could be modulated [Decher91, Decher97]. The Caruso’s group has extensively worked on this approach and demonstrated the fabrication of a wide spectrum of nanostructured materials. For instance, they described coating of polystyrene (PS) colloidal particles with silica coated gold or silver nanoparticles (Figure II.12) [Salgueirino-Maceira03, Spasova05, Karg07].

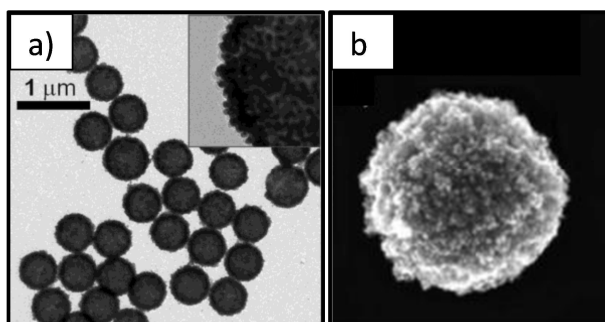


Figure II.12 – Two examples of polyelectrolytes (PDDA/PSS) modified PS spheres coated with (a) Au@SiO₂ nanoparticles/PDDA multilayers (760 nm total diameter) [Salgueirino-Maceira03] and (b) two layers of magnetic Fe₂O₃ nanoparticles then two layers of Au@SiO₂ nanoparticles (760 nm total diameter) [Spasova05].

Note that by exploiting this LbL approach, only large dielectric spherical colloidal particles with submicron diameters (500 nm – 5 μ m) have been so far used for the deposition of nanoparticles (5–30 nm).

Very recently, biological linker has been employed for the fabrication of raspberry-like nanoclusters of small overall diameter. Dionne *et al.* reported the first fabrication of nanoclusters based on 90-nm PS beads functionalized with streptavidin and 36-nm silver nanoparticles with biotin terminated poly-ethylene glycol (PEG) ligands [Sheikholeslami13]. Thanks to the highly specific chemical recognition of the protein streptavidin to the biotin antibody, silver nanoparticles strongly interacted with latexes to form raspberry-like nanoclusters.

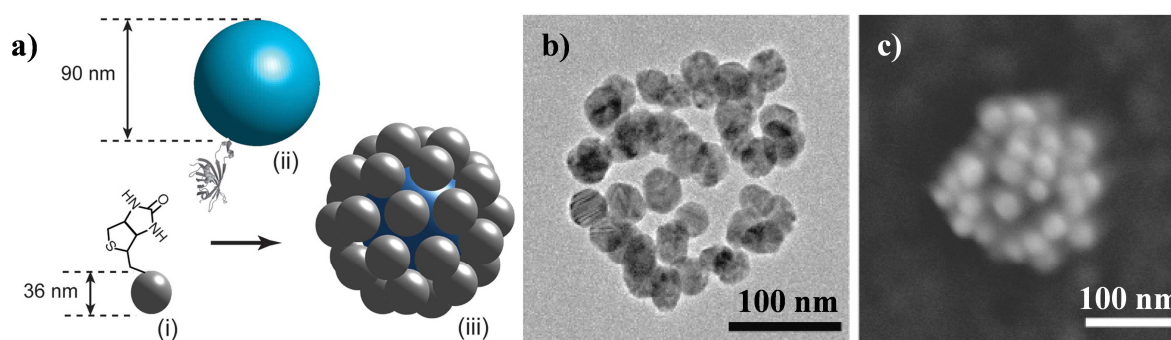


Figure II. 13 – (a) Schematic illustration of the protein-directed assembly. (i) Ag nanoparticles are functionalized with biotin terminated ligands and mixed in a high ionic strength buffer with (ii) streptavidin coated PS nanoparticles to form (iii) raspberry-like nanoclusters. (b) TEM and (c) SEM images of the obtained nanoclusters. [Sheikholeslami13]

A.3 Summary

From this short review, it emerges that the methods based on electrostatic interactions are the most versatile ones for generating raspberry-like nanoclusters. Not surprisingly, the density of charges on the silica surface strongly influences the surface density of attached metallic nanoparticles. In most of the reported cases, the satellite particles are spherical gold nanoparticles exhibiting a diameter much smaller (3 - 30 nm) than the one of the silica core (100 - 300 nm) *i.e.* a ratio at least above 10 between the core's and satellites' diameter. The resulting particles possess novel optical properties. However, their optical resonances are at a frequency where the cluster size is equivalent to $\lambda/2$ and no effective medium in assembled composites is expected to form by so big clusters. In our work, the challenge lies in the fabrication of nanoclusters for which the size ratio in between the dielectric core and the metallic nanoparticles is lower than 3 (100 nm for the silica and 30 nm for silver spherical nanoparticles) but also in the generation of nanoclusters made of anisotropic metallic particles with sharp tips. The raspberry-like nanoclusters have to be produced in large quantity for further use as building blocks for the construction of more complex nanostructures, such as 3D dense colloidal crystals.

B. Synthesis of the silica beads as dielectric core particles

B.1 Generalities

The amorphous silicon dioxide, commonly named “silica”, can be obtained from various processes, *e.g.* precipitated silica, silica gel, pyrogenic silica. Among the synthetic methods, the “sol-gel” way offers undoubtedly the best control on the silica morphology at the nanoscale [Brinker90]. Additionally, this way is a soft chemistry route, *i.e.* a chemistry occurring in conditions close to ambient temperature and pressure, reducing the cost and technical constraints.

By the sol-gel approach, the silica formation occurs from molecular precursors, generally alkoxysilanes $\text{Si}(\text{OR})_4$ where R is an alkyl group ($\text{C}_n\text{H}_{2n+1}$), through the combination of two reactions: the hydrolysis and the condensation. Hydrolysis of alkoxysilanes induces hydroxyl intermediates, such as silicic acid $\text{Si}(\text{OH})_4$ in the case of a full hydrolysis. Then, the polycondensation of the Si-OH groups leads to the formation of siloxane links Si-O-Si, then to oligomers and ramified macromolecules, up to a tridimensional network. The competition between both reactions conditions the growth phenomenon and the lattice densification. By modulating the experimental conditions, such as the nature of R, the catalyst or the medium (pH, solvent ...), it is possible to control this hydrolysis-condensation and the superficial charges of particles, and thus the final state of the obtained silica. In order to obtain colloidal suspension of dense and spherical particles, a basic catalysis is required for the hydrolysis of the alkoxysilanes. Note that the IEP of the pristine silica is close to pH 2, *i.e.* for a pH value higher than 2 the silica particles progressively become negatively charged and for a pH higher than 4 the suspension of the silica nanoparticles is colloidally stable.

The first synthesis of spherical silica particles with controlled size (from ~100 nm to ~2 μm) was proposed by Stöber, Fink and Bohn [Stoeber68]. The process, which is now known as “Stöber’s process”, consists in the hydrolysis-condensation of an alkoxysilane in a hydro-alcoholic medium containing ammonium hydroxide as catalyst. They preferred the use of tetraethylorthosilicate (TEOS) as silica precursor and ethanol as solvent. Many efforts of process optimization have been made to obtain spherical objects in a relatively wide range of sizes [Bogush91]. However, the size distribution did not appear so narrow and the repeatability of experiments was often poor [Wong03].

Recently, a promising method using amino acids as basic catalysts and a biphasic non-alcoholic medium was reported by Hartlen *et al.* [Hartlen08]. As in the Stöber’s process, the TEOS hydrolysis is the limiting step but major differences in the experimental conditions allows a better control of the particles formation. The introduction of an amino acid in low quantity in the aqueous solution (5

– 35 mM) permits relatively soft basic conditions (pH = 9-10) – unlike those of an ammonia medium (pH = 11-12) – and reduces the hydrolysis rate. Furthermore the medium being biphasic, the TEOS can only be hydrolyzed at the interface between the aqueous solution and the organic phase promoting a controlled nucleation rate. After the nucleation step, the pH limits the solubility of the silica and promotes the species condensation. Thus the TEOS is progressively hydrolyzed and diffuses overtime to a limited extent in the aqueous solution, is directly condensed on the silica particles which then grow according to a well-controlled mechanism of monomer addition. Thereafter, via a successive seed-mediated growth steps, they obtained particles of 15 – 200 nm of diameter and homogeneous in size.

Lastly, the synthesis of well-calibrated silica particles (PDI < 1.005) was optimized in our lab [Desert11, Desert12]. The process is in two steps: (i) the synthesis of silica seeds via the Hartlen's technique followed by (ii) a seeded-growth through a modified Stöber's process. Because in the present work, we also needed of silica particles in high amount, high yield and with a narrow size distribution, we chose this procedure which is described below (Protocol 9).

B.2 Synthesis of calibrated silica beads through the seeded-growth process

First, tiny silica nanoparticles were synthesized by hydrolysis-condensation of TEOS in a biphasic medium water/cyclohexane and in presence of an amino acid, the *L*-arginine, as basic catalyst and buffer according to the Hartlen's work (Protocol 9).

Protocol 9 - Synthesis of silica seeds

345 mL of an aqueous solution containing 7.5 mM of L-Arginine were introduced in a 500-mL rounded-beaker. 22.5 mL of cyclohexane were added on the top of the aqueous solution and the mixture was heated at 60°C. 37.5 mL of TEOS were introduced in the top organic phase. The stirring was tuned in order to create an interface of constant area between both phases and was maintained during 24 h. Then the cyclohexane was removed in a rotavapor at 50°C under partial vacuum. The concentration in silica seeds was determined by dry extract.

It was found that the higher the volume of TEOS, the higher the size of the silica seeds, while their number remained relatively constant. Thus, the concentration in particles (N_{SiO_2}) was calculated from the experimental values of the TEOS volume introduced (V_{TEOS}) and the diameter of silica seeds (D_{SiO_2}) by the following equation where M and ρ are the molar mass and the density of each entity:

$$D_{\text{SiO}_2} = \sqrt[3]{\frac{6 \cdot V_{\text{TEOS}} \cdot \rho_{\text{TEOS}} \cdot M_{\text{SiO}_2}}{\pi \cdot N_{\text{SiO}_2} \cdot \rho_{\text{SiO}_2} \cdot M_{\text{TEOS}}}} \quad (\text{II.1})$$

These seeds were then grown in a hydro-alcoholic medium containing ammonia and wherein the TEOS was slowly and continuously introduced (Protocol 10). The final size D_f of particles, with an initial diameter known D_i , introduced in concentration (N_{SiO_2}) kept constant during the growth, only depended on the amount of reagent (V_{TEOS}) according to the following relation:

$$V_{\text{TEOS}} = \frac{M_{\text{TEOS}} \cdot \rho_{\text{SiO}_2}}{M_{\text{SiO}_2} \cdot \rho_{\text{TEOS}}} (N_{\text{SiO}_2}) \cdot \frac{\pi}{6} \cdot (D_f^3 - D_i^3) \quad (\text{II.2})$$

To avoid a secondary nucleation of silica, TEOS has to be fully used for the growth of the seeds. So its concentration has to be controlled and adapted to the overall surface area of the seeds to grow, *i.e.* a surface of silica higher than $50 \text{ cm}^2/\text{cm}^3$ [Desert11].

Protocol 10 - Growth of silica seeds from 28 to 100 nm

50 mL of ethanol, 5 mL of ammonium hydroxide (1 M), and 5 mL of the aqueous suspension of the silica seeds were mixed in a 150-mL round-beaker. 8.68 mL of TEOS diluted in 20 mL of absolute ethanol were added at a rate of 1 mL/h thanks to an automatic syringe pump. The final concentration of silica beads was determined by the dry extract method.

As previously mentioned, the size control of nanoparticles and their aggregation state at the end of each synthesis step are essential to elaborate homogeneous nanoclusters in the further step. The as-prepared silica seeds were characterized by TEM (Figure II.14). They appeared relatively spherical and their diameter was estimated to $(28 \pm 4) \text{ nm}$.

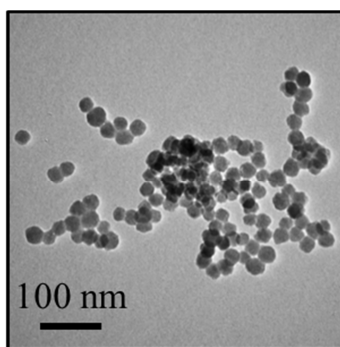


Figure II.14 - TEM image of the as-obtained silica seeds

Two batches of different-sized silica nanoparticles (one with an expected diameter of 80 and another one with an expected diameter of 100 nm) were synthesized from the preformed silica seeds and observed by TEM (Figure II.15). In both cases, the particles were spherical. The first batch of silica particles exhibited a very narrow size distribution with a mean diameter estimated to $(89 \pm 2) \text{ nm}$ and will be noted “SiO₂-89”. The second batch was made of silica beads with a mean diameter of $(106 \pm 3) \text{ nm}$ and will be noted “SiO₂-106”. For both batches, the PDI of the silica beads were calculated to 1.002 revealing the highly monodispersity of the particles.

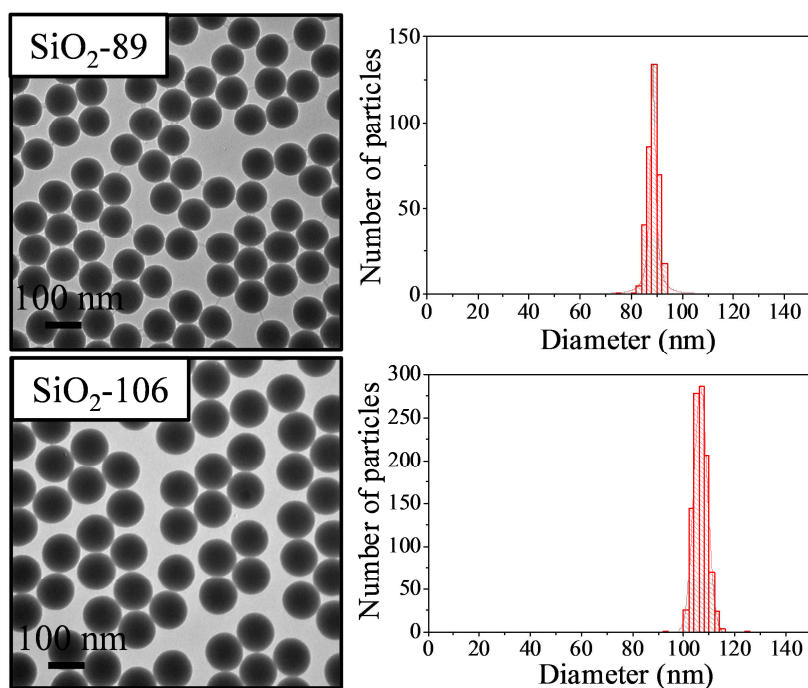


Figure II.15 - TEM images and corresponding size-distribution of two batches of silica beads (SiO₂-89 and SiO₂-106) obtained via the seed-mediated route. The size distributions of SiO₂-89 and SiO₂-106 were calculated from 351 and 1040 particles, respectively.

This synthesis approach of silica nanoparticles allowed to get highly monodisperse silica core particles. The Table II.1 summarizes the characteristics of the different nanoparticles synthesized in this work and available for the next assembly step.

Table II.1 - Summary of the physicochemical characteristics of the different nanoparticle batches.

	scheme	Diameter (nm)	PDI	λ_{\max} (nm)	[Nps] output synthesis	stabilizing agent	overall charge (pH ~ 7)
SiO ₂ -86		89 ± 2	1.002		2.4 × 10 ¹⁶		negative
SiO ₂ -106		106 ± 3	1.002		3.1 × 10 ¹⁶		negative
AuNP10		10 ± 1	1.02	520	1.9 × 10 ¹⁶	citrate	negative
AuNP20		20 ± 3	1.04	518	1.8 × 10 ¹⁵	citrate + ascorbate	negative
AuNP30		33 ± 6	1.07	522	1.2 × 10 ¹⁴	citrate + ascorbate	negative
AuNP40		40 ± 9	1.09	525	1.2 × 10 ¹⁴	citrate + ascorbate	negative
AuNP50		50 ± 8	1.07	530	3.1 × 10 ¹³	citrate + ascorbate	negative
AgNP		26 ± 5	1.12	404	5.0 × 10 ¹⁶	PVP	negative
AgNPprisms		l = 45 ± 7; t = 8 ± 1		~ 600	1.3 × 10 ¹⁴	MUA	negative

C. Assembly of metal nanoparticles on silica beads via the electrostatic approach

From the literature overview, the electrostatic approach appears to be the most efficient one in order to assemble metal nanoparticles onto a silica core particle and get high levels of surface coverage. To ensure electrostatic interaction between silica and metallic nanoparticles described in the chapter I, the both components have to exhibit opposite surface charges. However, all the particles at the final step of their synthesis (silica and metal) exhibit a negative overall charge (Table II.1). Since the chemistry of silica is well-known and its surface easy to functionalize, we decided to modify the surface charge of the silica beads for further fabrication of the raspberry-like nanoclusters (Figure II.16).

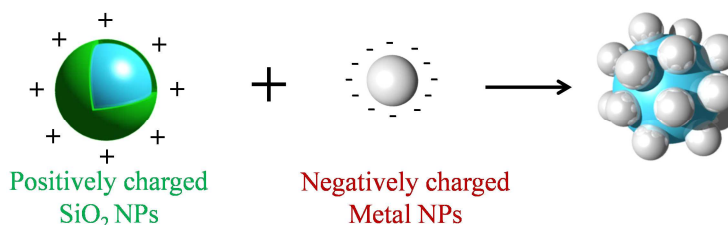


Figure II.16 – Assembly approach via electrostatic interactions between positively-charged silica cores and negatively-charged metal satellites.

In the following section, we present the two approaches adopted to generate positive charges on the silica cores surface: (i) the grafting of an aminosilane and (ii) the use of the LbL technique to deposit several layers of polyelectrolytes with the outer layer being a polycation. The resulting nanoclusters will be called “first-” and “second-generation” of raspberry-like nanoclusters, respectively.

C.1 “First generation” of raspberry-like nanoclusters

C.1.1 Functionalization of silica beads with an aminosilane

The most common approach to modify the surface of silica particles in aqueous medium consists in the use of an organosilane R_nSiX_{4-n} where X is a hydrolysable group ($X = Cl, OR', \dots$). The co-condensation of several silanes leads to the formation of a polysiloxane film made of a few layers of silane precursor and functionalized by non-hydrolysable R groups which may be able to form covalent bonds or interact with molecular species (Figure II.17).

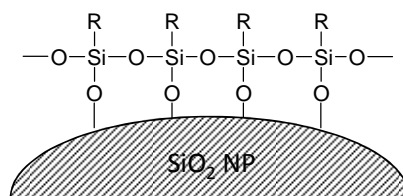


Figure II.17 – Schematic showing the surface arrangement of trialkoxysilane molecules (self)-condensed on the surface of a silica nanoparticle.

A wide variety of organosilanes exists, conferring to the modified silica particles various surface physicochemical properties. An aminosilane appears a pertinent choice because it ensures a positive overall charge of the silica particles on a large range of pH and the amine groups strongly coordinate to the metal nanoparticles surface. The aminosilane chosen in our case is the EDPS (Figure II.8) which exhibits simultaneously a primary and a secondary amine group.

The grafting protocol of EDPS on the surface of the silica nanoparticles was derived from the works of Dr. Stéphane Mornet [Mornet02]. It was performed directly after the growth of the silica beads in Stöber's medium (Protocol 11). The volume of EDPS (V_{EDPS}) necessary to the full coverage of the silica particles was calculated as follows:

$$V_{EDPS} = d_{EDPS} * S_T * \frac{M(EDPS)}{\rho(EDPS)} * \text{purity} * \text{excess} \quad (\text{II.3})$$

where d_{EDPS} is the grafting density of EDPS, S_T is the total surface area of silica (m^2), $M(EDPS)$ and $\rho(EDPS)$ are its molar mass ($222.36 \text{ g.mol}^{-1}$) and density (1.028 g.cm^{-3}), respectively. Note that a value of $4.9 \mu\text{mol.m}^{-2}$ was chosen for d_{EDPS} . This value was only an estimation based on experimental results [Mornet02, Reinhardt13]. An excess of 20 regarding to the “optimal” grafting density of EDPS was applied to ensure a maximal grafting of the molecules on the surface of the silica beads.

At the end of the surface modification with EDPS, a moderate heating under vacuum and in glycerol was performed in order to improve the density and robustness of the grafting on the silica surface. In few words, it is supposed to further the dehydration of the particles and therefore help in changing the spontaneous electrostatic interaction between the ammonium groups and the silanolates into covalent siloxane bonds (flip mechanism) [Mornet02]. The glycerol, having a boiling point of 290°C , was used as wetting agent during the deshydration and allowed to prevent the irreversible flocculation of the nanoparticles.

Protocol 11 – Surface modification of silica beads with EDPS in ethanolic medium

Under vigorous stirring, a volume V_{EDPS} of EDPS aqueous solution was quickly added to 20 mL of the suspension of the as-prepared silica nanoparticles. The reaction mixture was stirred overnight. Then the mixture was transferred in a 100-mL round beaker and 10 mL of glycerol were added under stirring. Once the dispersion homogenized, it was placed on a rotavapor and heated at 40°C for the extraction of the ethanol then at 70°C

for the water, under reduced pressure during 1 h. A thermal treatment was then performed during 3 h at 100°C under partial vacuum. After cooling, 70 mL of ethanol was added under slow stirring. The mixture was placed in two 45-mL tubes and centrifuged at 15000 g during 20 min at 20°C. The supernatant, containing glycerol, ethanol and oligomers of silanes was removed and the pellet, containing the modified particles, was redispersed in ethanol by sonication. This cycle was repeated 6 times. After the removal of the last supernatant, 100 mL of water was added. To promote the redispersion of the modified silica beads and maintain the adhesion of the polysiloxane film on the surface of the beads, an acidification was performed by gradual step of one pH unity, by adding a few drops of 1M acetic acid, under vigorous stirring. In acidic conditions (~ pH 6), the silica beads started to disperse. The suspension was adjusted to 5 and kept under stirring during 24 h. The pH was again measured and readjusted to 5. The mixture was finally placed on a rotavapor at 40°C, under reduced pressure, to eliminate the residual ethanol. The suspension was redispersed in 100 mL of water and the concentration of the modified silica beads was determined by dry extract.

After functionalization with EDPS, no change in size and shape of the silica particles was observed by TEM (not shown here). To confirm the surface modification of silica particles with the aminosilane, the diffuse reflectance infrared Fourier transform (DRIFT) spectra, before (SiO₂-89) and after functionalization (SiO₂-89@EDPS and SiO₂-50@EDPS), were compared (Figure II.18). The aminosilane was only grafted on the surface of silica nanoparticles, therefore the quantity of aminosilane detected was very small compared to the silica. To increase the ratio aminosilane/silica, we recorded the DRIFT spectrum of modified-silica nanoparticles with a smaller diameter (50 nm). Thus in this case, the bands characteristic of amine functions appeared more intensely.

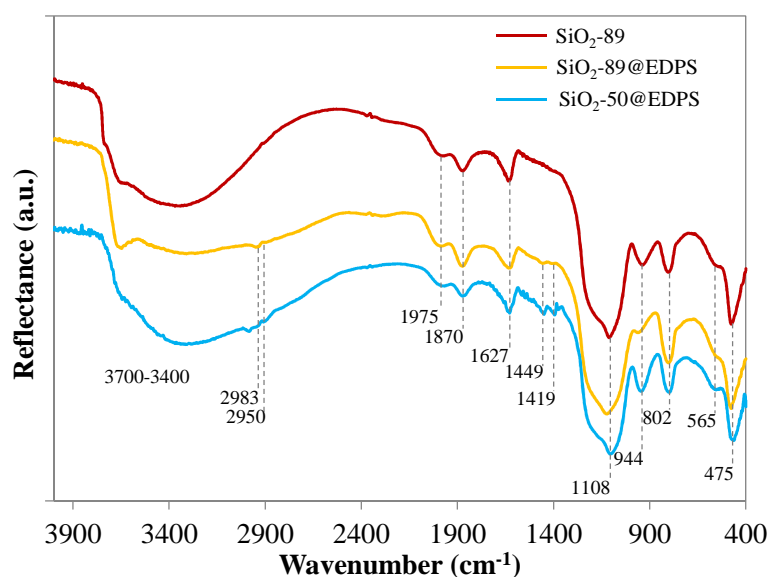


Figure II.18 – DRIFT spectra of silica nanoparticles before and after modification with EDPS.

All the bands were attributed to different vibrations and are summarized in the Table II.2. Compared to the spectrum of the unmodified silica, additional bands at 2983 and 2950 cm⁻¹ and in

the 1400-1500 cm^{-1} range were observed in the spectra of EDPS-modified silica nanoparticles. These observations confirmed the successful grafting of EDPS molecules on the silica surface.

Table II.2 - Summary table of the observed vibration bands on silica NPs (SiO_2 -89) and EDPS-modified silica NPs (SiO_2 -89@EDPS and SiO_2 -50@EDPS). Abbreviations: s, strong; m, medium; w, weak intensity; ν_{sym} , symmetric stretching; ν_{asym} , asymmetric stretching; δ , bending; ρ , rocking vibrations.

ν (cm^{-1})	Intensity	Attribution	SiO_2 -89	SiO_2 -89@EDPS	SiO_2 -50@EDPS
3700-3400	s	$\nu(\text{OH})$	x	x	x
2983	m	$\nu_{\text{asym}}(\text{CH}_x)$		x	x
2950	m	$\nu(\text{NCH}_x)$		x	x
1975	shoulder	typical silica overtone	x	x	x
1870	w	typical silica overtone	x	x	x
1627	w	$\delta(\text{H}_2\text{O})$ enclosed water	x	x	x
1449	w	$\delta(\text{NCH})$		x	x
1419	w	$\delta(\text{CN}^+)$		x	x
1108	s	$\nu_{\text{asym}}(\text{Si-O-Si})$	x	x	x
944	s	$\nu_{\text{sym}}(\text{Si-O-Si})$	x	x	x
802	s	$\delta(\text{Si-O-Si})$	x	x	x
565	m	cyclic (Si-O-Si)	x	x	x
475	s	$\rho(\text{Si-O-Si})$	x	x	x

The grafting of EDPS on the silica nanoparticles modified the physicochemical properties and especially affected the overall charge of the particles. The measurement of the ζ -potential of the colloidal suspension before and after the grafting of EDPS allowed to highlight this phenomenon (Figure II.19).

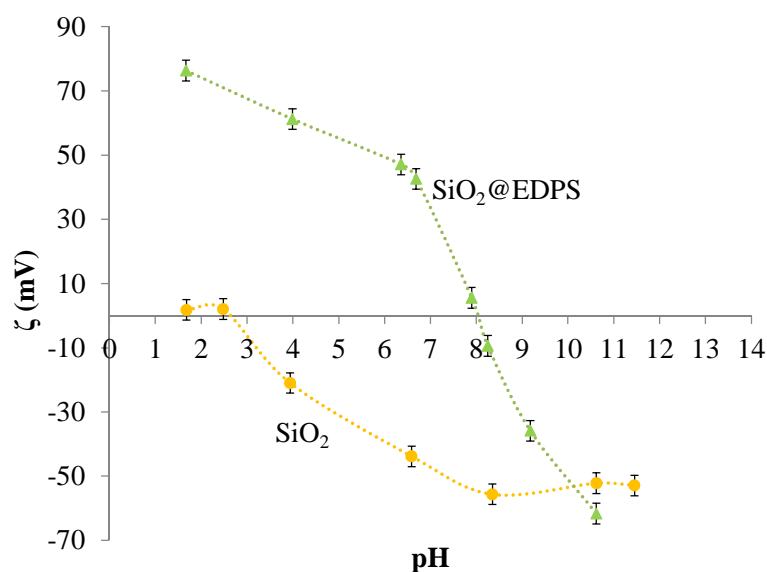


Figure II.19 - Isothermal variation of ζ -potential of 106-nm silica nanoparticles before (SiO_2) and after (SiO_2 @EDPS) surface modification with EDPS as function of pH

The IEP of the pristine silica particles was around pH \sim 2.5 induced by the deprotonation of surface silanol groups. After functionalization of the silica beads with EDPS, the IEP was determined around pH \sim 8 confirming the presence of amine groups on the silica surface. However, it was expected that EDPS-modified silica particles were positively charged on a more large range of pH with an IEP around 9-10 corresponding to the pKa value of the aminosilane [Metwalli06]. The lower value obtained can be attributed to an incomplete coverage of the silica particles with EDPS or to an interaction of the amine groups with surface silanol groups via hydrogen bonding.

C.1.2 Assembly of silver spherical nanoparticles on EDPS-modified silica cores

The first trials of assembly were performed with the 26-nm silver spherical nanoparticles which were naturally negatively charged due to the protective layer of PVP on their surface (Protocol 12).

Protocol 12 – Assembly of Ag spherical nanoparticles on the EDPS-modified silica beads

Typically, in an Eppendorf tube, 0.2 mL of a diluted suspension of silica beads (5.16×10^{14} part/L) were dropwise introduced in 1 mL of the silver spherical nanoparticles suspension (5×10^{16} part/L). The mixture was stirred overnight at room temperature and protected from light exposure.

To obtain dense, close-packed nanoparticles coatings on the surface of the silica, we observed that the core particles had to be in large default compared to the satellite particles. Moreover, the higher the particle concentration in the reactive medium, the faster the assembly process since the higher the probability of contact between particles. The limiting colloidal suspension in terms of concentration in particles was ever the one of metal nanoparticles which were produced in lower quantity than the silica beads. Thus to optimize the deposition procedure, a range of assemblies was prepared by varying the ratio of concentration $[\text{AgNPs}]/[\text{SiO}_2 \text{ cores}]$. The Figure II.20 shows images of these preliminary tests performed from a ratio of 1 to 160. For a ratio equal to 1, there was as many silver particles as silica particles and for a ratio of 160, there was 160 times more silver particles than silica beads.

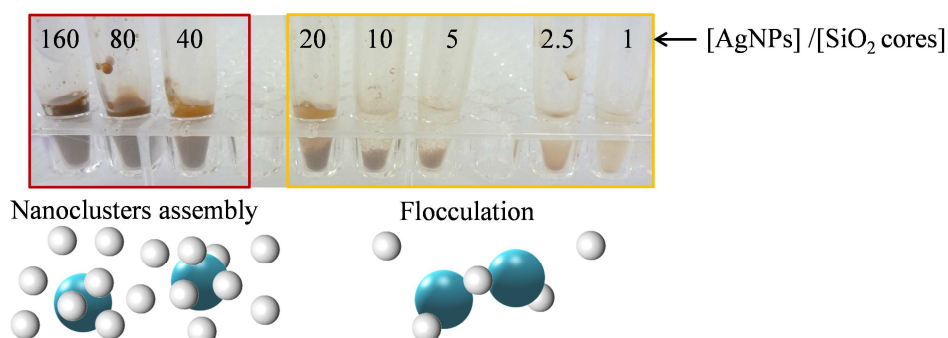


Figure II.20 – (Top) Photograph of the range of assemblies performed by varying the ratio $[\text{AgNPs}]/[\text{SiO}_2 \text{ cores}]$ from 1 to 160 and (Bottom) schematic illustration of the two different phenomena observed.

Regarding the size ratio between the satellite and core particles, the maximal number ($N_{p_{\max}}$) of satellite particles of radius “r” which can be attached to the surface of a core particle of radius “R” can be estimated as follows:

- When the size ratio $R/r \geq 10$, the approximate equation (II.4) can be used which disregarding the curvature of the core particle and considering that satellites form a 2-dimensional hexagonal arrangement on a planar substrate (Figure II.21-a).

$$N_{p_{\max}} = \frac{2\pi}{\sqrt{3}} \left(\frac{R}{r} + 1 \right)^2 \quad (\text{II.4})$$

- When the size of the satellites increases and becomes close to the one of the core ($R/r < 10$), this formula cannot be applied (Figure II.21-b). This time, the maximal number of satellites attached to a core particle can be estimated from the angular distance (α) between two satellites attached to the surface of the core through the following equation:

$$\alpha = 180 - 2 * \left\{ \cos^{-1} \left(\frac{r}{R+r} \right) \right\} \quad (\text{II.5})$$

Basing on the works of N. J. A. Sloane, R. H. Hardlin and W.D. Smith, it is possible to determine the number of points on the surface of a central sphere from the angular distance between these points [Conway98]. A table of spherical codes corresponding to the optimal 3-dimensional arrangement of points on a sphere (with $N_{p_{\max}} = 4$ to 130) was published electronically at NeilSloane.com/packings/.

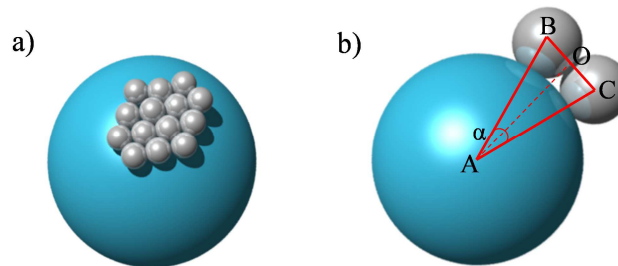


Figure II.21 – Schematic illustration of the packing of satellite particles on the core one regarding the size ratio r/R .

By applying the first approximate formula, we estimate that it is possible to attach 74 silver nanoparticles of 26-nm diameter on a silica bead of 89-nm diameter. But since the size ratio r/R is lower than 10, this tend to overestimate the value of $N_{p_{\max}}$. The second formula gives a distance angular of 26.1° in between two satellites, corresponding to a 3D-arrangement of 64 silver particles on one silica bead. However, it is important to note that these two calculation ways do not take account of the various interactions which could exist between the different particles and particularly the repulsive electrostatic forces between the silver nanoparticles. So these values of $N_{p_{\max}}$ are only upper boundaries and allow us to define the excess of satellite particles necessary for their assembly on the silica beads.

Experimentally, we observed that when the ratio $[\text{AgNPs}]/[\text{SiO}_2\text{cores}]$ (in particles/L) was lower than 43, silver particles interacted with several silica beads and formed agglomerates of particles, evidenced by the flocculation of particles (Figure II.20). However when the ratio was higher than or equal to 43, stable dispersions were obtained. Moreover, as expected the greater the excess of satellite particles, the faster the reaction and the higher the probability to form raspberry-like nanoclusters. The assemblies were characterized by TEM (Figure II.22). An effective interaction was observed between silver and silica particles since each silica particle was surrounded by a large number of silver particles. A control experiment was performed by assembling the silver nanoparticles on pristine silica beads: no interaction between particles was observed, confirming indirectly the successfully grafting of EDPS on the surface of silica (TEM image not shown here).

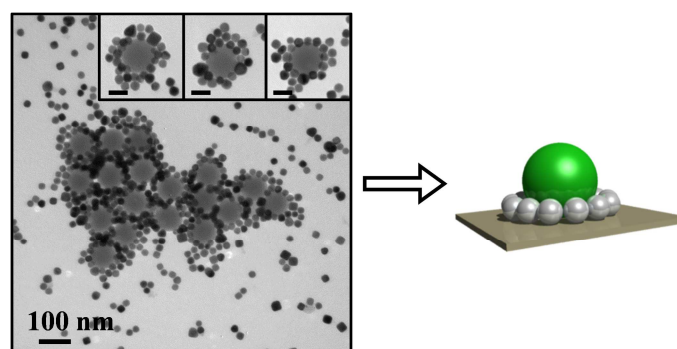


Figure II.22 – (Left) TEM image of nanoclusters obtained with an excess of 160 of the 26-nm silver particles with regard to 89-nm silica cores. Inset scale bars: 50 nm. (Right) Schematic illustration of Ag satellite particles fallen-in on the membrane.

TEM images revealed the presence of the nanoclusters, but they agglomerated one to each other. Moreover, the satellite particles were systematically observed in a “daisy-like arrangement” around the silica core: they obviously found their final position in contact simultaneously with the silica and the carbon film of the TEM grid, resulting from a falling-in mechanism during the drying step (Figure II.22). It evidences the attractive forces between the silica core and the silver satellites were not strong enough for withstanding the capillary forces inherent of the drying process and therefore maintaining the satellites in a raspberry-like morphology.

Nevertheless, the electrostatic approach for driving the assembly process was not questioned. Many efforts to optimize the assembly process and get a higher coverage were performed such as *e.g.* by changing the ratio $[\text{AgNPs}]/[\text{SiO}_2\text{cores}]$, the pH of the reaction medium, the rate of stirring and the rate of addition of core particles into the excess of the satellite particles. For instance, in order to get a homogeneous diffusion rate between SiO_2 and Ag particles and thus to expect a higher level of coverage, the assembly was performed in a microfluidic device [Hassan13]. The microfluidic procedure is illustrated in the Figure II.23. The devices were fabricated at the Laboratory of Future (LOF, Bordeaux). The system was made of a PDMS micro-reactor with two inlets and one outlet. The aqueous colloidal suspension containing the silver particles was injected

in one of the two inlets and the aqueous suspension of modified silica particles was injected in the second inlet with the same flow rate of $Q = 400 \mu\text{L/h}$. The mixture evolved in the channel and enters in an oily medium to form aqueous drops. Then the drops evolved in the serpentine channels to promote the intimate mixing of both aqueous colloidal suspensions in the drop. At the outlet of the micro-reactor, a “water-in-oil” emulsion was obtained. Finally, the oil phase was separated from the aqueous suspension containing the nanoclusters by a slow centrifugation. The strong advantage of this technique is the high reproducibility and a better homogeneity of the diffusion reaction of the metal nanoparticles towards the silica core. The reaction is exactly the same whatever the drop. At the end of the process, expected nanoclusters with a more monodisperse raspberry-like architecture should be collected.

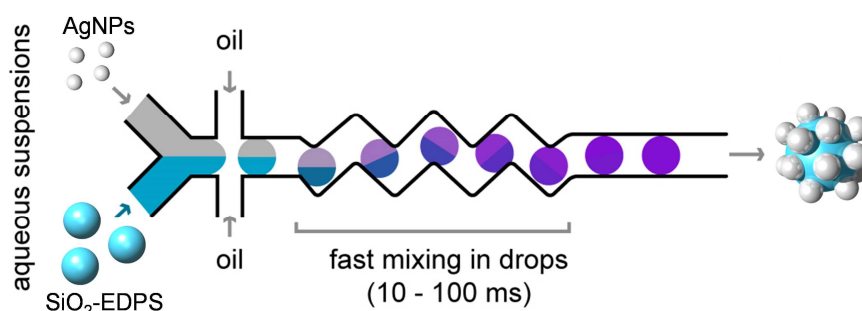


Figure II.23- Microfluidic synthetic procedure for the assembly of silver nanoparticles onto silica beads.

Figure II.24 shows pictures of the microfluidic assisted assembly of the Ag nanoparticles (yellow suspension) onto the EDPS-modified silica beads (white suspension) at different steps in the microfluidic chip. At the beginning the two colloidal suspensions were well-separated. Then as the drop evolved in the serpentine channel, the mixture between the two species of particles occurred and yielded to a mixture with a homogeneous color.

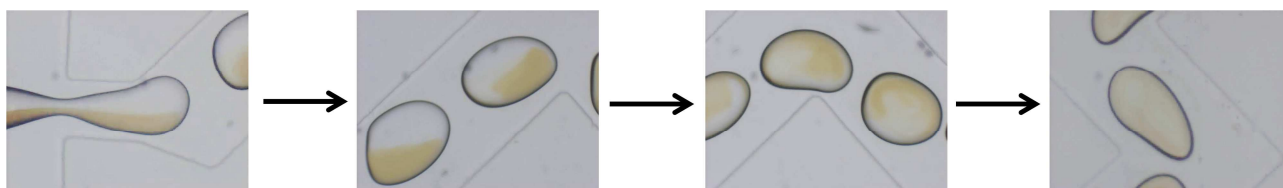


Figure II.24 - Photographs of the microfluidic assisted assembly of Ag nanoparticles (yellow suspension) onto the EDPS-modified silica beads (white suspension) at different steps in the microfluidic chip.

Compared to the direct assembly, the microfluidic approach did not seem to have a real influence on the final morphology of the nanoclusters (Figure II.25). Most of the clusters assembled together in agglomerates and the satellite particles had fallen-in on the TEM grid (Figure II.22).

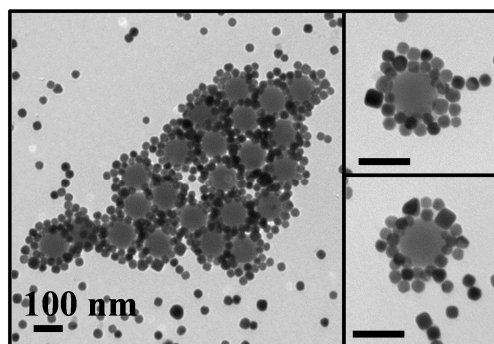


Figure II.25 - TEM images the nanoclusters obtained by microfluidic assisted assembly. Insert scale bars: 100 nm.

We thus had to find out a way to reinforce the colloidal stability of the raspberries. This was performed by coating the nanoclusters with silica after removal of the excess of satellite particles.

To improve their colloidal stability during the washing step, an aqueous PVP solution was firstly added to the colloidal suspension in order to stabilize the particles via steric hindrance. Then centrifugation cycle was performed to remove the free Ag nanoparticles from the heavier nanoclusters (Protocol 13).

Protocol 13 – Washing procedure of raspberry-like nanoclusters

The colloidal suspension was diluted in 30 mL of an aqueous PVP solution (0.5 g/L). After 2 h, the mixture was three times washed by centrifugation at 3000 g for 20 min and redispersed in water.

The TEM images before and after washing of the colloidal suspension are shown in Figure II.26 (-a and -b). No aggregation and no deterioration of the Ag nanoparticles was observed revealing the capping of particles with PVP. The centrifugation allowed to remove much of the silver particles excess, however agglomerates of clusters were still observed. Furthermore, the density of metallic nanoparticles was systematically lower than the one observed before washing.

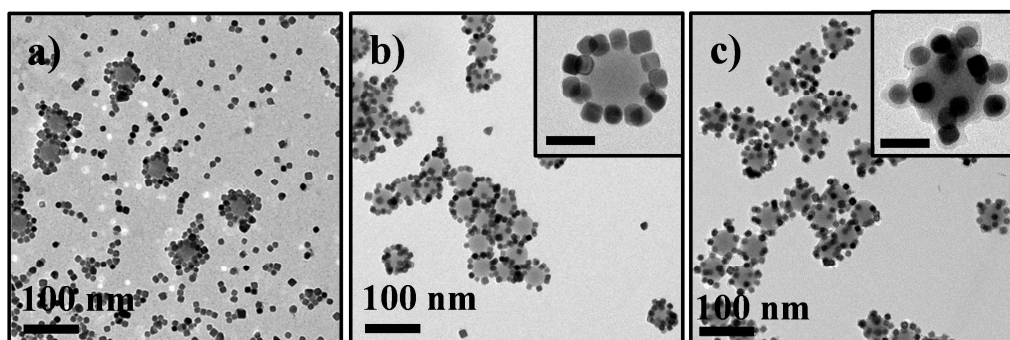


Figure II.26 – TEM images of raspberry-like nanoclusters (a) after assembly of Ag nanospheres (26 nm) onto EDPS-modified silica beads (89 nm), (b) after washing step and (c) after encapsulation in silica shell. Insert scale bars: 50 nm.

In order to better consolidate the PVP-stabilized nanoclusters and confirm the assembly of silver particles all around the dielectric core, the nanoclusters were encapsulated with a silica shell by using a conventional Stöber process (Protocol 14). The necessary volume (V_{TEOS}) of silica precursor was calculated as previously from the equation (II.2), by considering that all EDPS-modified silica

beads were conserved during the washing steps and approximately 20 silver particles were assembled by silica bead.

Protocol 14 – Encapsulation of nanoclusters with a 8-nm silica shell

After centrifugation, nanoclusters were dispersed in a minimum of water (~ 0.5 mL), the volume was completed to 4.94 mL with ethanol and 60 μ L of ammonium hydroxide were added to solution. Then 2 μ L of TEOS diluted in 200 μ L of ethanol were dropwise injected into the solution with an addition rate fixed to 0.5 mL/h.

A thin layer (~ 10 nm) of silica was deposited on all the nanoclusters (Figure II.26-c) under these conditions. The clusters were isolated and uniformly distributed on the carbon grid. The position of satellite particles on the silica beads was “frozen” by the deposition of the silica shell. This encapsulation allowed to confirm the interaction between silver particles and the EDPS-modified silica beads and the raspberry-like morphology of the nanoclusters. However, a slight fragmentation of some silver nanoparticles in the inorganic layer was observed (Figure II.27). Tiny silver nanoparticles of few nanometers coexisted with the initial ones. Their formation was due to the aerial oxidation of the metallic particles driven by the ammonia used as catalyst for silica growth.

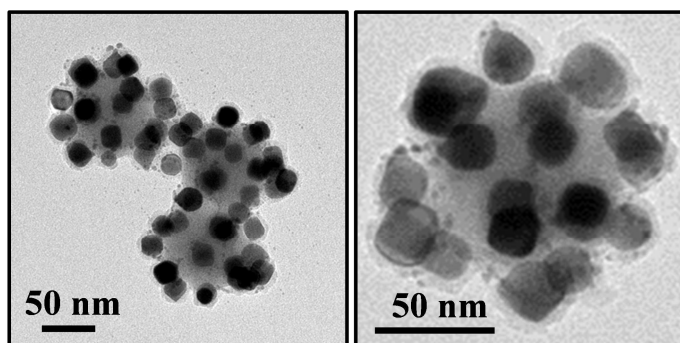


Figure II.27 - TEM images of PVP-stabilized nanoclusters encapsulated with a silica shell via the Stöber process.

C.1.2.1 Optical properties of the raspberry-like nanoclusters suspension

The extinction spectra of the 26-nm silver nanoparticles and the nanoclusters, before and after silica coating, are shown in Figure II.28. No difference was observed between both the spectrum of the dispersed satellite nanoparticles and the one of the nanoclusters. The nanoclusters retain the plasmon resonance characteristics of the dispersed satellites. This could be assigned to the absence of interparticle interactions or to the presence of a high amount of satellites particles in comparison to the amount of the nanoclusters. Upon deposition of the thin silica layer on the raspberry-like nanoclusters, a red-shift and a widening of the surface plasmon band was observed. The thin layer of silica allowed to wash the colloidal suspension and the removal of the excess of free metallic particles. The red-shift was assigned either to the interparticle interactions and to the change of the

electronic properties of the medium surrounding the particles. Silica is electronically inert but its refractive index is different from that of water. The red-shift in the position of the absorption band could thus be due to an increase of the local refractive index around the particles. Additionally, the long tails in the spectrum indicates the presence of light scattering in the systems.

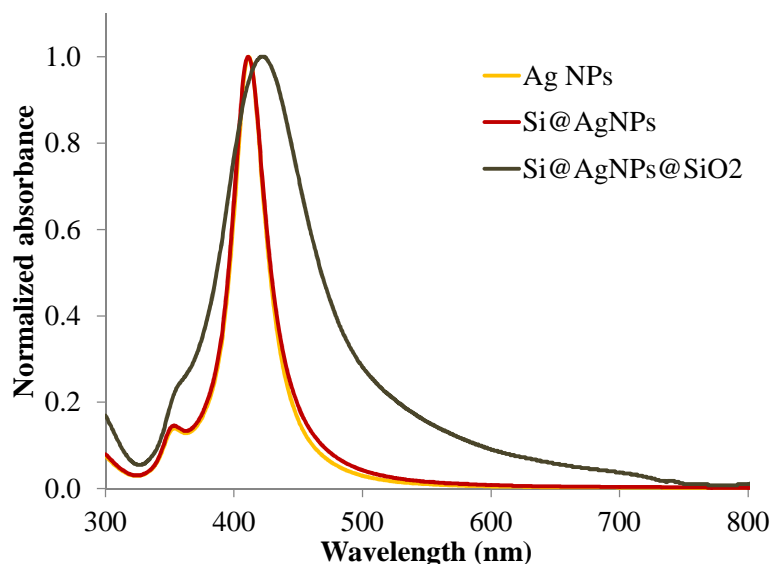


Figure II.28 – Normalized absorption spectra of colloidal suspension containing silver nanoparticles (AgNPs), PVP-stabilized nanoclusters (Si@AgNPs) and nanoclusters encapsulated in a silica shell (Si@AgNPs@SiO₂).

C.1.2.2 “Full” characterization of a single nanocluster

In order to understand the physical origins of the observed properties, single nanocluster characterization was performed by electron tomography (3D-STEM) and Spatial Modulation Spectroscopy (SMS) implemented at the IPCMS (Strasbourg) and the Laboratoire de Spectrométrie Ionique et Moléculaire (LASIM, Lyon), respectively. The SMS technique, developed in the group of F. Vallée at the LASIM, is based on spatial modulation of the position of a given nanoparticle under a tightly focused laser light spot and detection of the concomitant modulation of the transmitted light. It is the only technique permitting quantitative determination of the extinction cross-section of the studied nanoparticles. It thus permits a comparison of experimental and theoretical results. The principle and implementation of the SMS technique are described in the Annex 1. The electron tomography technique, developed in the group of O. Ersen at IPCMS, allows to determine the structure, the morphology and the chemical characteristics of nano-objects with nanometer resolution. In order to avoid the damages of the nano-objet that could be induced by the electron beam, the Figure II.29 presents the ‘route’ adopted to perform SMS and 3D-STEM measurements on a same particle. Firstly, the colloidal suspension containing the raspberries was spin-coated on a silica substrate. To ensure the optical separation of the nanocluster (*i.e.* interparticle distance $\geq 1 \mu\text{m}$), the dilution of the suspension was previously adjusted. The individual nanocluster was first crudely localized on the substrate, taking low magnification TEM

images then its optical spectrum was subsequently measured by SMS. Once the nanocluster optically characterized, it was analyzed by electron tomography to determine its real structure.

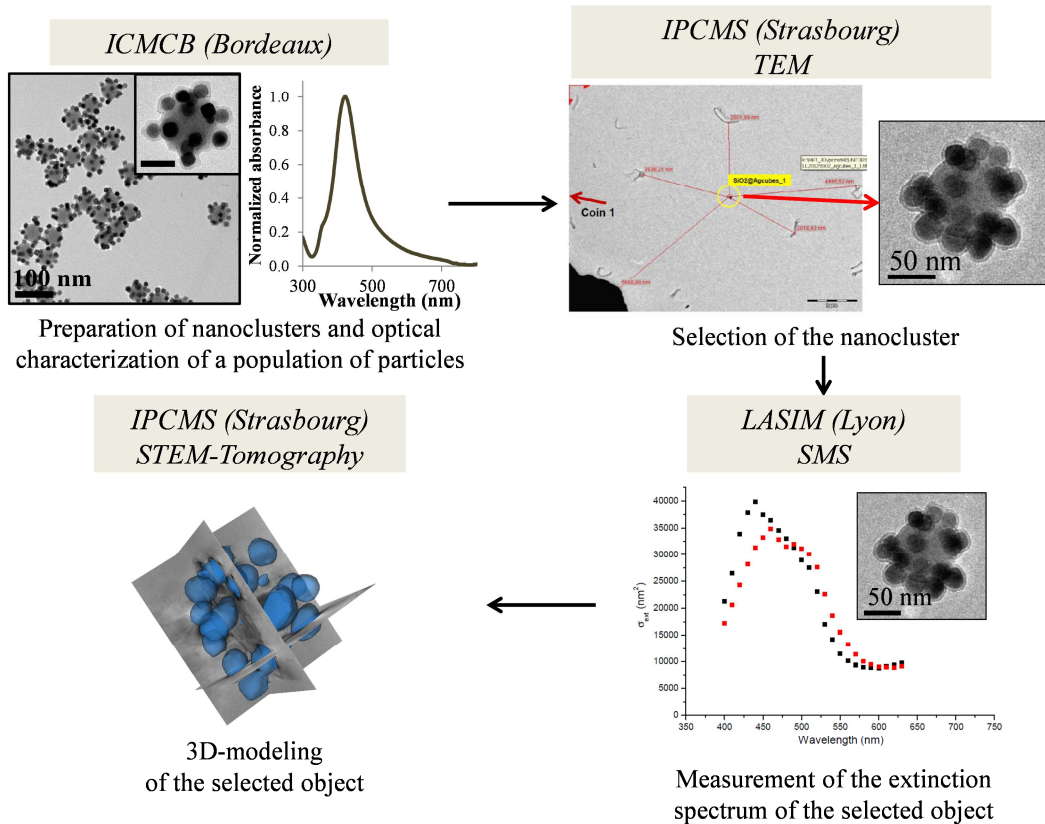


Figure II.29 - Strategy adopted to characterize the morphology and the optical properties of a single nanocluster.

- Characterization of single nanocluster by Spatial Modulation Spectroscopy (SMS)

The optical extinction spectra of two single nanoclusters not coated by silica deposited on silica membrane were first measured (Figure II.30). In the absence of silica, the nanoclusters were systematically constituted of a silica bead surrounded by “a ring” of silver spherical nanoparticles felt on the substrate. The polarization angle used for the measurements was whenever determined by searching the polarization of light maximizing the amplitude of measured signal at the surface plasmon resonance of the nano-object (around 420 nm).

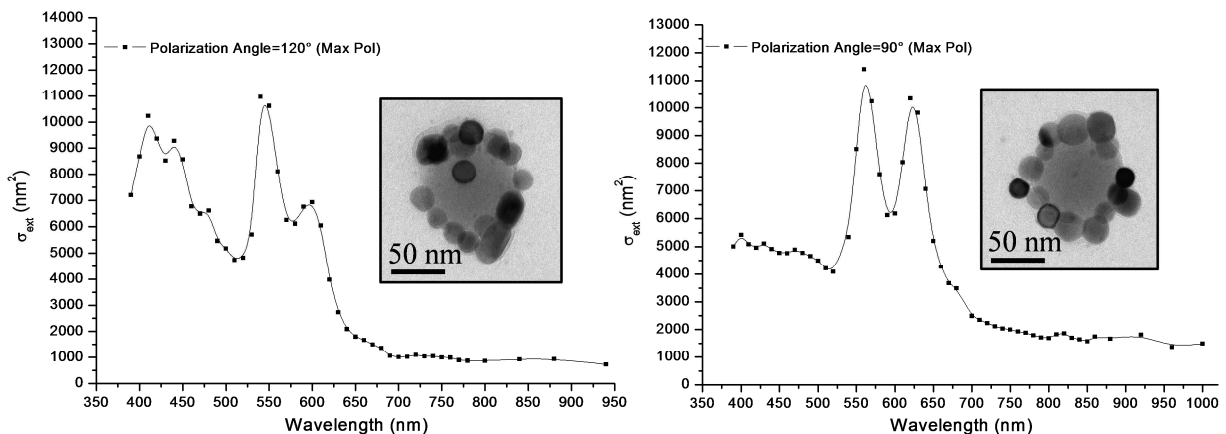


Figure II.30 – Optical extinction spectra and corresponding TEM images of two individual PVP-stabilized nanoclusters measured by SMS.

On the first extinction spectrum (Figure II.30-left) we could observe that, additionally to the plasmon band characteristic of the free 26 nm silver nanoparticles at about 400 nm, new resonances appeared at longer wavelengths (near 550-600 nm). These bands could be attributed to coupling modes between metallic nanoparticles. It is well-known that when plasmonic nanoparticles are in close interaction, *i.e.* when the distance between them is lower than the radius of the nanoparticles, a modification of the distribution of the electric field occurs. The individual plasmon oscillations can couple with each other resulting in the appearance of coupling LSPR modes [Hao04, Amendola10, Jain10]. This is generally characterized by a strong red-shift of the LSPR wavelength because a lower energy is required to drive the coupled plasmon oscillation modes of the assembly [Jain07]. However, the plasmon oscillation coupling is promoted only when the polarization is oriented along the interparticle axis and it is inhibited when the polarization angle is orthogonal to the interparticle axis.

The extinction spectrum of another nanocluster (Figure II.30-right) also exhibited these additional bands but with different intensities at longer wavelengths. The distribution of metallic particles was different from one cluster to another one that was making the interpretation of the experimental data very difficult.

The same type of experiments was performed on silica covered raspberry-like nanoclusters. The Figure II.31 shows the extinction spectra of two individual nanoclusters encapsulated in silica shell. For both nanoclusters, the main plasmon band near 420 nm characteristic of silver nanoparticles (in silica environment) was present. In both case, the spectrum also exhibited another resonance at longer wavelength (in the 500-550 nm range) due to interparticle interactions. By varying the polarization of the incident light, the intensity of these bands was modified evidencing the inhomogeneity in the material distribution. The polarization angle used for the measurements was whenever determined by searching the polarization of light maximizing or minimizing the amplitude of measured signal ($\Delta T/T = (P_{\text{trans}} - P_{\text{inc}}) / P_{\text{inc}}$) at the surface plasmon resonance of the nano-object (here around 420 nm). For example, in the case of the nanocluster shown in the Figure II.31 (right), the amplitude was minimal at $\alpha = 50^\circ$ and maximal at $\alpha = 140^\circ$. Theoretically, if the silica bead was uniformly covered with the metallic particles, the nanocluster may exhibit an overall isotropic structure and all the silver nanoparticles see each other in the same way.

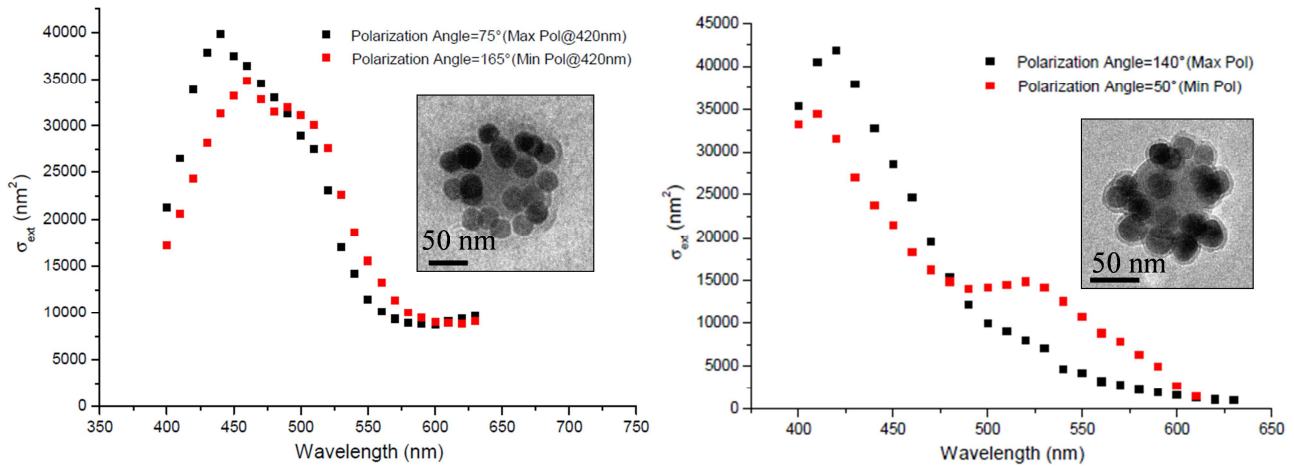


Figure II.31 - Optical extinction spectra of two nanoclusters encapsulated in silica shell measured by SMS for two polarization angles (black and red squares) in each case and their corresponding TEM images

From these overall results, it clearly appeared that the synthetic procedure for the generation of the nanocluster had to be optimized to get more uniform and dense coatings of nanoparticles and further understand the effect of interaction of its material components.

- Structural characterization of single nanocluster by electron tomography

To determine the exact position and number of metallic particles attached to the surface of the EDPS-modified silica bead, electron tomography analysis was performed. The characterization was performed on the “most” robust nanocluster *i.e.* the cluster encapsulated in a silica shell. The Figure II.32 shows TEM and STEM micrographs of the selected nanocluster before and after the optical SMS analysis. Before SMS measurements, the silica shell surrounding the nanocluster was clearly visible. After the optical measurements, the silver nanoparticles became more rounded. Moreover, additional tiny particles within the silica shell were clearly visible on the TEM images. These tiny silver particles were due to a photo-fragmentation of silver under the photon beam during the SMS measurements.

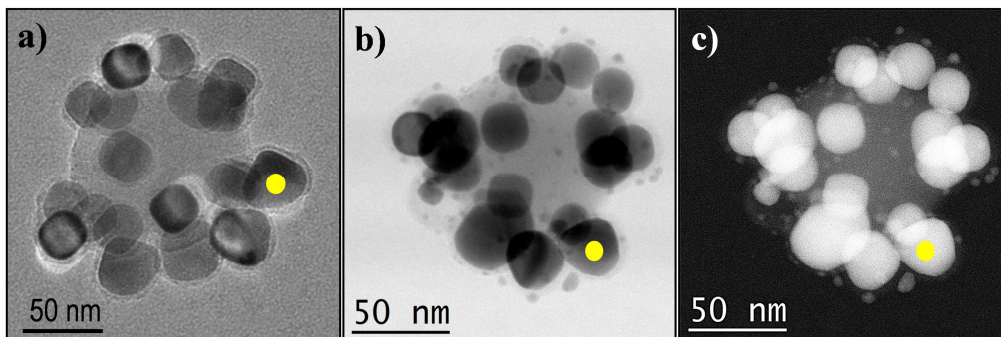


Figure II.32 - (a) TEM image of the chosen nanocluster before SMS analysis, (b) BF- and (c) HAADF- STEM images of the nanocluster after SMS analysis. The yellow dot allows to label the same silver satellite particle on each image.

The tomography was performed in STEM mode and images were collected by covering an angular range from -72.5° to $+62.5^\circ$ with an increment of 2.5° . The STEM mode allows to increase the contrast in the images between each element of the nanocluster compared to the TEM mode due

to its higher sensitivity to the mean atomic number ($Z_{\text{Si}} = 14$ and $Z_{\text{Ag}} = 47$) and thus facilitate the spatial separation of each component from the calculated volume. By combining all the STEM projections, the volume of the nanocluster was successfully reconstructed (Figure II.33-right).

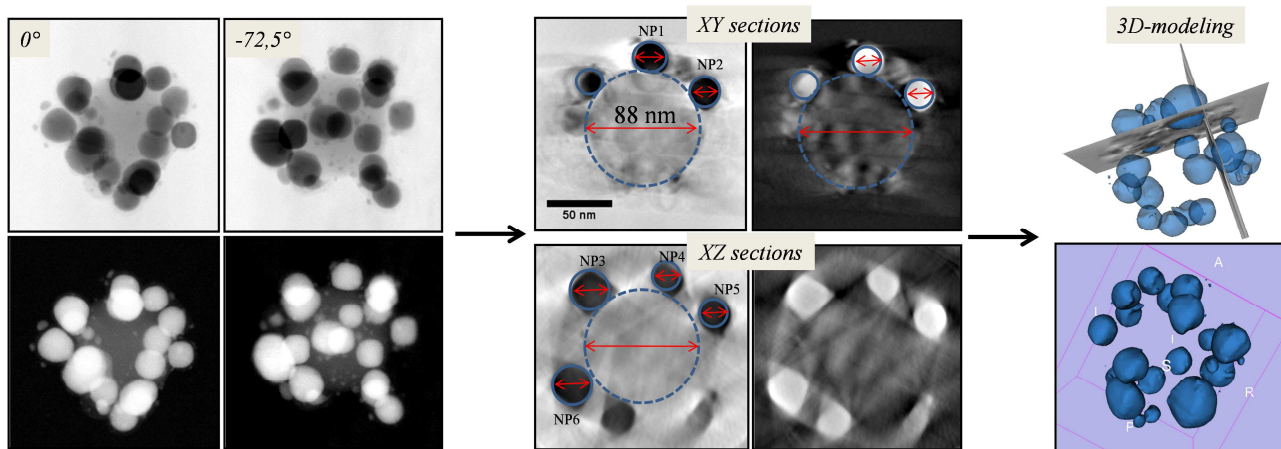


Figure II.33 – (Left) BF- and HAADF-STEM images extracted at 0° and -72.5° from tilt series; (Middle) Extracted BF- and HAADF-sections in XY and XZ axis from the reconstruction of the nanocluster; (Right) 3D-modeling of the nanocluster with silver particles in blue, the silica bead was not represented for a better observation of the satellite particles.

From the 3D-modeling, we observed a relative homogeneous distribution of the Ag nanoparticles on the surface of the silica particle. The nanocluster was composed of seventeen Ag nanoparticles. From the two sections presented on the Figure II.33 (middle), the diameter of many particles could be measured. The diameter of the silica bead was estimated to 88 nm and the mean diameter of six satellite particles was estimated around 23 nm. Two larger Ag particles (~ 34 nm) were also observed. Finally, many tiny silver particles were observed with sizes between 2 and 7.5 nm. The comparison of HAADF-STEM images of the investigated nanocluster, before and after tomography analysis, allows to ensure that the analysis did not damage the overall morphology (Figure II.34).

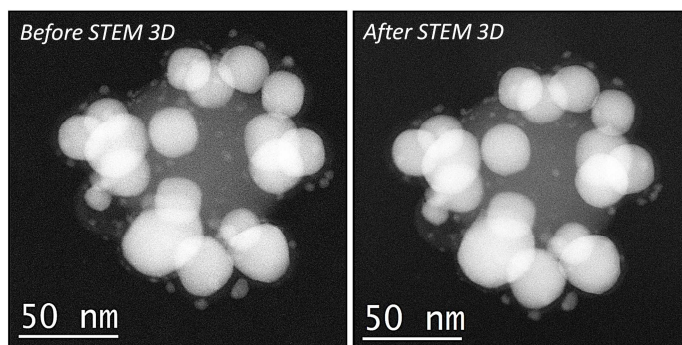


Figure II.34 – HAADF-STEM images of the studied silica-coated nanocluster before and after the tomography analysis.

C.1.3 Assembly of silver nanoprisms on EDPS-modified silica beads

By using a procedure similar to the one described to assemble silver spherical nanoparticles on the surface of silica, silver nanoprisms were deposited on EDPS-modified 89-nm silica beads. In this case, the Ag nanoprisms (AgTNPs) were stabilized by both citrate and PVP which ensured them an

overall negative charge. A preliminary step of washing by centrifugation (8000 g, 20 min at 4°C) was required in order to eliminate the excess of organic molecules (ascorbate, citrate and PVP) present in the solution. Similarly to the spherical nanoparticles, a range of assemblies was performed by varying the ratio $[\text{AgTNPs}]/[\text{SiO}_2\text{cores}]$ (Figure II.35). Flocculation was observed for a ratio lower than 5 evidencing the formation of chains-like agglomerates of particles. For a ratio higher than 5, the dispersion remained stable and raspberry-like nanoclusters were obtained.

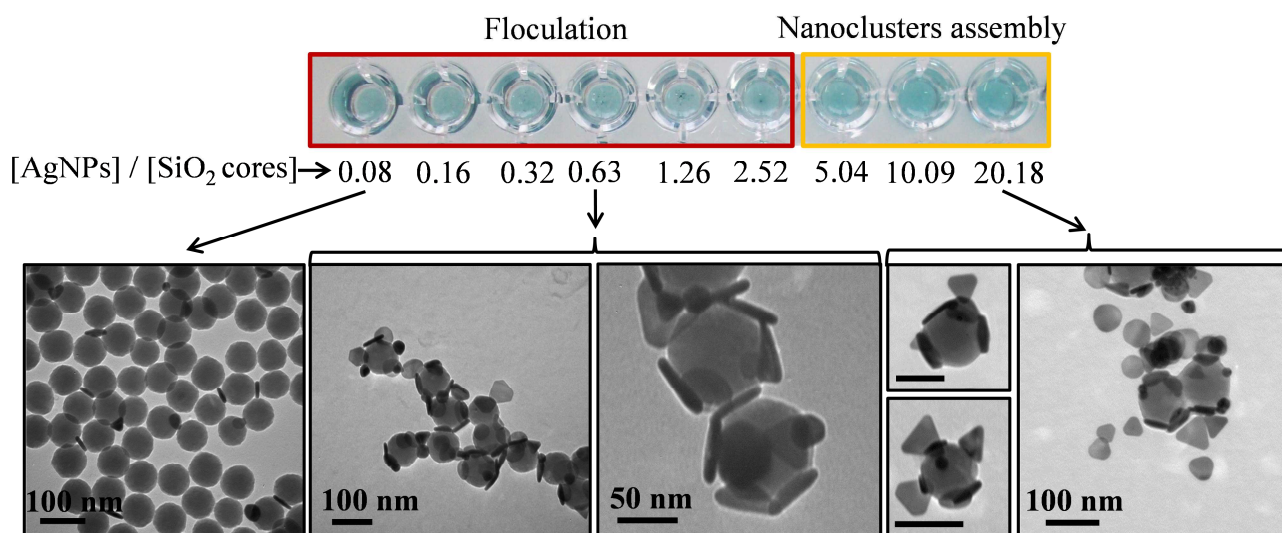


Figure II.35 - (Top) Photography of the range of assemblies performed by varying the ratio $[\text{AgTNPs}]/[\text{SiO}_2\text{cores}]$ from 0.08 to 20.18 and (Bottom) TEM images of nanoclusters obtained for different ratios.

After a washing step similar to the one described earlier (Protocol 13), TEM images show the effective deposition of the Ag nanoprisms on the surface of the dielectric colloids (Figure II.36). However, we observed that the washing step induced a selective etching of the tips of the nanoprisms, making them more rounded. We also observed that the overall material distribution was very sensitive to the observation time under the electron beam of the microscope.

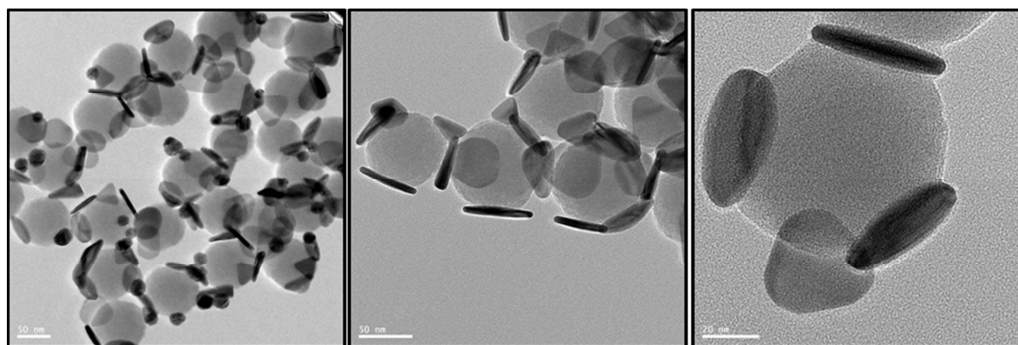


Figure II.36 - HRTEM images of washed nanoclusters obtained with an excess of 20 of Ag nanoprisms compared to EDPS-modified silica cores.

By focusing the electron beam of the microscope on one object during the TEM characterization, we observed a “melting” of the silica particle (Figure II.37). The longer the observation time was, the thicker the coverage of the silver particles by silica. For instance, we

observed that after ~ 5 min of observation, the metallic particles were totally immersed in a silica matrix.

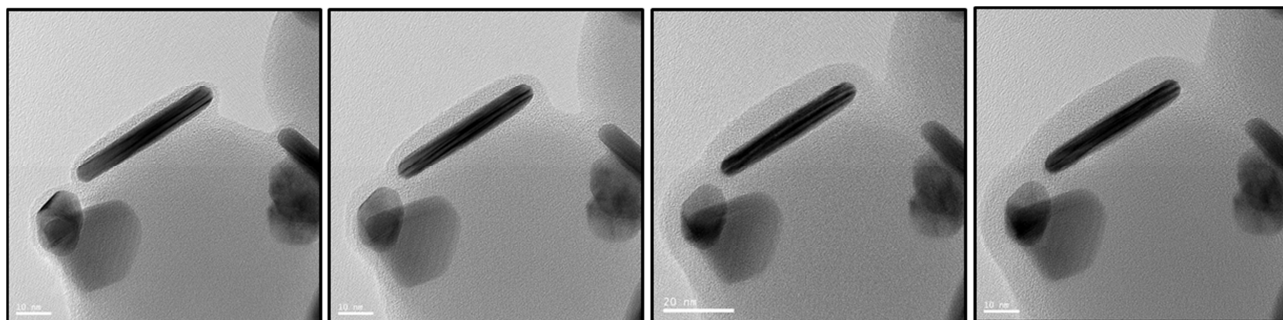


Figure II.37 – HRTEM images focusing on one Ag nanoprism attached on an EDPS-modified silica bead and showing the evolution under electron beam in a time interval of 5 min.

Despite the instability detected, we tried to perform electron tomography analyses on a single nanocluster coated with only one silver nanoprism. The analysis was performed in STEM mode and images were collected by covering an angular range from -70° to $+72^\circ$ with an increment of 2.5° . After analysis, the nanocluster had undergone strong modification in its morphology (Figure II.38). Due to a too long exposition under electron beam (~ 2.5 hours), the silica “melted” and encapsulated the silver nanoprisms making the volume reconstruction impossible.

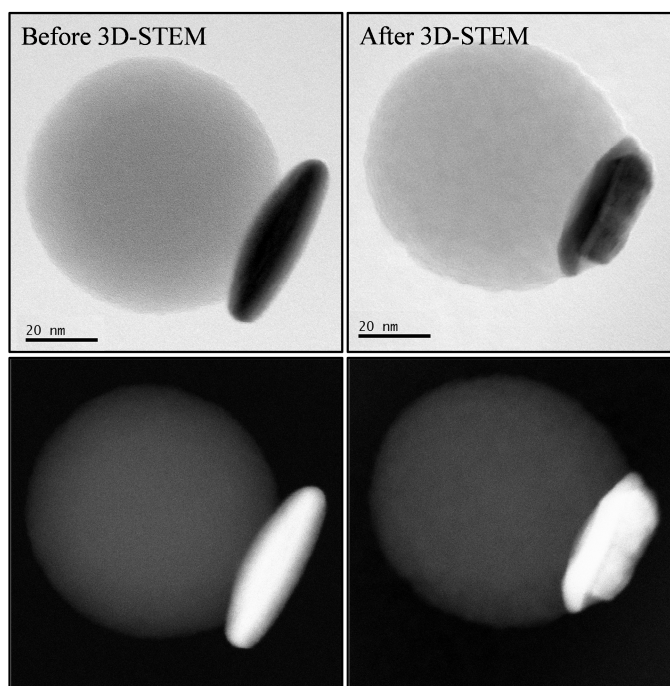


Figure II.38 – (Top) BF- and (Bottom) HAADF-STEM images of a single nanocluster having only one Ag nanoprism assembled on the silica core before and after the electron tomography.

We also tried to perform the analysis at a lower magnification to avoid damage of the object (Figure II.39). Two agglomerated nanoclusters were chosen for the study. The extracted HAADF sections in the XY axis obtained from the reconstructed volume of the nanoclusters revealed that the lower magnification allowed to decrease the morphology alteration. However, we still had the same problem of colloidal stability of the nanoclusters. Without silica coating, the silver triangles

fell-in on the carbon grid. Optimization of the self-assembly procedure is necessary to obtain stable nanoclusters.

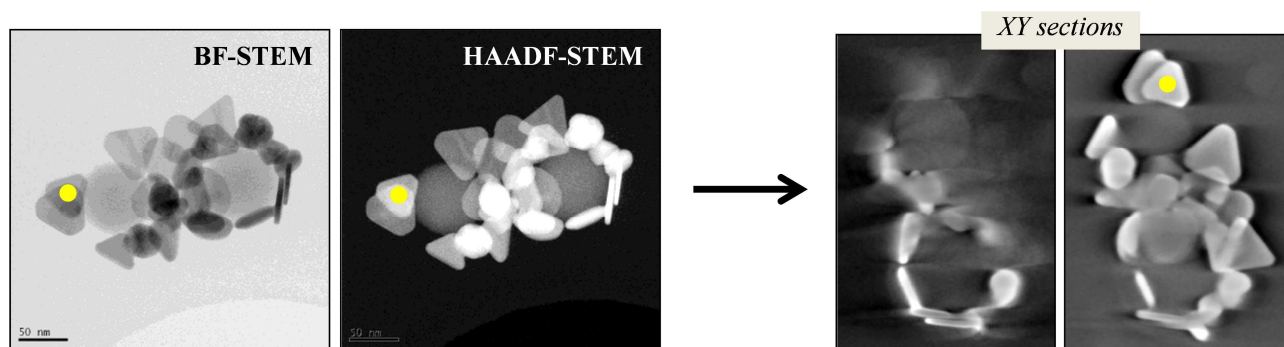


Figure II.39 – (Left) BF- and HAADF-STEM images extracted at 0° from tilt series and (Right) HAADF sections in XY axis from the reconstruction of the nanoclusters. The yellow dot allows to label the same silver satellite particle on each image.

Despite these colloidal instabilities of the nanoclusters once deposited on a substrate, the optical properties of the nanoclusters in suspension were studied by UV-Vis spectroscopy (Figure II.40). The deposition of the silver nanoprimers onto the silica beads led to a blue-shift of the peak of the isolated nanoprimers instead of the red-shift expected. This was due to the change of morphology of the primers during the grafting process. The tips of the silver nanoprimers being progressively etched during the assembly process, it yielded to the blue-shift of the main absorption band position.

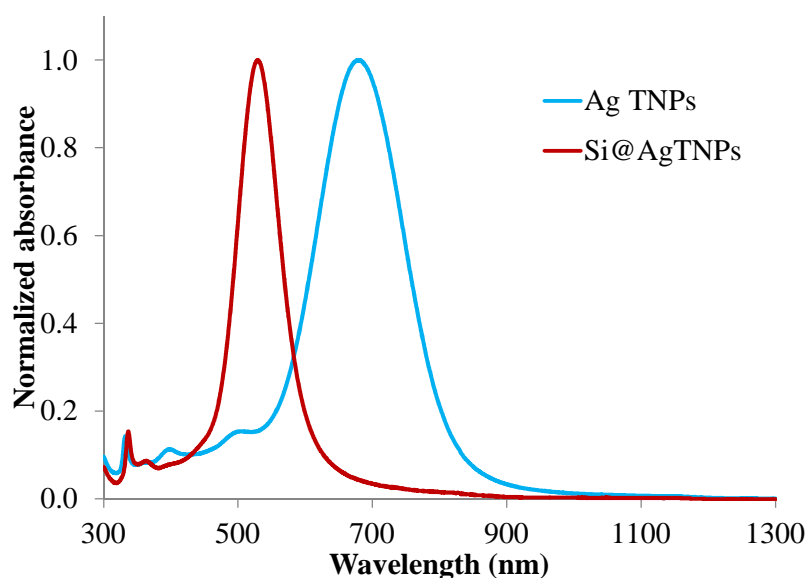


Figure II.40 – Normalized absorption spectra of suspensions containing silver triangular nanoparticles (AgTNPs) and PVP-stabilized nanoclusters (Si@AgTNPs).

Figure II.41 shows the optical properties of two single nanoclusters measured by SMS. Several resonances were observed at longer wavelengths evidencing interparticle interactions. However, as for the spherical particles, due to the strong inhomogeneities from one nanocluster to another one, it was not possible to understand the effect of interaction of the material components.

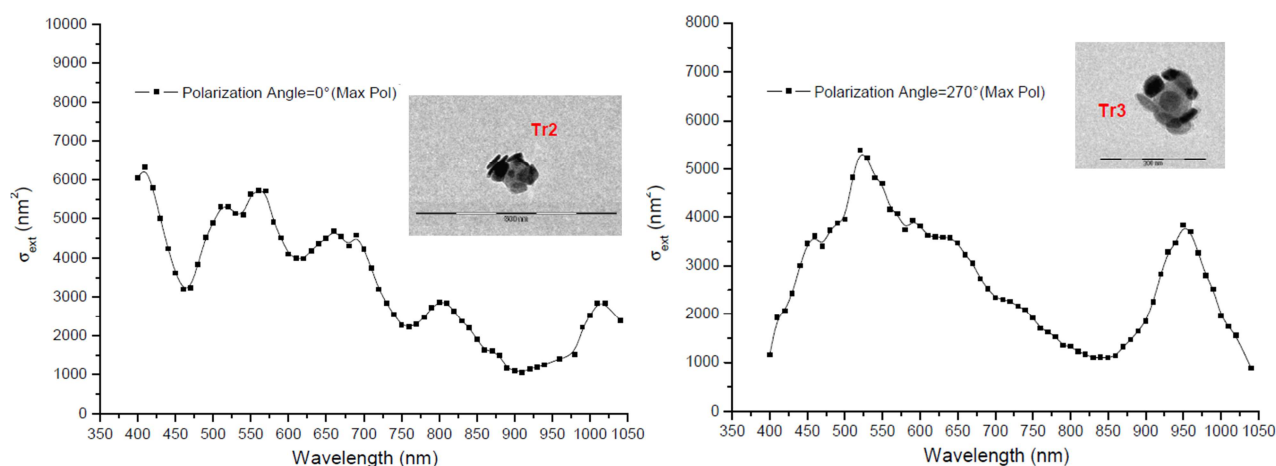


Figure II.41 - Optical extinction spectra of single PVP-stabilized raspberry-like nanoclusters measured by SMS and their corresponding TEM images.

By coating the silver nanoprisms with a thiol-alcane such as MUA (*cf.* Protocol 8), the shape of the silver triangular particles could be preserved even during the assembly process (Figure II.42).

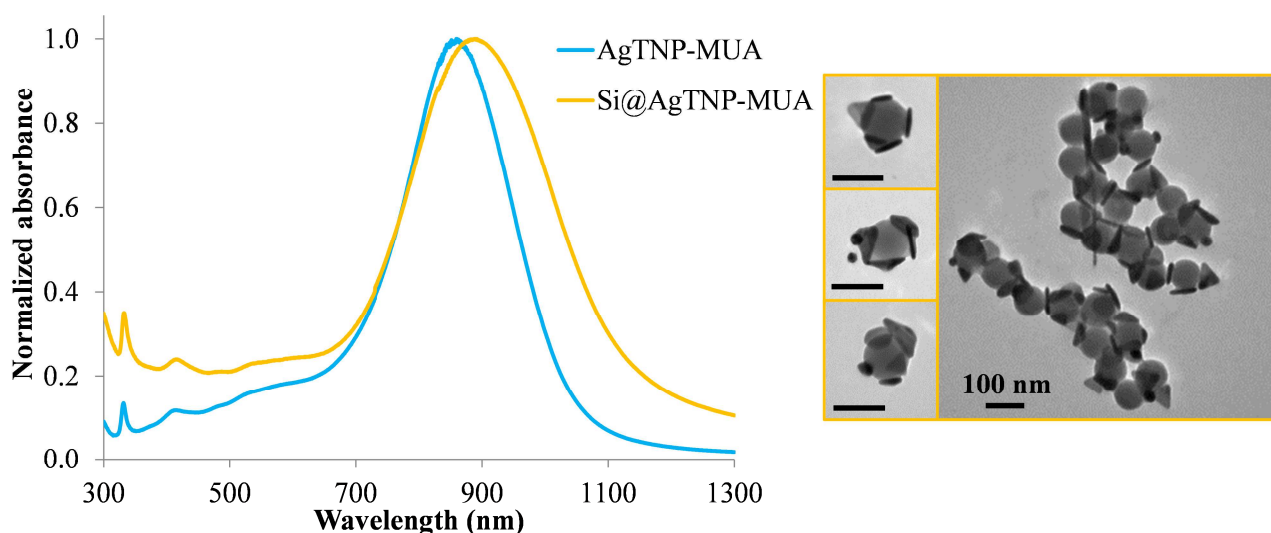


Figure II.42 – (Left) UV-Vis spectra of colloidal suspensions containing the MUA-coated Ag nanoprisms alone (AgTNP-MUA) and the washed nanoclusters obtained by assembling the MUA-coated Ag nanoprisms on the EDPS-modified silica beads (Si@AgTNP-MUA) and (Right) corresponding TEM images of the nanoclusters. Insert scale bars: 100 nm.

Consequently, the trends in the optical properties measured were similar to those reported for spherical particles. The dominant plasmon band peak position slightly shifted toward longer wavelengths. However, optimization of the deposition procedure was necessary to obtain more dense, close-packed and robust nanoclusters.

C.1.4 Conclusion on this strategy of direct assembly

The assembly approach via electrostatic interactions has been found suitable for generating nanoclusters with a raspberry-like morphology. However, the nanoclusters have to be coated with PVP or with a silica shell to improve their colloidal stability. The optical study of their properties allowed us to highlight coupling plasmon modes due to interparticle interaction. However, their full

understanding was difficult since the obtained colloidal suspensions contained nanoclusters with large composition distribution. The correlation study of analytical 3D-TEM and optical spectroscopy on a single raspberry has also revealed some modifications of shape or material distribution of the nanoclusters after long period of characterizations. The synthesis protocol has thus to be modified to improve the density of metallic particles on the surface of the dielectric, their composition distribution and their colloidal stability to fully understand and model their optical properties.

C.2 “Second generation” of raspberry-like nanoclusters

In order to obtain a denser packing of the metallic nanoparticles, we used the LbL technique to generate a uniform surface charge and smooth coating onto the silica beads. By depositing a polyelectrolyte having a quaternary ammonium, *e.g.* PDDA, onto the silica, it would act as electrostatic molecular glue between each metallic particle and the dielectric. The PDDA polyelectrolyte was chosen in order to provide a higher charge density compared to a polyelectrolyte with a primary or secondary amine group such as PEI or poly(allylamine hydrochloride) (PAH), respectively [Ashayer08, Xue07]. The use of long polymer chains was also expected to allow a higher surface of contact between the satellite and core particles since the multilayer of polymers brings a “soft brush” expected to facilitate the adhesion.

C.2.1 Surface modification of silica beads via Layer-by-Layer process

The two oppositely charged polyelectrolytes selected for the multilayer assembly were PPDA and PSS (Figure II.43). PDDA allowed a permanent positive charge in a large range of pH due to its quaternary ammonium groups and thus allowed a larger range of pH to perform assembly.

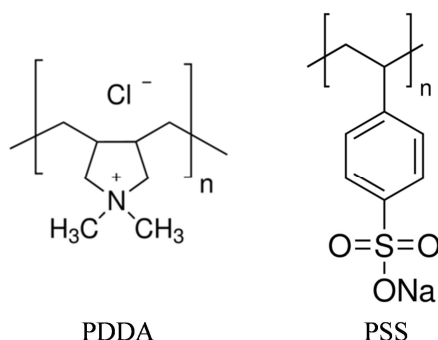


Figure II.43 - Molecular structures of PDDA and PSS.

The experimental procedure established for our purpose is described in Protocol 15. It consisted in the successive deposition of PDDA and PSS on the surface of the preformed silica beads (Figure II.44).

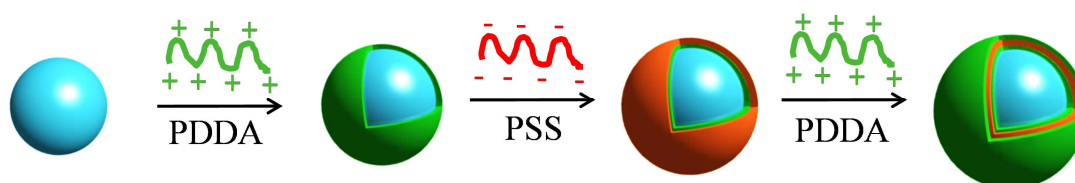


Figure II.44 - Schematic illustration of the LbL approach used to modify the surface of the silica nanoparticles.

As the silica was initially negatively charged, the first layer was made with the PDDA polycation, then PSS as polyanion and finally a last layer of PDDA to ensure a final positive charge. The polyelectrolyte multilayer was deposited on silica beads of 106-nm and 89-nm diameter. PSS and silica were negatively charged at pH 7.4 while PDDA was positively charged at this same pH, thereby all the PDDA or PSS solutions, and silica suspensions were prepared in phosphate-buffered saline (PBS).

Protocol 15 – LbL adsorption of polyelectrolytes on silica particles

Firstly, the silica nanoparticles were washed three times by centrifugation at 9000 g for 10 min and redispersed in a solution of phosphate-buffered saline (PBS) (0.01M) at pH 7.4. The solutions of 2 mg/mL PDDA and of 3mg/mL PSS were prepared in pH 7.4 PBS (0.01M). 10 mL of the dispersion of silica nanoparticles were added to 20 mL of the solution of PDDA. The adsorption was allowed to proceed for 30 min under stirring with a roller mixer from Stuart (SRT6D). The excess of PDDA was then eliminated by centrifugation at 6000 g for 10 min and the particles were redispersed in 10 mL of PBS. After three washing cycles, the colloidal suspension was injected into 20 mL of PSS solution. The adsorption procedure was similar to the one used for the PDDA layer. Finally, a last layer of PDDA was assembled on the silica particles and the last washing cycle was performed in water. The final concentration in silica beads was determined by dry extract.

The Figure II.45 (-a and -b) shows the TEM images corresponding to the two different sized silica beads after the assembly of three successive layers PDDA/PSS/PDDA. No aggregation, no change in shape and smooth and regular coating of the particles were observed. However, in both cases, an increase of the diameter of approximately ~ 7 nm evidenced the success of the assembly giving a multilayer thickness of ~ 3.5 nm. The multilayer was spotted by focusing on a single silica particle (Figure II.45-c). The thickness was evaluated to ~ 3.5 nm even if the contrast difference between the silica and polyelectrolyte layer is low. This value of multilayer thickness was coherent with previous values reported in literature. Indeed, Ai *et al.* measured by using a Quartz Crystal Microbalance (QCM) a bilayer (PDDA/PSS) thickness of ~ 2 nm [Ai02]. With the same technique, Caruso *et al.* determined a thickness of (1.4 ± 0.3) nm per layer for the successive deposition of PAA and PAH and confirmed this value with the Single-Particle Light Scattering (SPLS) technique [Schuetz03].

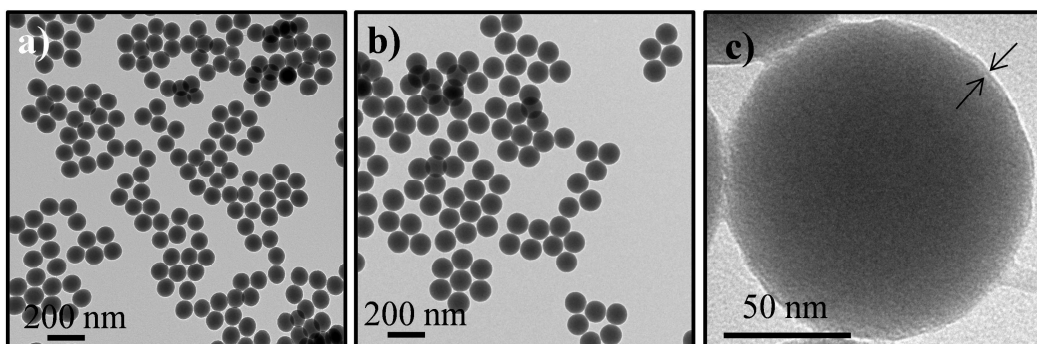


Figure II.45 - TEM images of (a) 89-nm and (b) 106-nm silica nanoparticles after the deposition of PDDA/PSS/PDDA multilayer. (c) Zoom on a single modified silica nanoparticle, the two arrows delimitate the multilayer of polyelectrolytes.

The successive deposition of polyelectrolytes on the silica surface was also monitored by micro-electrophoresis (Figure II.46). A regular alternation of ζ -potentials was observed suggesting the successful deposition of PDDA and PSS at pH 8. After the deposition of the first PDDA layer, a ζ -potential of +39 mV was observed while after the second layer of PDDA (following the PSS layer) a ζ -potential of +50 mV was recorded. This increase of ζ -potential revealed an increase of the positive overall charge density.

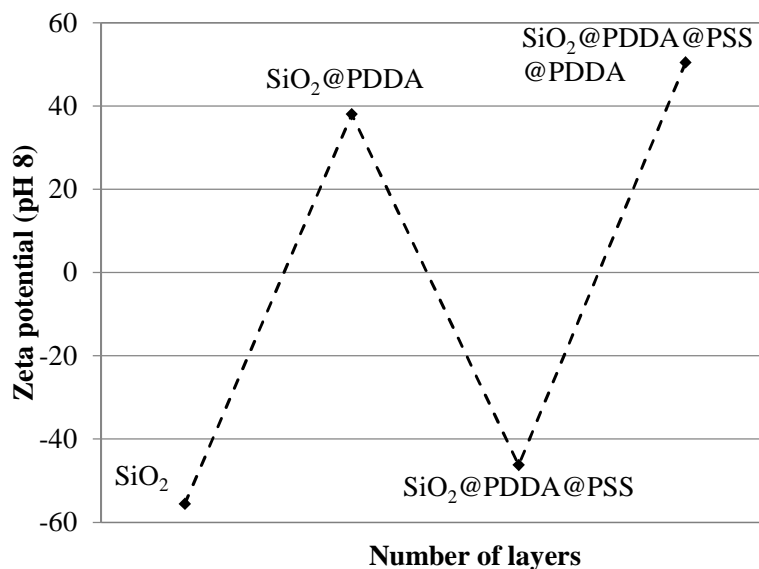


Figure II.46 – ζ -potential values of the PDDA/PSS/PDDA coated 106-nm silica nanoparticles as a function of the number of layers deposited at pH 8.

Once the multilayer of polyelectrolytes was deposited, with the outermost layer of PDDA (subsequently noted SiO₂@PDDA), the IEP of the silica was strongly shifted from ~ 2.5 to ~ 10.2 , revealing the successful adsorption of the quaternary ammonium groups on the surface of the silica (Figure II.47). This value of IEP is higher than the value of 8 obtained for EDPS-modified silica. This is due to the substitution of amine groups by quaternary ammonium groups which ensure a permanent and higher density of positive charges. Moreover, in the pH range wherein the assemblies were performed, *i.e.* pH ~ 6 -8, the LbL deposition of polyelectrolytes ensured a much larger amount of positive charges adsorbed on the silica surface compared to the ones adsorbed by using EDPS.

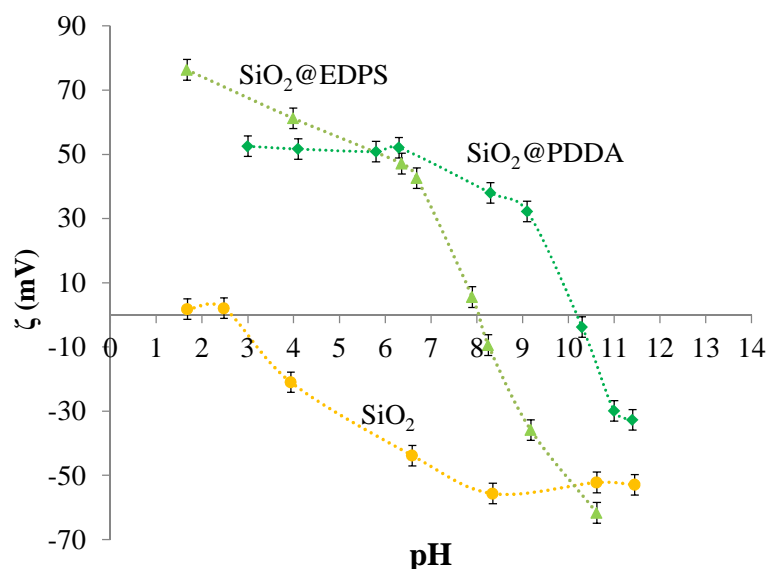


Figure II.47 – Isothermal variation of ζ -potential of the 89-nm silica nanoparticles before (SiO_2) and after EDPS-surface modification (SiO_2 @EDPS) or after the multilayer deposition with the outermost layer of PDDA (SiO_2 @PDDA).

From the characterization of the silica nanoparticles modified by polyelectrolyte multilayer (PEM), we highlighted a net improvement of the density of positive charges on the silica surface thanks to the high amount of quaternary ammonium present in the PDDA and the successive deposition of oppositely charged macromolecules.

C.2.2 Assembly of silver spherical nanoparticles on PEM-modified silica beads

The first trial was performed with the 26-nm Ag spherical nanoparticles (Protocol 16). The maximal number $N_{p_{\max}}$ of 26-nm Ag nanoparticles that could be attached on a 89-nm silica bead was estimated to 64 (with an angular distance $\alpha = 26.0^\circ$) while for the 106-nm silica beads it was 85 ($\alpha = 22.72^\circ$). Experimentally, twice more Ag particles than necessary were used to ensure a full coverage of the silica beads.

Protocol 16 – Assembly of silver spherical nanoparticles on PEM-modified silica beads

Typically, 1 mL of a diluted suspension of PEM-modified silica beads (1.5×10^{13} part/L) was dropwise introduced into 1 mL of the isotropic silver nanoparticles solution. The mixture was stirred overnight.

The nanoclusters were characterized by Scanning Electron Microscopy (SEM, Annex 1) after deposition on a silicon wafer previously functionalized with (3-aminopropyl)triethoxysilane (APTES). The Figure II.48 shows representative images of the obtained raspberry-like nanoclusters. They demonstrate the homogeneous coverage and close packing of the silver nanoparticles as well as the production of raspberry-like nanoclusters in high yield and high amount.

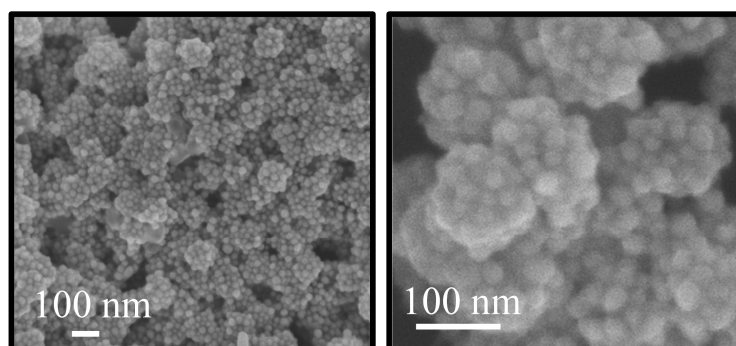


Figure II.48 – HR-SEM micrographs of nanoclusters obtained by assembly 26-nm silver nanoparticles onto PEM-modified silica beads of 106 nm in diameter ($\text{SiO}_2\text{-106@PDDA}$).

Compared to the assembly performed with EDPS-modified silica particles (Figure II.22), the LbL assembly clearly generated more stable nanoclusters. Upon deposition on the TEM grids, no satellite particles fell-in on the membrane (Figure II.49). TEM images revealed the high and uniform quality of the coatings and an increase of the density of metallic particles was observed when the core particle diameter increased from 89 to 106 nm.

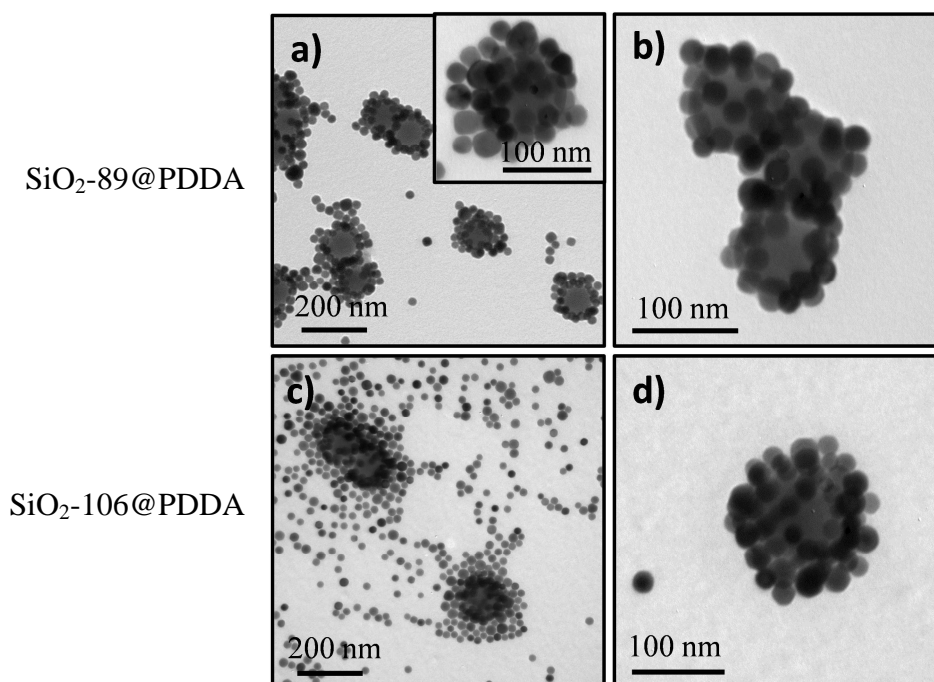


Figure II.49 - TEM images of raspberry-like nanoclusters obtained after assembly of Ag nanospheres (26 nm) onto the PEM-modified silica beads: (a, b) $\text{SiO}_2\text{-89@PDDA}$ and (c, d) $\text{SiO}_2\text{-106@PDDA}$.

The removal of the excess of metal particles after nanoparticles assembly on the silica spheres was accomplished (Protocol 17). To ensure their colloidal stability during the process, an additional layer of PDDA was deposited on the surface of the nanoclusters. The washing step yielded to the removal of the excess of metallic particles; but also to a decrease of the density of coverage (Figure II.50-b). An additional layer of silver nanoparticles was thus deposited on the PDDA-stabilized nanoclusters (Figure II.50-c), followed by a typical washing step, to get denser packing of the nanoparticles on the silica beads.

Protocol 17 – Washing of raspberry-like nanoclusters

10 mL of the colloidal suspension were diluted in 20 mL of an aqueous solution of 2 mg/mL PDDA. After 30 min, the mixture was washed three times by centrifugation at 3000 g for 20 min and redispersed in water (or a PBS solution (0.01M) at pH 7.4).

The extinction spectra of a series of coated nanoclusters were measured as shown in Figure II.50. After the metal particles removal, a new band appeared near 480 nm due to interparticle interactions. The deposition of an additional nanoparticles layer leads to a slight red-shift of this additional peak surface plasmon resonance as well as an increase of its intensity.

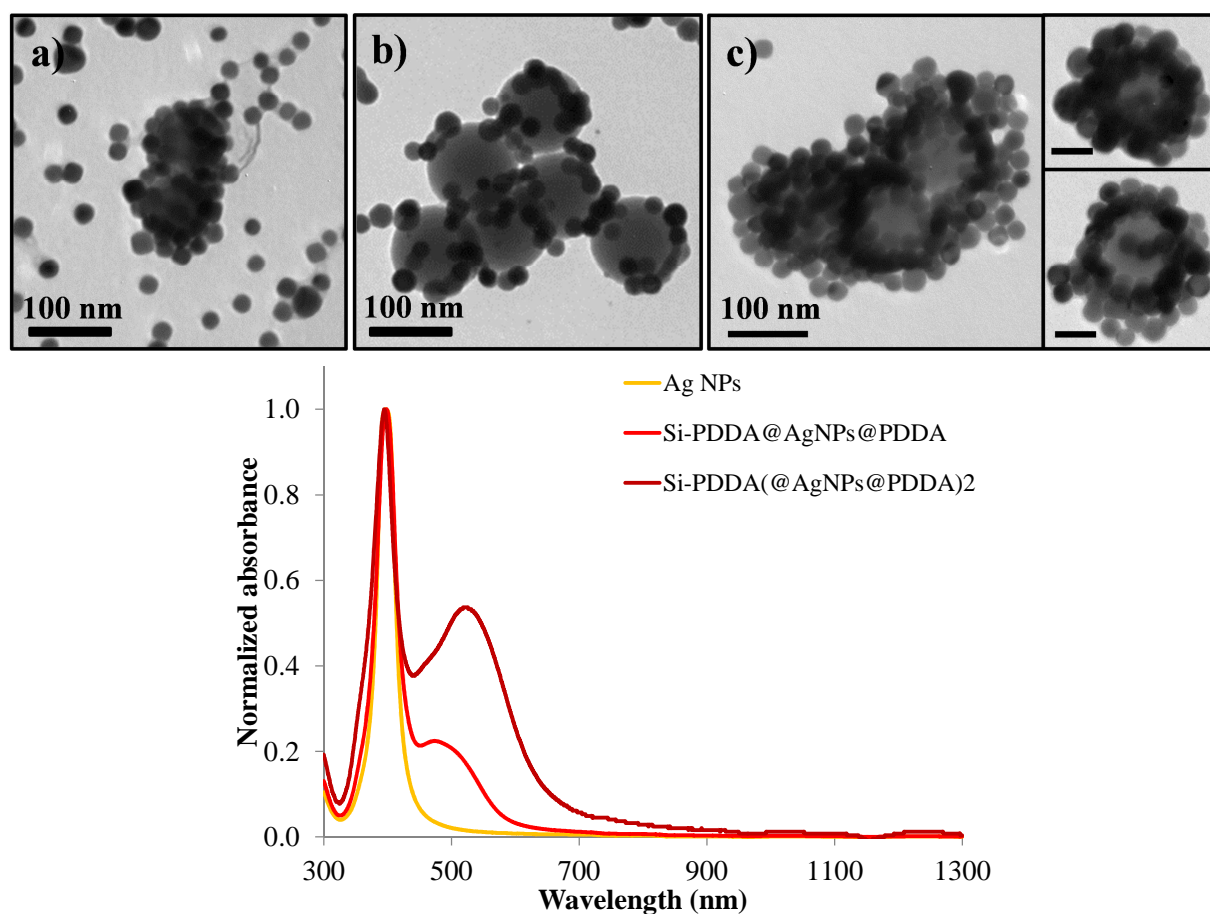


Figure II.50 – (Top) TEM images of nanoclusters (a) obtained by assembly of Ag nanoparticles on PEM-modified 106-nm silica beads, (b) after washing and stabilization with PDDA and (c) after deposition of a second layer of Ag; (Bottom) corresponding normalized absorption spectra of suspensions containing Ag nanoparticles alone (Ag NPs), PDDA-stabilized nanoclusters (Si-PDDA@AgNPs@PDDA) and PDDA-stabilized nanoclusters having a bilayer of Ag particles (Si-PDDA(@AgNPs@PDDA)₂).

In order to improve the washing step and to increase the colloidal stability of the nanoclusters, we studied the possibility to convert the interlayer forces from weak supramolecular interactions to strong covalent bonds by post-crosslinking the self-assembled multilayer of polyelectrolytes. For that, we proposed to post-infiltrate a photo-sensitive cross-linker: the 4,4'-diazido-2,2'-stilbenedisulfonic acid disodium salt (DAS) in the reactive medium. This molecule exhibits two phenyl azide groups and is easily photolyzed upon UV irradiation to generate a highly reactive

nitrene intermediate which reacts with almost all kinds of organic matter to form covalent bonding (Figure II.51). Zhang *et al.* previously obtained promising results by using this molecule as photo-cross-linking agent in order to increase the robustness of conventional PEMs of PAH/PAA deposited on a planar substrate [Zhang12].

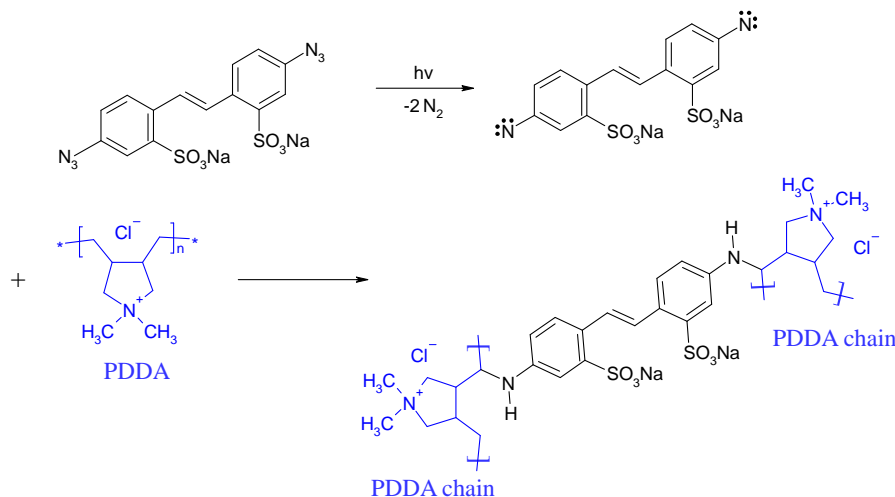


Figure II.51 – Chemical equation of the crosslinking reaction of PDDA by DAS.

In aqueous solution, the DAS was characterized by an absorption band near 340 nm (Figure II.52-blue curve) due to the azide ($-N_3$) groups. The absorption intensity was linearly proportional to the amount of present azide groups. Under UV irradiation, we observed a deep yellow coloration of the solution with the release of gas. It was evidenced on the UV-Vis spectrum by a gradual decrease of the 340-nm band with the concomitant appearance of a shoulder near 410 nm (yellow curve). This decrease suggested the decomposition of the azide groups under UV irradiation into the highly reactive nitrene intermediate accompanied by a release of nitrogen. After 5 min of irradiation, no change in the absorption spectrum was observed evidencing the full consumption of the azide groups of DAS.

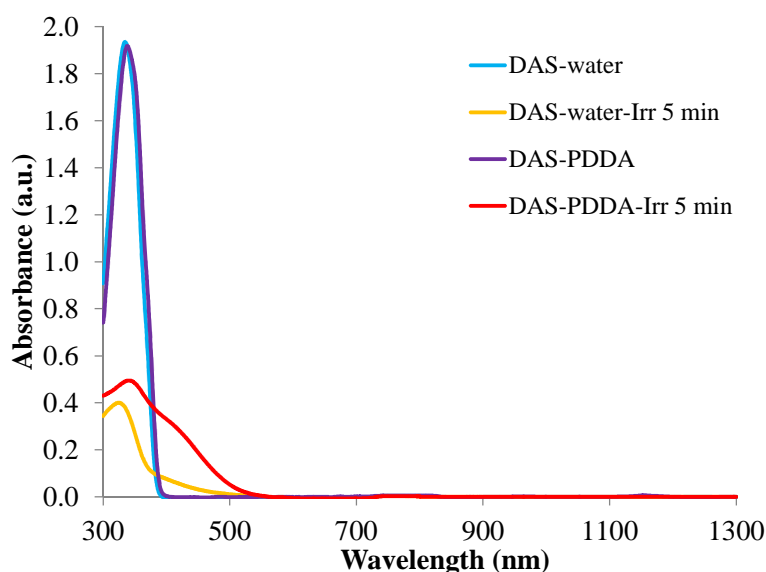


Figure II.52 – UV-Visible spectra of an aqueous DAS (0.05 mM) solution with or without PDDA, before and after UV irradiation.

As a control test, a similar experiment was performed by introducing the DAS into an aqueous solution of PDDA. Before irradiation, the absorption spectrum (purple curve) was the same than the one obtained with DAS in water. However after irradiation (red curve), the shoulder near 410 nm was significantly more intense than as previously observed, probably because the nitrene groups reacted with the carbon chains of PDDA to form secondary amine bonds (Figure II.51).

The DAS was then introduced in the aqueous suspension containing the raspberry-like nanoclusters. It was expected to form covalent bridges between the different polyelectrolytes layers of PSS and PDDA. The experimental procedure of strengthening with DAS is described in the Protocol 18. After the UV irradiation, the colloidal suspension was washed by centrifugation. Since the free DAS molecules exhibited a yellow color due to the degradation of azide groups, it was possible to ensure that no residual DAS molecules were remained in the suspension at the end of the washing cycle by controlling the absorption spectrum of each supernatant.

Protocol 18 – Strengthening of raspberry-like nanoclusters with DAS

An aqueous solution containing 0.05 mM of DAS was prepared in dark. Then, 1 mL of the DAS solution was added to 1 mL of the PDDA-stabilized colloidal suspension in dark. After 4 h, the mixture was placed in a quartz cell and irradiated for 5 min under stirring with a 150 W Xenon lamp at a distance of 15 cm. Finally the suspension was washed by centrifugation at 4000 g for 10 min. The yellow supernatant containing the excess of free DAS was removed and the bottom was redispersed in water. The centrifugation cycle was repeated until the supernatant became free of DAS molecules i.e. until the disappearance of the DAS characteristic absorption band on the UV-Visible spectrum.

It is clear that this procedure allowed a more efficient metallic particles removal. The intensity of the peak surface plasmon band due to interparticle interactions strongly increased in intensity in comparison to the plasmon band assigned to the free metallic particles (Figure II.53). The morphology of the nanoclusters was preserved in suspension or once deposited. However, we also observed that DAS treatment strongly increase the proportion of agglomerates of nanoclusters which were difficult to dissociate by sonication. Therefore, although the cross-linking of PEM with a photo-sensitive molecule appeared as an original and promising approach to strengthen the nanoclusters, this strategy was not extended in the following of this work.

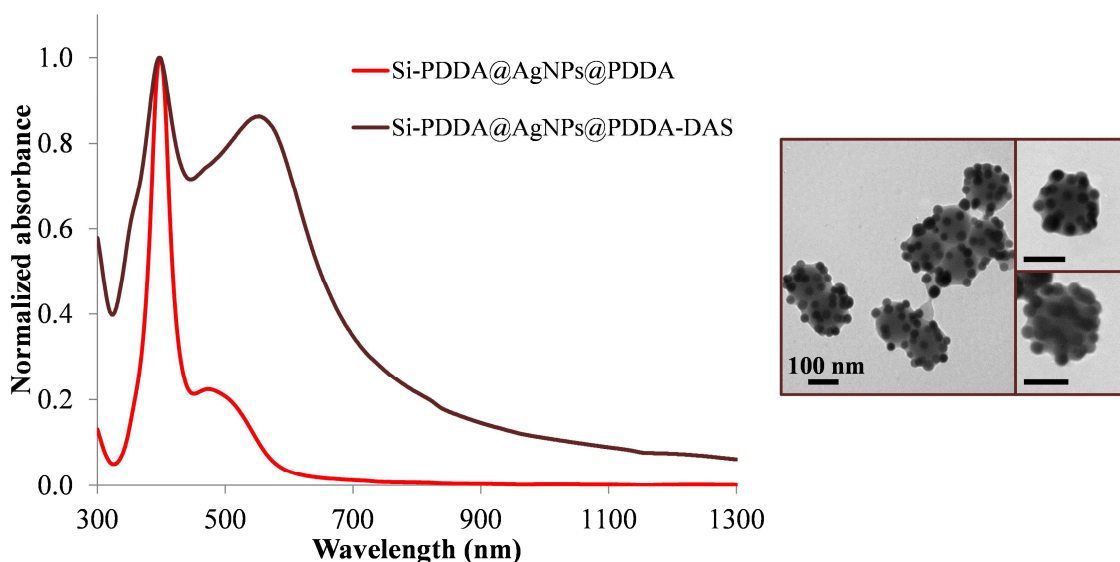


Figure II.53 – (Left) Absorption spectra of PDDA-stabilized nanoclusters suspensions before and after the consolidation with DAS. (Right) TEM images of the DAS- strengthened nanoclusters.

C.2.3 Assembly of gold spherical nanoparticles of different sizes on PEM-modified silica beads

In order to investigate the potentialities of the LbL assembly approach to deposit metallic particles of larger size, we performed assembly experiments with metallic particles of different sizes. This study would allow to determine the dependence of the optical properties on the size of the metallic particles. A narrow size distribution in the satellite size is one of the prerequisite to achieve reproducible optical properties of the composite colloids. To study this size effect, gold nanoparticles were used instead of silver. It is indeed much easier to produce large spherical particles of gold with a narrow size distribution rather than with silver.

We used gold nanoparticles, stabilized with citrate, with different diameters from 10 to 50 nm. In order to remove the excess of citrate present in the solution, the metallic particles were first washed by centrifugation or filtration. The protocol of assembly was similar to the one described for the Ag nanoparticles (Protocol 16). The concentration of the PEM-modified 106-nm silica beads suspension was kept constant for all of the assemblies ($\sim 1.5 \times 10^{13}$ particles/L), whatever the size of the satellite particles, in order to obtain in each case the same final concentration in raspberry-like nanoclusters ($\sim 7.7 \times 10^{12}$ raspberries/L). The Table II.3 summarizes the experimental concentrations used for each suspension of metal particles. These values of concentration were calculated from the maximal number ($N_{p_{max}}$) of satellites which could be attached to the surface of one 106-nm silica bead and by using 2.5 times more of satellite particles for 10- and 20-nm gold nanoparticles or twice more for 30-, 40- and 50-nm gold nanoparticles.

Table II.3 – Maximal number of satellites attachable per silica bead ($N_{p_{max}}$) calculated from the equations II.5 or II.6 and experimental concentrations (in particles/L) of metal and silica colloidal suspensions used for the assemblies.

	AuNP10	AuNP20	AuNP30	AuNP40	AuNP50	AgNP26
$N_{p_{max}}$	488 ^(II.4)	132 ^(II.5)	68 ^(II.5)	44 ^(II.5)	32 ^(II.5)	85 ^(II.5)
[Si-106@PDDA]	1.5×10^{13}	1.5×10^{13}	1.5×10^{13}	1.5×10^{13}	1.5×10^{13}	1.5×10^{13}
[satellites]	1.9×10^{16}	4.9×10^{15}	2.0×10^{15}	1.3×10^{15}	9.6×10^{14}	2.6×10^{15}
[raspberries] _{final}	7.7×10^{12}	7.7×10^{12}	7.7×10^{12}	7.7×10^{12}	7.7×10^{12}	7.7×10^{12}

Figure II.54 shows high resolution SEM of the different composites produced. Whatever the diameter of the gold nanoparticles, a strong interaction in between gold and silica particles was observed. With the 10-nm gold nanoparticles, all the silica particles were fully covered and nanoclusters had a real raspberry-like morphology. They were obtained in high yield and high amount. When the diameter of the satellites increased from 10 to 50 nm, the density of metallic nanoparticles became lower and it became more and more difficult to distinguish individual nanoclusters.

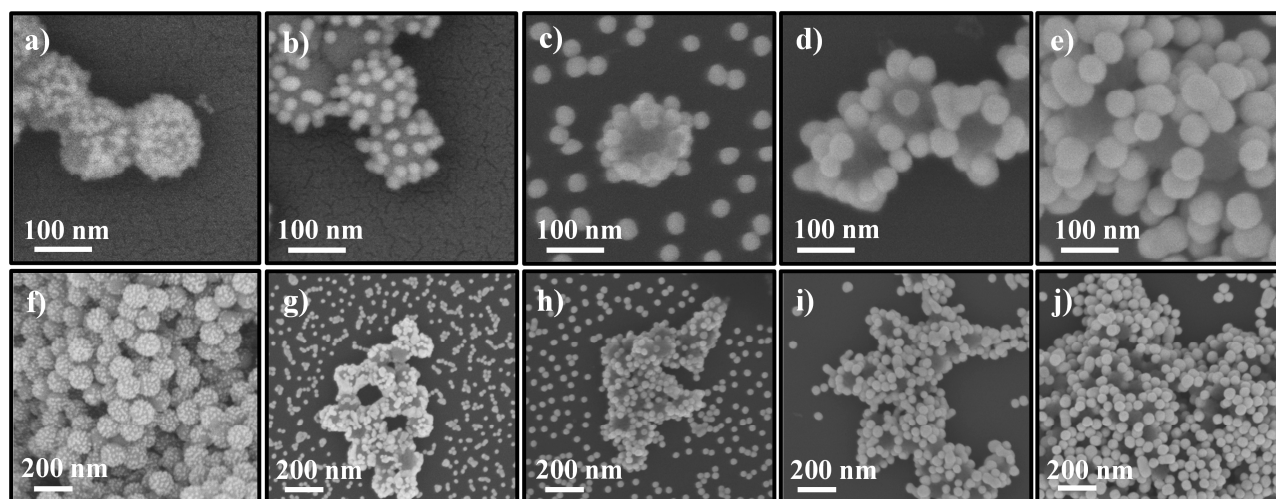


Figure II.54 – SEM images of raspberry-like nanoclusters obtained by assembly gold nanoparticles with different diameters of 10 nm (a, f), 20 nm (b, g), 30 nm (c, h), 40 nm (d, i) and 50 nm (e, j) on the PEM-modified silica beads.

Before characterization of their optical properties, the different suspensions were stabilized with PDDA and washed by centrifugation to eliminate the gold nanoparticles excess. The TEM images of each raspberries batch revealed that this step did not damage the nanoclusters (Figure II.55). The nanoclusters obtained with gold nanoparticles of 10 to 30 nm in diameter kept their well-defined raspberry-like morphology. However, the ones obtained with gold particles of 40 and 50 nm exhibit a lower density of coverage. The gold nanoparticles probably became too heavy and some of them fell-in on the carbon grid all around the silica core (gold density $19.3 \text{ g}\cdot\text{cm}^{-3}$).

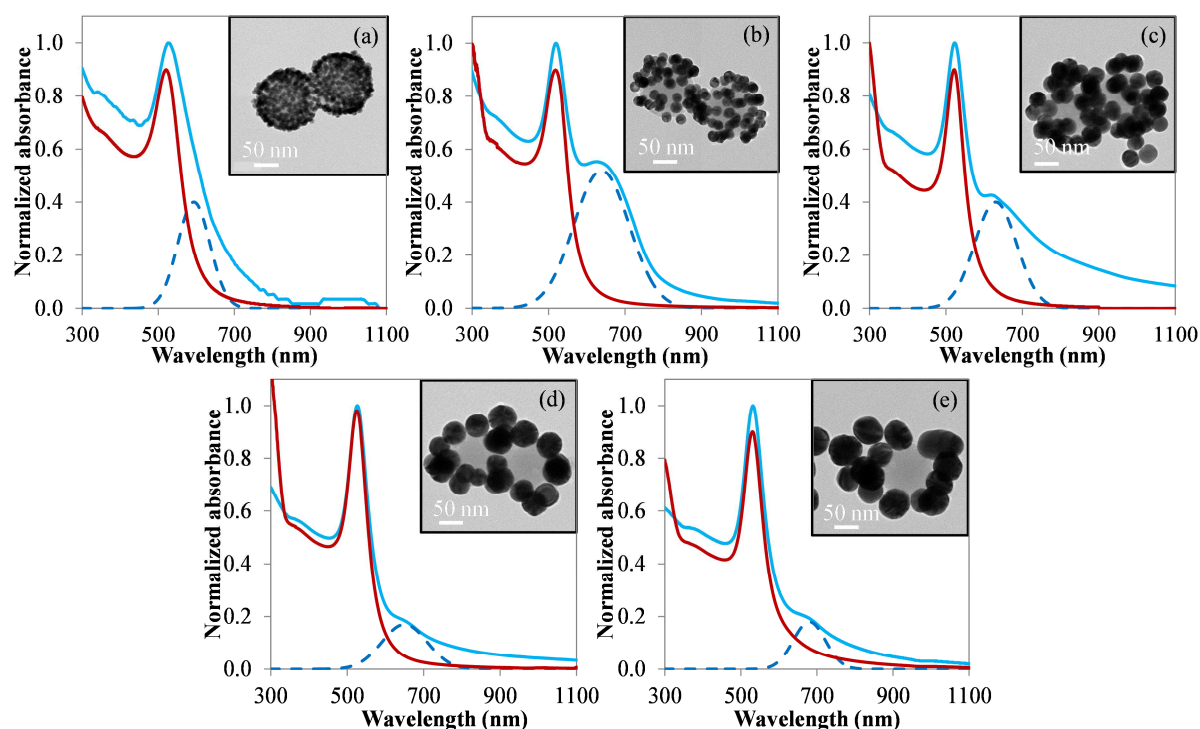


Figure II.55 – Normalized absorption spectra of Au nanoparticles alone (red curves) and PDDA-stabilized raspberry-like nanoclusters obtained by assembling Au nanoparticles with different diameters of (a) 10, (b) 20, (c) 30, (d) 40 and (e) 50 nm on the PEM-modified silica beads (light blue curves) and their corresponding HRTEM images. The dashed blue curves correspond to the coupling mode contributions.

The extinction spectra of the different raspberry-like nanoclusters were measured (light blue curves) and compared to the ones of the isolated gold nanoparticles of similar diameter (red curves). As expected the trend observed in the measured optical properties were similar to those observed for silver. Assembly of gold particles led to a plasmon band red-shift in comparison to the one of the corresponding free metallic particles. This band clearly revealed strong coupling effects between the metallic particles. The peak position of this plasmon band red-shifted with the increase of the size of the metallic particles (dotted spectrum). However, its intensity decreased when the density coverage was lower, for instance for the raspberries made with 40 nm and 50 nm gold nanoparticles layer.

Optimization of the “washing procedure” was necessary to remove the excess of the metallic particles and permitted a better characterization of the optical properties of the as-produced nanoparticles. This was accomplished by encapsulating the nanoclusters with a thin silica shell. Two encapsulation protocols were tested: the classical “Stöber process” and a biphasic approach.

- Via the Stöber’s process

Firstly, the nanoclusters were coated with a silica shell by using the conventional Stöber’s process. The strategy adopted was similar to the one previously used for the encapsulation of the first generation of raspberries. At the output of assembly, the nanoclusters needed to be stabilized

with PVP (Protocol 17) instead of PDDA in order to increase the interaction between the metal surface and the silica precursor (TEOS). Then they were placed in a hydro-alcoholic medium containing ammonia and wherein TEOS was slowly and continuously introduced (Protocol 18). After the washing and stabilization step with PVP, the nanoclusters kept their raspberry-like morphology as shown in Figure II.56-a. However, even if some raspberries were isolated and evenly encapsulated with a silica shell (Figure II.56-c), most of them were agglomerated with a diffuse surrounding silica film (Figure II.56-b).

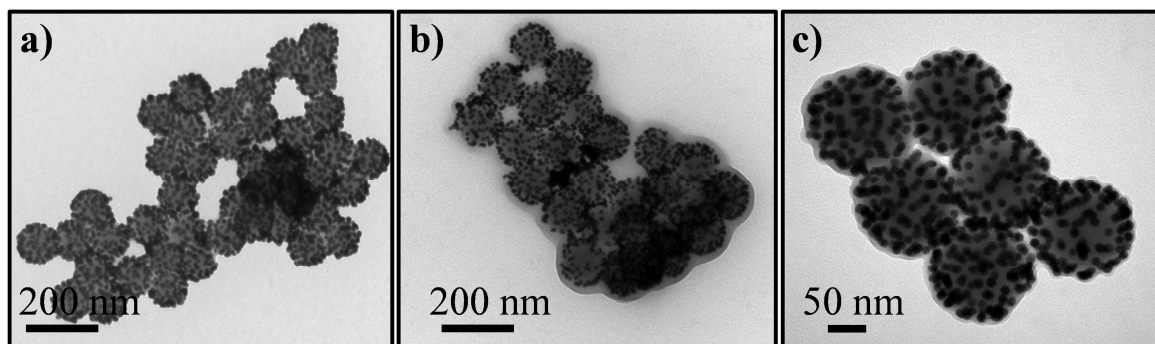


Figure II.56 – TEM images of PVP-stabilized nanoclusters before (a) and after (b, c) encapsulation with a thin silica shell via the conventional Stöber process in hydro-alcoholic medium.

Moreover, the density of metallic particles appeared lower than the one observed before the Stöber's process. This could be due to the fact that the silica coating of the nanoclusters via this process required a medium concentrated in particles (surface area of nanoparticles higher than $50 \text{ cm}^2/\text{cm}^3$) and a transfer of the particles from aqueous to ethanolic medium through several washing steps, promoting damage and colloidal destabilization of the nanoclusters.

- Via a biphasic approach

Another strategy was thus developed for keeping the raspberry-like morphology of the nanoclusters by avoiding the transfer in the ethanol which was an agglomeration-prone liquid. Recently, Schulzendorf *et al.* proposed the controlled silica coating of gold nanoparticles by using an approach inspired from the Hartlen's work [Hartlen08] and passing through a stepwise ligand exchange [Schulzendorf11]. Briefly, the citrate-stabilized gold nanoparticles were firstly exposed to *L*-arginine, which ensured a higher stability of the particles and a slightly basic medium required for the silica growth. Then they were exposed to an aminosilane (MPTMS) in order to promote the condensation of the silica precursor on the vitreophilic surface of the gold nanoparticles. By slightly modifying and adjusting the experimental conditions to our system, the nanoclusters were encapsulated in a thin silica shell (Protocol 19). The process was directly applied to our nanoclusters at the output of the assembly, *i.e.* no washing, concentrating or stabilizing step with a polymer was required. Note that the *L*-arginine should be present in the suspension in sufficient

concentration (20.7 mM) to allow a controlled catalysis of the TEOS hydrolysis but also to ensure a colloidal stability of the particles by fully covering their surface.

Protocol 19 – Encapsulation of nanoclusters with a silica shell in biphasic medium

Typically, 10 mL of the raspberry-like nanoclusters suspension were diluted into 200 mL of water in a 500-mL rounded-beaker. Then, 5 mL of an aqueous L-arginine solution (20.7 mM) were added to the medium under moderate stirring. 50 mL of cyclohexane containing 45 μ L of MPTMS were layered on the top of the aqueous suspension. After 1 h, the mixture was heated at 60°C and 5 mL of TEOS were introduced in the organic phase. The reaction was occurred for ~ 8 h. The mixture was then placed on a rotavapor at 50°C under vacuum to remove the cyclohexane. Finally the solution was allowed to cool down. In order to remove the excess of silane, the mixture was centrifuged at 3000 g for 10 min at 20°C. The supernatant, containing oligomers of silanes, was removed and the pellet, containing the encapsulated nanoclusters, was redispersed in ethanol by sonication. This washing step was repeated 6 times with the three last redispersions performed in water.

This protocol was applied to the different nanoclusters made of gold nanoparticles (from 10 to 50 nm). For the different nanoclusters, it was difficult to observe the thin layer of silica by TEM analyses (Figure II.57). However, indirect evidences came from their colloidal stability after each centrifugation cycle in ethanol medium and the fact that whatever the size of the gold satellites, they did not fall-in from the silica beads upon deposition on the carbon grid. Moreover, by using this procedure, the silica coating was directly performed at the output of the assembly, without any washing step. This allowed to not modify the particles density and avoid the agglomeration of the particles.

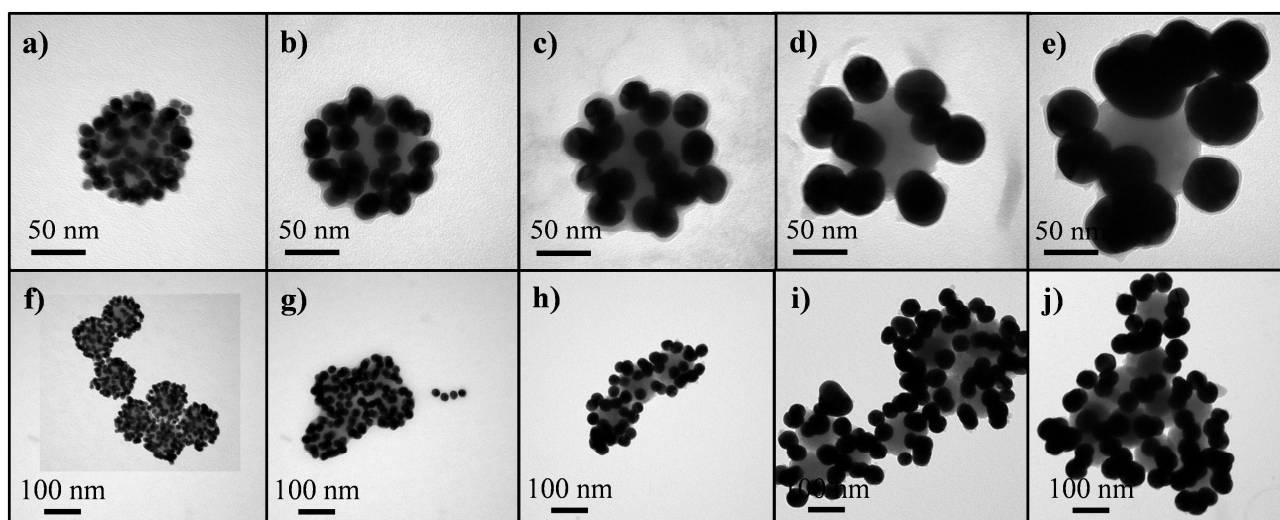


Figure II.57 – TEM images of the nanoclusters obtained by assembling gold nanoparticles of different diameters of (a, f) 10, (b, g) 20, (c, h) 30, (d, i) 40 and (e, j) 50 nm on the PEM-modified silica beads after encapsulation with a thin silica shell via the biphasic medium approach.

The extinction spectra of the different coated particles were measured (Figure II.58-green curves). It is clear that the silica encapsulation allowed a strong removal of the metallic particles excess. The contribution of the raspberry-like nanoclusters became dominant or more important in the absorption spectrum than the one observed before silica coating step (Figure II.55). The plasmon band was consistently shifted toward longer wavelengths in comparison to the free satellite particles (red curves). It is also shifted as the diameter of the metallic satellite increased. However, the long tails in the spectra indicated the presence of light scattering in the systems. The larger the satellite particles, the larger the scattering of the light.

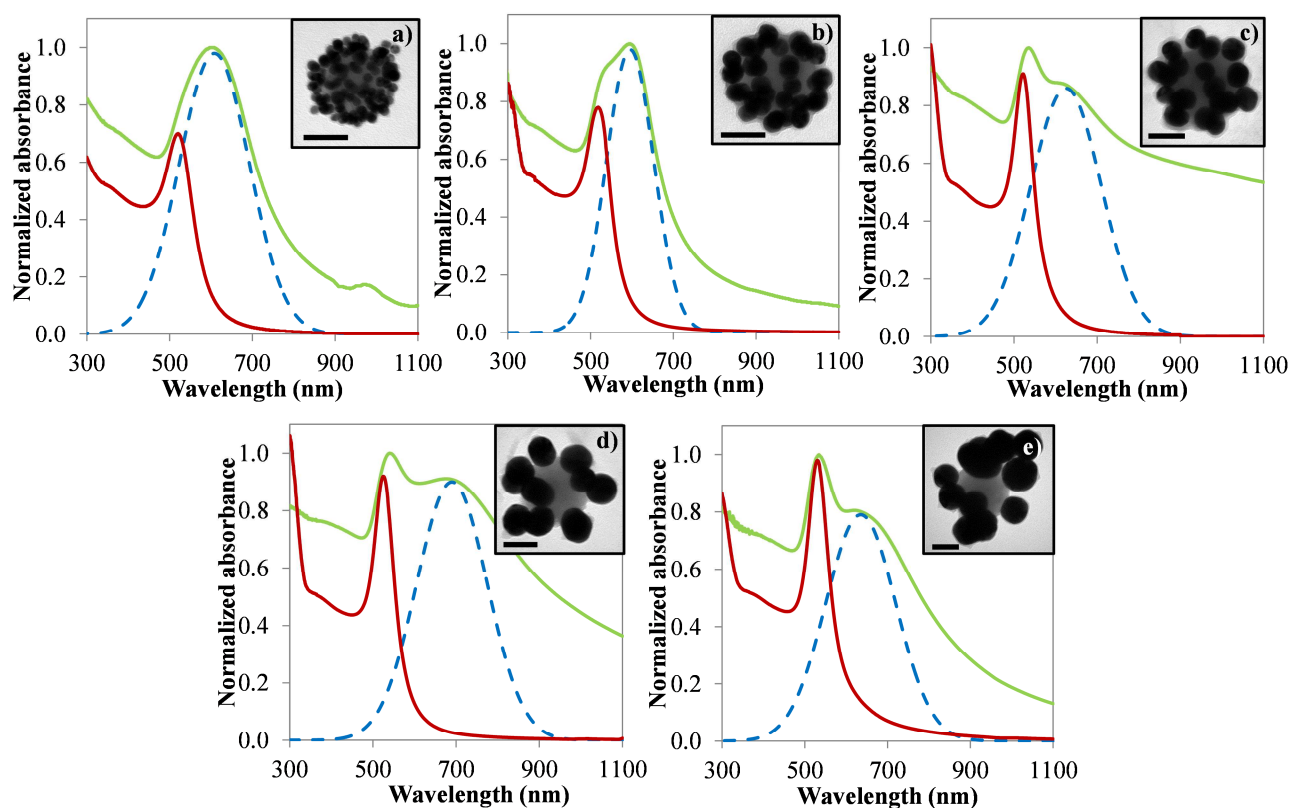


Figure II.58 – Normalized absorption spectra of Au nanoparticles alone (red curves) and silica coated raspberry-like nanoclusters obtained by assembling Au nanoparticles of different diameters of (a), 10, (b) 20, (c) 30, (d) 40 and (e) 50 nm on the PEM-modified silica beads (green curves) and their corresponding TEM images. The dashed blue curves correspond to the coupling mode contribution.

Analysis of the optical properties of the different nanoclusters by coupling 3D-STEM and SMS techniques, is still in progress. So far, the detailed analysis of the optical response of single silica-coated raspberry made of 10-nm gold nanoparticles was performed. The analysis was made for five different particles and the extinction cross-sections collected is consistent for all systems. The extinction cross-section of the raspberries exhibited a weak polarization dependence confirming the high and uniform quality of the coatings. Two of them are shown in Figure II.59. For both, a main plasmon band centered at 590 ± 30 nm was observed whatever the polarization angle. The amplitude of the cross-sections was evaluated to 18000 ± 700 nm². The strong red-shift of the main plasmon band characteristic of the 10-nm gold nanoparticles from 520 nm to ~ 590 nm clearly

evidenced the strong interaction between the metal particles onto the silica surface. Note that the band position was close to the one measured for the corresponding colloidal suspension (Figure II.59 - green curve).

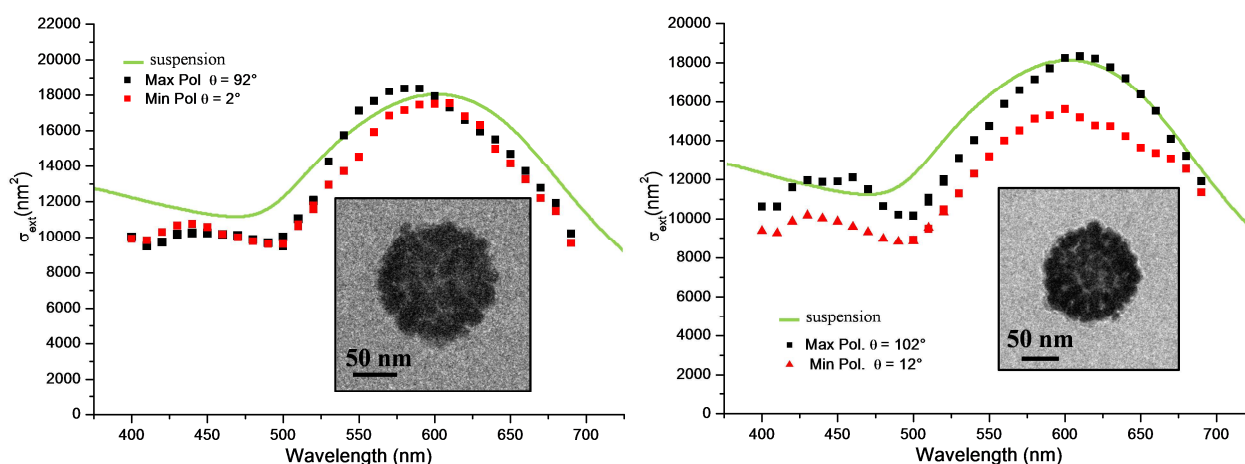


Figure II.59 - Optical extinction spectra of two silica-coated raspberry-like nanoclusters obtained by assembling 10-nm Au nanoparticles on PEM-modified silica beads, measured by SMS for two polarization angles (black and red squares) in each case and their corresponding TEM images. The green curve corresponds to the UV-Vis spectrum of the corresponding suspension.

The measured optical properties will be compared to the computed ones in the section C.3. Such detailed comparison would allow to understand the physical origins of the optical properties of the nano-raspberry and in particular the origin of the resonance observed.

C.2.4 Assembly of silver nanoprisms on PEM-modified silica beads

A similar study was also performed for silica spheres coated with silver nanoprisms. The LbL assembly approach allowed to deposit silver nanoprisms protected with MUA. As previously, the concentration of silica suspension was kept equal to $\sim 1.5 \times 10^{13}$ particles/L during the deposition process. At the output of the assembly, we observed the effective deposition of Ag nanoprisms onto the silica beads (Figure II.60-right). However, the deposition of silver nanoprisms was complicated by the strong anisotropy of the nanoprisms. Large and flat facets of the prisms promoted simultaneous interaction with two silica particles. In addition to their high anisotropy, the strong charge density provided by the MUA-functionalization induced a higher electrostatic repulsion between them and affected the coverage density on the silica beads. Consequently, the coating was far to be uniform from one object to another.

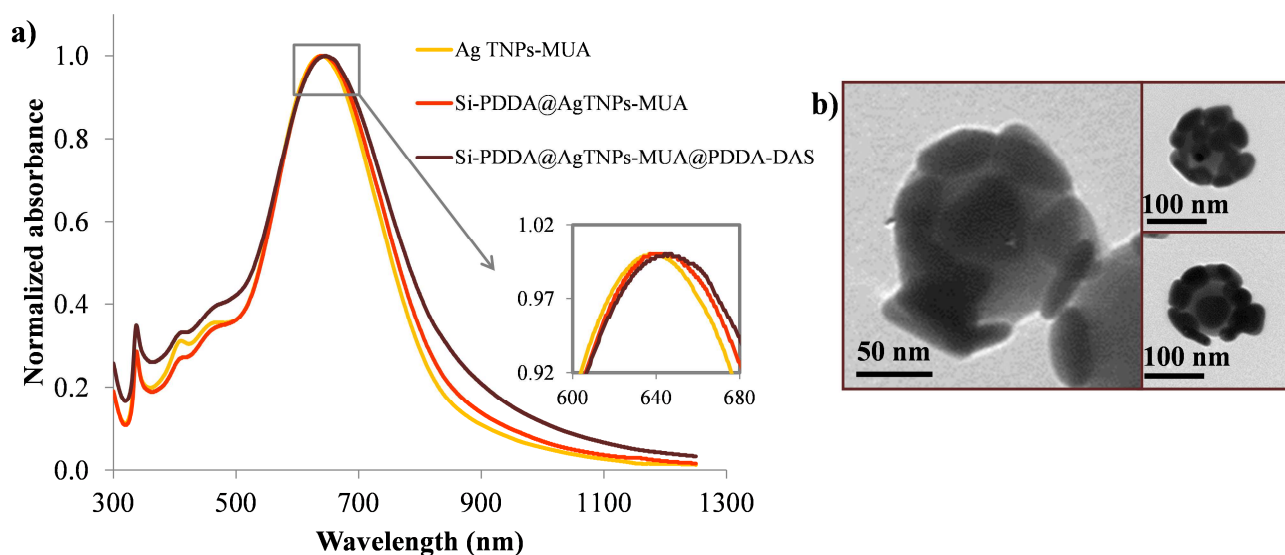


Figure II.60 – (Left) Normalized absorption spectra of MUA-coated Ag nanoprisms alone (Ag TNPs-MUA) and PDDA-stabilized nanoclusters before (Si-PDDA@AgTNPs-MUA) and after crosslinking with DAS (Si-PDDA@AgTNPs-MUA@PDDA-DAS); (Right) TEM images of some nanoclusters.

The optical measurements did not evidence strong change on the position of the dominant peak (Figure II.60-left). A broadening was observed due to the inhomogeneity of the nanoclusters and the existence of different coupling modes induced by the various kinds of interactions (tip-to-tip, face-to-face or tip-to-face).

C.2.5 Conclusion of the LbL assembly

The LbL approach allowed the assembly of metallic particles onto silica spheres of various sizes. It allowed to generate uniform and smooth coatings. This approach could be used for both gold and silver nanoparticles whatever their size and shape. However, the higher the dimensions of the satellites, the trickier the assembly of silver satellites. By stabilizing the nanoclusters with an additional layer of polymer or encapsulating them in a silica shell, the excess of satellite particles used to ensure the dense coverage of the silica cores could be removed. The optical responses of the final composite particles are dependent on the morphology of the satellites, their size and the number of particles deposited on the dielectric.

C.3 Comparison of the UV-Visible absorption spectra with theoretical simulations

The theoretical optical response of the raspberry-like nanoclusters previously synthesized was investigated in order to study and analyse the physical origin of their measured linear response.

In the case of the nanoparticles with a simple shape such as spheres or spheroids, analytical solutions could be found. However, when the morphology of the particles became more complex, the analytic calculations became tricky and numerical methods should be used. In order to model the optical spectra of the different raspberry-like nanoclusters, the Single Dipole Approximation

(SDA) modeling approaches was used. The numerical studies were investigated by the group of Pr. M. Albani (Metachem project partner) from the Department of information engineering and Mathematics (DIISM) of the University of Siena in Italy. They used a modeling approach [Vallecchi11] based on the SDA [Bohren83]. SDA could be thought as an approximation of the Discrete Dipole Approximation (DDA) which is usually used for clusters of particles in which only one dipole was assigned to each particle. In the simulations, it is assumed that the nanoclusters were illuminated by a linear polarized plane wave propagating in the z direction and polarized in the x direction. However the orientation of the coordinate system was arbitrary due to the isotropy of the nanoclusters. The scattered field was then expanded into spherical harmonics and the various equivalent multipoles of the nanocluster were derived [Hansen88].

The frequency position and intensity of the nanoclusters resonances were identified through the analysis of the extinction, scattering, and absorption cross-sections (C). The nature of the various resonances of the nanoclusters was recognized by decomposing the total scattering cross-section C_{sca} , into the contributions originated by the induced electric and magnetic dipole moments, C_{sca}^{Pe} and C_{sca}^{Pm} respectively, and that was associated with all the remaining higher order multipoles C_{sca}^{mps} which were plotted separately.

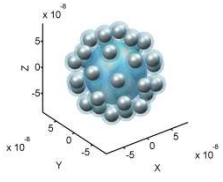
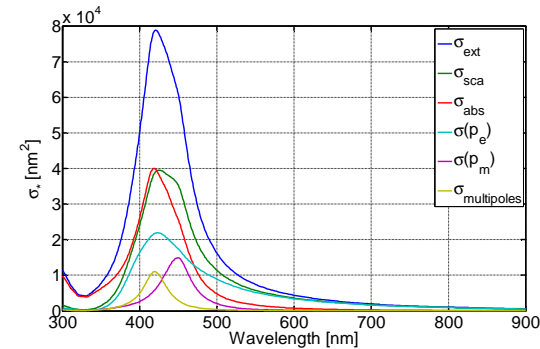
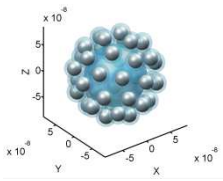
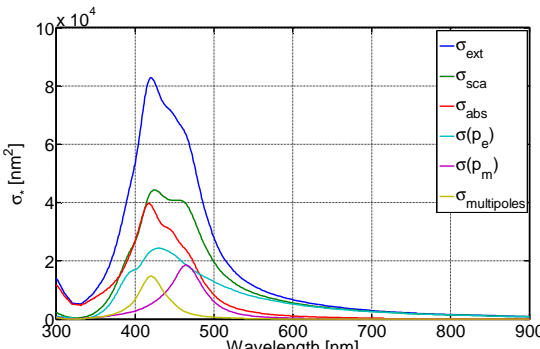
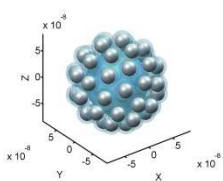
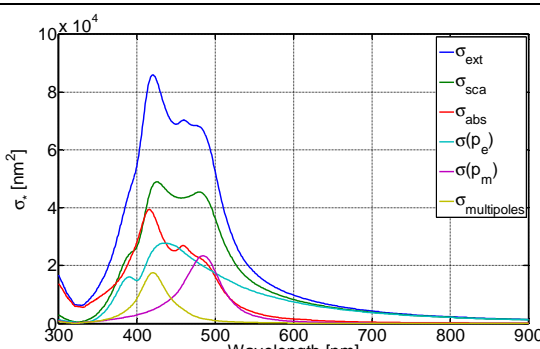
$$C_{sca} = C_{sca}^{Pe} + C_{sca}^{Pm} + C_{sca}^{mps} \quad (\text{II.6})$$

The theoretical extinction and scattering spectra of the raspberry-like nanoclusters constituted of the 26-nm silver nanoparticles attached on 106-nm silica beads were simulated. Due to some uncertainty regarding the exact number of satellites (*i.e.* the exact level of coverage) and their geometrical disposition around the silica core, the parametric analyses of the optical response of the silver nanocluster were performed at variable number of silver spherical satellites. Three configurations of the silver nanoclusters were investigated, and their corresponding simulated extinction and scattering cross-sections are shown in the Table II.4. Since the size of the silica core was fixed to 106 nm (*i.e.* close to the experimental value), the minimum interparticle distance between silver satellites was variable and reduced with increasing the number of satellites *i.e.* the level of coverage. Note that in all the simulations, the nanoclusters were considered as encapsulated in a 5-nm silica shell having a relative dielectric permittivity $\epsilon_{\text{SiO}_2} = 2.25$ and that the environment medium was water, with a relative dielectric permittivity $\epsilon_{\text{H}_2\text{O}} = 1.77$.

All considered nanocluster configurations exhibited significant levels of absorption. Nonetheless, plots from Table II.4 also show that the nanoclusters exhibited both an electric (turquoise curve) and a magnetic (purple curve) dipole resonance. For the nanoclusters with the smaller number of silver satellites, the electric and magnetic dipole resonances occurred at close frequencies, with the magnetic resonance slightly red-shifted with respect to the electric one. For

the high density of metallic particles, the magnetic resonance increasingly red-shifted, due to the stronger coupling between silver satellites, and its position apparently coincided with the red-shifted peak of the extinction. Moreover, the contribution of scattering to the total extinction of a nanocluster became predominant with respect to absorption for nanoclusters comprising a larger number of silver satellites. A weak higher order (quadrupole) contribution in all the nanocluster configurations was also observed. This quadrupole resonance was located at shorter wavelengths compared to both the magnetic and electric dipole resonances, even if the distances between these resonances reduced for decreasing number of silver satellites. The effect of this quadrupole moment was an increased absorption of the nanocluster near its resonance.

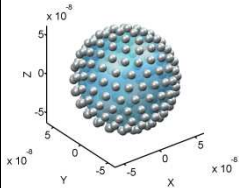
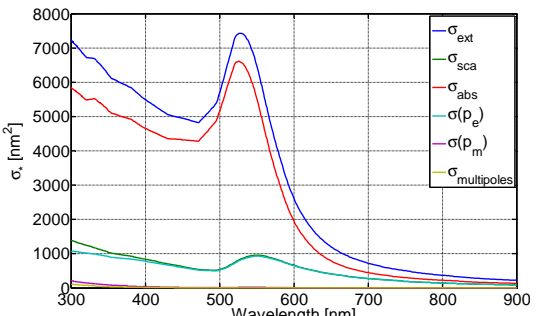
Table II.4 - Sample configurations of silver nanoclusters (NC) with 106-nm silica core and a variable number of 25-nm silver satellites encapsulated in a 5-nm shell and their corresponding simulated extinction, scattering and absorption cross-sections noted σ_{ext} , σ_{sca} , σ_{abs} , respectively. The total scattering cross-section is decomposed into the contributions originated by the induced electric ($\sigma(p_e)$) and magnetic dipole moments ($\sigma(p_m)$) and that associated with all the remaining higher order multipoles ($\sigma_{\text{multipoles}}$) which are plotted separately.

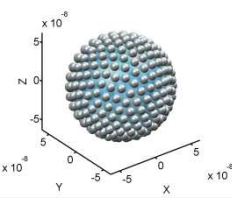
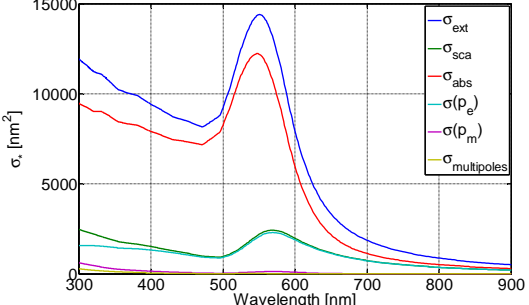
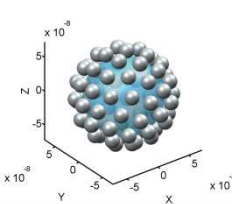
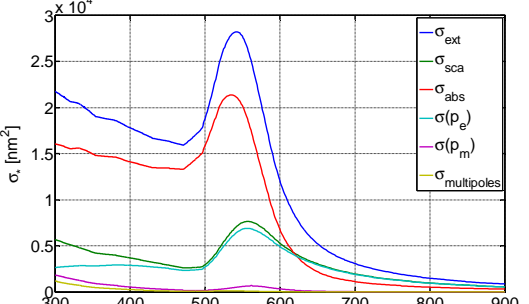
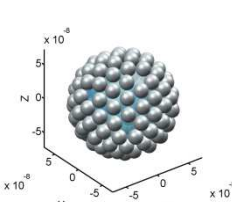
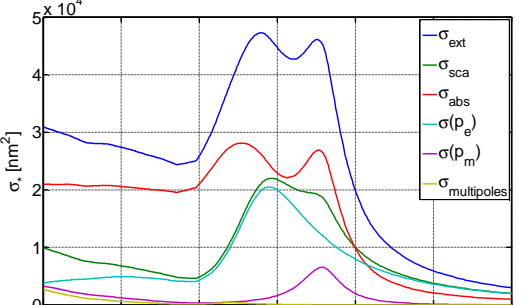
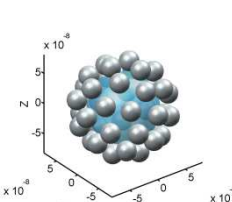
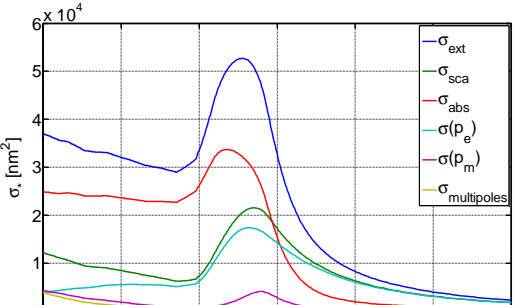
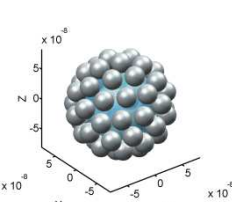
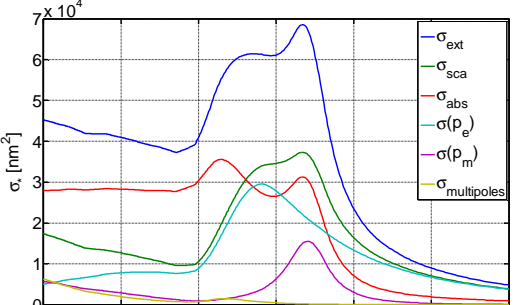
NC ID	Geometry sketch	Number of satellites	Surface-to-surface minimum distance (nm)	Cross-sections
Ag32		32	10.2	
Ag40		40	3.8	
Ag48		48	2.4	

Similarly to the case of silver nanoclusters, the parametric analyses of the optical response of each type of gold nanoclusters were performed with satellites of given different diameter, at variable numbers of satellites. The analysed gold nanocluster configurations are shown in Table II.5 with their relevant geometrical parameters and their corresponding simulated extinction and scattering cross-sections.

The optical response of all nanoclusters formed by smaller satellites, *i.e.* 10 and 20 nm, was dominated by absorption losses, which was not unexpected since absorption losses dominate also at the level of the single nanoparticles. Nanoclusters formed by satellites with diameter of 30 nm exhibited increasingly stronger electric and magnetic dipole resonances as the number of gold satellites became larger and the interparticle distance reduced. As in the silver nanoclusters, the magnetic resonance increasingly red-shifted in the more densely populated nanoclusters, due to the stronger capacitive coupling between the satellites, and its frequency position apparently coincided with the red-shifted peak of the extinction. However, for the considered nanocluster configurations, the scattering contribution became at most of the same level as that of absorption losses. Note also that the higher order (quadrupole) contributions were very weak in all the gold nanocluster configurations, and did not affect the nanocluster extinction, differently from the case of silver nanoclusters. This was likely the consequence of the absence of shell enclosures around the nanoparticles that allowed a more compact arrangement of nanoparticles around the core and provided a smaller overall nanocluster size for a given number of satellites.

Table II.5 - Sample configurations of gold nanoclusters with a 106-nm diameter silica core with a variable number of satellites and satellite radii and their corresponding simulated extinction, scattering and absorption cross-sections noted σ_{ext} , σ_{sca} , σ_{abs} , respectively. The total scattering cross-section is decomposed into the contributions originated by the induced electric ($\sigma(p_e)$) and magnetic dipole moments ($\sigma(p_m)$) and that associated with all the remaining higher order multipoles ($\sigma_{\text{multipoles}}$) which are plotted separately.

NC ID	Geometry sketch	Number of satellites	Satellite diameter (nm)	Surface-to-surface minimum distance (nm)	Cross-sections
Au10-180		180	10	4.68	

Au10-300		300	10	1.26	
Au20-72		72	20	7.2	
Au20-120		120	20	1.15	
Au30-40		40	30	7.39	
Au30-56		56	30	1.42	

The analyses have shown that size of the metallic nanoparticles have a great impact on the optical response of nanoclusters due to the size dependent damping constant of metals. The silver nanoclusters, constituted of 25-nm silver satellites, and gold nanoclusters formed by satellites with diameter of 30 nm exhibited increasingly stronger electric and magnetic dipole resonances as the number of satellites became larger. The magnetic resonance was shown to increasingly red-shift in the more densely populated nanoclusters, due to the reduced distances and stronger coupling between the satellites, and to produce a red-shifted peak of the extinction. However, while for the considered silver nanoclusters the contribution of scattering could become predominant with respect to absorption for nanoclusters comprising the larger number of satellites, in the gold nanocluster configurations the scattering contribution became at most of the same level as that of absorption losses.

Experimentally, we recorded the global extinction spectrum of a population of nanoclusters. We could not dissociate the absorption and the scattering contributions to the total extinction of the nanoclusters. The simulations performed allowed us to understand the optical response of the raspberry-like nanoclusters. The extinction spectrum could be decomposed on the scattering cross-section into electric, magnetic and multipolar contributions. By comparing the theoretical and experimental data we could explain the observed evolution of the optical responses of the nanoclusters in function of the composition, size and level of coverage of the satellite particles attached on central silica beads.

In the case of gold, the calculations revealed that for the small gold nanoparticles, the extinction spectrum of the nanoclusters was dominated by the absorption contribution (Figure II.61). When the number of particles adsorbed on the silica increased, a red-shift was obtained as experimentally observed for the 10- and 20-nm gold nanoclusters. When the size of the gold particles became larger, the scattering became predominant. Additionally, the higher the coverage density, the higher the intensity and the red-shift of the magnetic contribution, due to the stronger coupling between the nanoparticles when their interparticle distance became smaller. These predictions confirmed the experimental observations. The perpetual observed red-shift of the plasmon band was due to the intensification of the scattering contribution (both electric and magnetic resonances) which shifted to longer wavelengths when the coupling between particles increased. It also allowed us to conclude that the apparition of the shoulder at longer wavelengths is due attributed to the magnetic contribution.

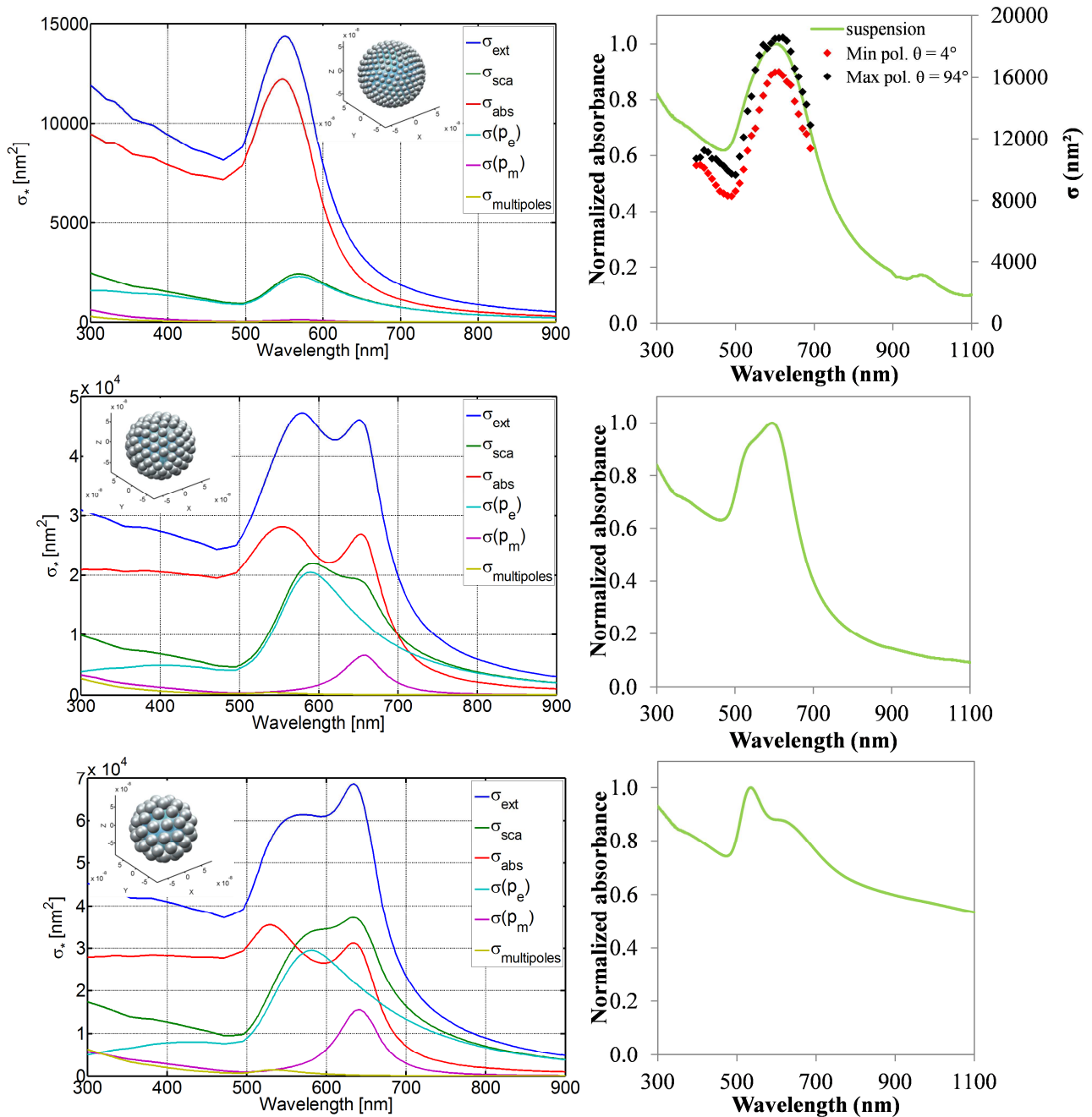


Figure II.61 – Comparison of (Left) theoretical and (right) experimental spectra of silica coated nano-raspberries made of (top) 10- (middle) 20- and (bottom) 30-nm gold nanoparticles.

In the case of silver, although the total extinction spectrum was dominated by absorption losses, both electric and magnetic resonances also contributed whatever the number of silver particles attached onto the silica beads. The higher the coverage density of the nanoclusters, the higher the red-shift of the magnetic resonance compared to the electric one. That was in agreement with the experimental optical responses obtained for silver nanoparticles and the new red-shifted plasmon band could be attributed to the intensification of the scattering contribution which became predominant when a large number of satellites were attached on the silica (Figure II.62).

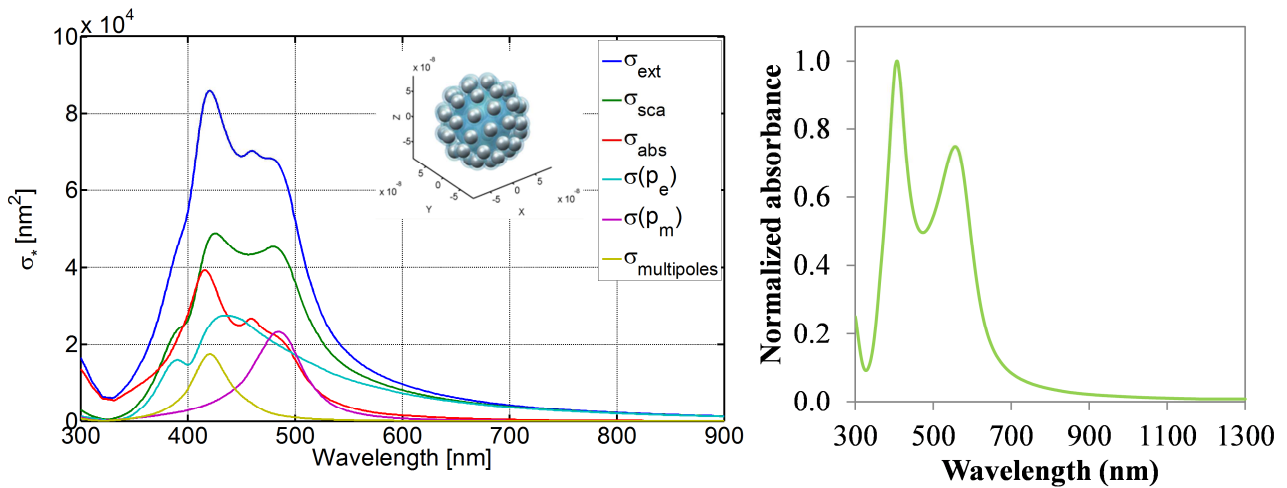


Figure II.62 – Comparison of (Left) theoretical and (right) experimental spectra of silica coated nano-raspberries made of 26-nm silver nanoparticles.

D. Conclusion

Electric and/or magnetic nanoresonators of size below than 150 nm (nearly at $\lambda/4$) with narrow size distribution have been obtained by associating plasmonic particles onto the surface of silica spherical particles. A higher density of metallic particles was successfully obtained by using self-assembly strategy based on layer-by-layer electrostatic approach instead of the direct chemistry functionalization approach. By using such route, the integrity of the metallic nanoparticles was preserved (no coalescence) due to the presence of a thin polymeric spacer (1 - 2 nm). The method enables to produce nanoclusters in sufficient amounts for the preparation of extended dense 3D arrays. The comparative analysis of the theoretical and experimental of their optical response strongly suggests that the nanoclusters exhibit optical magnetism in the visible frequencies.

References

- [Ai02] Ai H., Fang M., Jones S.A., Lvov Y.M. *Biomacromolecules*, 2002. 3(3), p. 560
- [Alivisatos96] Alivisatos A.P., Johnsson K.P., Peng X., Wilson T.E., Loweth C.J., Bruchez Marcel P. J., Schultz P.G. *Nature (London)*, 1996. 382, p. 609
- [Amendola10] Amendola V., Bakr O., Stellacci F. *Plasmonics*, 2010. 5(1), p. 85
- [Ashayer08] Ashayer R., Mannan S.H., Sajjadi S. *Colloids Surf, A*, 2008. 329, p. 134
- [Bogush91] Bogush G., IV C.Z. *J. Colloid Interface Sci.*, 1991. 142(1), p. 1
- [Bohren83] Bohren C. *Absorption and scattering of light by small particles*. John Wiley & Sons, Incorporated, 1983
- [Brinker90] Brinker C. J. Scherer G.W. *Sol-Gel Science, 1st Edition The Physics and Chemistry of Sol-Gel Processing*. Academic Press, 1990, 912 p.
- [Brousseau III99] Brousseau III L.C., Novak J.P., Marinakos S.M., Feldheim D.L. *Adv. Mater.*, 1999. 11(6), p. 447
- [Conway98] Conway J.H., Sloane N.J.A. *Sphere Packing, Lattices and Groups*. 1998
- [Decher91] Decher G., Hong J.D. *Makromolekulare Chemie. Macromolecular Symposia*, 1991. 46(1), p. 321
- [Decher97] Decher G. *Science*, 1997. 277(5330), p. 1232
- [Desert11] Desert A. *Colloides hybrides silice/polystyrene de morphologie controlee*. Ph.D. thesis, University of Bordeaux 1, 2011
- [Desert12] Desert A., Chaduc I., Fouilloux S., Taveau J.C., Lambert O., Lansalot M., Bourgeat-Lami E., Thill A., Spalla O., Ravaine S., Duguet E. *Polym. Chem.*, 2012. 3(5), p. 1130
- [Hansen88] Hansen J.E. *Spherical near-field antenna measurements*. Peter Peregrinus Ltd., 1988. ISBN: 0-86341-110-X
- [Hao04] Hao E., Schatz G.C. *J. Chem. Phys.*, 2004. 120, p. 357
- [Hartlen08] Hartlen K.D., Athanasopoulos A.P.T., Kitaev V. *Langmuir*, 2008. 24(5), p. 1714
- [Hassan13] Hassan N., Cabuil V., Abou-Hassan A. *Angew. Chem., Int. Ed.*, 2013. 52(7), p. 1994
- [Jain07] Jain P.K., Huang W., El-Sayed M.A. *Nano Lett.*, 2007. 7, p. 2080
- [Jain10] Jain P.K., El-Sayed M.A. *Chem. Phys. Lett.*, 2010. 487, p. 153
- [Jankiewicz12] Jankiewicz B., Jamiola D., Choma J., Jaroniec M. *Adv. Colloid Interface Sci.*, 2012. 170(1-2), p. 28
- [Karg07] Karg M., Pastoriza-Santos I., Perez-Juste J., Hellweg T., Liz-Marzan L.M. *Small*, 2007. 3, p. 1222
- [Kim06] Kim J.H., Kim J.S., Choi H., Lee S.M., Jun B.H., Yu K.N., Kuk E., Kim Y.K., Jeong D.H., Cho M.H., Lee Y.S. *Anal. Chem.*, 2006. 78, p. 6967
- [Liang11] Liang Z., Liu Y., Ng S.S., Li X., Lai L., Luo S., Liu S. *J. Nanopart. Res.*, 2011. 13, p. 3301
- [Liu07] Liu X., He J. *J. Colloid Interface Sci.*, 2007. 314(1), p. 341
- [Loweth99] Loweth C.J., Caldwell W.B., Peng X., Alivisatos A.P., Schultz P.G. *Angew. Chem., Int. Ed.*, 1999. 38, p. 1808
- [Maye09] Maye M.M., Nykypanchuk D., Cuisinier M., van der Lelie D., Gang O. *Nat. Mater.*, 2009. 8, p. 388
- [Metwalli06] Metwalli E., Haines D., Becker O., Conzone S., Pantano C. *J. Colloid Interface Sci.*, 2006. 298(2), p. 825

- [Mornet02] Mornet S. *Synthese et modification chimique de la surface de nanoparticules de maghemite a des fins d'applications biomédicales*. Ph.D. thesis, University of Bordeaux I, 2002
- [Muhlig11] Mühlig S., Cunningham A., Scheeler S., Pacholski C., Bürgi T., Rockstuhl C., Lederer F. *ACS Nano*, 2011. 5(8), p. 6586
- [Nakamura08] Nakamura M., Ishimura K. *Langmuir*, 2008. 24, p. 5099
- [Novak01] Novak J.P., Nickerson C., Franzen S., Feldheim D.L. *Anal. Chem.*, 2001. 73(23), p. 5758
- [Pham02] Pham T., Jackson J.B., Halas N.J., Lee T.R. *Langmuir*, 2002. 18(12), p. 4915
- [Reinhardt13] Reinhardt N. *Modification chimique de surface de nanoparticules de silice pour le marquage d'ADN dans des lipoplexes*. Ph.D. thesis, University of Bordeaux 1, 2013
- [Romo-Herrera11] Romo-Herrera J.M., Alvarez-Puebla R.A., Liz-Marzan L.M. *Nanoscale*, 2011. 3, p. 1304
- [Salgueirino-Maceira03] Salgueirino-Maceira V., Caruso F., Liz-Marzán L.M. *The Journal of Physical Chemistry B*, 2003. 107(40), p. 10990
- [Schuetz03] Schuetz P., Caruso F. *Adv. Funct. Mater.*, 2003. 13(12), p. 929
- [Schulzendorf11] Schulzendorf M., Cavellius C., Born P., Murray E., Kraus T. *Langmuir*, 2011. 27(2), p. 727
- [Sheikholeslami13] Sheikholeslami S.N., Alaeian H., Koh A.L., Dionne J.A. *Nano Lett.*, 2013. 13(9), p. 4137
- [Spasova05] Spasova M., Salgueirino-Maceira V., Schlachter A., Hilgendorff M., Giersig M., Liz-Marzan L.M., Farle M. *J. Mater. Chem.*, 2005. 15, p. 2095
- [Stoeber68] Stoeber W., Fink A., Bohn E. *J. Colloid Interface Sci.*, 1968. 26(1), p. 62
- [Vallecchi11] Vallecchi A., Albani M., Capolino F. *Opt. Express*, 2011. 19(3), p. 2754
- [Wang08] Wang L., Xia L., Li G., Ravaine S., Zhao X.S. *Angew. Chem., Int. Ed.*, 2008. 47, p. 4725
- [Westcott98] Westcott S.L., Oldenburg S.J., Lee T.R., Halas N.J. *Langmuir*, 1998. 14(19), p. 5396
- [Wong03] Wong S., Kitaev V., Ozin G.A. *J. Am. Chem. Soc.*, 2003. 125(50), p. 15589
- [Xue07] Xue J., Wang C., Ma Z. *Mater. Chem. Phys.*, 2007. 105, p. 419
- [Yan09] Yan B., Thubagere A., Premasiri W.R., Ziegler L.D., Dal Negro L., Reinhard B.M. *ACS Nano*, 2009. 3(5), p. 1190. PMID: 19354266
- [Yi04] Yi G.R., Manoharan V., Michel E., Elsesser M., Yang S.M., Pine D. *Adv. Mater.*, 2004. 16(14), p. 1204
- [Zhang12] Zhang X., Jiang C., Cheng M., Zhou Y., Zhu X., Nie J., Zhang Y., An Q., Shi F. *Langmuir*, 2012. 28(18), p. 7096

Overall conclusion

The main goal of this study led to the fabrication of a new 3D isotropic metamaterial based on the design of nanoclusters proposed by Simovski and Tretyakov. Our strategy led to the fabrication of nanoclusters by arranging gold or silver nanoparticles onto a central dielectric particle with an overall diameter close to 150 nm. This particular type of architecture allowed the control of magnetic and electric resonances in the visible regime.

In the first chapter, the synthesis of a number of different metallic nanoparticles which could be scaled up for mass production had been achieved (Figure 1-b). Silver spherical particles of diameter larger than 20 nm was achieved by a polyol approach which was a reliable strategy able to provide metallic particles in gram-scale in aqueous solution. Gold spherical nanoparticles of diameter ranging from 10 to 50 nm were produced via a colloidal seed-mediated route. Silver nanoprisms were also produced via a seed-mediated growth approach. We improved the synthetic method which enabled large-scale production in order to control their size within a narrow distribution. By comprehensively exploring the role of the seeds and organic stabilizers in the growth rates process, the best conditions for producing uniform Ag nanoprisms with tunable sizes have been found and a growth mechanism was proposed. The side-face structure of the triangular nanostructure was determined in detail using electron tomography and HRTEM. It has been found that they are built-up by {100} side-facets with a single parallel twin plane. This approach provides also a route to synthesize Ag nanodisks and Au nanocages and Ag/Au triangular nanoboxes in high yields (*cf.* Annex 2).

In chapter II, these optimized metallic nanoparticles were then self-assembled on preformed silica beads in order to elaborate raspberry-like nanoclusters via two approaches:

(i) Direct chemistry functionalization. Although many structures similar to the desired nanoclusters were observed, the surface coverage was not always 100 % homogeneous and complete, but more importantly their colloidal stability was fairly poor and the purification of single clusters was difficult.

(ii) Exploiting electrostatic interactions induced by deposition of a polyelectrolytes multilayer. This approach allowed to successfully produce the raspberry-like nanoclusters made of the different metallic particles (Figure 1). High density of metallic particles onto the dielectric core was obtained. Their architecture were close to the desired geometry and size of the isotropic resonators proposed by theoretical investigations of C. Simovski. The interest of this approach also lay in its potential to graft randomly anisotropic nanoparticles such as triangular silver particles. The as-obtained nanoclusters were compatible with a biphasic silica coating process and thus were easily coated

with silica of arbitrary thickness without any purification while preserving their architecture. This outer silica thin shell allowed to improve their mechanical and colloidal stability for further 3D assembly. The method also enabled to produce nano-objects in sufficient amounts for the preparation of extended dense arrays.

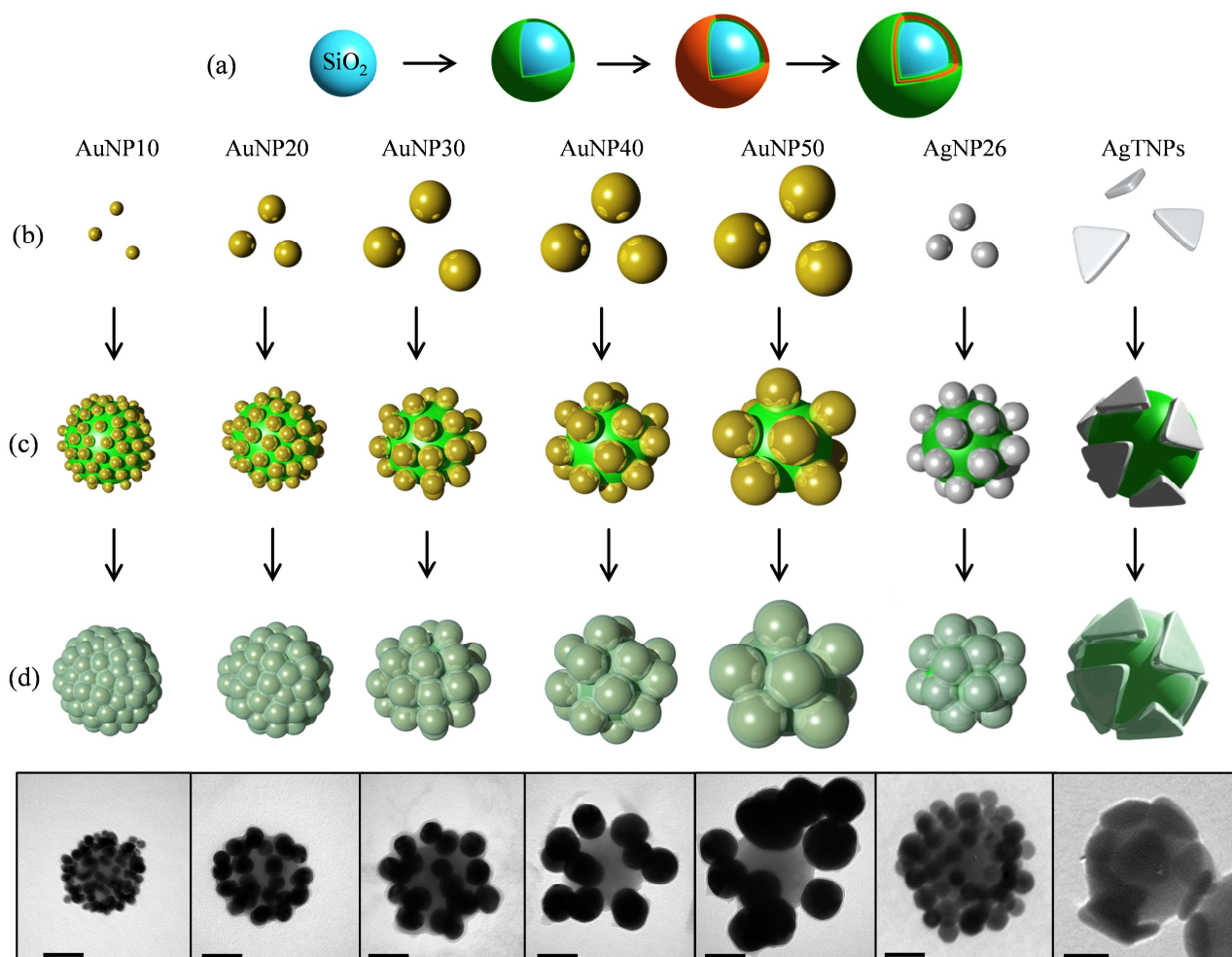


Figure 1 – Schematic illustration summarizing the main colloidal objects elaborated in this thesis. (a) Synthesis and surface modification of the silica beads through the LbL process. (b) Synthesis of the different metal satellite nanoparticles. (c) Assembly of the metal satellite nanoparticles on the modified silica beads to form raspberry-like nanoclusters. (d) Silica coating of the raspberry-like nanoclusters and (Down) TEM images of the silica-coated gold raspberries and uncoated silver raspberries. Scale bar = 50 nm.

The optical characteristics of the different as-obtained nanoclusters have been experimentally investigated using conventional UV-spectroscopy and/or using SMS technique. In this latter case, the results were correlated to the individual morphology of the nanocluster determined from their 2D-TEM images. The measured optical responses were compared to the computed ones. Good reproduction of the measured spectra was obtained in the case of the nano-raspberries made of spherical silver or gold particles in term of spectral position, with the numerical model using the TEM measured size of the particles as an input and taking into account the chemical environment. The comparative study allowed us to conclude that the nanoclusters exhibit both electric and magnetic resonances at optical frequencies. To confirm these results, it will be interesting to

experimentally probe and quantify these two contributions. From the recent works of Dionne *et al.*, it would be possible to directly probe, the electric and magnetic contributions of a single raspberry-like nanocluster by using the scattering dark-field microscopy coupled with a spectrometer [Sheikholeslami13].

Preliminary experiments in order to obtain a dense 3D-metamaterial made of the nanoclusters exhibiting magnetic response have been carried out but need further improvements.

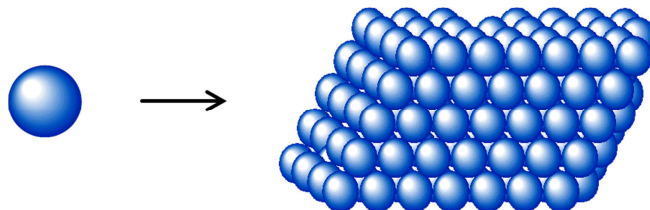


Figure 2 – Schematic illustration of an extended assembly of nano-objects acting as building blocks.

Among the different techniques existing to elaborate a three dimensional extended assembly of nanoparticles (*e.g.* sedimentation, electrophoresis, spin-coating, drying ...), the microfluidic based processes, developed by J. Leng and coworkers at LOF, allows to build-up, in a short time, homogeneous dense materials from a diluted suspension of nanoparticles [Angly13, Masse13]. The principle of this process is described in Annex 3. Figure 3 shows SEM images of a dense material made of silver nano-raspberries ($\text{SiO}_2@Ag_n@SiO_2$).

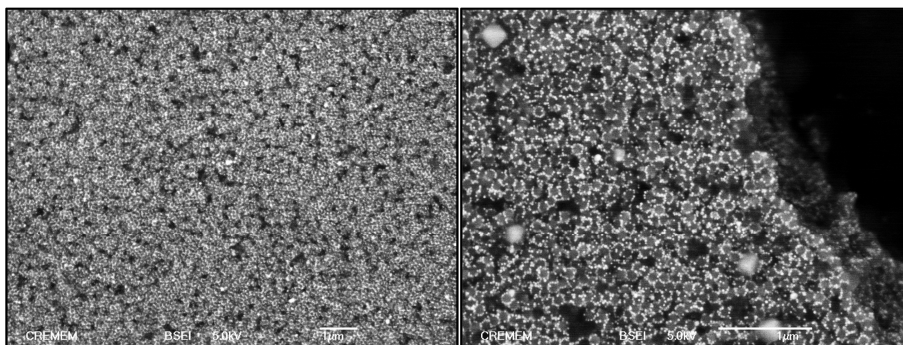


Figure 3 - SEM images of the extended assembly obtained from the dilute suspension containing the first generation of raspberry-like nanoclusters encapsulated in a silica shell ($\text{SiO}_2@Ag@SiO_2$).

The raspberries form a tightly-packed state with extended dimensions but many defects can be observed that induce a random organization of the nanoclusters in the 3D material. An optimization of the process is in progress to improve the local order of the nanoresonators, likely to be a key issue of self-assembled metamaterials. The original optical properties of the metamaterial will be then measured by ellipsometry in order to extract the complex refractive index of the sample. Such dense materials integrating several nano-objects with dimensions much lower than the wavelength of light may display promising electromagnetic properties and thus innovative applications.

Additionally to the applications for metamaterials, the nano-raspberries exhibiting local electromagnetic enhancement excited from collective oscillations of free electrons on a highly roughened metal surface can be very interesting for applications in surface-enhanced Raman spectroscopy (SERS). Preliminary tests of detection of a probe molecule by SERS have been performed with the raspberry-like nanoclusters containing the 10-nm gold nanoparticles. The experimental details and the first results obtained are described in Annex 4. Due to the unique structures such as their rough surface, the as-prepared nano-raspberries appear to be very promising as high-performance SERS substrates.

The simple and scalable colloid approach developed in this study opens avenues for the development of advance materials. In the future, it will allow to fabricate building blocks made of more complex metallic components such as dimer or trimers, nano-stars onto dielectric or magnetic beads. It will also allow the development of building blocks made of a controlled number of metallic nanocrystals well-positioned in relation to each other onto a central dielectric core. This is of strong interest, in particular in the case of nanoclusters made of silver nanoprisms. By substituting the conventional silica beads by silica beads bearing “sticky patches” it will allow to develop novel structure and new building units (Figure 4).

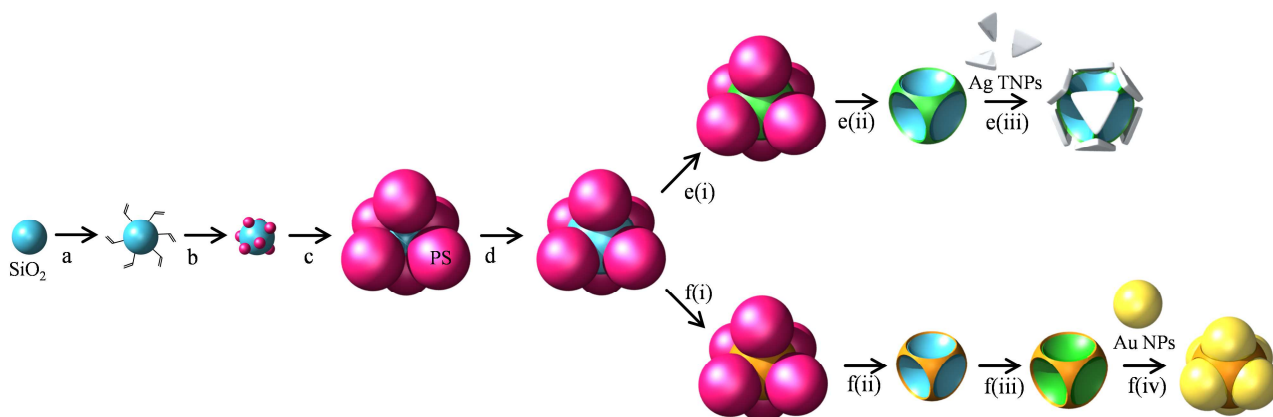


Figure 4 - Schematic illustration of the elaboration of raspberry-like nanoclusters having a controlled number of satellites attached on the silica beads. (a) surface modification of the silica beads with a coupling agent, (b and c) nucleation-growth of PS nodules on the silica by seeded emulsion polymerization, (d) growth of the central silica, (e(i)) surface modification of the available silica with *e.g.* an aminosilane, (e(ii)) removal of the PS nodules leaving their imprints, (e(iii)) assembly of only eight silver nanoprisms on the surface of the modified silica. Another possible strategy: (f(i)) surface modification of the available silica with *e.g.* a passivation agent, (f(ii)) removal of PS nodules, (f(iii)) surface modification of pristine silica with *e.g.* an aminosilane and (f(iv)) assembly of six gold nanoparticles on the patches.

We have developed in the group a synthetic approach that allows to produce large quantities of colloidal entities made of a central silica core surrounded by a precise number of polystyrene nodules. These multipod-like structures could be used as precursors for the synthesis of spherical particles with a precise number of well-located patches at their surface, which is based on the use of

the PS nodules as protective masks. The further adsorption of satellite particles on the “inter-patches” or “patches” areas should provide the next generation of raspberry-like nanoclusters. Their 3D assembly into complex ordered materials will provide unique chances for original functional structures and open the development to a novel domain of “bottom-up” chemistry with enough potential to compete with the “top-down” approaches of nanolithography.

References

- [Angly13] Angly J., Iazzolino A., Salmon J.B., Leng J., Chandran S.P., Ponsinet V., Desert A., Le Beulze A., Mornet S., Treguer-Delapierre M., Correa-Duarte M.A. *ACS Nano*, 2013. 7(8), p. 6465
- [Desert11] Desert A. *Colloides hybrides silice/polystyrene de morphologie controlee*. Ph.D. thesis, University of Bordeaux 1, 2011
- [Desert12] Desert A., Chaduc I., Fouilloux S., Taveau J.C., Lambert O., Lansalot M., Bourgeat-Lami E., Thill A., Spalla O., Ravaine S., Duguet E. *Polym. Chem.*, 2012. 3(5), p. 1130
- [Masse13] Masse P., Mornet S., Duguet E., Treguer-Delapierre M., Ravaine S., Iazzolino A., Salmon J., Leng J. *Langmuir*, 2013. 29(6), p. 1790
- [Sheikholeslami13] Sheikholeslami S.N., Alaeian H., Koh A.L., Dionne J.A. *Nano Lett.*, 2013. 13(9), p. 4137
- [Thill12] Thill A., Desert A., Fouilloux S., Taveau J.C., Lambert O., Lansalot M., Bourgeat-Lami E., Spalla O., Belloni L., Ravaine S., Duguet E. *Langmuir*, 2012. 28(31), p. 11575

Annexes

Annex 1: Characterization techniques

- *UV-Visible spectroscopy*

Metal nanoparticles exhibit specific color and resonance modes in the visible range. UV-visible spectroscopy provides valuable information regarding size, shape and aggregation of nanoparticles. The absorption spectra were recorded in the range of 300-1300 nm with an UV-3600 Shimadzu UV-Vis-NIR spectrophotometer. Ten-mm optical path length plastic or quartz cells were used. The data were recorded and treated with the UVProbe software.

- *Inductively Coupled Plasma Optical Emission Spectrometry (ICP-OES)*

The number of silver particles per batch was indirectly determined via chemical analyses performed by ICP-OES on a Varian 720-ES spectrometer at the ICMCB. This physical method enables the detection of trace metals. This emission spectroscopy uses the inductively coupled plasma to produce excited atoms and ions that emit electromagnetic radiation at wavelengths characteristic of a particular element. In the case of silver, the characteristic wavelengths are 328.068 nm and 279.553 nm. The intensity of the emission at these wavelengths is indicative of the ionic silver concentration of the sample.

In order to obtain reliable results, 5 measures per sample were performed. One measure required 5 mL of solution and the minimum concentration of silver in solution had to be 0.5 mg/L. In plastic Falcon tube, the silver nanoparticles were beforehand dissolved by adding a small volume of regia aqua in the colloidal suspension. To get back to the amount of silver nanoparticles per batch, it was necessary to suppose that all silver ions present in sample after dissolution treatment came from metallic nanoparticles and they exhibited the same dimensions.

- *Diffuse Reflectance Infrared Fourier Transform Spectroscopy (DRIFT)*

The DRIFT spectroscopy allows to characterize the different species adsorbed and/or grafted on the surface of the nanoparticles by measuring the bending and stretching vibrations of molecules having specific functional groups when they are excited by an infrared beam. These vibrations produce bands in well-defined regions characteristic of specific class of compounds.

A volume of the EDPS-modified silica nanoparticles suspension was dried at 100°C. 9 mg of the dried sample were added to 281 mg of dessicated KBr (spectroscopy grade). The mixture was grinded in an agate mortar and the powder was deposited on the conical sample holder. The sample was then introduced into the Bruker IFS Equinox 55 spectrometer and the measurements were performed in a Selector Graseby Specac reflection cell. After 30 min of degassing, the installation

of the sample in the cell, the infrared spectrum was recorded by the acquisition of 120 measurements with a resolution of 2 cm^{-1} .

- **Titrimetry**

Measure and regulation of pH

To evaluate the influence of the pH during the growth step of silver nanoprisms and to maintain the solution at a constant pH value, a Mettler Toledo Titrator T70 equipped with a DGi115-SC electrode was used. The nature of reagent used to regulate the pH, its concentration (an acid such as HNO_3 0.1M or a base such as NaOH 0.1M) and the type of sensor used with its measure unity (mV, pH) had first to be defined and the stirring rate was maintained constant throughout the measure. A curve calibration of the pH electrode was determined with three standard solutions (buffers at pH 4.01, 7.01 and 10.1). A pre-titration step was required to bring the solution to the desired potential *i.e.* the desired pH value. Once the desired potential was reached, a step of regulation was set to maintain the desired potential in solution, insofar as possible. For that, it was necessary to define a regulation range but also the trend (positive or negative) of the signal of the sensor when the reagent was added in the sample. The measure and regulation of the potential were stopped few minutes after the end of the growth of silver nanoprisms. All the values were recorded by using the *LabX light titration* software.

Measure of pAg

The concentration of free Ag^+ ions present in solution was determined by substituting the calomel electrode by a perfectION™ combination Silver/Sulfide electrode from Mettler Toledo. An electrode potential depending of the amount of free silver ions in solution was developed across the detection membrane and was measured against a constant reference potential with a T70 Titrator from Mettler Toledo). The measured potential was described by the Nernst equation:

$$E = E_0 + S \times \log(A)$$

where E is the measured electrode potential, E_0 the reference potential (a constant), A the silver ion activity level in solution and S the electrode slope (about 57 mV per decade for silver). The silver ion activity is related to free silver ion concentration, C_f , by the activity coefficient, y_i .

$$A = y_i \times C_f$$

Beforehand to determine the concentration of Ag^+ ions in solution, it was necessary to determine a calibration curve with three standard solutions that bracket the expected sample range

and differ in concentration by a factor of ten. The electrode potentials of standard solutions were measured and plotted on the linear axis against their concentrations on the log axis (Figure A.1).

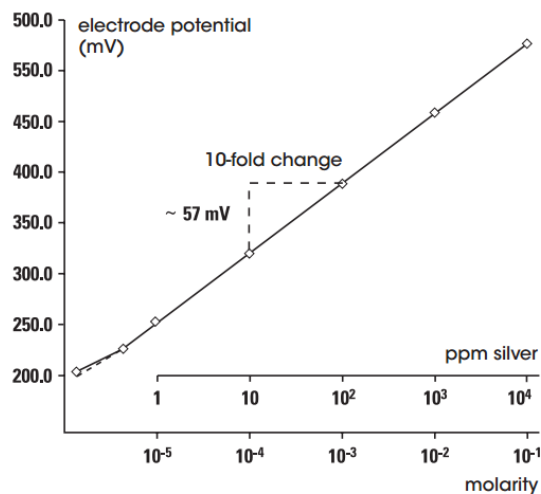


Figure A.1 - Typical silver calibration curve.

Note that the reproducibility was limited by factors such as temperature fluctuations, drift and noise. With hourly calibrations, direct silver measurements reproducible to 2% could be obtained.

- *Electron microscopy*

Transmission Electron Microscopy (TEM)

Electron microscopies were used to collect information on the morphology, the structure and the composition of the elaborated nano-objects. The studied objects by TEM were observed in image mode to determine their dimensions and in diffraction mode to determine the organization and orientation of the crystallites constituting the material. Complementary studies by High Resolution TEM (HRTEM) were also performed and allowed to visualize the material at atomic scale and thus to determine directly on the image the nature of present planes.

Scanning Transmission Electron Microscopy (STEM)

Another mode of illumination used in this study is the scanning transmission. Contrarily to TEM mode which used a parallel beam in the formation of images, in the STEM mode, the beam was focalized on the sample and it scanned uniformly the sample. In this mode, by using two kinds of detectors, we could count transmitted electrons from different angles in order to form images which could contain complementary information. Two images could be simultaneously acquired by collecting on the one hand, the electrons diffused at a certain angle, detected with an Angular Dark Field detector (ADF) and on the other hand the electrons transmitted or diffused at very shorter angles detected with a circular detector situated on the axis of the microscope (Bright Field detector

(BF)) (Figure A.2). These two images contained complementary information, concerning the morphology (BF image) and the chemistry (ADF image) of the nano-object.

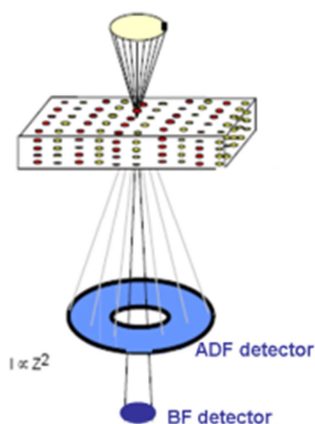


Figure A.2 - Principle of STEM mode with the detectors used to form the two images BF with transmitted electrons and the image DF with the diffused electrons.

Energy-dispersive X-ray Spectroscopy (EDX)

The composition of the Ag/Au nanoprisms was evaluated by EDX spectroscopy. This technique allowed to determine the qualitative elementary composition of a sample by investigating its emitted X-ray spectrum when it is excited with a focused electron beam. All elements can be detected since each one has a unique atomic structure allowing a unique set of peaks on its X-ray spectrum. The characteristic X-rays result from the electron transitions between inner orbits (K, L or M), which are normally full, when the sample is excited by an electron beam. An electron is excited and removed from the inner orbit and a vacancy is created. Another electron from an orbit further out can thus fill the hole, and the difference in energy between the outer and the inner orbit may be released in the form of an X-ray. The number and energy of the X-rays emitted from the sample are measured by an energy-dispersive spectrometer. An element distribution image or “map” can be produced by scanning the sample with the incident beam.

Implementation of the TEM, HRTEM, STEM and EDX

The conventional TEM experiments were performed on a Philips CM20 microscope operating at 75 kV at the Centre of Recherche Paul Pascal (CRPP, Pessac) and on a Hitachi H7650 microscope operating at an acceleration voltage of 80 kV at the Bordeaux Imaging Center (BIC, Bordeaux). The HRTEM, STEM and EDX analyses were performed with a JEOL 2200FS microscope operating at 200 kV at the Centre de Ressource en Microscopie Electronique et Microanalyse (CREMEM, Talence). For EDX analysis, a 1-nm probe was used in the bright field STEM mode and the Analysis program software from JEOL was used.

All the samples characterized by TEM and STEM were prepared as follow: one drop of the colloidal solution was deposited on carbon-coated copper grids. The particles were dried on the grid and placed in a box away from dust.

Scanning Electron Microscopy (SEM)

The SEM was used to visualize the elaborated nanoclusters by scanning them with an electron beam. The primary electrons interact with the atoms of the sample surface, causing emission of energetic electrons which are collected by a detector producing an image. The signal produced could contain information about the sample's surface size, shape, texture and composition.

High Resolution SEM was performed on a JSM 6700F microscope at the CREMEM. The nanoclusters were deposited on a pretreated silicon wafer. Firstly, the wafer was first cleaned in hydrofluoric acid solution (HF, 40%, VWR Prolabo) during 5 min to dissolve the protective layer of silica. Then it was amply rinsed with deionized water. To ensure a positive charge on its surface, the wafer was functionalized with APTES in an organic medium. For that, the wafer was successively dipped during 2 min in ethanol then toluene. The substrate was then immersed in a toluene solution of APTES (0.1% vol.) for 45 min. Finally, the inverse cycle was reproduced to wash the substrate (dip in toluene then ethanol and finally water). Finally, one drop of the nanoclusters suspension was deposited on the dried pre-treated silicon wafer then dried on the support and placed in a box away from dust.

- *Electron tomography*

Most of the techniques of imagery and spectroscopy introduced in an electronic microscope produce only a projection of the interesting signal in a plan (2 dimensions). This type of characterization is often insufficient because these nano-objects have a complex morphology and are structured and organized in 3 dimensions. The electron tomography is a work mode in TEM which is used to characterize in three dimensions the nano-objects. The characteristics can be the morphology, the porosity, the crystallography, the surface chemistry or the spatial organization of nanometric entities.

This technique is able to reconstruct the volume of the nano-objects from two-dimensional observations and is the only technique able to provide the resolved information in three-dimensions and in a range from micrometer to nanometer. It consists to record a series of image in projection of an object that is rotated around an axis orthogonal to the direction of electron beam, this series is commonly named: "tilt series". The intensities of equivalent pixels projections allow, through an

iterative process, to calculate the intensity of a voxel, the 3D-equivalent of a pixel, of the image of the object in 3D.

The experimental data for tomography were acquired by means of a spherical aberration (Cs) probe corrected JEOL 2100F transmission electron microscope with a field emission gun operating at 200 kV at the Institut de Physique et Chimie des Matériaux de Strasbourg (IPCMS). The STEM mode was chosen to obtain tomographic reconstructions free of diffraction artefacts and with a better resolution. Moreover, this mode offers the possibility to record two tilt series simultaneously with two detectors, the first in bright-field (BF-STEM) and the second in high angle annular dark-field (STEM-HAADF). Before the introduction of the sample in the microscope, the microscopy grids were gone to “plasma cleaner” (Solarus model). This device uses a combination of two gases argon/hydrogen, to obtain plasma used to clean the microscopy grids with the sample deposited on the membrane.

The implementation of electron tomography passes through four essential steps: the acquisition of series of projection images, the alignment of all the projections of the series, the calculation of the object volume from the series and finally its visualization and its analysis.

– Acquisition of projections series

The acquisition of STEM - HAADF tilt series was performed in the scanning mode, using the HAADF annular detector and a 10-cm camera length corresponding to inner and outer semi-angles for the HAADF detector of 60 and 160 mrad, respectively. Using a 100-mm condenser aperture provides a probe diameter of approximately 0.12 nm and to a current density of about $0.5 \text{ pA}/\text{Å}^2$. The depth of focus during the STEM acquisitions was estimated to be about 20 nm, ensuring thus that the whole nanoparticle is inside the focal volume. The acquisition software, plugged into the Digital Micrograph software, automatically increases by increments the tilt angle of the sample holder, simultaneously controlling the defocusing and the specimen drift at each tilt angle. In addition, it allows the automatic tuning of the focus of the beam in order to keep the focal point on the tilted specimen. An image was recorded for each position of the sample holder with an exposure time for each pixel in the images set to 40 ms, giving an acquisition time of 10 s for a typical 1024/1024 STEM-HAADF image. The pixel size in both images was 0.09 nm. Using a high tilt sample holder from the GATAN Company, HAADF tilt series was acquired with angles spanning from ± 70 every 2.5° .

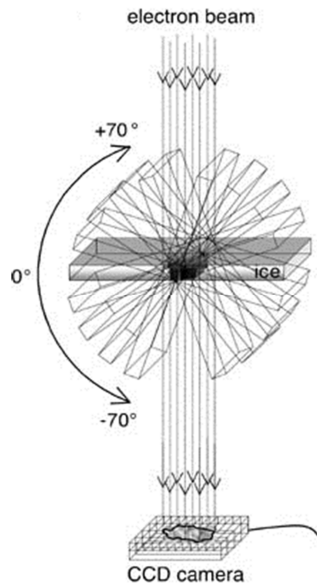


Figure A.3 - Principle of acquisition of a projection series.

– Alignment of images from projections series

Once the acquisition of the tilt series was completed, the images were first roughly aligned using a cross-correlation algorithm. The result consists in the convolution product between two successive images calculated from different relative positions of the second image in relative to the first one. The second image is then translated to a position corresponding to the best resemblance between the two. This operation is repeated for each binomial of two successive images.

A refinement of this initial alignment and a precise determination of the tilt axis direction were then obtained using the IMOD software. It consists in the use of geometrical template defined by fiducial markers. For that, just follow the variation of the different referential points defined on the image at tilt 0°, in function of the tilt angle then translate and rotate the others images in consequence. In general these references points are gold beads (from 5 to 30 nm), deposited on the membrane supporting the sample. These beads are much contrasted and they have the same shape whatever the observation direction.

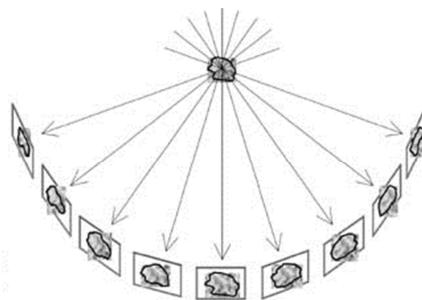


Figure A.4- Illustration of the images projected by a specimen at successive tilt angles. After translationally and rotationally aligning all of these projection images, the imaged object is.

– Reconstruction or calculation of the volume

The volume of the studied object was then calculated using algebraic reconstruction techniques (ARTs) implemented in the TomoJ software with the number of iterations not exceeding 20. Visualization and quantitative analysis of the final volume were carried out using Slicer and ImageJ softwares. To obtain the 3D models corresponding to the nanoparticle surfaces, a data segmentation procedure based on a simple selection of the voxels as a function of their intensities was used.

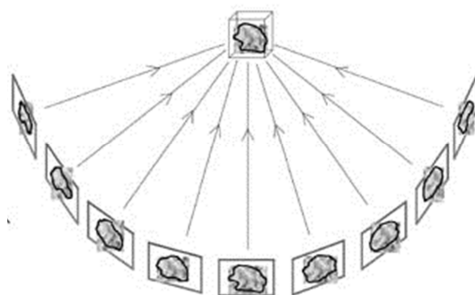


Figure A.5 – Reconstruction of the volume by a data segmentation procedure.

– Visualization and analysis of the volume

Finally, once the volume calculated, the last step concerns its 3D visualization, necessary to highlight the most interesting information for the study of the object. The most common technique consists in the extraction of slices with a defined orientation, with thickness equal to the pixel size in the start images. Another possibility is to represent the surface of the interesting object by using segmentation methods. This representation has the advantage to really be visualized in 3D.

• **Zetametry**

The ζ -potential measurements were performed on a Zetasizer 3000HS from Malvern Instrument which uses a method of capillary electrophoresis associated to an interferometer laser with Doppler effect. The exploitation device PCS v1.41 from Malvern was used to calculate the ζ -potential from the measured electrophoretic mobility (μ_e in $\mu\text{m}\cdot\text{s}^{-1}/\text{V}\cdot\text{cm}^{-1}$) through the following relation:

$$\zeta = 12.8 * \mu_e$$

The samples were prepared as follow: A volume of 50 mL of silica particles suspension ($\text{pH} \approx 7$) was divided in two beakers. In the first, few drops of NaOH 1M were added into the sol to obtain basic values of pH and samples of 8 mL were removed every 0.7 unity of pH. In the second, the same protocol was performed but this time by adding few drops of HNO₃ 1M to obtain acidic values of pH. The samples were injected in the zetameter at least 1 h after the sample preparation to ensure stabilization of pH. Finally, the pH of each sample was once again measured after analysis.

- *Spatial Modulation Spectroscopy (SMS)*

When a particle is illuminated by a light spot, it produces losses in the transmitted light intensity proportional to its absorption cross-section, which is the sum of absorption and diffusion. In the case of a nanoparticle, the light spot can be at most focused on a stain of the order of $1 \mu\text{m}^2$ and the losses introduced by the nanoparticle are minimal, of the order of 10^{-3} to 10^{-5} , which makes it very difficult to detect. However, if the position of the nanoparticle is modulated in the light spot at the frequency f , it is noted that the spot intensity is modulated at the modulation frequency of the nanoparticle (Figure A.6). By detecting the signal component at frequency f , then it is possible to detect the presence of a nanoparticle, and measure the absolute extinction coefficient. By performing this measurement at different wavelengths, it is possible to obtain the extinction spectrum of this particle.

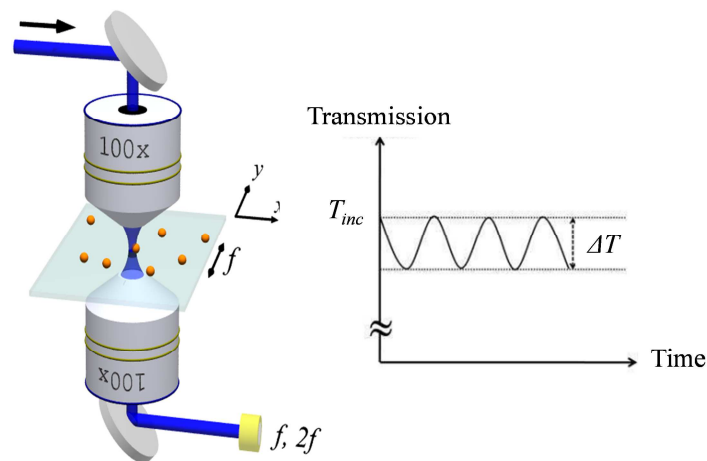


Figure A.6– Principle of the SMS to detect and record the extinction of single nano-objects. The right figure illustrates the change of transmitted power due to the modulation of the position of the particle in the focal area.

The SMS was performed at Laboratoire de Spectrométrie Ionique et Moléculaire (LASIM). In order to study a single nano-object, it is necessary that only one object is in the lighted area. For that, diluted samples are used. They are deposited on a substrate with a density lower than one particle/ μm^2 . The samples were prepared by spin coating on a transparent substrate (glass slice or TEM carbon grid). This method consists in the deposition of one droplet of colloidal suspension on the substrate in rotating. The solvent is removed by the effect of the centrifugal force. Once a single object deposited on a carbon TEM grid, it is lighted with a focused visible electron beam and the transmitted light after the nanoparticle was measured by a light detector (photodiode) connected to a lock-in amplifier (Figure A.7). A one-axis oscillation (1 kHz) is applied to the sample holder, in order to the isolated nanoparticle enters and returns periodically from the profile of the laser. The lock-in amplifier (frequency f) measures the change in the detected intensity between the two extreme positions of the nanoparticle. This variation is maximal when the particle is on the edge of

the Gaussian profile of the laser and equal to zero to the particle center. By slowly sweeping the sample, it is possible to make a map, each nanoparticle being identified by a pair of peaks.

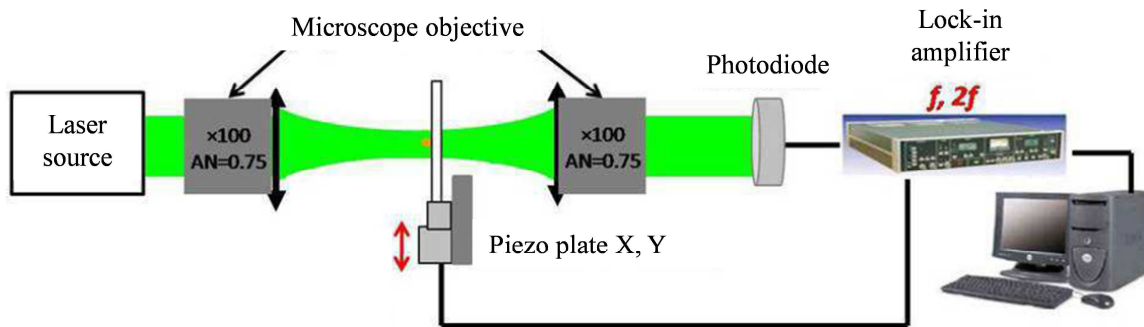


Figure A.7 - Experimental device of the SMS by using a laser source.

Annex 2: Anisotropic reactivity of silver nanoprisms

In the search for the development of new morphologies from this approach, a further study was performed on the formation of silver disks, gold nanocages and gold nanoprisms from the silver triangular nanoplates.

- *Etching of the tips with halides (X)*

Different authors studied the reactivity of Ag nanoprisms with halides [An08, Roh10]. According to these previous studies, the dissolution of silver only takes place on the tips. The experimental protocol to form silver nanodisks is described below.

Protocol 20 - Chemical reshaping of silver nanoprisms with halide

20 μL of HCl (0.1 M) was added at once into 1 mL of as-prepared silver nanoprisms (1.3×10^{14} part. L^{-1}) under stirring. The modified silver particles were then directly characterized without additional washing.

The Figure A.8 shows the color evolution of the Ag nanoprisms dispersion when Cl^- ions were added (2.0 mM). During oxidation, the initially blue color gradually evolved passing by purple, pink, orange and finally yellow.

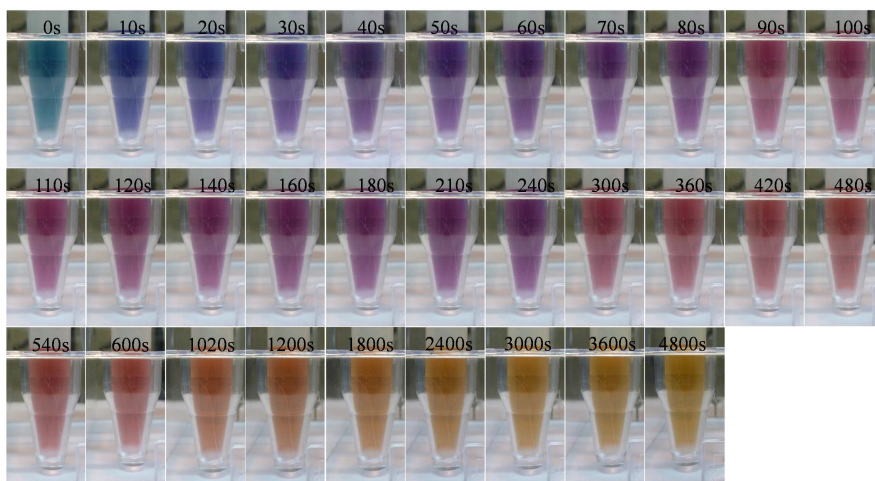


Figure A.8– Pictures of silver nanoprisms dispersion at different times after addition of chloride ions (2 mM).

The absorption spectra corresponding to the silver dispersion before and after the etching and TEM images of final products are presented in Figure A.9. Upon addition of Cl^- , the main surface plasmon peak of silver triangular nanoparticles exhibited a significant blue-shift (from 670 to 473 nm), indicating that the triangular particles had been transformed into disks. Moreover, the weak resonance band at 335 nm red-shifted until 340 nm due to an increase of the nanoparticles thickness. The TEM study confirmed these conclusions regarding the particle morphology. Monodisperse nanodisks with a mean diameter of about 30 ± 10 nm and a thickness of 12 ± 1 nm

were obtained. Most of them tended to stack upon each other face-to-face and stand vertically on their edge upon deposition on TEM grid.

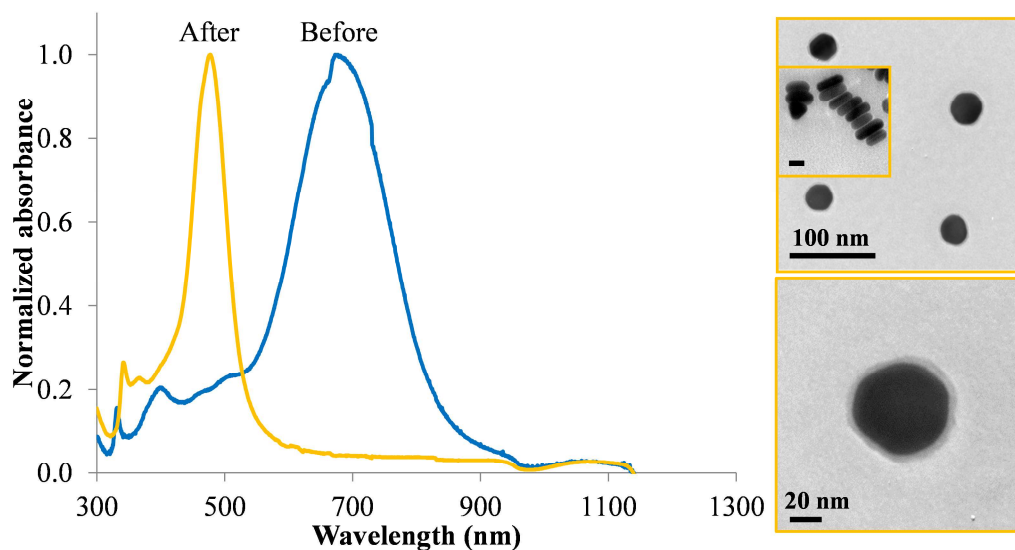


Figure A.9 – (Left) Absorption spectra of the Ag colloidal suspensions before and after etching with chloride ions and (Right) the TEM images of the obtained nanodisks. Inset scale bar = 20 nm.

Interestingly, the morphological transformation during the tip oxidation process could not be reversed; the thick disks generated from the truncation of Ag nanoprisms could not be regrown into triangles when incorporated in a solution containing AgNO_3 , PVP and citrate. This is due to the passivation of the silver surface by AgCl . This passivation layer (2-5 Å) is observable (Figure A.9).

- **Galvanic etching with gold precursor**

As previously mentioned the tetrachloroaurate ions are well known to oxidize the silver atoms in Ag^+ and selectively remove the silver atoms of {111} facets, keeping the basic triangular structure. This has been observed by others [Aherne10, Metraux03, Shahjamali12, Skrabalak07]. Indeed, gold triangular nanorings might be obtained by adding gold salt to the silver nanoprisms dispersion (Protocol 21). Since the ascorbic acid was in excess, the amount of gold salt added was calculated to correspond to a full consumption of the reducing agent.

Protocol 21 - Galvanic etching of silver nanoprisms with gold precursor

At the end of the silver nanoprisms synthesis, 12.4 mL of an aqueous gold(III) chloride trihydrate solution ($\text{HAuCl}_4 \cdot 3\text{H}_2\text{O}$, 2.5 mM) was dropwise added to the dispersion containing silver nanoprisms while stirring vigorously. The addition rate was set as 10 mL/h by using a syringe pump.

Figure A.10 shows the TEM images and corresponding absorption spectra before and after the addition of gold salt. When gold salt was added a strong modification in the optical spectrum was observed: the color of the dispersion evolved from blue to purple with an increase of the diffusion, traducing a blue-shift and a decrease in intensity of the predominant band of the absorption

spectrum (Figure A.10-a and -b). On the TEM images, we observe the substitution of silver nanoprisms by gold ring-like nanoparticles with a hollow interior. Note that gold appeared darker than silver by TEM due to its higher electron density.

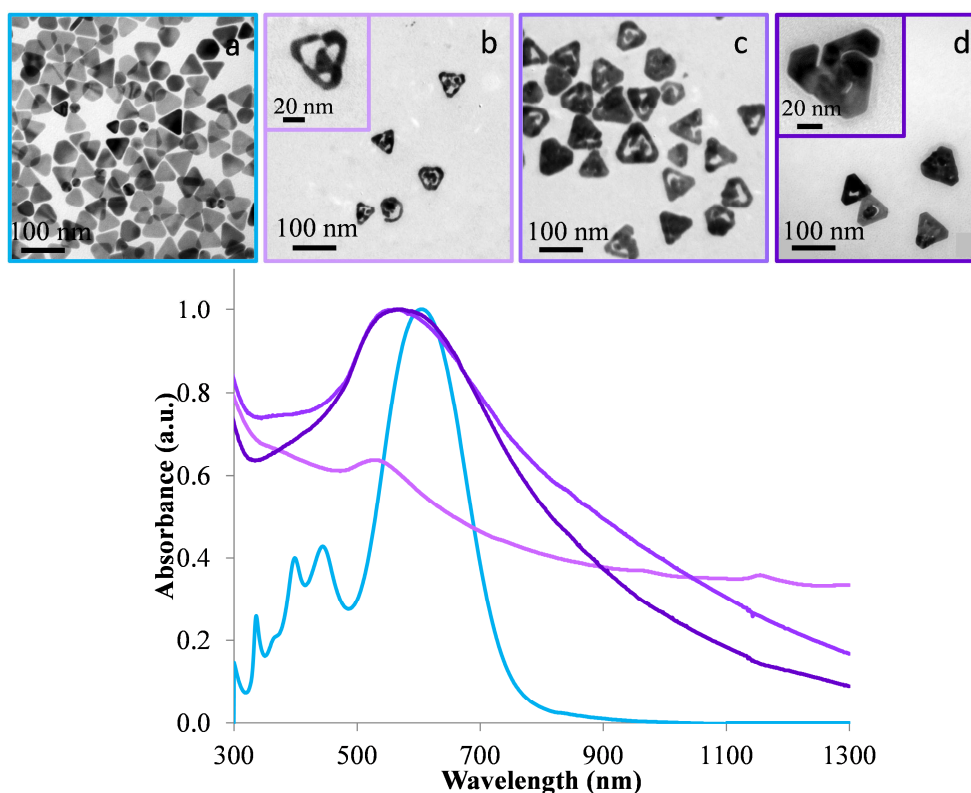
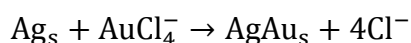
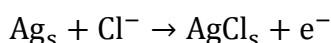


Figure A.10 – TEM images and corresponding absorption spectra of silver nanoprisms (a) before and after (b) galvanic etching with HAuCl_4 ; and after the refilling process repeated (c) 3 and (d) 6 times.

Initially, the reduction of gold ions was promoted at the surface of nanoprisms which served as nucleation sites due to the good matching between their crystalline structure (both gold and silver structures are fcc) and their lattice constants (4.0786 and 4.0862 \AA for gold and silver, respectively). Since the (100) surfaces constituting the lateral faces of silver nanoprisms were more reactive than the (111) surfaces of the top and the bottom of silver nanoprisms, gold preferentially deposited along the (100) faces promoting the lateral growth of silver nanoprisms through the following reaction:



However, because the redox potential of the $\text{AuCl}_4^-/\text{Au}$ ($+0.99 \text{ V}_{\text{NHE}}$) couple is higher than that of the Ag^+/Ag ($+0.799 \text{ V}_{\text{NHE}}$) couple, silver nanoparticles were simultaneously oxidized to Ag^+ with AuCl_4^- , but also with Cl^- ions released during the reduction of gold ions on the silver nanoparticles surface.



Since the corrosion-like process needed three Ag atoms to produce only one Au atom, the emergence of hole in the silver nanoparticles was inevitable. As a result, the hole continued to serve as an active site for the reduction process of gold ions (Figure A.11). Thus the dissolution of silver transformed each silver nanoprism into a structure with a hollow interior. The process occurred until the full consumption of the reducing agent.



Figure A.11 - Formation of a triangular gold nanoring from a silver nanoprism.

Once the gold triangular nanorings obtained, it was possible to refill the interior by adding additional gold salt and reducing agent as proposed by Shahjamali *et al.* [Shahjamali12].

Protocol 22 - Refilling of gold nanorings

1 mL of aqueous hydroxylamine hydrochloride solution (3 mM) and 1 mL of aqueous HAuCl₄ solution (0.27 mM) were added into the suspension containing the as-prepared gold nanorings through two separate tubes on a mechanical syringe pump under vigorous stirring. The addition rate was set as 1 mL/h. The process could be repeated as many times as desired.

The TEM images and absorption spectra corresponding to the backfilling process repeated three and six times are presented on Figure A.10 (-c and -d). TEM images revealed an increase of the gold nanorings thickness from approximately 5 to 16 nm and a decrease of the holes dimension in the interior of nanoparticles. This was traduced on the absorption spectrum by a progressive increase in intensity of the plasmon band near 550 nm associated to the gold nanoparticles with a concomitant decrease of the diffusion phenomenon at higher wavelengths. At this time, a co-reduction of AuCl₄⁻ and Ag⁺ (from the Ag nanoprisms oxidation) by hydroxylamine occurred inducing backfilling of holes by deposition of an alloy Ag/Au onto the inner edges of the nanorings.

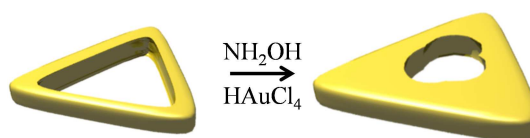


Figure A.12 - Backfilling process of gold nanorings by adding additional gold salt and reducing agent.

- *Formation of AuAg triangular nanoboxes from Ag nanoprisms as template*

In the presence of the gold precursor and an excess of reducing agent, the reduction of the gold precursor on the surface of the silver nanoprisms was promoted and the oxidation process was prevented [An08, Aherne09]. Thus, the silver nanoprisms can be converted in gold nanoprisms (Protocol 23).

Protocol 23 - Gold capping of silver nanoprisms

825 μL of ascorbic acid (10 mM) was added to 13.9 mL of the silver nanoprisms dispersion under vigorous stirring. Then 10 mL of an aqueous HAuCl_4 solution (10 mL, 0.5 mM) was dropwise added at a rate of 1 mL/h via a syringe pump into the reaction medium.

After the gold deposition on the 50-nm silver nanoprisms in presence of a large excess of ascorbic acid, only two resonances were observed on the absorption spectrum (Figure A.13-red curve). The interband contribution of gold was observed at short wavelengths and the main plasmon band was strongly red-shifted compared to the one of silver nanoprisms confirming the growth of the nanoprisms.

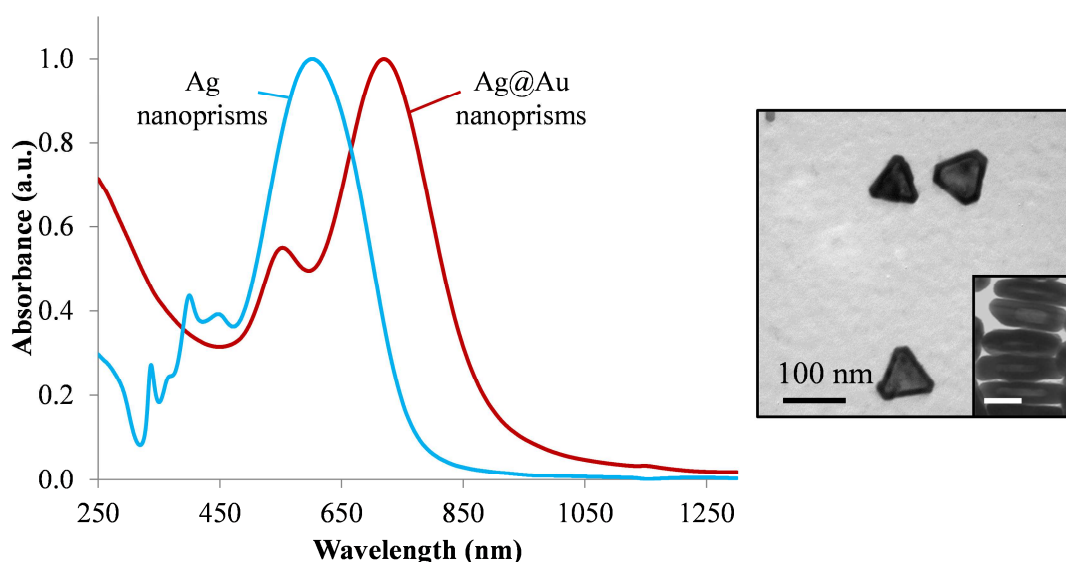


Figure A.13 - Absorption spectra and TEM images of Ag nanoprisms and Ag@Au triangular nanoplates after gold deposition. Inset scale bar = 20 nm.

TEM analyses revealed a homogeneous darker shell around the silver nanoprisms (Figure A.13). It confirmed the deposition of gold on the surface of silver nanoprisms. The triangular shape was maintained but the tips were slightly truncated. In order to elucidate the real composition of the as-obtained nanoparticles, an EDX analysis was performed on some isolated objects. The principle and the experimental procedure of this technique are described in the Annex 1. The EDX analysis was performed in STEM mode and the element distribution images called “map” was collected with 26 sweep counts for the gold and silver elements (Figure A.14). The map of the nanoprism clearly reveals a core-shell morphology with a higher proportion of both elements found in the shell. The corresponding electron diffraction pattern presents a six-fold rotational symmetry with a first set of plots assigned to the $\{220\}$ Bragg reflection and the second one (inner circle of plots) indexed to the forbidden $1/3\{422\}$ reflection traducing a homogeneous crystalline structure of the object. To study more finely the composition of the object, the percentage of each element was determined in a defined area along a line from one tip of the nanoprism to its opposite side. Whatever the analysis

position on the particle we found a constant proportion of each element, typically 70% of gold and 30% of silver (Figure A.14-bottom left). Then by reporting the intensity of counts recorded for each element along the same area one observed a higher proportion of elements at both ends of the nanoprism (Figure A.14-bottom right). These observations suggested that the nano-objects exhibited core-shell morphology with a hollow core and a homogeneous and dense shell constituted by an Au/Ag alloy.

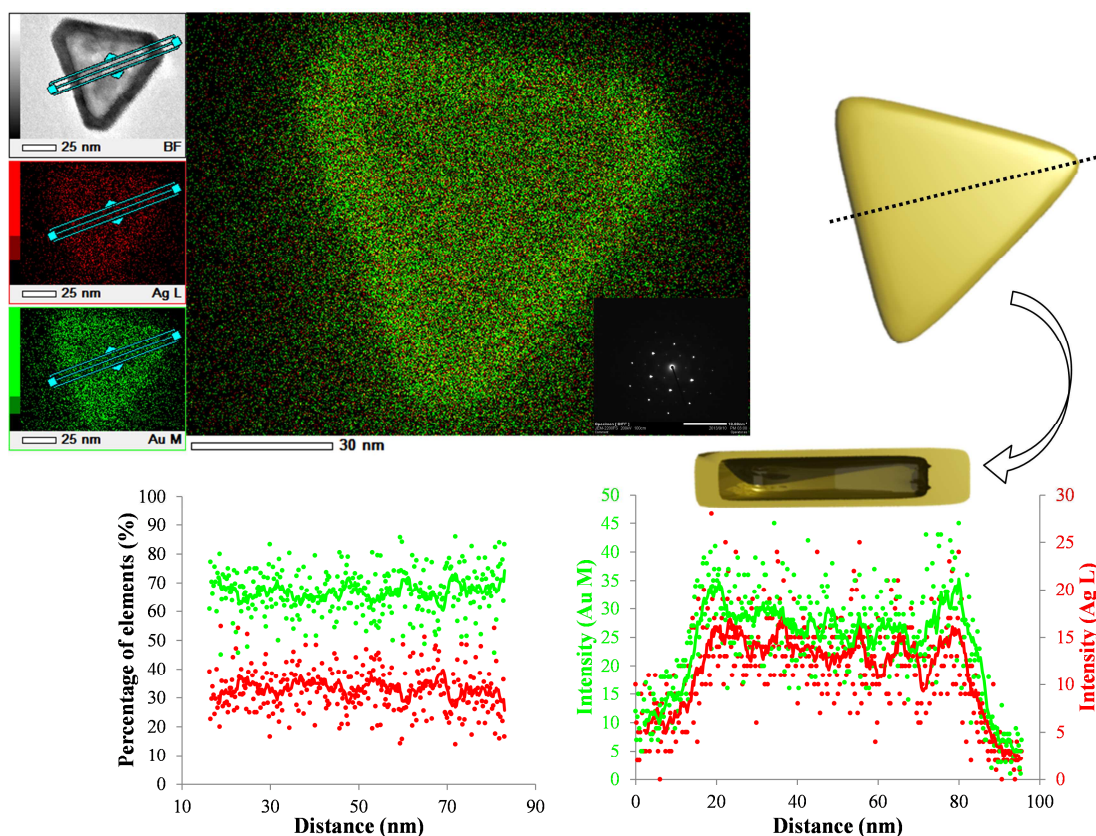


Figure A.14 – (Top) Elements map and schematic illustration of the Ag@Au nanoprism. Insert: corresponding electron diffraction pattern ([111] zone axis). (Bottom) –left: curve of percentage and –right: curve of counts intensity of the gold (green) and silver (red) in the selected area defined by the blue arrows on the elements maps.

Initially, the gold precursor was reduced by ascorbic acid on the surface of the silver nanoprisms with the concomitant oxidation of Ag atoms. Since the large excess of reducing agent in the medium, both Ag and Au ions were then co-reduced on the surface of the nanoprism. Due to their close lattice constants, a homogeneous alloy Au/Ag progressively formed around the initial silver nanoprisms which served as both template and silver ions source. Once every silver atom was oxidized and re-reduced elsewhere, hollow core appeared. If the medium was continuously alimented in gold precursor, the proportion of silver in the shell slowly decreased and a final outer gold shell could be obtained. These results are in accordance with the recent works of Aherne *et al.* which also proposed a similar growth mechanism [Aherne09, Keegan13].

Annex 3: Principle of the microfluidic evaporation approach and preliminary test of extended assembly

• Principle

The microfluidic assisted evaporation technique allows to concentrate a dilute colloidal suspension to shape-up a three-dimensional material of densely packed nanoparticles (typical size of the final material $10\ \mu\text{m} \times 50\ \mu\text{m} \times 1\ \text{cm}$) in only one step. The technique is based on the selective permeability of an integrated membrane to extract the solvent of dispersion but not the nanoparticles (Figure A.15).

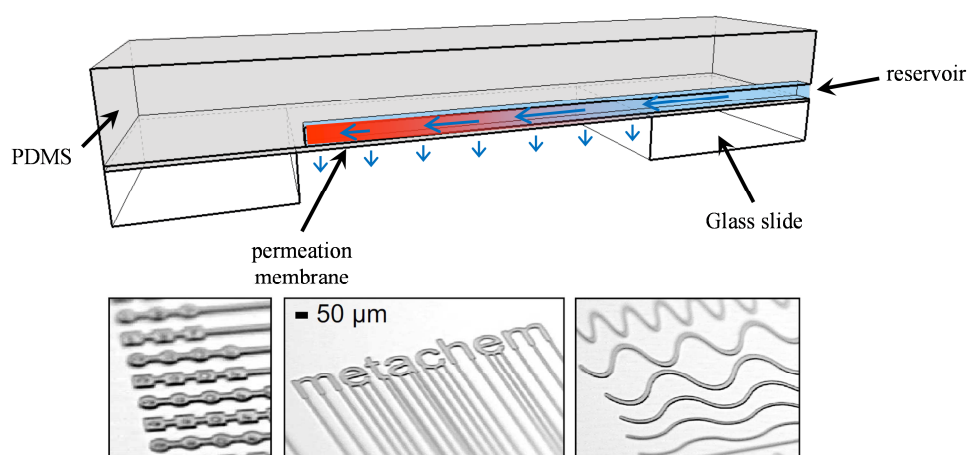


Figure A.15 - (Top) Evaporation-based cell used for guided assembly of nanoparticles. (Bottom) Images of several resist-on-silicon patterns used for the fabrication of microfluidic devices.

The geometry of the micro-channels is neatly defined by the soft lithography technique hence an infinite variety of designs could be realized (Figure A.15-bottom). Once the nanoparticles reach a given concentration, densification of the particles takes place leading to a dense state of nanoparticles growing from the tip of the micro-channel. The key parameter to a successful assembly via the micro-evaporation approach is the sufficient colloidal stability of the nanoparticles. From that, it works for a large set of solutes, from molecules to large colloids. However, the colloidal suspension should be as clean as possible. The presence of pollutants solubilized in water (excess of molecules, polymers...) can play the role of destabilizing agent. Indeed, the evaporation-based device leads to an increase of the concentration of all species although at different rates and the localized increase of pollutant can induce the aggregation of the dispersion.

• First results

Prior to assemble the raspberry-like nanoclusters in a dense 3D-material, some preliminary tests were performed only from the different silver nanoparticles used as satellites. All the

experimental details and further study on the mechanisms which occurred during the assembly by micro-evaporation are described in this article [Angly13, Masse13].

Initially the dilute suspension of silver nanoparticles (stabilized with PVP) exhibited a yellow color, upon the solvent extraction process, the color turned to red, purple and finally blue traducing the densification of the particles leading to a shape-up of a material (Figure A.16-c). At the end, a millimeter long dense colloidal extended assembly was obtained. SEM micrographs of the final extended assembly reflected a brick-like edifice with a neat, flat and large facet but the close-packed nanoparticles did not exhibit a well-defined organization (Figure A.16-a and -b).

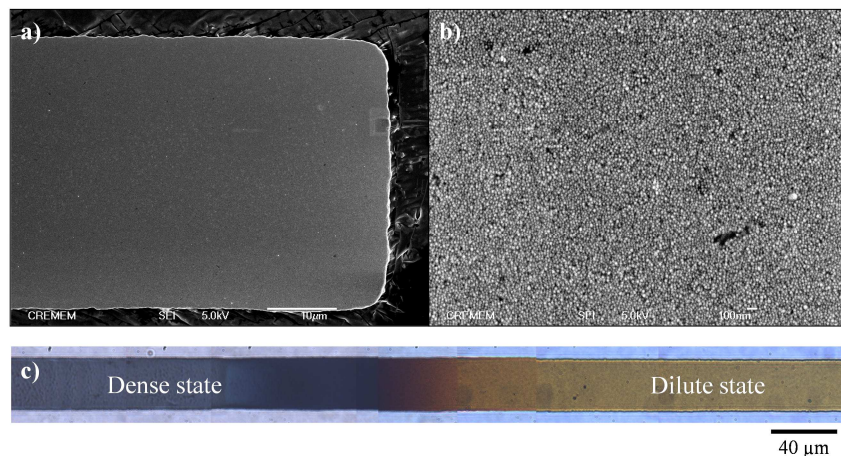


Figure A.16 – (a, b) SEM images of a dense array obtained from silver isotropic nanoparticles stabilized with PVP and (c) a panoramic optical image of the concentration gradient observed at the tip of the micro-channel.

Insofar as the suspension of the raspberry-like nanoclusters should be free pollutant, it will be necessary to encapsulate them in a silica shell to provide the electrostatic repulsion necessary to grant their colloidal stability at high concentration. Hence, we also assembled the silver spherical nanoparticles previously encapsulated in a silica shell. The bottom-up assembled final material nicely replicated the top-down designed microfluidic chambers (Figure A.17). The structure of the colloidal extended assembly was not ordered at long-range. The organization of the particles was probably limited by the slight size dispersity of the core-shell Ag@SiO₂ nanoparticles.

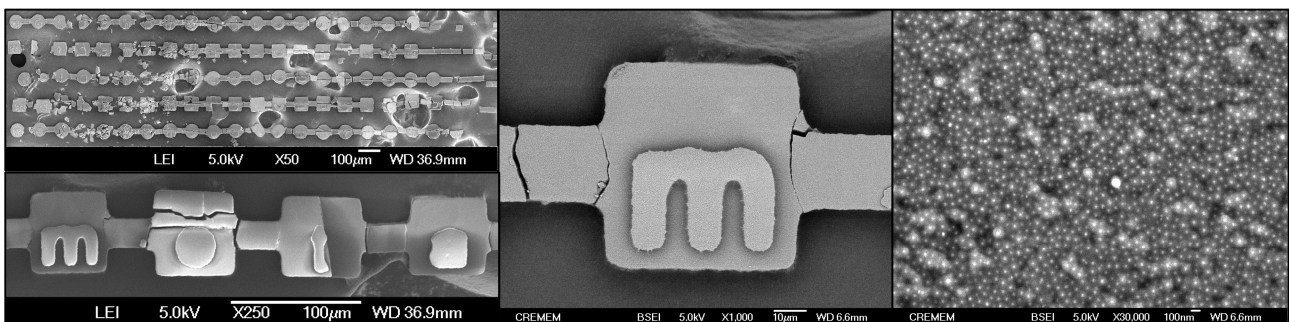


Figure A.17 – SEM images of colloidal crystal made of Ag@SiO₂ by micro-evaporation approach.

The extended assembly of silver nanoprisms, used as satellites in the preparation of the raspberry-like nanoclusters, was also performed. At the output of the synthesis, they were stabilized

with both PVP and citrate. Note they could not be washed enough to eliminate all the molecules in excess due to their low stability induced by their anisotropy. Upon the evaporation process, a color evolution of the colloidal suspension from light blue to dark red was observed (Figure A.18-b). As previously, the structure of the extended assembly finely replicated the shape of the microfluidic channel (Figure A.18-a). Firstly a dense 3D-material of nanoprisms seemed to be formed, but a closer inspection of the extended assembly revealed a “tubular” structure with all the particles concentrated along the walls of the micro-channel (Figure A.18-c and -d). Inside this structure, a “viscous film” was observed probably due to the agglomeration of the residual molecular species (PVP and citrate) still present in suspension.

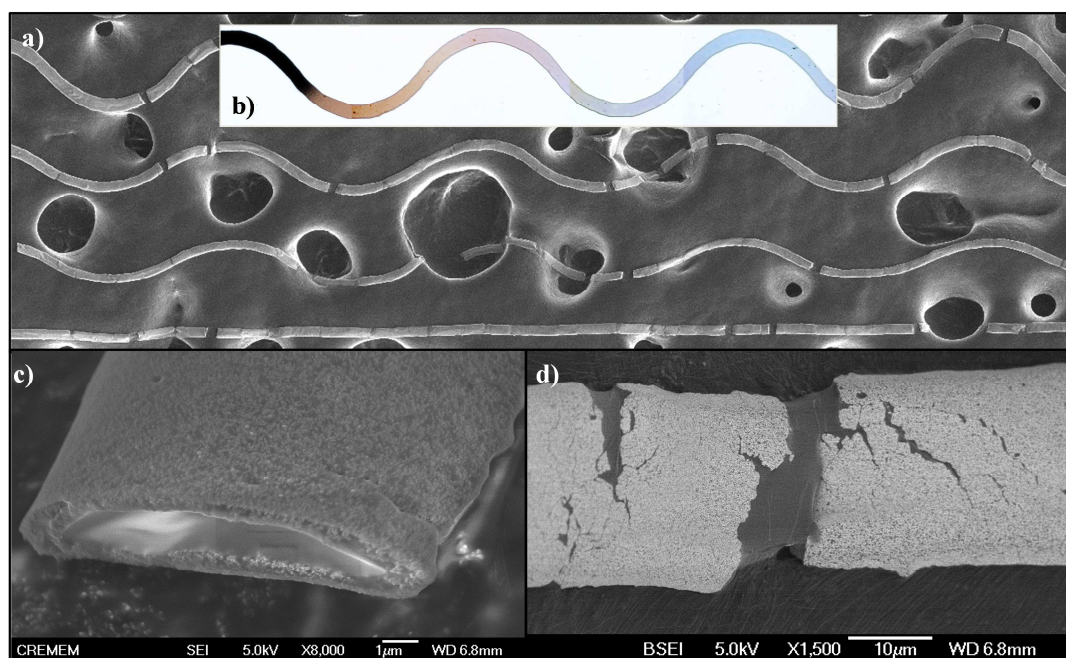


Figure A.18 – (a, c, d) SEM images of the arrays obtained from the dilute suspension containing nanoprisms stabilized with PVP and citrate. (b) Optical panoramic image of a gradient of concentration observed in the micro-channel.

Thus it appeared crucial to eliminate all pollutants initially present in suspension prior to assemble them via the micro-evaporation process. The encapsulation of the nano-objects in a silica shell also appeared as a well-compromise to clean the colloidal suspension without degrading the fragile particles or clusters and thus to ensure a sufficient colloidal stability for the further extended assembly.

Moreover, to avoid the precipitation of both pollutants (if there) and nanoparticles at the same level in the micro-channel, a colloidal filter was constructed. It is based on a millimeter-long colloidal crystal PS beads (diameter of 200 nm) permeable to water but not to nanoparticles (pores' size ~ 10 nm). Thus, the water along with traces of pollutants can flow inside the colloidal filter which retains the nanoparticles, forcing them to pack and grow without any pollutant. This work is described in more details in this article [Angly13]. This improved micro-evaporation process containing a bed of latexes as filter was applied to the assembly of the raspberry-like nanoclusters

constituted of silver spherical nanoparticles around silica core and encapsulated in a thin silica shell (Figure A.19-a). After the junction with the colloidal filter, the raspberries form a tightly-packed state with extended dimensions. However many defects were still observed inducing a random organization of the nanoclusters in the 3D material.

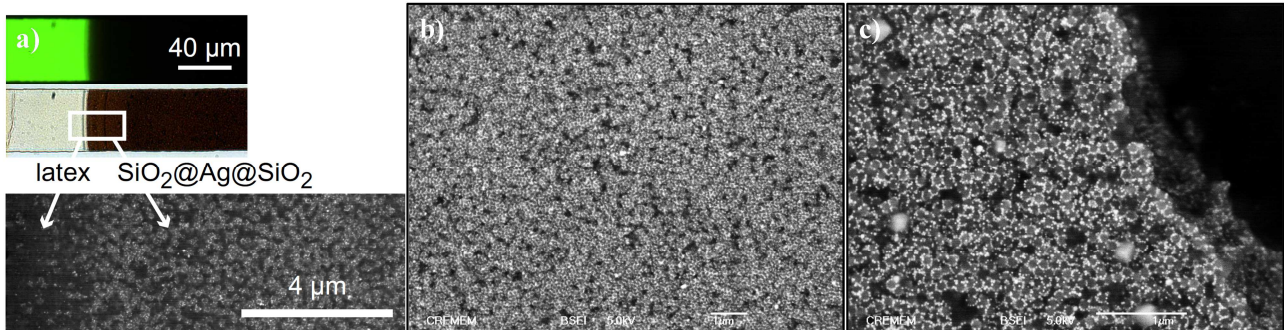


Figure A.19 – (a) Image of the simple junction between the bed of large latexes as colloidal filter (tagged with fluorescein) and the raspberry-like nanoclusters. (b, c) SEM images of the extended assembly obtained from the dilute suspension containing raspberry-like nanoclusters encapsulated in a silica shell (SiO₂@Ag@SiO₂).

- *Optical properties of the extended assembly of silver spherical nanoparticles*

The 3D-material from the extended assembly of silver spherical nanoparticles (or nanoclusters) exhibited relatively flat and large faces. It is randomly close-packed so the interparticle distance was very small compared to the incident wavelength. The large dimensions and the high degree of homogeneity of the material allowed a direct optical characterization by using spectroscopic ellipsometry in order to determine the refractive index of the 3D-material [Baron13]. From the optical measurements, it appeared that the extended assembly of the silver spherical nanoparticles induced a strong red-shift (from 400 nm to 616 nm) and broadening of the main plasmon resonance (Figure A.20-red curve). These significant changes of the resonance properties came from the strong interparticle coupling which was large due to the random close-packing of the silver nanoparticles in the extended assembly. The material had a real part of the refractive index which rose across the visible spectrum from 0.5 to 3.7 at 700 nm with decreasing absorption above 650 nm well into the IR (Figure A.20-blue curve).

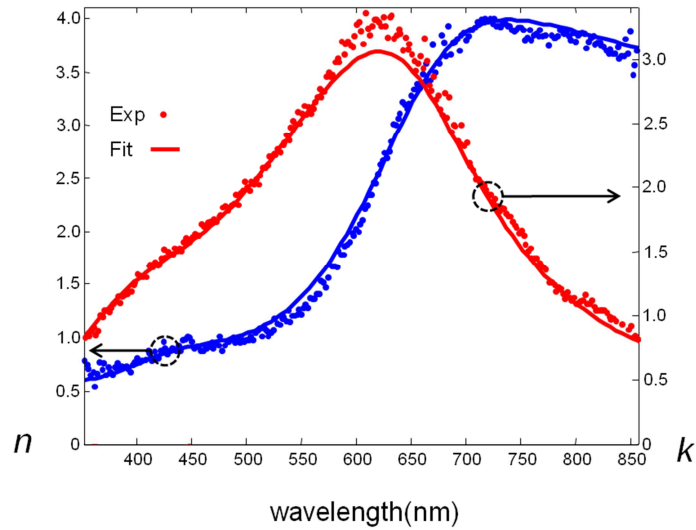


Figure A.20 – Spectral evolution of the measured real (blue) and imaginary (red) part of the refractive index of the extended assembly of silver spherical nanoparticles. Dots represent the values obtained by ellipsometry and the continuous lines represent the fit using the Lorentz-oscillator model for the dielectric constant of the material.

Thus, it appears that the microfluidic evaporation approach allows to build-up a homogeneous optical metamaterial with large dimensions from a diluted suspension of silver spherical nanoparticles. This kind of material reach high values of refractive index and low absorption in the deep red and the near-IR part of the spectrum.

Annex 4: Raman gain properties of the raspberry-like nanoclusters

The SERS is a powerful technique used for the detection of traces of organic molecules. It is based on the Raman gain which is due to the exaltation of the electromagnetic field in the vicinity of metal nanoparticles. This enhancement of Raman intensity comes from the entry in resonance of the surface plasmon. In presence of hot spots, the detection of a single molecule becomes possible because of the huge exaltation of the Raman scattering cross-section. However, the Raman experiments performed in colloidal suspensions give non-reproducible gains more or less varying from one measurement to the other. In order to obtain a better reproducibility in the results, it appears preferable to prepare substrates containing a large amount of coupling particles generating hot spots.

Some preliminary tests of SERS effects were performed with the raspberry-like nanoclusters containing the 10-nm gold nanoparticles attached on the PEM silica beads and stabilized with PVP. The experiments were performed by the N. Felidj group at the Itodys (Paris). The exaltation of the Raman scattering was performed by using a probe molecule: the trans-1,2-bis(4-pyridyl)ethylene (BPE, Figure A.21). For all the experiments, the wavelength of the laser was 633 nm and the concentration of BPE in the aqueous solutions was fixed to $1 \times 10^{-5} \text{M}$. At this concentration, the detection of BPE was not allowed without SERS exaltation.

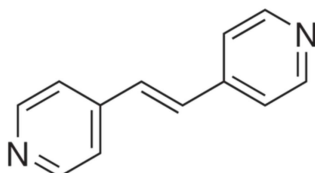


Figure A.21- Molecular structure of BPE

Before to deposit the nanoclusters onto an appropriate substrate, first tests were performed by adding the probe molecule directly into the aqueous colloidal suspension in order to validate the SERS effect. The Figure A.22 shows the extinction spectrum of the colloidal suspension containing the raspberries and the PBE. We observed exclusively the plasmon band characteristic near 560 nm of the gold nanoclusters since the PBE did not absorb in the visible range. The plasmon band presented similar look and no modification of its position was observed after the addition of PBE traducing the good stability of the PVP-stabilized nanoclusters in presence of the probe molecule.

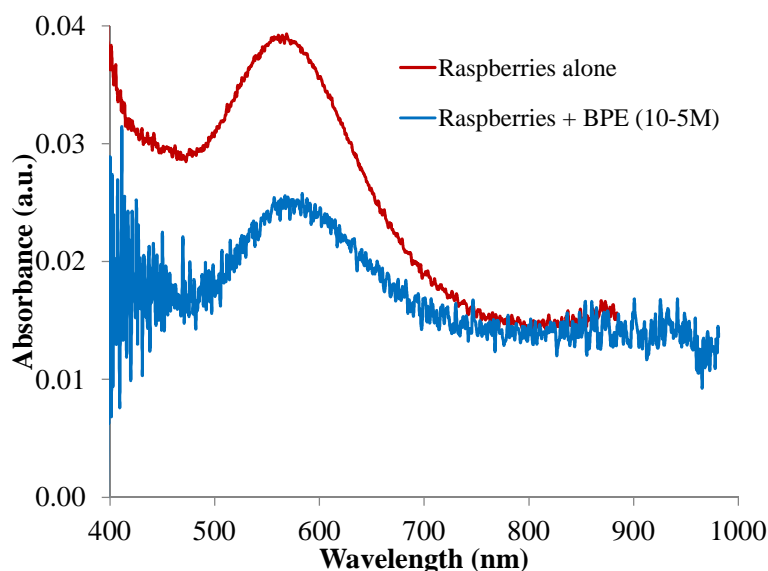


Figure A.22 - Extinction spectra of the suspension containing the 10-nm gold raspberry like nanoclusters alone and the one containing both raspberries and the probe molecule BPE (10^{-5}M).

The SERS spectra of the colloidal suspension before and after the addition of 10^{-5}M of PBE were presented in the Figure A.23. When the PBE was present in the solution, one observed the appearance of an intense doublet of bands near $1600\text{-}1640\text{ cm}^{-1}$ and another less intense band with a wavenumber lower than 1200 cm^{-1} . The wavenumbers and assignments for these three major bands are given in the table next to the SERS spectra [Zhuang07]. The longer mixing time of PBE with the colloidal suspension, the higher Raman intensity of the molecule. After 24h the intensity became stable.

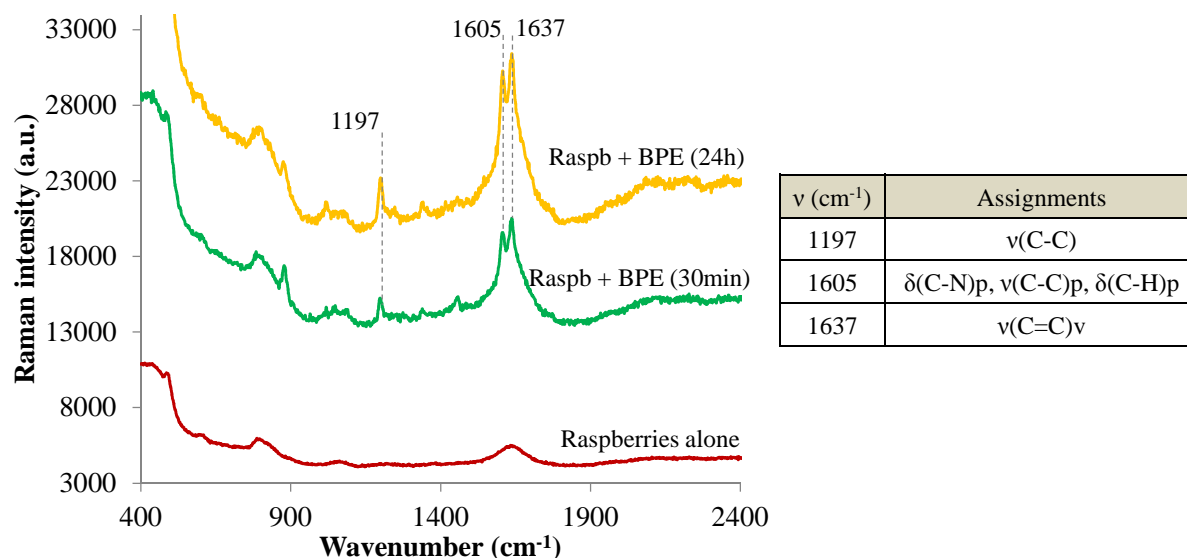


Figure A.23 – (Left) Raman spectra of raspberries suspension before and after (30 min and 24h) the PBE addition (10^{-5}M). (Right) Table of observed vibration bands of BPE. Abbreviations: ν , stretching; δ , bending vibrations; p, pyridyl; v, vinyl.

Since the detection of the PBE in the suspension, this first result allowed to bring out the production of hot spots on the surface of the raspberry-like nanoclusters due to the coupling between the gold nanoparticles. The nanoclusters were previously stabilized with PVP which decrease the interaction between the molecules and the metal particles and thus decrease the signal

intensity. Thereby, in order to improve the detection and obtain a more intense Raman signal, it would be preferable to adsorb the probe molecule directly on the surface of the raspberries before to stabilize them with PVP.

As previously mentioned, in order to obtain the most reproducible Raman signal, it was necessary to deposit the nanoclusters on a substrate. The samples preparation for SERS measurements is described in Protocol 24. The spectrum of the PBE deposited on the prepared substrate exhibited a better defined Raman signal of the PBE with the presence of the doublet of bands near 1600-1640 cm^{-1} and the single band near 1200 cm^{-1} (Figure A.24-c)

Protocol 24 – Samples preparation for SERS experiments

A substrate of Indium Tin Oxide (ITO) was immersed for 30 min in an ethanolic solution containing APTMS (10 %vol.). It was then rinsed, dried and heated at 100°C. After 1 h of heating, the APTMS-modified ITO substrate was immersed in the colloidal suspension containing raspberry-like nanoclusters for 12 h then dried. Finally, the substrate was immersed in the aqueous PBE solution (10^{-5}M) during 24 h then washed and dried before SERS measurements.

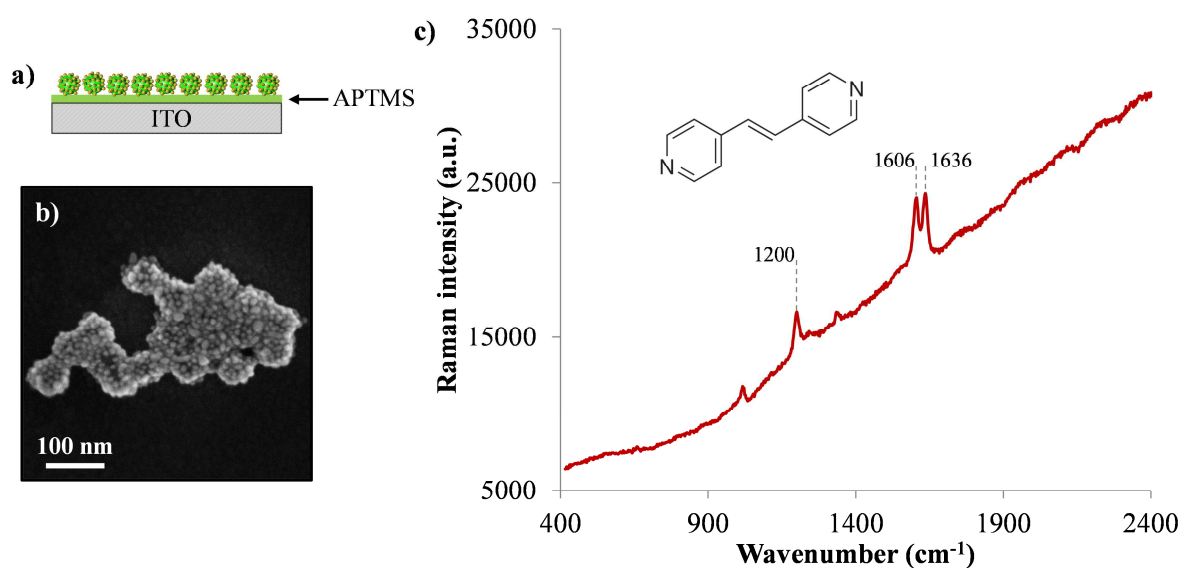


Figure A.24 – (a) Schematic illustration and (b) SEM image of the SERS substrate prepared by deposition of nanoclusters on an APTMS-modified ITO substrate. (c) SERS spectrum of the DPE molecules deposited on the prepared substrate.

However, on the SEM image of the substrate, one could observe an agglomeration of the nanoclusters and a coupling can occur in between the raspberries. It was thus tricky to define the origin of the SERS effect which could be due to the coupling of the gold satellites on the surface (“intra-nanocluster”) or to the coupling between the raspberries (“inter-nanocluster”). To discriminate these two coupling modes, it will be interesting to use a substrate with holes obtained by lithography permitting to fix and study isolated nanoclusters (Figure A.25). Once the preparation

of substrate optimized, it will be interesting to study the influence of the size, shape and composition of the satellite particles.



Figure A.25- Schematic illustration of a substrate presenting a network of lithographed holes in which only one nanocluster could be deposited.

Annex 5: List of reagents

Name	abbreviation	chemical formula	purity	provenance
Ammonium hydroxide		NH ₄ OH	28-30%	J.T. Baker
<i>L</i> -Arginine		C ₆ H ₁₄ N ₄ O ₂	≥ 98%	Sigma-Aldrich
<i>L</i> -Ascorbic acid	AA	C ₆ H ₈ O ₆	99%	Sigma-Aldrich
Bis(p-sulfonatophenyl) phenylphosphine dihydrate dipotassium salt	BSPP	C ₁₈ H ₁₃ K ₂ O ₆ PS ₂ ·2H ₂ O	≥ 99%	Sigma-Aldrich
Cyclohexane		C ₆ H ₁₂	≥ 99.7%	Sigma-Aldrich
4,4'-diazido-2,2'-stilbenedisulfonic acid disodium salt	DAS	C ₁₄ H ₈ N ₆ Na ₂ O ₆ S ₂ ·H ₂ O	≥ 99%	Fluka
Ethanol		C ₂ H ₆ O	99%	Atlantic Labo
Ethylene glycol	EG	C ₂ H ₆ O ₂	99%	J.T. Baker
Glycerol		C ₃ H ₈ O ₃ ·xH ₂ O	≥ 86%	Sigma-Aldrich
gold (III) chloride trihydrate		HAuCl ₄ ·3H ₂ O	99.99%	Sigma-Aldrich
Hydrochloric acid		HCl	37%	VWR Prolabo
Hydroxylamine hydrochloride		NH ₂ OH·HCl	99.0%	Sigma-Aldrich
<i>L</i> -malic acid disodium salt		C ₄ H ₆ O ₅	≥ 99%	Sigma-Aldrich
(3-mercaptopropyl)trimethoxysilane	MPTMS	HS(CH ₂) ₃ Si(OCH ₃) ₃	95%	Sigma-Aldrich
11-mercaptoundecanoic acid	MUA	C ₁₁ H ₂₂ O ₂ S	98%	Sigma-Aldrich
11-mercaptoundecyl)- <i>N,N,N</i> -trimethylammonium bromide	MUTAB	C ₁₄ H ₃₂ BrNS	95 %	Sigma-Aldrich
<i>N</i> -[3-(trimethoxysilyl)propyl] ethylenediamine	EDPS	C ₈ H ₂₂ N ₂ Si	97%	Sigma-Aldrich
Nitric acid		HNO ₃	65 wt.%	Scharlau
Phosphate buffered saline pH7.4	PBS			Sigma-Aldrich
Poly-(vinylpyrrolidone)	PVP	(C ₆ H ₉ NO) _n , M _w ~ 55,000 g.mol ⁻¹		Sigma-Aldrich
Poly(diallyldimethylammonium chloride)	PDDA	M _w ~ 200-350,000 g.mol ⁻¹	20wt. %	Sigma-Aldrich
Poly(sodium 4-styrenesulfonate)	PSS	(C ₈ H ₇ O ₂ S) _n , M _w ~ 70,000 g.mol ⁻¹	30wt. %	Sigma-Aldrich
Potassium gold (III) chloride		KAuCl ₄	99.99%	Sigma-Aldrich
Silver nitrate		AgNO ₃	99.999%	Sigma-Aldrich
Sodium borohydride		NaBH ₄	99.8%	Sigma-Aldrich
Sodium 3-mercapto-1-propanesulfate	MPS	C ₃ H ₇ NaO ₃ S ₂	90 %	Sigma-Aldrich
Sodium succinate dibasic	succinate	C ₄ H ₄ Na ₂ O ₄	≥ 98%	Sigma-Aldrich
Sodium citrate dihydrate	citrate	C ₆ H ₅ Na ₃ O ₇ ·2H ₂ O	≥ 99%	Sigma-Aldrich
Tetraethyl orthosilicate	TEOS	C ₈ H ₂₀ O ₄ Si	≥ 90%	Sigma-Aldrich

Annex 6: Protocols

For all the experiments, any glassware was cleaned in a bath of freshly prepared aqua regia (HCl/HNO₃, 3:1), then rinsed thoroughly with H₂O and dried at 90°C in an oven before use. Ultrapure water (18.2 MΩ.cm⁻¹) was used directly from a LaboStar 7 UV TWF system (Odémi, Grisy, France).

- *Protocol 1 - Synthesis of silver spherical nanoparticles*

In two different vials, 16.9 mg of sodium hydrosulfide were dissolved into 10 mL of ethylene glycol (EG) and 450 mg of PVP (M_w ~ 55,000 g.mol⁻¹) in 15 mL of EG. Both solutions were left to age for 4 h under stirring. One hour and half after the preparation of both solutions, 60 mL of EG were introduced in a three-necked rounded flask equipped with a reflux condenser and heated at 150°C for 2 h 30, under stirring. The two others necks were sealed with septa. Two hours later, Argon flow was introduced in the rounded-beaker via needle with a large diameter. The extremity of the needle should be placed at the surface of the EG (not in the solution). Thirty min later, 35 μL of NaHS solution and 15 mL of PVP solution were introduced via a syringe in the EG. Then, 5 mL of EG solution containing 120 mg of silver nitrate were quickly introduced. During the first 5 min, the solution colored dark yellow, then orange after about 6 min. At this time, the reaction should be stopped. For that, the rounded-beaker was placed in an ice-bath and 50 mL of absolute ethanol was added to decrease more quickly the temperature of the reaction. Finally, the silver nanoparticles dispersion was firstly concentrated (from 130 to ~ 10 mL) by using a Millipore Stirred Ultrafiltration Cell with a regenerated cellulose membrane (100 kDa). Then they were transferred from EG to water by repeating 5 times the ultrafiltration cycle with an ethanol solution containing PVP (3 g/L) to ensure the colloidal stability of the particles and finally 5 times with ultrapure water.

- *Protocol 2 - Synthesis of 10-nm gold nanoparticles*

700 mL of ultrapure water were placed in a two-necked rounded flask mounted with a reflux condenser and heated at 100-110°C under moderate stirring. Then 50 mL of aqueous potassium gold(III) chloride solution (0.83 mM) were introduced in the reaction medium. When the gold salt solution reached 100°C, 75 mL of aqueous trisodium citrate solution (5.2 mM) were quickly added. The solution progressively colored from yellow to deep red. The stirring was maintained for 15-20 min at 110°C.

- *Protocol 3 - Synthesis of gold spherical nanoparticles*

A certain amount of 10-nm gold seeds dispersion was diluted to 20 mL of deionized water in a three-necked flask. Then 10 mL of a solution **A** containing KAuCl_4 and 10 mL of the reducing solution **B** containing trisodium citrate and AA, were added simultaneously but separately to the medium at room temperature via two syringe pumps under stirring and over a time of 45 min. As soon as the addition was complete, the mixture was brought to boiling ($T = 90^\circ\text{C}$) and was maintained at this temperature for about 1 h under stirring. Finally the solution was allowed to cool down. The solution **A** was prepared by diluting a KAuCl_4 stock solution (5.29 mM) to 10 mL and the solution **B** was prepared by diluting a mixture of an AA stock solution (56.8 mM) and a trisodium citrate stock-solution (34 mM) again to 10 mL. Note that the relative volume ratio (Au:AA:Citrate) of all three stock solutions were maintained constant for every growth (8:2:1). Once the diameter and the concentration of the gold nanoparticles determined, it was possible to use them as seed-particle for a next growth to calculate the required amount of gold precursor to achieve a certain particle diameter for a next growth.

For example, the synthesis of 20-nm gold nanoparticles using 10-nm gold seeds was performed as follows: 2 mL of 10-nm gold seeds ($[\text{AuNP10}] = 2 \times 10^{15} \text{ particles.L}^{-1}$) was added to 18 mL of deionized water in a three-necked flask. The solution **A** was prepared by adding 2.71 mL of KAuCl_4 stock solution to 10 mL, corresponding to the quantity of gold salt required ($n_{\text{Au}^{3+}} = 14.3 \times 10^{-6} \text{ mol}$). The solution **B** was separately prepared by adding 677 μL ($= 2.71/4$) of AA stock solution and 339 μL ($= 2.71/8$) of citrate stock solution to 10 mL of deionized water. The **A** and **B** solutions were added simultaneously but separately to the medium at room temperature via two syringe pumps under stirring and over a time of 45 min. Directly after the addition was complete, the mixture was brought to boiling ($T = 90^\circ\text{C}$) and is maintained at this temperature for about 1 h under stirring. Finally the solution was allowed to cool down.

- **Protocol 4 - Synthesis of silver seeds for the photochemical route**

A 47.5 mL aqueous solution containing silver nitrate (0.10 mM) and trisodium citrate (0.31 mM) was prepared in a 100 mL two-neck round beaker and immersed in an ice-bath. Argon was bubbled through the solution for 20 min to remove oxygen then the Argon flow was kept constant at the surface of the solution throughout the reaction. Under vigorous stirring, 1 mL of cold and freshly prepared aqueous sodium borohydride (50 mM) was quickly added into the solution. Finally, 0.5 mL of aqueous BSPP (5 mM) was added. After 1 h of reaction, the flask was removed from the ice bath. Stirring and argon flow were maintained for 5 h at room temperature. The solution colored light yellow after NaBH_4 addition and the color intensified as the reaction continued at room temperature reflecting the formation of tiny particles ($d < 5 \text{ nm}$) in the solution. The seeds were then used for the photo-conversion process 4 h after their preparation.

- ***Protocol 5 - Synthesis of silver seeds for the chemical approach***

Typically, 49 mL of an aqueous solution containing AgNO_3 (0.1 mM) and trisodium citrate (0.3 mM) were prepared in a 100 mL two-necked round bottom flask and immersed in an ice-bath. The solution was bubbled with argon under constant stirring for 30 min to remove oxygen. Then the argon flow was kept constant at the surface of the solution throughout the reaction. Under vigorous stirring, 0.5 mL of aqueous NaBH_4 (cold and freshly prepared, 50 mM) was quickly added into the ice-cold solution. The reaction was allowed to proceed for 15 min, and during this time, 3-5 drops of NaBH_4 solution were added every 2 min to the solution to ensure complete reduction of the Ag^+ ions. Finally, 0.5 mL of aqueous PVP or PSS (5 mg/mL) and 0.25 mL of NaBH_4 were added to the solution in a drop wise fashion over a 5-min time period. After 1 h of reaction, the flask was removed from the ice bath. Stirring and argon flow were maintained for 4 h at 20°C to allow the excess of borohydride to be decomposed by water.

- ***Protocol 6 – Preparation of silver nanoprisms***

Typically, 100 mL of ultrapure water were mixed with 100 mL of aqueous AA (0.5 mM), 3.5 mL of as-prepared 4 h-aged seeds, 38 mL of aqueous PVP (0.7 mM in terms of monomer units), 38 mL of aqueous trisodium citrate (30 mM) in a 500 mL round flask. Then, under magnetic stirring, 12.5 mL of aqueous AgNO_3 (2.5 mM) was added to the solution in a dropwise fashion with a rate of addition fixed at 10 mL/h. The solution progressively changed color via yellow, orange, pink, purple and finally blue then it was intensifying as the addition of silver precursor was continuing. Throughout the reaction, the mixture was maintained under ambient atmosphere and at $\sim 20^\circ\text{C}$. Moreover, the silver precursor solution and the round flask containing the growth solution were protected from light exposure.

- ***Protocol 7 - Synthesis of gold seeds stabilized with citrate only***

250 μL of an aqueous solution of KAuCl_4 (10 mM) and 500 μL of an aqueous citrate solution (10 mM) were introduced into 20 mL of water under moderate stirring. Then 30 μL of a cold aqueous NaBH_4 (0.1 M) solution was quickly added under vigorous stirring. Stirring was maintained for 1 h at 20°C .

- ***Protocol 8 – Coupling of MUA (or MPS or MUTAB) in aqueous medium***

The grafting of MUA on the silver particles surface was performed directly in the growth medium. A volume V_{MUA} – calculated by the equation I.16 – of a 25 mM MUA aqueous solution

adjusted at pH 10 corresponding to an excess of 50 compared to the grafting density of MUA ($d_{\text{MUA}} = 4$ molecules/nm²), was quickly added into the silver suspension, under magnetic stirring. The growth solution and the MUA solution were pre-adjusted to pH 10 in order to solubilize the molecules in water. The reaction mixture was stirred overnight. In order to eliminate the excess of thiols, the mixture was placed in two 45-mL tubes and centrifuged at 8000 g during 20 min at 20°C. The supernatant containing free thiols was removed and the bottom, containing the modified particles, was redispersed in water by sonication. This washing step was repeated 4 times. Same protocol was performed for the grafting of MPS (by considering $d_{\text{MPS}} = 4$ molecules/nm²) and MUTAB (by considering $d_{\text{MUTAB}} = 2$ molecules/nm²). However, for these two coatings it was not necessary to initially adjust the pH value of the solution.

- ***Protocol 9 – Synthesis of silica seeds***

345 mL of an aqueous solution containing 7.5 mM of L-Arginine were introduced in a 500-mL rounded-beaker. 22.5 mL of cyclohexane were added on the top of the aqueous solution and the mixture was heated at 60°C. 37.5 mL of TEOS were introduced in the top organic phase. The stirring was tuned in order to create an interface of constant area between both phases and was maintained during 24 h. Then the cyclohexane was removed in a rotavapor at 50°C under partial vacuum. The concentration in silica seeds was determined by dry extract.

- ***Protocol 10 – Growth of silica nanoparticles from 28 to 100 nm***

50 mL of ethanol, 5 mL of ammonium hydroxide (1 M), and 5 mL of the aqueous suspension of the silica seeds were mixed in a 150-mL round-beaker. 8.68 mL of TEOS diluted in 20 mL of absolute ethanol were added at a rate of 1 mL/h thanks to an automatic syringe pump. The final concentration of silica beads was determined by the dry extract method.

- ***Protocol 11 – Surface modification of silica beads with EDPS in ethanolic medium***

Under vigorous stirring, a volume V_{EDPS} of EDPS aqueous solution was quickly added to 20 mL of the suspension of the as-prepared silica nanoparticles. The reaction mixture was stirred overnight. Then the mixture was transferred in a 100-mL round beaker and 10 mL of glycerol were added under stirring. Once the dispersion homogenized, it was placed on a rotavapor and heated at 40°C for the extraction of the ethanol then at 70°C for the water, under reduced pressure during 1 h. A thermal treatment was then performed during 3 h at 100°C under partial vacuum. After cooling, 70 mL of ethanol was added under slow stirring. The mixture was placed in two 45-mL tubes and centrifuged at 15000 g during 20 min at 20°C. The supernatant, containing glycerol, ethanol and oligomers of silanes was removed and the pellet, containing the modified particles, was redispersed

in ethanol by sonication. This cycle was repeated 6 times. After the removal of the last supernatant, 100 mL of water was added. To promote the redispersion of the modified silica beads and maintain the adhesion of the polysiloxane film on the surface of the beads, an acidification was performed by gradual step of one pH unity, by adding a few drops of 1M acetic acid, under vigorous stirring. In acidic conditions (\sim pH 6), the silica beads started to disperse. The suspension was adjusted to 5 and kept under stirring during 24 h. The pH was again measured and readjusted to 5. The mixture was finally placed on a rotavapor at 40°C, under reduced pressure, to eliminate the residual ethanol. The suspension was redispersed in 100 mL of water and the concentration of the modified silica beads was determined by dry extract.

- ***Protocol 12 – Assembly of silver spherical nanoparticles on EDPS-modified silica cores***

Typically, in an Eppendorf tube, 0.2 mL of a diluted suspension of silica beads (5.16×10^{14} part/L) were dropwise introduced in 1 mL of the silver spherical nanoparticles suspension (5×10^{16} part/L). The mixture was stirred overnight at room temperature and protected from light exposure.

- ***Protocol 13 – Washing procedure of raspberry-like nanoclusters***

The colloidal suspension was diluted in 30 mL of an aqueous PVP solution (0.5 g/L). After 2 h, the mixture was three times washed by centrifugation at 3000 g for 20 min and redispersed in water.

- ***Protocol 14 – Encapsulation of nanoclusters with a 8-nm silica shell***

After centrifugation, nanoclusters were dispersed in a minimum of water (\sim 0.5 mL), the volume was completed to 4.94 mL with ethanol and 60 μ L of ammonium hydroxide were added to solution. Then 2 μ L of TEOS diluted in 200 μ L of ethanol were dropwise injected into the solution with an addition rate fixed to 0.5 mL/h.

- ***Protocol 15 – LbL adsorption of polyelectrolytes on silica particles***

Firstly, the silica nanoparticles were washed three times by centrifugation at 9000 g for 10 min and redispersed in a solution of phosphate-buffered saline (PBS) (0.01M) at pH 7.4. The solutions of 2 mg/mL PDDA and of 3mg/mL PSS were prepared in pH 7.4 PBS (0.01M). 10 mL of the dispersion of silica nanoparticles were added to 20 mL of the solution of PDDA. The adsorption was allowed to proceed for 30 min under stirring with a roller mixer from Stuart (SRT6D). The excess of PDDA was then eliminated by centrifugation at 6000 g for 10 min and the particles were redispersed in 10 mL of PBS. After three washing cycles, the colloidal suspension was injected into 20 mL of PSS solution. The adsorption procedure was similar to the one used for the PDDA layer.

Finally, a last layer of PDDA was assembled on the silica particles and the last washing cycle was performed in water. The final concentration in silica beads was determined by dry extract.

- ***Protocol 16 – Assembly of silver spherical nanoparticles on PEM-modified silica beads***

Typically, 1 mL of a diluted suspension of PEM-modified silica beads (1.5×10^{13} part/L) was dropwise introduced into 1 mL of the isotropic silver nanoparticles solution. The mixture was stirred overnight.

- ***Protocol 17 – Washing of raspberry-like nanoclusters***

10 mL of the colloidal suspension were diluted in 20 mL of an aqueous solution of 2 mg/mL PDDA. After 30 min, the mixture was washed three times by centrifugation at 3000 g for 20 min and redispersed in water.

- ***Protocol 18 – Strengthening of raspberry-like nanoclusters with DAS***

An aqueous solution containing 0.05 mM of DAS was prepared in dark. Then, 1 mL of the DAS solution was added to 1 mL of the PDDA-stabilized colloidal suspension in dark. After 4 h, the mixture was placed in a quartz cell and irradiated for 5 min under stirring with a 150 W Xenon lamp at a distance of 15 cm. Finally the suspension was washed by centrifugation at 4000 g for 10 min. The yellow supernatant containing the excess of free DAS was removed and the bottom was redispersed in water. The centrifugation cycle was repeated until the supernatant became free of DAS molecules i.e. until the disappearance of the DAS characteristic absorption band on the UV-Visible spectrum.

- ***Protocol 19 – Encapsulation of nanoclusters with a silica shell in biphasic medium***

Typically, 10 mL of the raspberry-like nanoclusters suspension were diluted into 200 mL of water in a 500-mL rounded-beaker. Then, 5 mL of an aqueous L-arginine solution (20.7 mM) were added to the medium under moderate stirring. 50 mL of cyclohexane containing 45 μ L of MPTMS were layered on the top of the aqueous suspension. After 1 h, the mixture was heated at 60°C and 5 mL of TEOS were introduced in the organic phase. The reaction was occurred for ~ 8 h. The mixture was then placed on a rotavapor at 50°C under vacuum to remove the cyclohexane. Finally the solution was allowed to cool down. In order to remove the excess of silane, the mixture was centrifuged at 3000 g for 10 min at 20°C. The supernatant, containing oligomers of silanes, was removed and the pellet, containing the encapsulated nanoclusters, was redispersed in ethanol by

sonication. This washing step was repeated 6 times with the three last redispersions performed in water.

- ***Protocol 20 - Chemical reshaping of silver nanoprisms with halide***

20 μL of HCl (0.1 M) was added at once into 1 mL of as-prepared silver nanoprisms (1.3×10^{14} part. L^{-1}) under stirring. The modified silver particles were then directly characterized without additional washing.

- ***Protocol 21 - Galvanic etching of silver nanoprisms with gold precursor***

At the end of the silver nanoprisms synthesis, 12.4 mL of an aqueous gold(III) chloride trihydrate solution ($\text{HAuCl}_4 \cdot 3\text{H}_2\text{O}$, 2.5 mM) was dropwise added to the dispersion containing silver nanoprisms while stirring vigorously. The addition rate was set as 10 mL/h by using a syringe pump.

- ***Protocol 22 - Refilling of gold nanorings***

1 mL of aqueous hydroxylamine hydrochloride solution (3 mM) and 1 mL of aqueous HAuCl_4 solution (0.27 mM) were added into the suspension containing the as-prepared gold nanorings through two separate tubes on a mechanical syringe pump under vigorous stirring. The addition rate was set as 1 mL/h. The process could be repeated as many times as desired.

- ***Protocol 23 - Gold capping of silver nanoprisms***

825 μL of ascorbic acid (10 mM) was added to 13.9 mL of the silver nanoprisms dispersion under vigorous stirring. Then 10 mL of an aqueous HAuCl_4 solution (10 mL, 0.5 mM) was dropwise added at a rate of 1 mL/h via a syringe pump into the reaction medium.

- ***Protocol 24 – Samples preparation for SERS experiments***

A substrate of Indium Tin Oxide (ITO) was immersed for 30 min in an ethanolic solution containing APTMS (10 % vol.). It was then rinsed, dried and heated at 100°C. After 1 h of heating, the APTMS-modified ITO substrate was immersed in the colloidal suspension containing raspberry-like nanoclusters for 12 h then dried. Finally, the substrate was immersed in the aqueous PBE solution (10^{-5}M) during 24 h then washed and dried before SERS measurements.

References

- [Aherne09] Aherne D., Charles D.E., Brennan-Fournet M.E., Kelly J.M., Gun'ko Y.K. *Langmuir*, 2009. 25(17), p. 10165
- [Aherne10] Aherne D., Gara M., Kelly J.M., Gun'ko Y.K. *Adv. Funct. Mater.*, 2010. 20(8), p. 1329
- [An08] An J., Tang B., Zheng X., Zhou J., Dong F., Xu S., Wang Y., Zhao B., Xu W. *J. Phys. Chem. C*, 2008. 112(39), p. 15176
- [Angly13] Angly J., Iazzolino A., Salmon J.B., Leng J., Chandran S.P., Ponsinet V., Desert A., Le Beulze A., Mornet S., Treguer-Delapierre M., Correa-Duarte M.A. *ACS Nano*, 2013. 7(8), p. 6465
- [Baron13] Baron A., Iazzolino A., Ehrhardt K., Salmon J.B., Aradian A., Vasyl K., Grigorenko A.N., Leng J., Le Beulze A., Treguer-Delapierre M., Correa-Duarte M.A., Barois P. *Optical Materials Express*, 2013. 3(11), p. 1792
- [Keegan13] Keegan G.L., Aherne D., Defrancq E., Gun'ko Y.K., Kelly J.M. *J. Phys. Chem. C*, 2013. 117(1), p. 669
- [Masse13] Masse P., Mornet S., Duguet E., Treguer-Delapierre M., Ravaine S., Iazzolino A., Salmon J., Leng J. *Langmuir*, 2013. 29(6), p. 1790
- [Metraux03] Metraux G.S., Cao Y.C., Jin R., Mirkin C.A. *Nano Lett.*, 2003. 3, p. 519
- [Roh10] Roh J., Yi J., Kim Y. *Langmuir*, 2010. 26, p. 11621
- [Shahjamali12] Shahjamali M.M., Bosman M., Cao S., Huang X., Saadat S., Martinsson E., Aili D., Tay Y.Y., Liedberg B., Loo S.C.J., Zhang H., Boey F., Xue C. *Adv. Funct. Mater.*, 2012. 22(4), p. 849
- [Skrabalak07] Skrabalak S.E., Au L., Li X., Xia Y. *Nature Protocols*, 2007. 2, p. 2182
- [Zhuang07] Zhuang Z., Cheng J., Jia H., Zeng J., Han X., Zhao B., Zhang H., Zhang G., Zhao W. *Vibrational Spectroscopy*, 2007. 43(2), p. 306

Titre : Synthèse et caractérisation de nano-résonateurs pour une application métamatériaux dans le domaine du Visible

Résumé :

Les métamatériaux forment une nouvelle classe de matériaux composites artificiels aux propriétés électromagnétiques extraordinaires. Ces propriétés inédites reposent sur l'inclusion, dans le métamatériau, de résonateurs plasmoniques dont la fabrication et l'assemblage posent un défi auquel se heurtent les techniques de gravure habituellement utilisées. Cette thèse est consacrée à la de ces nano-résonateurs de morphologie framboise, constitués d'un cœur diélectrique et de nanoparticules plasmoniques, sphériques ou triangulaires. Ces objets ont été élaborés en grande quantité tout en respectant la contrainte du milieu effectif qui impose des tailles très inférieures à la longueur d'onde. La réponse optique des nano-résonateurs individuels a été mesurée et comparée aux modélisations. Des résonances électriques et magnétiques intenses ont été mises en évidence. Ces objets sont prometteurs pour la première réalisation de matériau massif à perméabilité magnétique artificielle.

Mots clés : métamatériau, résonance plasmon, nanoparticule, nanoprisme, argent, or, silice, assemblage, couplage.

Title: Synthesis and characterization of nanoresonators for metamaterials application in the Visible range

Abstract:

Metamaterials are artificial composites materials exhibiting extraordinary electromagnetic properties. These original properties are based on the inclusion in the metamaterial of plasmonic resonators for which the fabrication and the assembly remain challenging. This thesis is dedicated to the synthesis through colloidal approach and the structural and optical characterization of these "raspberry-like nanoresonators" constituted of a dielectric core and spherical or triangular plasmonic nanoparticles.

These objects are elaborated in large amount while respecting the constraint of effective medium which requires sizes much smaller than the wavelength. The optical response of individual nanoresonators was measured and compared with theoretical simulations. Intense electric and magnetic resonances are highlighted. These objects are promising for the first elaboration of a bulk material with artificial magnetic permeability.

Keywords: metamaterial, plasmon resonance, nanoparticle, nanoprism, silver, gold, silica, assembly, coupling.